Device Integration for Silicon Microphotonic Platforms

by

Desmond Rodney Lim Chin Siong

Submitted to the Department of Electrical Engineering and Computer Science
in partial fulfillment of the requirements for the degree of

Doctor of Philosophy

at the

MASSACHUSETTS INSTITUTE OF TECHNOLOGY

June 2000

Author .....
Department of Electrical Engineering and Computer Science
May 12, 2000

Certified by .....
Lionel C. Kimerling
Thomas Lord Professor of Materials Science and Engineering
Thesis Supervisor

Accepted by .....
Arthur C. Smith
Chairman, Department Committee on Graduate Students

Device Integration for Silicon Microphotonic Platforms

by

Desmond Rodney Lim Chin Siong

Submitted to the Department of Electrical Engineering and Computer Science
on May 12, 2000, in partial fulfillment of the
requirements for the degree of
Doctor of Philosophy

Abstract

Silicon ULSI compatible, high index contrast waveguides and devices provide high density integration for optical networking and on-chip optical interconnects. Four such waveguide systems were fabricated and analyzed: crystalline silicon-on-insulator (SOI) strip, polycrystalline silicon (polySi) strip, silicon nitride strip and SPARROW waveguides. The loss of 15 dB/cm measured through an SOI waveguide was the smallest ever measured for a silicon strip waveguide and is due to improved side-wall roughness. The TM mode of a single mode polySi strip waveguide with a 1:2.5 aspect ratio exhibited, surprisingly, smaller loss than the TE mode. Further, analysis shows that high index contrast waveguides are more sensitive to polarization dependent loss in the presence of surface roughness. Single mode bends and splits in both silicon and silicon nitride were studied. 0.01 dB/turn loss has been measured for 2 micron radius silicon bends. Polarization dependent loss was also observed; the bending loss of a TM mode was, as expected, much larger than that of a TE mode. The splitting losses for two-degree Y-split was 0.15 dB/split. A 1x16 multi-mode interferometer splitter occupied an area of 480 sq-microns and exhibited loss of 3 dB. ULSI compatible waveguide structures integrated with micro-resonators have been studied. Qs of 10000 and efficiencies close to 100% were achieved in high index contrast ring resonators and Qs of 100 million were achieved in microsphere resonators. A thermal and mechanical tuning mechanism was demonstrated for micro-ring resonators. In addition, >95% coupling efficiency between SPARROW waveguides and microspheres was achieved, the first microspheres to be coupled to integrated optics waveguides. 1x4 wavelength division multiplexing devices have been, for the first time, demonstrated in high index contrast silicon and silicon nitride strip waveguide systems. These systems have a component density of 1-million devices/sq-cm. Higher order filters made from multiple rings exhibited flat top responses and the expected steeper roll-off resonance response. Integrated modulators and switches based on waveguides and rings were also studied. Finally, the integration of the components in systems applications was analyzed. A study of the effect of polarization and loss in silicon microphotonics waveguide systems is presented.

Thesis Supervisor: Lionel C. Kimerling
Title: Thomas Lord Professor of Materials Science and Engineering

Acknowledgments

Ad Maiorem Dei Gloriam

In the four years that it took for me to prepare this document, I learnt through trial and tribulation that fabrication of optical components was an undertaking I could not complete without the help of many people.

Thanks, Kim, for the guidance, for the intuition and for the patience especially in the years of slow progress; Professor Haus for the brilliant insight and for the encouragement; Professor Reif for the precious time and direction.

Thanks to Mike Morse and Harry Fujimoto at Intel and Paul Maki, at Lincoln Labs, for the fruitful collaboration and all the help with processing, without which this thesis would have been a lot thinner. Thanks also to Xiaoman for her TEM pictures.

To the staff and engineers, especially Joe Walsh, Paul Tierney and Vicky Diadiuk, at MTL, where I spent way too many hours inhaling purified air; for the help, I am grateful.

A special tribute to the friends I made while working together on projects which appear in this document: Andy, Anu, Christina, Dan, JP, Kazumi, Kevin, Laura, Shiou-Lin and Thomas: thanks for the long hours in lab spent arguing, laughing, talking and thinking.

To each and every member of EMAT, postdocs, graduate students, UROPs and Kim's awesome administrative staff, both past and present, thanks for the wonderful research and work environment. I learnt a lot and I hope I contributed a little too.

To all the friends, who, throughout the four years, helped keep me sane, thanks!

Thanks to my Mum and Dad; without you, there won't be me! Thanks for always pushing me to do more and for always being there for me.

Last but certainly not least, to my fianceé and soon to be wife, Beata. Thanks for your love, your understanding and for taking care of me over the past few months even through my most grumpy moments. I am totally clueless.

Dedicated to B and my parents.

Contents

List of Figures

List of Tables

Chapter 1

Introduction

1.1 Motivation for silicon microphotonics

Silicon microphotonics is the optical analog to silicon microelectronics, the foundation of the computer revolution. The idea in silicon microphotonics is to use fabrication techniques developed in the microelectronics industry and apply them to optics. In doing so, high density and high functionality optical circuits can be built. The applications for silicon microphotonics are three-fold: improving current micro-electronic technology by solving and alleviating interconnect problems; improving photonics technology by miniaturizing photonic systems with micro-electronic fabrication techniques and finally using the integration of both technologies in applications like optical sensors.

Since the fabrication of the first integrated circuit, silicon has been the semiconductor substrate of choice, with most integrated circuit chips being fabricated on silicon wafers. Silicon has significant advantages over many other semiconducting materials because it has a good oxide and is relatively easy to process. However, in certain niche applications, like in high speed, high performance applications and in optoelectronic applications, silicon is disadvantaged when compared to materials like gallium arsenide. These disadvantages stem from two main sources, the first being the indirect band gap nature of silicon, which implies a much longer minority carrier lifetime and more importantly, the lack of an efficient intrinsic light emission system. Furthermore, systems like GaAs exhibit much smaller effective electron mass than silicon resulting in higher electron mobilities, i.e. faster devices.

While integrated optoelectronics in III-V systems have been extensively studied, high degrees of integration have not yet been achieved. In this thesis, I explore the possibility of

using silicon in integrated sub-micron optoelectronic systems to take advantage of silicon's processing strengths to yield sub-micron devices which may be used to build systems with a high degree of integration and have applications in optical communications systems.

1.1.1 Optical interconnects for silicon I/O

As mentioned above, one potential application for silicon microphotonics is optical interconnects for silicon I/O. As devices are scaled to ever shrinking sizes and systems are clocked at ever increasing rates, over 1000 MHz at the time of writing, greater demands are being placed on interconnects. Interconnects cannot be scaled as rapidly as electronic devices due to electro-migration and RC delay [13]. Furthermore, interconnect delay has begun to dominate gate switching delay. Optical interconnects will alleviate such RC delay problems.

1.1.2 Optical interconnects for optical clocking

Optical interconnection may play an even more important role in a special form of interconnect – clock distribution. Current reports indicate that in high speed microprocessors, about 50% [14] of power is dissipated as a result of clock distribution requirements which in turn results in very stringent heat sink requirements. This problem is further compounded by the large number of pin-outs used for power distribution on a microprocessor, (for example, on the COMPAQ Alpha chip, over half the pin-outs are used for power distribution). This large power requirement coupled with the large amount of area that a clock uses, implies that an alternative technology like optical clock distribution, which brings savings in space and power consumption, may have a large payoff.

1.2 Outline of thesis

This thesis will continue in chapter two with a treatment of ULSI compatible silicon waveguides which form the basis of microphotonics. Three devices: splitters, bends and switches, will be presented in chapter three followed by a discussion of ULSI compatible integrated optical filters in chapter four. Finally, in chapter five, the integration of devices for silicon microphotonics platforms will be discussed.

Chapter 2

Si ULSI compatible waveguides

In this chapter, a brief overview of the theory of waveguides is presented followed by a short discussion of the wavelength of choice in silicon microphotonics. This wavelength choice necessitates the selection of a ULSI compatible materials system for the waveguides. The advantages and disadvantages of each materials system will be discussed in turn. The optical properties of three ULSI compatible dielectric materials: silicon, silicon nitride and silicon dioxide are listed in table 2.1.

2.1 Background

In general, an optical waveguide consists of a region of higher average index refraction, known as the core, wrapped by a region of lower average index of refraction known as the cladding. The refraction of light as it travels through regions of different indices is governed by Snell's law,

$$n_{core} \sin\theta_{core} = n_{cladding} \sin\theta_{cladding} \tag{2.1}$$

where n_{core} and $n_{cladding}$ are the indices of refraction of the core and cladding respectively. If $n_{core} > n_{cladding}$ and $\theta_{core} > \sin^{-1}(\frac{n_{cladding}}{n_{core}})$, no energy is transmitted from the core to

Material	Index (1.55 μm)	Band Gap (eV)
Silicon	3.48 [15]	1.12 [16]
Silicon dioxide	1.48	$\approx$ 9 [16]
Silicon nitride	2.0	$\approx$ 5 [17]

Table 2.1: Optical properties of front end compatible ULSI materials

the cladding, that is total internal reflection occurs. Thus, if light in a waveguide core is incident at the core/cladding interface at angles greater than the critical angle, there will be no transmission at the core/cladding interface.

Optical waveguides support only a discrete number of modes. A guided mode, quite simply, is an electrical field profile, which when launched in the dielectric waveguide, will retain its shape and amplitude forever. The amplitude of the mode is maintained by total internal reflection while the shape is maintained by a conservation in phase. Thus, the guided mode is a standing wave in the direction perpendicular to propagation and is a traveling wave in the direction parallel to the propagation.

2.1.1 Analysis of waveguides

There are several of ways of analyzing waveguides, three of which are used in this thesis. The first is an approximate analytical method, the effective index method, the second is a numerical method known as the Beam Propagation Method (BPM) and the third is another more accurate numerical method, the Finite Difference Time Domain (FDTD) method. These three methods will be discussed in turn.

2.1.2 Effective Index method [1, 2, 3]

To determine the propagation constants of modes of a dielectric waveguide, an analytical method known as the effective method may be used. The effective index method is based on the fact that the solution for modes in an infinitely wide slab waveguide (a 2-D problem) is easy to obtain. Based on this solution an approximate solution to the effective index in 3-D may be obtained.

To find the modes, Maxwell's equations are applied to the waveguiding problem:

$$\vec{\nabla} \times \vec{E} = -\frac{d}{dt}\mu\vec{H} \tag{2.2}$$

$$\vec{\nabla} \times \vec{H} = \frac{d}{dt}\epsilon\vec{E} + \vec{J} \tag{2.3}$$

$$\vec{\nabla} \cdot \epsilon\vec{E} = \rho \tag{2.4}$$

$$\vec{\nabla} \cdot \mu\vec{E} = 0 \tag{2.5}$$

In the absence of current sources and charges, $\vec{J} = 0$, $\rho = 0$. Using the frequency domain

representation, Maxwell's Equations reduce to:

$$\vec{\nabla} \times \vec{E} = -j\omega\mu\vec{H} \tag{2.6}$$

$$\vec{\nabla} \times \vec{H} = j\omega\epsilon\vec{E} \tag{2.7}$$

$$\vec{\nabla} \cdot \epsilon\vec{E} = 0 \tag{2.8}$$

$$\vec{\nabla} \cdot \mu\vec{H} = 0 \tag{2.9}$$

Substituting (2.8) into (2.6) yields the Helmholtz equation. After some algebra and assuming that the medium is piece-wise isotropic or at least has a slowly varying ϵ such that $\vec{\nabla}\epsilon \approx 0$:

$$\left[\vec{\nabla}^2 + \omega^2\mu\epsilon\right]\vec{E} = 0 \tag{2.10}$$

A waveguide can be analyzed by substituting the correct ϵ profile into equation (2.10).

Solution of the infinite dielectric slab waveguide

In this section, I recapitulate the solution to the infinite dielectric slab which can be found in any optics textbook [2, 3, 18]. See figure 2-1. Region 2 is the core of the waveguide with index n_2, (where $n_2 > n_1$; $n_2 > n_3$) and with thickness d.

TE: The TE fields component can be written as:

$$\begin{aligned}
\vec{E}_1 &= \vec{y}E_1 \exp[-\alpha_{1x}x - jk_z z] \\
\vec{E}_2 &= \vec{y}(A\exp[jk_x x] + B\exp[-jk_x x])\exp[-jk_z z] \\
\vec{E}_3 &= \vec{y}E_3 \exp[+\alpha_{3x}x - jk_z z]
\end{aligned}$$

For a guided wave to propagate, a standing wave must be set up transverse to the direction of propagation. Thus, the round trip phase after one reflection off the top and one reflection off the bottom interface must equal a multiple of 2π. The phase shift off a reflection at a dielectric interface at total internal reflection (2.1) is given by the Goos-Hänchen phase shift:

$$\phi = -tan^{-1}\frac{\mu_2\alpha_{1,3}}{\mu_{1,3}k_x} \tag{2.11}$$

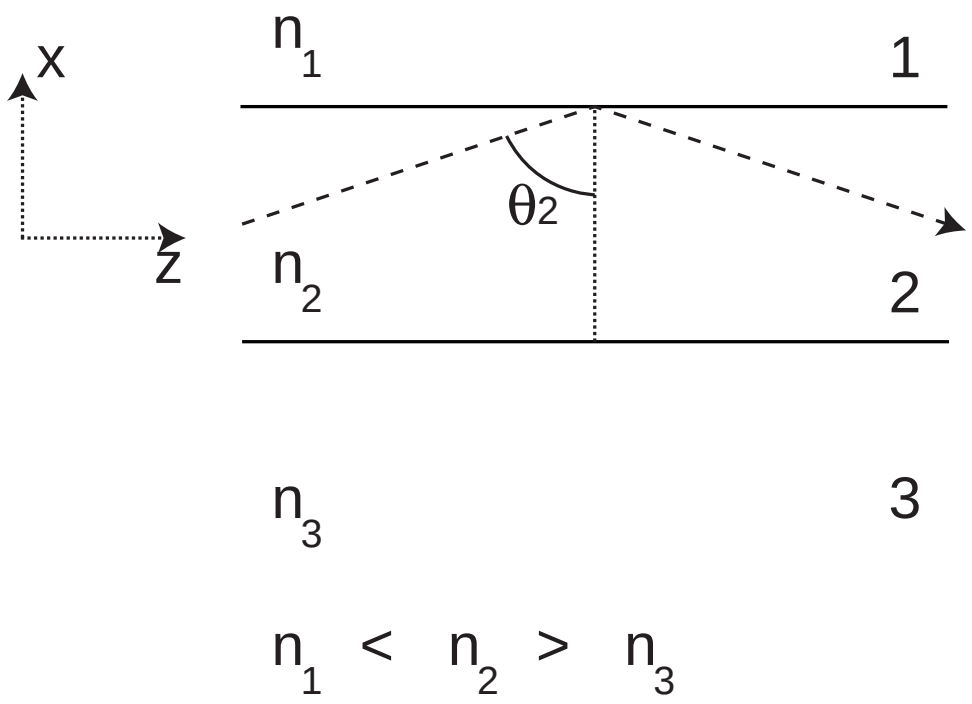

Figure 2-1: Infinite dielectric slab waveguide. Waveguide is infinite in extent in the y direction and propagation occurs in the z direction.

$$\phi_{1,3} = -tan^{-1}\frac{\sqrt{\epsilon_2 sin^2\theta_2 - \epsilon_{1,3}}}{\sqrt{\epsilon_2}\cos\theta_2} \tag{2.12}$$

where the subscripts 1,3 and 2 are for the transmitted and incident media respectively. μ is the permeability, $\alpha_{1,3}$ is the evanescent decay into the transmitted (cladding) media and k_x is the vector component of the propagation constant normal to the boundary in the material of higher index (the core). Thus, the round trip phase shift is given by

$$2k_x d - \phi_1 - \phi_3 = m\pi \tag{2.13}$$

where d is the height of the waveguide and m is an integer, which is the mode number.

The following normalized parameters can be defined

$$n_2 \sin\theta_{2,m} = n_{eff,m} \tag{2.14}$$

$$b_m = \frac{n_{eff,m}^2 - n_1^2}{n_2^2 - n_1^2} \tag{2.15}$$

$$V = k_o d\sqrt{n_2^2 - n_1^2} \tag{2.16}$$

$$a = \frac{n_1^2 - n_3^2}{n_2^2 - n_1^2} \tag{2.17}$$

where b_m is the normalized effective effective dielectric constant, V is the normalized frequency and a is the normalized asymmetry parameter.

Substituting into (2.12) and (2.13) yields the TE condition in Kogelnik/Ramaswamy notation.

$$V\sqrt{1-b_m} = m\pi + tan^{-1}\left[\sqrt{\frac{b_m}{1-b_m}}\right] + tan^{-1}\left[\sqrt{\frac{b_m+a}{1-b_m}}\right] \tag{2.18}$$

This equation can be easily solved by a root solver.

TM The TM equation is not easily renormalized into dimensionless units. However, the treatment above may be used to find a dispersion relation and the effective index of the TM mode can be found and expressed in terms of the indices of refraction of the three layers.

$$TE : k_o d\sqrt{n_2^2 - {n_{eff}}^2} = \nu\pi + \tan^- 1\left[\sqrt{\frac{n_{eff}^2 - n_1^2}{n_2^2 - n_{eff}^2}}\right] + \tan^- 1\left[\sqrt{\frac{n_{eff}^2 - n_3^2}{n_2^2 - n_{eff}^2}}\right] \tag{2.19}$$

$$TM : k_o d\sqrt{n_2^2 - {n_{eff}}^2} = \nu\pi + \tan^- 1\left[\frac{n_2}{n_1}\sqrt{\frac{n_{eff}^2 - n_1^2}{n_2^2 - n_{eff}^2}}\right] \tan^- 1\left[\frac{n_2}{n_3}\sqrt{\frac{n_{eff}^2 - n_3^2}{n_2^2 - n_{eff}^2}}\right] \tag{2.20}$$

In general the TM mode is not as tightly confined as the TE mode because there is a larger Goos-Hänchen phase shift at the boundaries at total internal reflection for the TM mode. This can be seen by comparing equations (2.19) with (2.20). The extra $\frac{n_2}{n_{clad}}$ in the arctangent results in a bigger phase shift.

Effective index method for 3-D waveguides [19, 1]

The effective index method uses the methodology developed for an infinite 2-D slab to solve for the effective index of a 3-D waveguide. See figure 2-2.

The effective index method is first applied to cross-sections 1, 2 then 3. The effective indices extracted are then n_1, n_2 and n_3 respectively. Using the effective indices derived from these cross-sections a fourth and final effective effective index is found; which is the effective index of the waveguide. This method is most accurately used with rib waveguides where the k-vector in one direction (perpendicular to the substrate) is much smaller than the k vector parallel to the substrate, allowing one to decouple the x, and y problems.

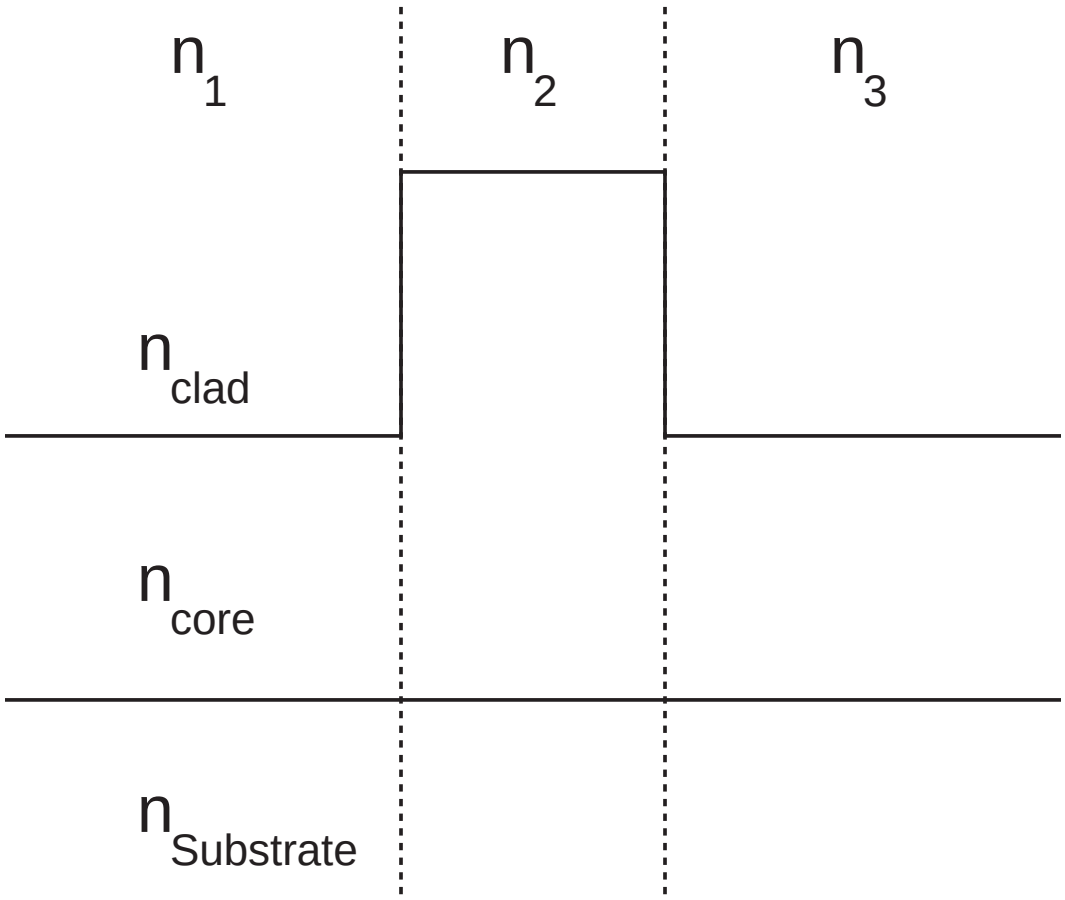

Figure 2-2: Schematic of the effective index method. The 2D slab waveguide effective index equations (2.19) and (2.20) are solved for regions 1, 2 and 3, to get n_1, n_2 and n_3 respectively. n_1, n_2 and n_3 are, in turn, used in equations (2.19) and (2.20) to generate n_{eff}.

2.1.3 Finite Difference Time Domain (FDTD) [4]

The FDTD method solves Maxwell's equations directly in the time domain with the only approximation being the numerical discretization error.

The major problem with with FDTD method is that the computation of the exact solution is computationally very expensive. Even with a CRAY supercomputer, a full vectorial 3-D simulation takes enough time that device optimization by this method is not tolerable. Hence, usually only 2-D simulations are used.

2.1.4 Beam Propagation Method (BPM) [4, 5]

The beam propagation method (BPM) solves Maxwell's equation with the assumption that there the field component in the direction of propagation, z, can be approximated by $\exp[-j\beta z]$. In this way, BPM solves a propagation problem by solving each point in the direction of propagation serially. Thus, instead of solving a second order P.D.E. over an entire index matrix (2-D problem) or index tensor (3-D problem), the second order P.D.E. is solved over an index vector (2-D problem) or index matrix (3-D problem). The reduction of one dimension gives BPM a huge advantage in computational efficiency over FDTD.

Since BPM solves the problem along the direction of propagation serially, BPM can only handle problems with one reflection. Thus, BPM is unable to handle a large number of reflections and is unsuitable in devices where there are multiple reflections, for example in high Q resonant cavities. On the other hand, BPM is useful for slowly varying single pass structures as it is very efficient.

Numerically solving for the waveguide modes [20, 5]

To numerically determine the mode of a waveguide, a cross-sectional profile of the ϵ profiles is used in the Helmholtz equation. The eigenmode problem, is numerically similar to the BPM problem but with a complex propagation constant. From Faraday's Law (2.6), Ampere's Law (2.7) and assuming that the permeability is a constant, μ:

$$\begin{aligned} \vec{\nabla} \times \vec{\nabla} \times \vec{E} &= -\vec{\nabla} \times \frac{d}{dt} \mu \vec{H} \\ \vec{\nabla}(\vec{\nabla} \cdot \vec{E}) - \vec{\nabla}^2 \vec{E} &= \omega^2 \mu_o \bar{\bar{\epsilon}} \vec{E} \end{aligned}$$

Assuming further that the E-field has an $\exp[-j\beta z]$ dependence in the direction of propagation, the relation reduces to:

$$\vec{\nabla}_T(\vec{\nabla}_T \cdot \vec{E}_T) - \vec{\nabla}_T^2 \vec{E}_T - \omega^2 \mu_o \bar{\bar{\epsilon}} \vec{E}_T = \beta^2 \vec{E}_T \tag{2.21}$$

where $\vec{\nabla}_T$ is the 2-dimensional $\vec{\nabla}$ operator transverse to the direction of propagation and the E_T is the transverse E field that we are trying to find.

After discretization, this reduces to a numerically tractable eigenmode equation:

$$\bar{\bar{A}} \vec{E}_T = \beta^2 \vec{E}_T \tag{2.22}$$

the solution of which is beyond the scope of this thesis. If β is real the mode is guided (non-lossy). If β has a non zero imaginary component, then the mode is lossy.

2.1.5 Lossy Modes

Some waveguides do not have guided modes in the strictest sense but have instead lossy modes. A lossy mode is an electric field profile which when launched down a waveguide will retain its shape (phase profile) but will shed its energy. If the characteristic decay length at which it radiates its energy is small compared to the propagation energy, the lossy mode may be used to guide optical power. A lossy mode would have a complex propagation constant, the imaginary part of which is proportional to the amplitude decay constant.

ARROW

An example of such a waveguide is the ARROW or Anti-Resonant Reflecting Oxide Waveguide (see section 2.2.4) which differs from the waveguides described in the previous section because it has a low index core which is clad with one or more thin high index layers [21, 22, 23, 24]. All modes in an ARROW are lossy. The idea in the ARROW waveguide is to use the low index core and alternating high and low index cladding layers to set up a reflection that will interfere constructively. See figure 2-3. The well known result is that to maximize reflectivity the layers have to be $\frac{\lambda}{4}$ thick. This condition is also known as the anti-resonant condition of the Fabry-Perot, which explains the name Anti-Resonant Reflecting Oxide Waveguides.

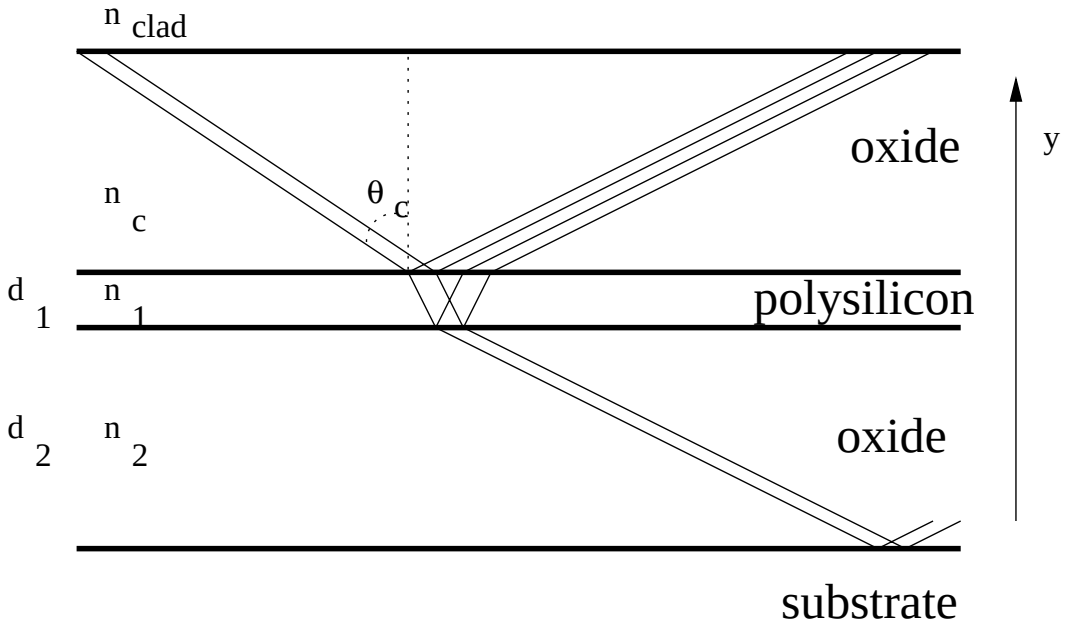

Figure 2-3: Schematic of an ARROW waveguide. The thin polySi layer has thickness d_1 given by equation (2.29). At this thickness, light reflecting off the top surface of the polySi interferes constructively with the light reflecting off the bottom surface of the polySi.

ARROW waveguide clad on one side [21, 25]

We now derive the layer thickness of the underlying layers, d_1 that will maximize reflection. From Snell's law,

$$n_c \sin\theta_c = n_1 \sin\theta_1 \tag{2.23}$$

$$\sin\theta_1 = \frac{n_c}{n_1}\sin\theta_c \tag{2.24}$$

$$\cos\theta_1 = \sqrt{1-\sin^2\theta_1} = \sqrt{1-\left(\frac{n_c}{n_1}\right)^2 \sin^2\theta_c} \tag{2.25}$$

Due to the interference condition for high reflectivity, the accumulated round trip phase shift in the y direction within material 1 must sum to an odd number of π. Thus,

$$2k_{1,y}d_1 = (2N+1)\pi \tag{2.26}$$

$$2k_1\cos\theta_1 d_1 = (2N+1)\pi \tag{2.27}$$

$$2\frac{2\pi n_1}{\lambda}\sqrt{1-\left(\frac{n_c}{n_1}\right)^2 \sin^2\theta_c}\, d_1 = (2N+1)\pi \tag{2.28}$$

$$d_1 = (2N+1)\frac{\lambda}{4n_1\sqrt{1-\left(\frac{n_c}{n_1}\right)^2 \sin^2\theta_c}} \tag{2.29}$$

where N is an integer. If a further approximation is made that the Goos-Hänchen phase shift is negligible, which would be the case for a high index difference between the core index and the top cladding index, then

$$k_c \cos\theta_c d_c = \pi \tag{2.30}$$

$$\cos\theta_c = \frac{\lambda}{2 d_c n_c} \tag{2.31}$$

Thus, equation (2.29) reduces to:

$$d_1 = (2N+1)\frac{\lambda}{4 n_1 \sqrt{1 - \left(\frac{n_c}{n_1}\right)^2 + \left(\frac{\lambda}{2 n_1 d_c}\right)^2}} \tag{2.32}$$

The generalized layer thickness d_i for $i = 1, 2, 3..$ can be determined by replacing the subscript 1 with i in equation (2.32). This equation gives the layer thickness for any number of index layers which are needed to form the high reflectivity cladding stack for the ARROW waveguide.

2D ARROWs

One of the problems with the basic ARROW concept is that it is a 1 dimensional structure, which means lateral confinement is most easily achieved by etching the side-walls partially, to make a strip loaded waveguide [21] or completely to make a sideways pedestal ARROW (SPARROW) waveguide. This implies that the waveguides have to be air clad. While it is possible to integrate air clad waveguides with ULSI, the packaging difficulties for such waveguides are enormous. Furthermore, the polarization sensitivity of air clad ARROW waveguides is large. As a result, I started studying 2-D clad ARROWs.

The design that I have come up with is an ARROW waveguide which is clad on all four sides with a thin layer of poly-crystalline silicon (polySi) and a thick layer of oxide with thickness determined by equation (2.32) as shown in figure 2-4. Using a core size of 4 μm, the calculated loss for this structure is 4 dB/cm at a free space wavelength of 1.55 μm. As the wavelength of light decreases or as the size of the core is increased, the transmission increases. At a free-space wavelength wavelength of 0.8 μm, the loss is less than 0.02 dB/cm.

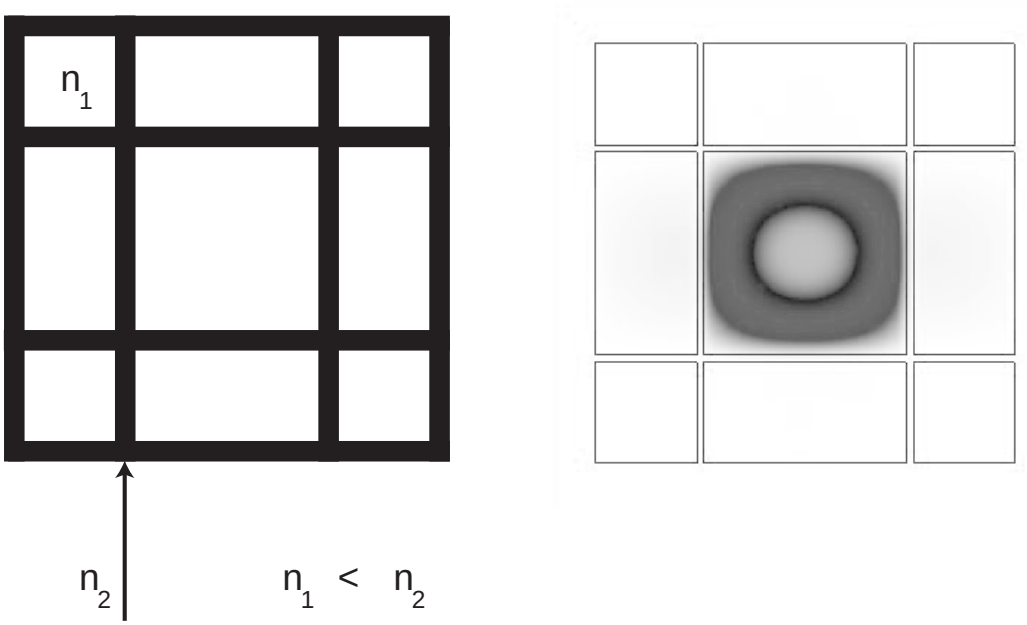

Figure 2-4: Schematic of a 2D ARROW waveguide. The 2-D ARROW is confined on all 4 sides, is polarization independent and can have a top cladding but is hard to fabricate. The mode is well confined to the core of the waveguide.

2.1.6 Waveguide dispersion [6, 3]

In general, different wavelengths will have different propagation speeds in a waveguide. Any signal which is not a pure sine wave would have a finite spread of wavelengths. Therefore, as this signal propagates through this waveguide, the difference in the propagation speed of the different wavelengths will affect the shape of the signal. This reshaping of the pulse on propagation is waveguide dispersion. Waveguide dispersion becomes a problem in optical transmission systems if the individual optical pulses which represent data broaden to the point where the pulses begin merge.

To understand how dispersion may be analyzed we start with the Helmholtz equation approximation (2.10) and solve it for waveguides for a single frequency ω. As described in the previous sections, a waveguide mode has a cross-sectional E-field $\vec{E}(x, y)$ profile which propagates down the waveguide. Introducing the term, β, or propagation constant we can describe the E-field solution to the Helmholtz equation as

$$\vec{E}(x, y, z, \omega) = \vec{E}(x, y) \exp[-j\beta(\omega)z] \tag{2.33}$$

$\vec{E}(x, y)$ is the mode E-field profile and the propagation constant $\beta(\omega)$ is written to make its

frequency dependence explicit. Substituting equation (2.33) into (2.10) we get for a single frequency:

$$\left[\vec{\nabla}_T^2 + \omega^2\mu\epsilon\right]\vec{E}(x,y) = \beta^2(\omega)E(x,y) \tag{2.34}$$

Now that we have solved for the single frequency we can generalize the solution of (2.34) for the case of a pulse. The solution can be written as

$$\vec{E}(x,y,z,\omega) = \vec{E}(x,y)a(z,\omega) \tag{2.35}$$

where,

$$a(z,\omega) = u(\omega)\exp[-j\beta(\omega)z] \tag{2.36}$$

$u(\omega)$ is now the weight on each ω. Rewriting (2.36) in differential form, we can eliminate this weighting term,

$$\frac{\partial a(z,\omega)}{\partial z} = -j\beta(\omega)a(z,\omega) \tag{2.37}$$

Assuming a narrow pulse with center frequency ω_o, and assuming a frequency spread so narrow that it has a fast varying propagation component $\exp[-j\beta(\omega_o)]$ and a slow varying envelope $A(z,\omega-\omega_o)$, $a(z,\omega)$ may be recast as

$$a(z,\omega) = A(z,\omega-\omega_o)\exp[-j\beta(\omega_o)] \tag{2.38}$$

Substituting (2.38) into (2.37) we get:

$$\frac{\partial A(z,\omega-\omega_o)}{\partial z} - j\beta(\omega_o)A(z,\omega-\omega_o) = -j\beta(\omega)A(z,\omega-\omega_o) \tag{2.39}$$

$$\frac{\partial A(z,\omega-\omega_o)}{\partial z} = -j(\beta(\omega)-\beta(\omega_o))A(z,\omega-\omega_o) \tag{2.40}$$

$(\beta(\omega)-\beta(\omega_o))$ may be expanded by the Taylor series expansion. Expanding to the second order term:

$$(\beta(\omega)-\beta(\omega_o)) = \left.\frac{d\beta}{d\omega}\right|_{\omega_o}(\omega-\omega_o) + \frac{1}{2}\left.\frac{d^2\beta}{d\omega^2}\right|_{\omega_o}(\omega-\omega_o)^2 \tag{2.41}$$

Thus, the equation of motion of the envelop term is

$$\frac{\partial A(z,\omega-\omega_o)}{\partial z} = -j\left(\left.\frac{d\beta}{d\omega}\right|_{\omega_o}(\omega-\omega_o) + \frac{1}{2}\left.\frac{d^2\beta}{d\omega^2}\right|_{\omega_o}(\omega-\omega_o)^2\right)A(z,\omega-\omega_o) \tag{2.42}$$

the Fourier transform of which is

$$\frac{\partial A(z,t)}{\partial z} = -\left.\frac{d\beta}{d\omega}\right|_{\omega_o}\frac{\partial A(z,t)}{\partial t} + \frac{j}{2}\left.\frac{d^2\beta}{d\omega^2}\right|_{\omega_o}\frac{\partial^2 A(z,t)}{\partial t^2} \tag{2.43}$$

The first term on the right hand side describes linear propagation, since the solution is a plane wave $A_o\exp[jk(x-v_gt)]$ where $v_g = \frac{d\omega}{d\beta}$ is the group velocity of propagation of the envelope. This means that if the second term on the right is zero, the envelope of pulse would be able to propagate forever without changing. The second order term $\frac{d^2\beta}{d\omega^2}$ describes group velocity dispersion, GVD. Positive GVD implies that the higher frequencies have smaller group velocity $\frac{d\omega}{d\beta}$ which means that the red components of the pulse would arrive before the blue components of the pulse. The amount of spreading in the group velocity is determined by the bandwidth of the spectrum, $\Delta\omega$.

$$\text{(spread in group velocity)}^{-1} = \Delta(\frac{1}{v_g}) = \frac{d^2\beta}{d\omega^2}\Delta\omega \tag{2.44}$$

$$\text{pulse spreading in time} = \Delta\tau = \Delta(\frac{1}{v_g})l = \frac{d^2\beta}{d\omega^2}\Delta\omega l \tag{2.45}$$

This spreading of the frequencies over time is known as chirp. Over long distances, the difference in arrival times becomes worse and pulse spreading or broadening occurs. See equation 2.45. Thus, dispersion is most severe in long distance transmission systems.

Group Index Dispersion

The group velocity in the waveguide $\frac{d\omega}{d\beta}$ can be related to the change of effective index with wavelength $\frac{dn_{neff}}{d\lambda}$ via

$$\left(\frac{d\omega}{d\beta}\right)^{-1} = \frac{d\beta}{dn_{eff}}\frac{dn_{eff}}{d\lambda}\frac{d\lambda}{d\omega} \tag{2.46}$$

Differentiating $\lambda\omega = 2\pi c$ with respect to λ, differentiating $\beta = \frac{2\pi n_{eff}}{\lambda}$ with respect to n_{eff} and substituting into equation (2.46) yields

$$n_g = n_{eff} - \lambda_o\frac{dn_{eff}}{d\lambda} \tag{2.47}$$

where n_g is defined as $\frac{c}{v_g}$. The dispersion may be easily found by differentiating (2.47) with respect to ω

$$\frac{dn_g}{d\omega} = -\frac{d\lambda}{d\omega}\frac{d}{d\lambda}\left(n_{eff} - \lambda_o \frac{dn_{eff}}{d\lambda}\right) \tag{2.48}$$

$$c\frac{d^2\beta}{d\omega^2} = -\frac{\lambda_o}{\omega}\left(\frac{dn_{eff}}{d\lambda} - \lambda_o \frac{d^2 n_{eff}}{d\lambda^2}\right) \tag{2.49}$$

$$\frac{d^2\beta}{d\omega^2} = -\frac{\lambda_o^2}{2\pi c}\left(\frac{dn_{eff}}{d\lambda} - \lambda_o \frac{d^2 n_{eff}}{d\lambda^2}\right) \tag{2.50}$$

We have therefore derived how the group velocity varies with wavelength and hence frequency in a waveguide. The dependence of n_g on $\frac{dn_{eff}}{d\lambda}$ implies that the dispersion depends on the variation effective index of the waveguide on wavelength. This variation can occur in two ways:

- from the structure or design of the waveguide or
- from the material

Thus,

$$\frac{dn_{eff}}{d\lambda} = \frac{dn_{eff}}{d\lambda}_{design} + \frac{dn_{eff}}{d\lambda}_{material} \tag{2.51}$$

The first term can be calculated by BPM methods while the second term is dependent on materials parameters.

2.1.7 High dielectric contrast waveguides

High dielectric contrast waveguides refer to waveguides with a high index core and a low index cladding resulting in a highly confined waveguide mode. Examples of high index contrast systems which are compatible with silicon ULSI processing are strip waveguides of silicon or silicon nitride sitting on a bed of silicon oxide, with index contrast ratios of 2.3 and 1.2 respectively. The difference in index of 2 and 0.5 respectively are much larger than the index difference in AlGaAs/GaAs waveguide systems or Ge doped optical fibers where the index contrasts can be as little as 0.01 [18].

One advantage of working with these waveguides is that small resonant cavities with large core intensities can be fabricated because the mode is more tightly confined. Furthermore, better confinement results in waveguides which exhibit small losses around tight

bends and Y-splits with large splitting angles. These waveguides can be packed much closer with minimal cross-talk [12] making the devices ideal for high density applications necessary for interconnection and integrated optics with a high degree of complexity. In general, optical and opto-electronic devices that are based on high dielectric contrast are smaller and faster.

There are, of course, disadvantages when working with these waveguides. As a result of the small dimensions of the single mode waveguides, coupling of light from off-chip fibers to on-chip waveguides is difficult. Furthermore, the extreme small size of these waveguides (0.5 μm wide for the single mode silicon on oxide waveguide) coupled with the requirement that the side-walls be smooth to about 0.01 μm, make these waveguides hard to fabricate [12].

2.1.8 Wavelength of choice

There are two major sets of optical wavelengths, separated at the band-gap of silicon, available to a designer of waveguides on silicon. The waveguide material of choice at wavelengths of less than one μm i.e. above the band-gap of silicon in terms of energy, is silicon nitride on oxide. On the other hand, silicon nitride, single crystalline silicon and poly-crystalline silicon (referred to henceforth as polySi) waveguides are available for use at wavelengths longer than one μm i.e. light which is below the band-gap of silicon in energy terms.

Above band-gap light

Systems which use wavelengths of less than one μm can be integrated with vanilla silicon detectors, which can be made reasonably fast and extremely efficient. This fact alone makes silicon nitride waveguides an attractive option. Another advantage is that this wavelength choice is compatible with GaAs based emitters like laser diodes which are cheap and readily available.

However, the drawbacks of using short wavelengths are numerous. The first is that the light can be absorbed by the silicon substrate resulting in electron-hole generation, which in turn can affect any electronics, in the underlying circuit. Thus care must be taken when integrating silicon nitride waveguides with CMOS circuitry.

Secondly, this wavelength choice limits the material choice of the core of any electro-optic modulator to silicon nitride. Since there is no direct electro-optic effect and no free

carrier effect for silicon nitride, one would have to rely on the Kerr effect, which is tiny [26], or on micro-mechanical or thermo-optic devices, which are slow. Thus, any system utilizing nitride waveguides will have to contend with slow on-chip modulation and possible interference of the electronics by the optical signals.

Furthermore, there is no apparent monolithic light emission scheme that would work at this wavelength, so the user may have to work with the integration of an off-chip, high speed modulated device as well. Another option would be to grow graded buffer layers so that III-V compounds can be grown on silicon.

Nevertheless, as a result of the ease of fabrication of the silicon nitride waveguide/silicon detector system, most of the work in the literature on the monolithic integration of waveguides with detectors on silicon has concentrated on this materials system. (See for example [27]). A possible application of this technology would be optical clock distribution on silicon integrated circuits.

In the literature, optical loss in nitride waveguides at a wavelengths of 538 nm and 632 nm have been reported and range from less than 1dB to more than 3dB [28, 29, 30, 31, 32, 33]. There are two reasons for this wide range in measured optical loss. The first is that high quality LPCVD nitride waveguides exhibit lower optical propagation loss than plasma deposited nitride waveguides indicating a difference in material quality. The second reason is that the oxide thickness of about one micron, which has been used frequently in previous work, leads to over 1 dB/cm loss.

Sub-band-gap light

Sub-band-gap light with wavelength of 1.3 μm or 1.55 μm is interesting because of the possibility of integration of the silicon based optical system with fiber optics communications systems.

Furthermore with the advent of erbium in silicon, room-temperature erbium silicon LEDs at 1.55 μm have been demonstrated [34, 35]. While substantial work remains before a viable light emission system can be fabricated, the possibility of such a system coupled with Ge or SiGe detectors to form a monolithically integrated optical system on silicon is too important to ignore.

Another significant advantage of working at these wavelengths is that silicon is essentially transparent to light at these wavelengths resulting in minimal opto-electronic cross-talk.

The drawbacks however, cannot be overemphasized. The first has already been alluded to. Work on Er in silicon still has not yielded on LED with high enough power or a laser capable of operating at 300K. More importantly, SiGe detectors at 1.55 μm have long absorption lengths, on the order of 100 μm. Pure Ge itself has an absorption of about 1000 cm^{-1}, which is adequate for building a detector with decent efficiency [36, 37]. The presence of substantial a quantity of silicon in SiGe reduces the strength of the absorption, making SiGe intrinsically less efficient than Ge. Thus, there are projects being undertaken to try to integrate pure Ge detectors on silicon [38].

Nevertheless there is significant interest in developing silicon and polySi waveguides on oxide because of the availability of free carrier refraction and absorption that one may use for fabricating switches and modulators [11, 39].

2.2 Types of ULSI compatible waveguide

In this section several types of single mode waveguides for ULSI will be presented. The following waveguides were studied in detail for loss:

- Single crystal silicon waveguides
- polySi waveguides
- Silicon nitride waveguides
- ARROW waveguides

2.2.1 Single crystal silicon waveguides

Much work in the literature has concentrated on rib waveguides using silicon on insulator technology [40, 41]. These waveguides are large and do not satisfy the high confinement properties of high index contrast waveguides, as seen in figure (2-5), since the effective index of the cladding and that of the core differ by a small amount. Their disadvantage is their relatively large size. However their advantages are also related to their large size, which eases coupling, reduces scattering losses, eases electrical contacts and increases fabrication tolerances.

We have chosen to focus our attention on high index contrast ULSI compatible silicon strip waveguides. See figure 2-6 for a field profile of a 0.5 by 0.2 μm^2 silicon waveguide.

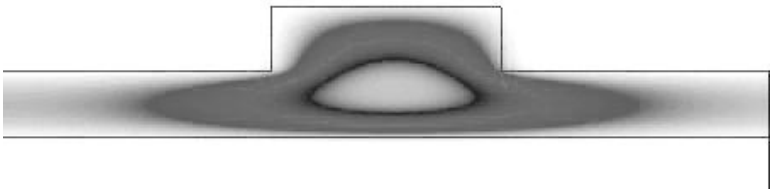

Figure 2-5: Field profile of a 3 μm wide x 5 μm high single mode silicon rib waveguide. Note the large extent of the field outside the core of the waveguide. The moded is effectively weakly guided in the plane of the substrate.

These waveguides require at least 7000Å of oxide cladding to keep optical losses to the substrate less than 1 dB/cm [42]. This oxide thickness is not compatible with SIMOX technology but is compatible with technologies like Bonded and Etched Back Silicon On Insulator (BESOI) and Smart Cut (tm) [41, 43, 44].

In BESOI material, two silicon wafers are oxidized thermally and bonded front to front by fusing the oxide at high temperature. Prior to bonding, one of the wafers will have received a high dose deep boron implant which would serve as an etch stop. The silicon substrate with the boron implant is polished after the oxide bonding step, until the etch stop is reached. Thus, this generally results in a thin rather highly doped silicon on oxide sample.

For Smart Cut (tm) material, the process steps are similar to the BESOI process but for the deletion of the boron implant step and the addition of a hydrogen implantation step prior to the bonding process. When annealed, the sample cleaves at the peak concentration of the hydrogen implant. This process generally yields good material quality.

One can immediately see from these process steps that these materials are relatively expensive to fabricate and do not easily allow multilevel waveguides. However, technologies like Smart Cut (tm) may in the future become standard in silicon IC processing since it will allow multiple device levels, resulting in higher device densities and this may in part alleviate the high cost of processing.

Fabrication of waveguides

The single crystal waveguide is defined by lithography, usually with UV lithography and invariably on a silicon on insulator (SOI) wafer substrate. Following the patterning the

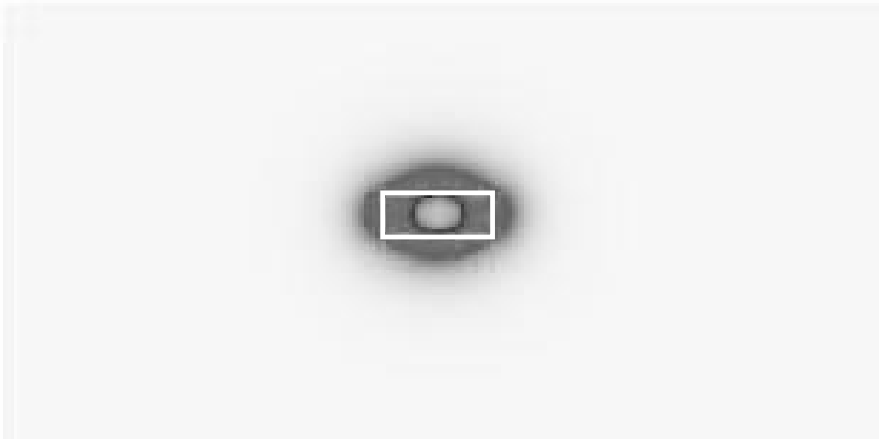

Figure 2-6: Field profile of 0.5 μm wide x 0.2 μm high silicon waveguide. The field is strongly confined to the core of the waveguide.

wafer is etched with a reactive ion etch. In addition, a chemical anisotropic etch may be used to smoothen the side walls. [42]

SOI waveguides were fabricated at Intel Corp. and at Lincoln Labs to take advantage of the short wavelength lithography tools available at those sites. The main difference between the Intel Corp. process and the Lincoln Labs process is that the former used a standard baseline process to get 0.5 μm lines while the latter used an optimized 248 nm lithography tool, with anti-reflection coating, a dark field mask and negative tone resist to achieve gap sizes less than 0.1 μm.

After fabrication, the wafers are die-sawed. Each chip is then polished twice, once on each facet.

2.2.2 PolySi waveguides

PolySi waveguides [14] are particularly useful because the fabrication technology is trivial when compared to other SOI technologies and because multilayer waveguide technology is easy to implement with polySi waveguides. Furthermore, current CMOS technology uses polySi interconnects, meaning that these waveguides are easily integrable with IC processing.

Recent results have shown a reduction of loss from 77 dB/cm [45, 46, 47, 48, 49], for the first waveguides that were fabricated, to 9 dB/cm [50, 51]. These results were achieved by carefully controlling top surface roughness introduced by processing as well as controlling the material quality of the film [50, 45]. With proper control of processing conditions, it may be possible to further reduce the polySi loss. If the optical loss of polySi waveguides can be reduced, the ease of integration with current CMOS technology as well as the ease of fabrication of polySi make it an attractive waveguide material.

Two methods of fabrication were used:

Direct Write Process [46] The starting material was a lightly doped silicon wafer. 1-2 μm of thermal oxide was grown on the silicon substrate by a wet oxidation process followed by the low pressure chemical vapor deposition (LPCVD) of 2000 Å of amorphous silicon at a temperature of about 560^oC. The waveguides were then annealed in nitrogen ambient, at a temperature of 600^oC. This annealing was designed convert the amorphous silicon into polySi. Another anneal, this time at 1100^oC anneal was performed. The wafers were patterned by photo-lithography, then etched to pattern the waveguides. The Intel process used a direct write process with a clear field mask and positive resist.

The Lincoln Labs process use a negative tone resist with an AR cladding and a dark field mask to optimize feature size. As a result sub-0.1 μm features is possible with the process. In addition, due to the fact that the thickness of the polySi grown at Lincoln labs was 2700Å, an additional etch step was performed to reduce the thickness of the polySi. See figure 2-7. The waveguides were usually covered with a layer of low temperature oxide or plasma enhanced deposited oxide. [45]

Damascene Process The Damascene process was proposed by Lincoln Labs as a means of controlling side-wall roughness. See section 2.3.3. The Damascene process is a very old fabrication process in which a mold of a design is made. The material that is desired is then poured or deposited into the mold and the top surface is levelled or polished. If one uses a mold which can be easily removed and is amorphous so that the surfaces of the exposed side-walls would be smoother than polySi.

For polySi waveguides the processing steps are as follows: First 1-2 μm of thermal oxide is grown on the starting silicon wafer. A 3000 Å thick layer of silicon nitride is then

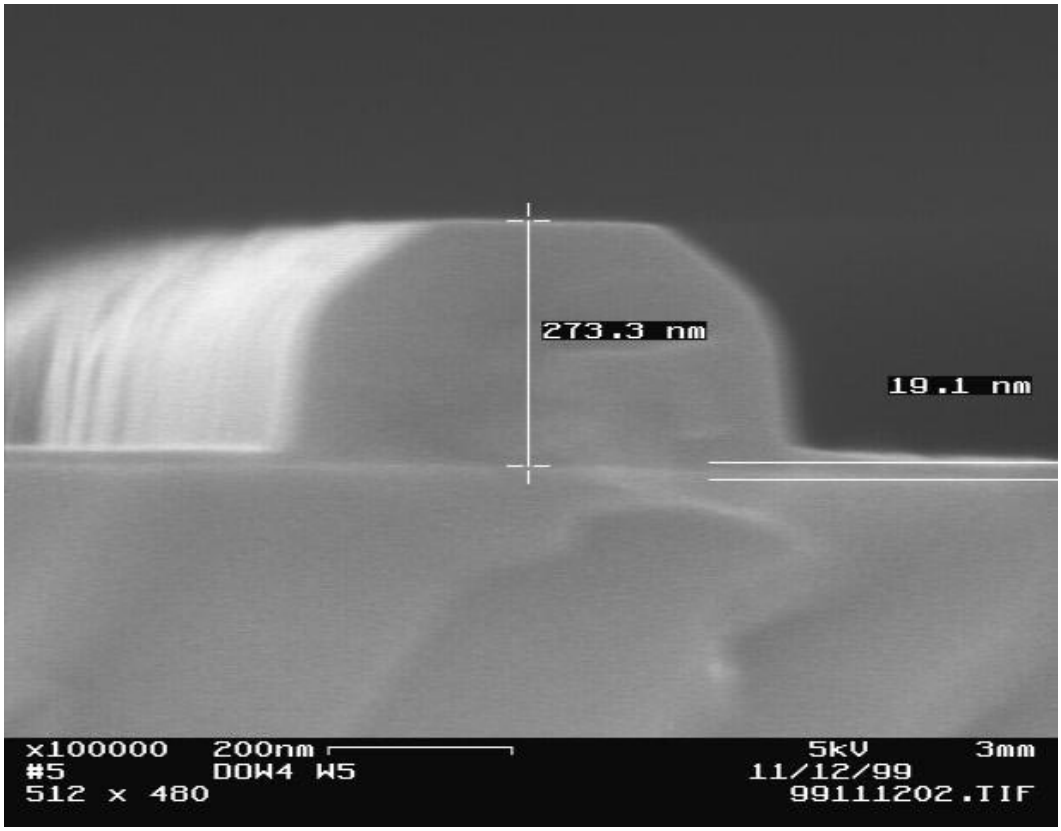

Figure 2-7: SEM of a polySi waveguide cross-section processed by the direct write process at Lincoln Labs. The rounded edges on the top surface of the waveguide are due to mask erosion. This mask erosion may have improved the side-wall smoothness of the waveguide.

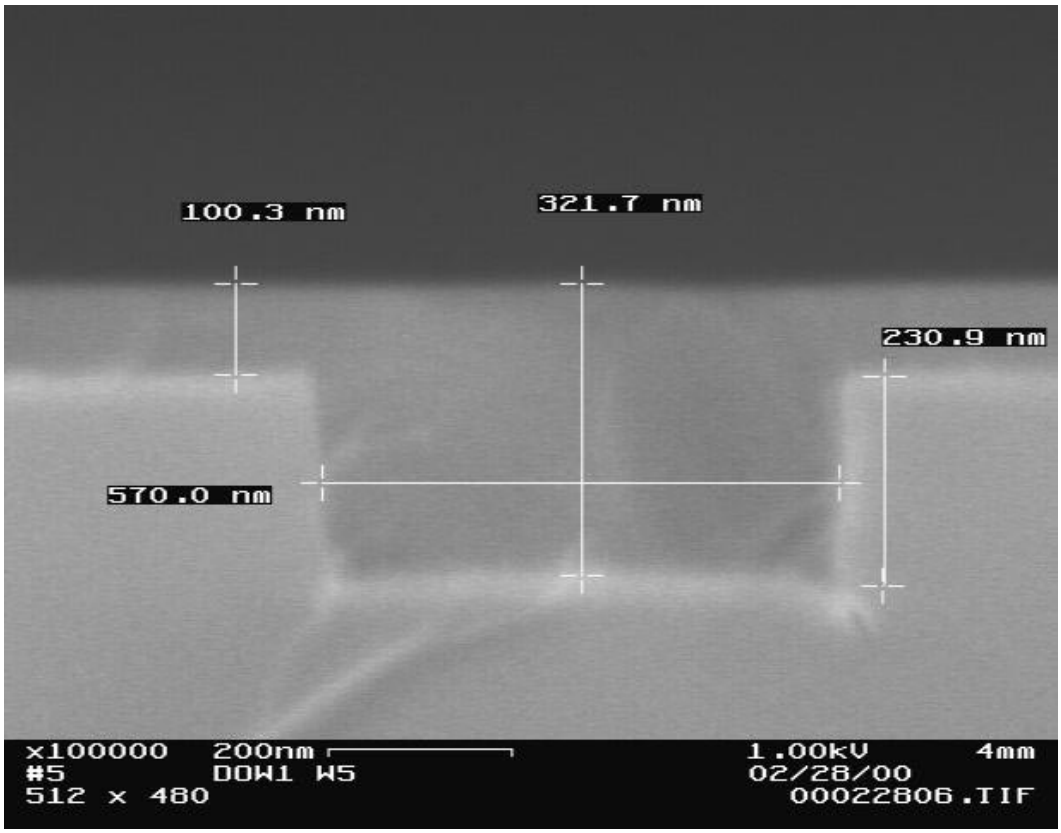

Figure 2-8: Cross-sectional SEM of a polySi waveguide processed by the Damascene process midway through CMP. The 321.7 nm thick polySi core is flanked by 100 nm of polySi. This excess material will be removed when CMP is complete. The surface smoothness of the polySi after CMP is excellent.

deposited by low pressure chemical vapor deposition (LPCVD). This silicon nitride layer is then patterned with the inverse of the desired polySi pattern and etched. A 4000 Å thick layer of polySi is deposited in the mold. The wafer is then annealed at 600^oC for 16 hr followed by an 1100^oC for 16hr. [45] At this point the wafers have The cross-section shown in figure 2-8. the waveguides are then polished via a Chemo-Mechanical Polishing method (CMP) and the nitride can be stripped by hot phosphoric acid. In terms of processing, the Damascene process is much more difficult than the direct write process and the yield of the process at the time of writing is much lower than in the simpler direct write process. Almost all the polySi waveguides used in this thesis were fabricated by the direct write process.

2.2.3 Silicon Nitride Waveguides

Although silicon nitride waveguides have been widely demonstrated (see for example [27]), small single mode strip waveguides have not been extensively investigated. Figure 2-9 shows the E-field profile of a silicon nitride waveguide. Simulations show that a 0.8 X 0.8 μm^2

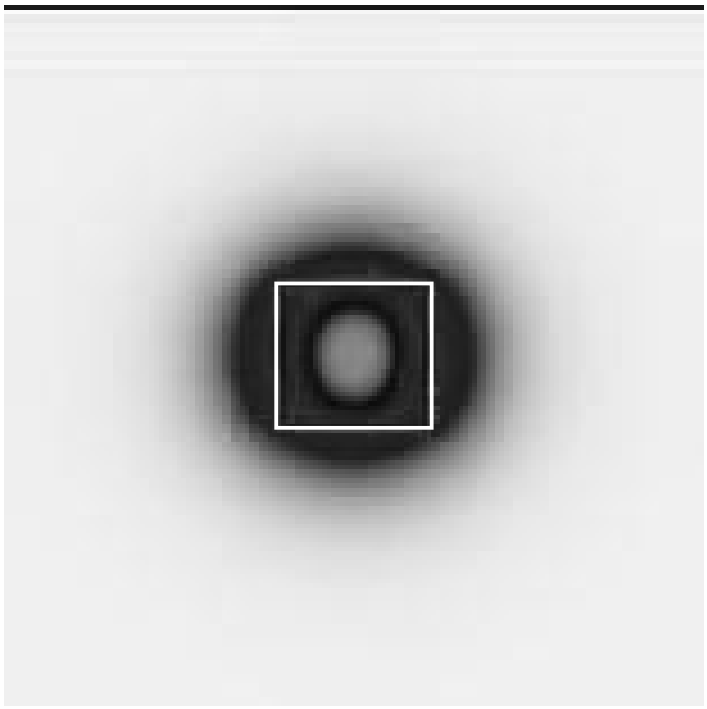

Figure 2-9: Field profile of 0.8 μm wide x 0.8 μm high silicon nitride waveguide. Again, the field is localized in the core of the waveguide, due to the high index contrast between the core and the cladding.

silica clad nitride waveguide has single mode characteristics and the propagation constants of the fundamental mode is shown in figure 2-10. The oxide thickness that is required for a 1 dB/cm loss is 1.5 μm as shown in figure 2-11.

As in the case of polySi waveguides, two types of fabrication methods were used:

Direct Write Process The starting material was a lightly doped silicon wafer. 1-2 μm of thermal oxide was grown on the silicon substrate by a wet oxidation process followed by the plasma enhanced chemical vapor deposition (PECVD) of 8000 Å of amorphous silicon at a temperature of about 400^{o}C. The wafers were patterned by photo-lithography, then etched to pattern the waveguides. The waveguides were usually covered with a layer of low

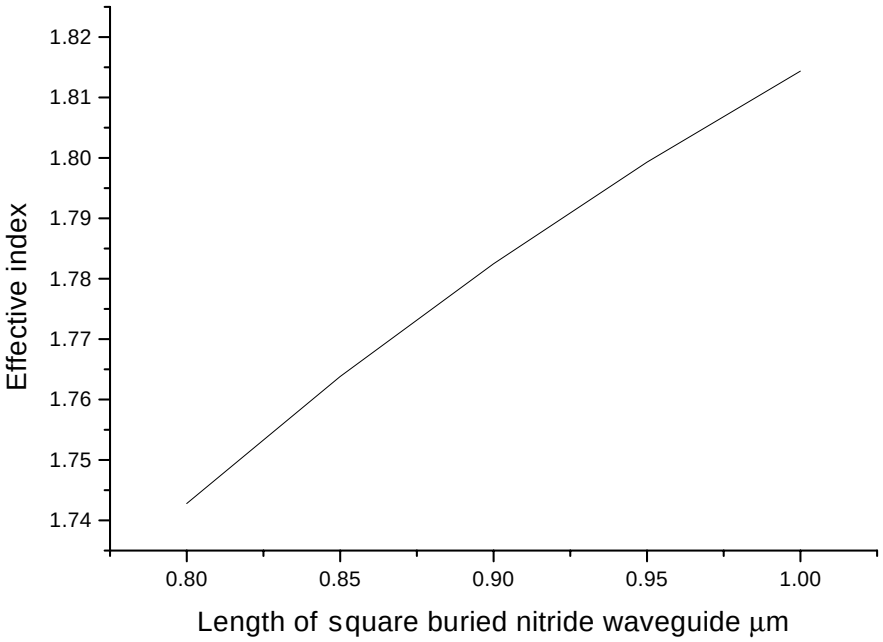

Figure 2-10: Simulated values of propagation constants of the fundamental mode of the silicon nitride waveguides

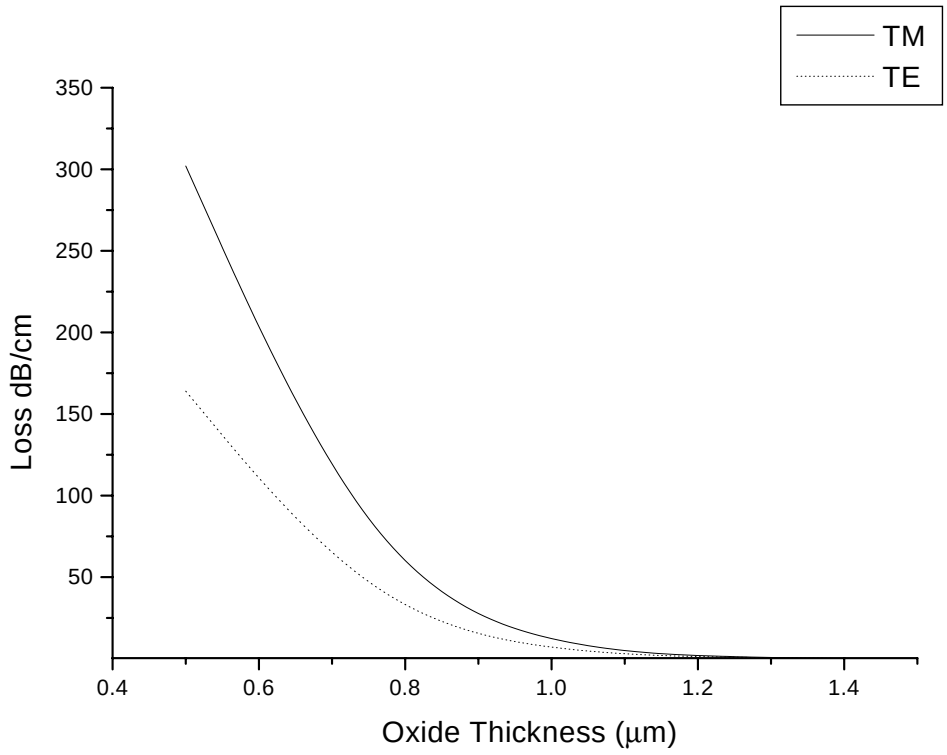

Figure 2-11: Simulated values of loss for 0.8 μm x 0.8 μm silicon nitride waveguides vs oxide thickness. The minimum oxide thickness for low loss is about 1.5 μm.

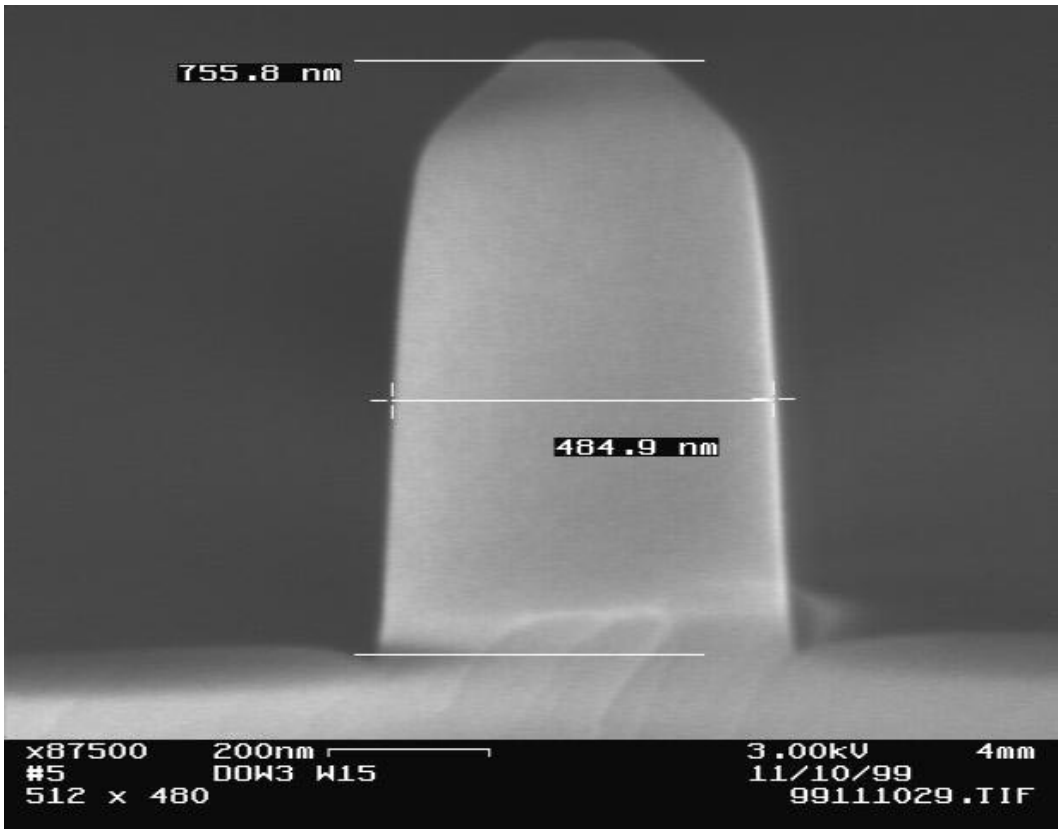

Figure 2-12: Cross-section of silicon nitride waveguide fabricated at Lincoln Labs. The trapezoidal top is due to mask erosion. Although mask erosion resulted in an unexpected cross-section, we believe that the mask actually helped reduce side-wall roughness

temperature oxide or plasma enhanced deposited oxide. The waveguide dimension that was fabricated at Lincoln Labs was 0.7 μm high and 0.5 μm high, with no top oxide cladding. See figure 2-12. This waveguide has a single guided mode (TM mode only) with an effective index of 1.577.

Damascene Process The nitride Damascene processing steps are as follows: First 1-2 μm of thermal oxide is grown on the starting silicon wafer. An 8000 Å thick layer of polySi is then deposited (via low pressure chemical vapor deposition (LPCVD)). This silicon layer is then patterned with the inverse of the desired polySi pattern and etched. An 8000 Å thick layer of silicon nitride is deposited by PECVD in the mold. The waveguides are then polished by Chemo-Mechanical Polishing (CMP) and the mold removed by a wet silicon etch. Again the yields of the Damascene processed waveguides was low and to date no nitride waveguides fabricated by this technique have been successfully measured.

2.2.4 ARROW waveguides

The ARROW structure can be made by a sequence of SIMOX implants [41] and epi regrowths or dielectric stack layers of CVD silicon on oxide. As explained in a previous section, this structure relies on the propagation of a leaky mode with a silicon oxide stack acting as a Bragg reflection (DBR) mirror.

SPARROW

The ARROW waveguides that are studied in this thesis are the Sideways Pedestal ARROW waveguides (SPARROW). A SPARROW waveguide is etched so that the top and the sides of the waveguide are exposed to air. Thus, total internal reflection occurs on 3 sides while the leaky high reflection off the thin silicon layer occurs on the side closest to the substrate. There are several advantages to this geometry. The first advantage is that a single mode SPARROW can be designed since there is confinement in both the horizontal and vertical directions. The second advantage is the index contrast of 1.5 to 1 enables relatively small 10 μm bends to be made. The major disadvantage to this design is that there is no easy way to clad the side-walls with a ULSI compatible material.

Fabrication

The SPARROW waveguides were fabricated from silicon wafer substrates. First a thick 1.5 μm thermal oxide layer is grown by wet oxidation at 1100^{o}C. A thin 120 nm layer of amorphous silicon is then deposited by LPCVD and the entire wafers is then coated with a 1.7 μm thick layer of PECVD oxide. This dielectric stack is then patterned and etched through the polySi layer to the silicon substrate, using reactive on etching through a thick 2 μm resist mask. Waveguide widths of between 4 and 10 μm were fabricated.

2.2.5 Silicon germanium waveguides

Another waveguide system which is compatible with silicon, is a silicon germanium waveguide core with a silicon cladding. Confinement maybe further improved using a strip type structure. Such a structure would exhibit strong confinement in the lateral direction and weak confinement in the vertical direction. One of the advantages of using silicon germanium is that it does not require an underlying oxide which simplifies processing. Furthermore,

this results in a guiding layer which is of rather high crystallinity. These waveguides have been used previously in the literature for integration with silicon germanium detectors.

As stated in previously at the top of this section, silicon germanium waveguides were not studied in this thesis but have been presented for completeness.

2.3 Transmission losses in waveguides

2.3.1 Background

Transmission losses in waveguides in waveguides stem from two main sources:

- core absorption or scattering
- surface scattering due to roughness

When the first polySi waveguides were fabricated, the optical losses were large because of the 25 nm rough top surface of the waveguides. However, these optical losses were reduced when the top surface was smoothed by CMP [45]. By depositing amorphous silicon and then annealing to form polySi, the surface roughness was shown to drop from 25 nm to 4 nm. Most of the optical losses of those waveguides processed in this way were attributed to core losses as a result of an experiment which showed that when the polySi core thickness was reduced from 1 μm to 0.2 μm, the squeezing of the mode out of the waveguide by using smaller dimensions reduced loss by 10 dB/cm [45].

2.3.2 Surface roughness and optical loss

Surface roughness is defined here as the roughness of the top surface of the waveguide.

The main source of the roughness of the top and bottom surfaces are

- grain boundary induced surface roughness, due to grain growth
- roughness induced by a rough underlying substrate

The fact that surface morphology of the polySi is correlated with the grain size, has been utilized by Lee to show that the grain size of the polySi can be readily determined using plan view Atomic Force Microscopy (AFM) measurements. The grains sized of obtained by AFM has been compared with that obtained by cross-sectional Transmission Electron Microscopy (XTEM) and has been shown to be identical [50].

In other materials system, a similar effect has been observed. As a result of large losses associated with grain growth several authors have reported that by using amorphous material with wide band-gap, the effect of surface roughness on waveguide loss is reduced [52].

Calculations and simulations of surface roughness loss

Calculations by Black [45] have used the analysis used derived by Tien et al [52]. Using surface roughness values obtained from Atomic Force Microscopy, a loss figure can be derived. For the best polySi waveguides, a surface roughness of RMS 4 nm (note that this is approximately 14 nm peak to peak) has been reported. When this roughness was used by Black in Tien's analysis for 1 μm thick waveguide a loss of 4 dB/cm loss was obtained which is reasonable.

However, if this same analysis is used on the 0.2 μm thick polySi waveguide which we are working on now, a loss of 100 dB/cm is obtained. This number is obviously in error since the losses reported in this material have been as low as 9 dB/cm. Tien's analysis neglects any consideration of roughness correlation lengths which may explain the difference in the experimentally measured losses and the losses derived from the analysis. Intuitively one might expect that for short correlation lengths (i.e. if the roughness varies much faster or slower than the propagation constant), the phase of the radiating centers changes rapidly resulting in diminished surface roughness loss.

More accurate numerical methods have been published in the literature to determine the effect of interface roughness and this will be explored in the thesis. A first order estimate of the effect of grain boundaries on polySi may be obtained by using the Beam Propagation Method (BPM). To see if BPM could give the correct order of magnitude of loss, a simulation was run with a 10 nm wide, 4 nm high notch in the waveguide (see figure 2-13). When multiplied by the correct number of grain boundaries in a unit length of waveguide, a loss of 10 dB/cm was obtained. Thus, BPM was able to produce the correct order of magnitude for the surface roughness loss in the waveguide.

Controlling surface roughness

The most obvious method would be to use either a single crystalline material (like Smart Cut (tm) silicon on insulator) or an amorphous wide band-gap material like silicon nitride

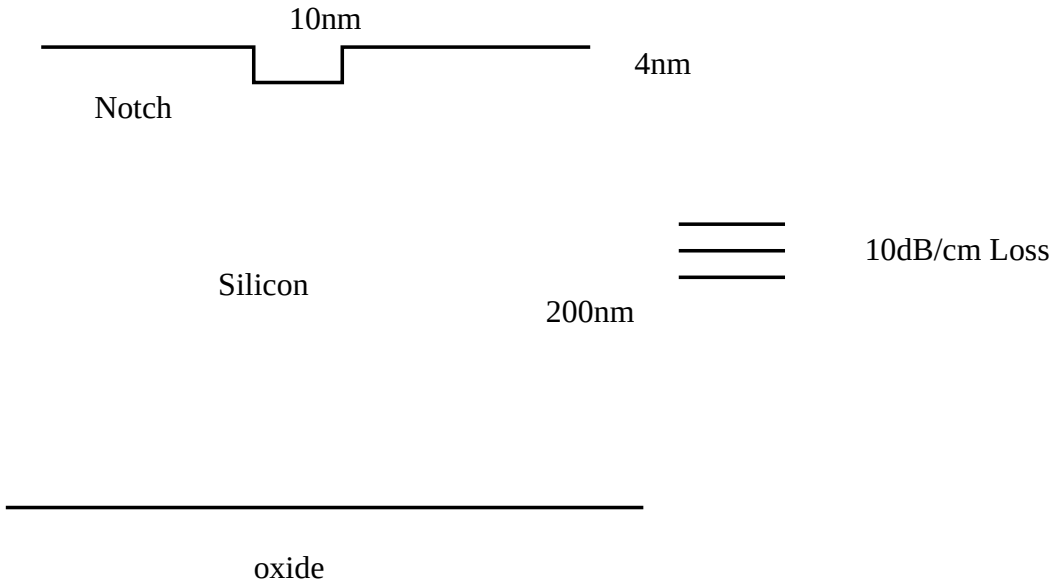

Figure 2-13: Schematic of notch simulated by BPM

or silicon oxide. The surfaces of these materials are much smoother because of the absence of grain boundaries.

If the use of polycrystalline material cannot be avoided, one could trade off the core loss with surface roughness by varying the thickness of the waveguide. Another method would be to use extremely fine grained polySi. This material could be created by using Rapid thermal annealing RTA of the polySi at high temperatures. In such a structure, the small size of the grains would result in smaller but faster varying roughness in the surface.

2.3.3 Side-Wall roughness

Another more pressing problem is side-wall roughness, apparent in 0.5 μm waveguides which are necessary for single mode waveguides [52, 53]. Several issues need to be dealt with here. Waveguides require an unusually high degree of smoothness over large distances (millimeters or centimeters). Furthermore processes which yield very good vertical smoothness with high aspect ratios need not yield good smoothness in the plane of the waveguide.

The Cr lift off process used by Foresi yielded 20 dB/cm loss for an SOI waveguide, as a result of about 10-20 nm roughness on the side-wall. This roughness could have been due to

- grain boundaries in the Cr
- finite PMMA molecule size
- diffraction
- statistical problems due to quantum fluctuations and noise from low photon numbers in the lithography

This roughness problem exists for both amorphous and single crystalline silicon.

2.3.4 Experimental methodology to determine transmission loss

Four methods were used:

- cutback
- paper-clip
- ring resonance Q extraction
- Fabry-Perot resonance [54]

Cutback

The method of cutback is simple. It involves preparing a sample, measuring its transmission, cutting it back to shorten its length and hence increase its transmission and then re-measuring. A variation of this method is to prepare several samples of different length. In order to get statistically significant results and to average over scattering sites several waveguides (usually 20) are measured on each sample. The resulting transmission data is plotted against sample length on a dB-linear scale, referenced against the input laser power. The slope of the linear regression is the loss in dB/unit length and the intercept is the coupling loss.

Cutback is a technique which has been widely used in the literature. See for example [50]. This method is easy to understand, although it does have some major drawbacks. First, if one sample is used and is cut back, the transmission of the waveguide will be measured over several different days, which leads to a lack of control. Secondly, if multiple samples are prepared and measured at the same time, there will be a lack of control in

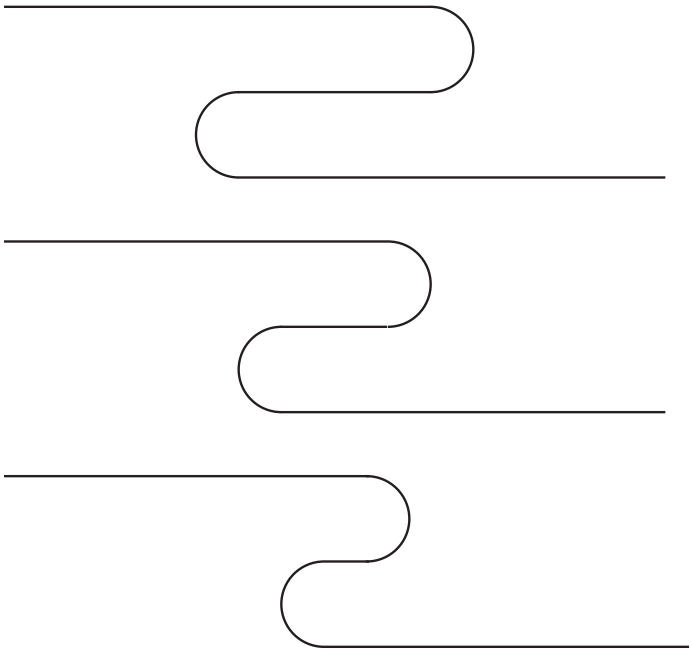

Figure 2-14: Schematic of paper-clip. The paper-clip allows the introduction of waveguides with varying lengths on a single sample, enabling the extraction of loss in waveguides with better accuracy.

terms of sample preparation. For example the sample facet quality may vary from sample to sample. Finally, this method is time consuming since a large number of facets have to be carefully prepared.

Paper-clip

The paper-clip attempts to alleviate the problems of the cutback method. A typical layout of the chip is shown in figure 2-14. The main idea in cutback is to introduce waveguides of different lengths on the same sample. The paper-clip idea uses the fact that in high index contrast waveguides, bending losses are very small. This enables us to layout multiple waveguides with bending radii of 25 μm. In the next section I will show that the loss of these bends are small. Furthermore, if the number of bends is conserved in each structure, then the loss due to the bends can be systematically be eliminated. In the paper-clip method. Transmission measurements are made from each of the waveguides. There are 5 or 10 waveguides of each length. Using a regression method similar to that of the cutback

method the resulting transmission data is plotted against sample length on a dB-linear scale, referenced against the input laser power. The slope of the linear regression is the loss in dB/unit length and the intercept is the coupling loss.

The main advantages of the paper-clip method is that it uses only one sample and the facets are polished only once which means better control of the facet quality than in the cut back method. The major disadvantage of this method is that it can only be used for single mode devices (up to 2 polarizations). The reason for this is that the paper-clips use bends to vary the length of waveguides on a single chip. Multi-moded waveguides would show very large variation because the power transmitted through a multi-moded bend depends strongly on the way it is excited.

Loss from a ring resonance

The loss of a waveguide can be determined from the loss quality factor Q_l of its ring resonance. This is because Q_l is a measure of how well the ring is able retain its energy vs. loss due to absorption or scattering. The determination of loss from a ring resonance is based on the extraction of the Q_l parameter from a ring resonance. The exact details of this parameter extraction requires a detailed analysis of the ring resonators and will be presented in chapter 4. From section 4.3.2,

$$Q_l = \frac{\beta}{\alpha} \tag{2.52}$$

$$Q_l = \frac{2\pi n_{\text{eff}}}{\lambda\alpha} \tag{2.53}$$

$$\alpha = \frac{2\pi n_{\text{eff}}}{\lambda Q_l} \tag{2.54}$$

Thus, the absorption coefficient in the waveguide α can be extracted. Note, however, that the number extracted will be an overestimate since the loss of a bent section of a waveguide is higher than the loss of a straight section. See section 3.1.

Analysis of Fabry-Perot fringes.

The end facets of a waveguide act as mirrors. Hence, if the facets are normal to the waveguides, a Fabry-Perot cavity is set up with the waveguide as the cavity. As a result, a transmission scan vs. wavelength for a waveguide with highly polished facets will result in Fabry-Perot fringes. See figure 2-16. The FSR, or the peak to peak distance of the

Waveguide type	Fabrication facility	Paper-clip	Resonance	Fabry-Perot
SOI	INTEL	26	-	-
	L. Labs	-	14	10
PolySi	INTEL	20	-	-
	L. Labs Direct	20	26	27
	L. Labs Damascene	-	-	17
Nitride	L. Labs Direct	-	66	20
SPARROW	MTL	4.5	-	-

Table 2.2: Table summarizing the loss of the four different waveguides which were studied.

resonances of a Fabry-Perot cavity is to first order

$$FSR = \frac{\lambda^2}{2nL} \tag{2.55}$$

where L is the length of the cavity and n is the effective index of the cavity. The reflectivity an interface can be calculated to be:

$$R = \left(\frac{n_o - n_{eff}}{n_o + n_{eff}} \right)^2 \tag{2.56}$$

Thus, the reflectivity of silicon, silicon nitride and SPARROW waveguides are 20%, 6.7% and 4% respectively. Fabry-Perot fringes should be eliminated in integrated optics devices. This can be done with an anti-reflective coating or with an angled facet. On the other hand, Fabry-Perot fringes may be useful in determining the loss in the waveguide. If the waveguide is lossless, the ratio of the minimum to maximum power of the fringes is zero. If there is loss, the reflected wave cannot make it all the way back to the front facet without attenuation and hence the ratio of the minimum to maximum power of the fringes is increased. It can be proved that with two identical facets of power reflectivity, R, the absorption coefficient can be calculated as

$$\alpha = \frac{1}{L} \ln \left(R \frac{1 + \sqrt{\frac{P_{min}}{P_{max}}}}{1 - \sqrt{\frac{P_{min}}{P_{max}}}} \right) \tag{2.57}$$

2.3.5 SOI Waveguide Loss

As mentioned in a previous section, there were two sources of SOI material. One from Intel and the other Lincoln Labs. The paper-clip method was applied to the measurement of loss

for waveguides from the Intel fabricated waveguides, while Q and Fabry-Perot extraction was applied to Lincoln Labs processed waveguides. The loss numbers that were extracted are summarized in table 2.2.

Intel Process The Intel paper-clip loss was extracted: 26 dB/cm. This number is large when compared to a measurement done by Foresi, [12] who reported a loss of 20 dB/cm, measured on a 0.6 μm wide single crystal waveguide. The 0.6 μm waveguide that Foresi measured allowed the transmission of both the TE and TM mode, while the waveguides fabricated at Intel were strictly singled (as verified with a polarization analyzer). The difference in the loss may be explained by the higher transmission loss of the TE mode than the TM mode as a result of surface roughness. This hypothesis is supported by polySi waveguide data in the next section.

Lincoln Labs Process The Lincoln Labs process used the SOI material made from the same batch as those processed at INTEL. The loss was extracted using two methods:

- Ring Q extraction method. From the ring, a loss Q of 33000 was extracted. The equivalent loss in dB/cm is 14 dB/cm, which is the lowest ever measured loss for a single mode silicon strip waveguide.

- The Fabry-Perot method was also used. A wavelength transmission scan through a SOI waveguide. The low loss nature of the waveguide yielded very large Fabry-Perot peaks $\frac{P_{min}}{P_{max}} = 0.6$, which corresponds to a loss of 10 dB/cm.

This improved loss is due to the much better control of side-wall roughness than in the Lincoln Labs process than in the Intel process. This result is all the more impressive given the fact that the loss was extracted from a waveguide with no top oxide cladding.

2.3.6 PolySi Waveguide Loss

PolySi single mode waveguides are expected to have higher loss than SOI waveguides of the same dimension, because of the larger top surface roughness due to grain boundaries meeting the surface of the waveguides. The losses extracted from polySi waveguides fabricated at Intel and Lincoln Labs are summarized in table 2.2.

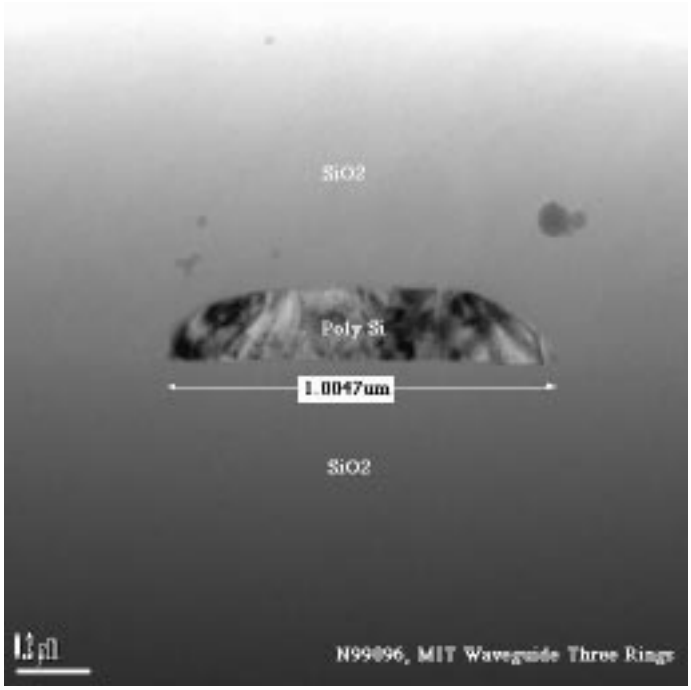

Figure 2-15: Cross-sectional TEM of polySi waveguide fabricated at INTEL Corp. The designed cross-section is 0.2 μm high X 0.5 μm wide. Although the thickness of this waveguide is approximately correct, the measured width is much larger than expected. The rounded edges hint at the possibility of polymerization at the edge of the resist mask that could have protected part of the polySi from being etched.

Intel Direct Write Process The Intel paper-clip loss was extracted: 20 dB/cm. This number is unexpected when compared to the 26 dB/cm number that was extracted for the SOI material fabricated at Intel, since SOI material should exhibit less loss than the polySi material. One of the possible reasons is that the polySi material is multi-moded. In fact a high resolution cross-sectional Transmission Electron microscopy shows that several waveguides were wider than expected. (See figure 2-15). This waveguide had dimensions of 1 μm by 0.2 μm which would enable it to have three TE modes and one TM mode. As mentioned in the previous section the 20 dB/cm loss reported by Foresi [12], was for a waveguide in which the TM mode was not cutoff.

Lincoln Labs Direct Write Process The Lincoln labs paper-clip loss was extracted: 20 dB/cm. This number is self consistent with the number obtained from the Intel SOI data. In addition, this number was independently supported from ring resonance data. The highest Q_l resonance ever extracted in a silicon ring was 17700, extracted from a ring with a radius of 5 μm, which corresponds to a loss of about 26 dB/cm. These values are in close

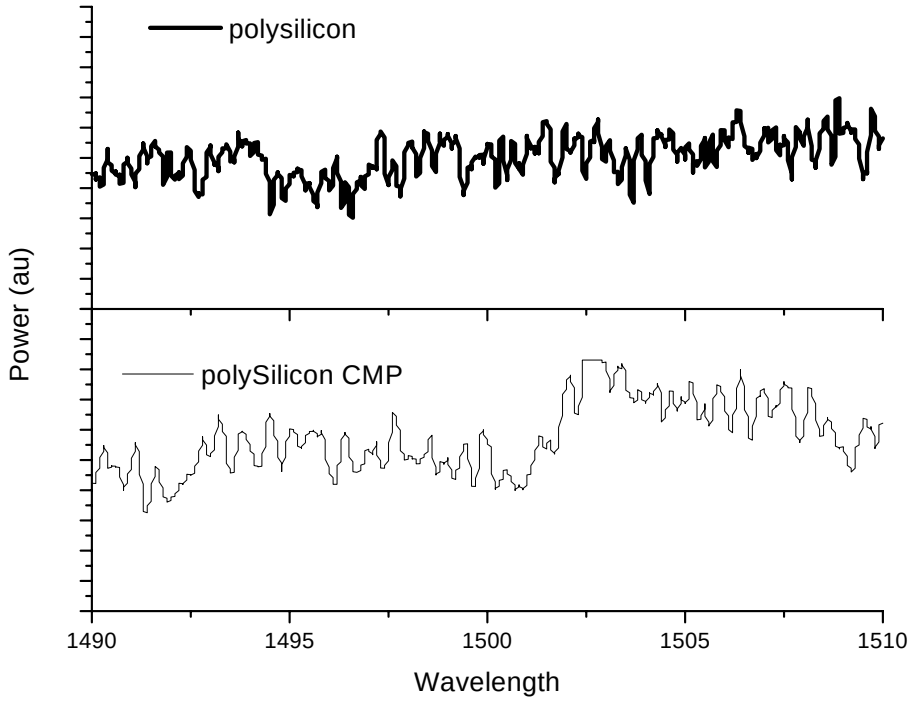

Figure 2-16: Wavelength scan across a 2 mm long polySi waveguide. This scan shows the fine Fabry-Perot resonance peaks, separated by approximately 0.3 nm, which corresponds to a sample length L of 2 mm. $\frac{P_{min}}{P_{max}} = 0.8$ for the direct write polySi sample and $\frac{P_{min}}{P_{max}} = 0.7$ for the Damascene sample.

agreement given that one expects the bending loss to be higher!

Lincoln Labs Damascene Process As has been previously stated, the yield of the Damascene Process was low and to this point no ring samples have been successfully measured. Furthermore, due to the small number of operating waveguides, cutback is not possible. In order to extract the loss from a single waveguide, the Fabry-Perot resonance technique is used.

Fabry-Perot fringes Strong Fabry-Perot fringes were observed in the transmission spectra of all the polySi waveguides; see figure 2-16. For a device length of 2 mm, the peak to peak separation of the Fabry-Perot fringes is 0.23 nm which is also the experimentally extracted number.

From the Fabry-Perot fringes, the extracted loss of the Damascene processed polySi is

17 dB/cm. The Fabry-Perot extracted equivalent loss number for the direct write processed polySi is 27 dB/cm. This difference is probably not statistically significant because there was some difficulty extracting the Fabry-Perot fringes from the Damascene sample.

2.3.7 Silicon nitride waveguide loss

Although single mode paper-clips were fabricated and tested for silicon nitride waveguides, attempts to extract meaningful loss data from these waveguides were unsuccessful. The transmission data was extremely scattered implying that either the material quality was not uniform or that the facets of the waveguides varied from waveguide to waveguide. Even with a clean waveguide sample with no scratches and dust particles, the variation was large. From experience this is indicative of the facet quality being poor.

The other interesting observation was that the power transmitted through a nitride waveguide is always much higher than in a polySi waveguide. This could have been due to the larger coupling efficiency due to the larger waveguide mode size and the lower reflectivity of the air-nitride interface relative to the air-silicon interface.

Analysis of Ring Resonances 66 dB/cm was extracted from a 4 μm ring with Q = 2000. The expected loss for a 4 μm ring is 390 dB/cm. These results are summarized in figure 2-17. This surprisingly low loss is due to the fact that silicon nitride index was higher than expected. More evidence for this will be presented in the next chapter.

Analysis of Fabry-Perot fringes. Fabry-Perot fringes were observed in the transmission spectra of all the silicon nitride waveguides; see figure 2-18. However, the amplitude of the Fabry-Perot fringes for the nitride waveguides is much smaller than for the silicon waveguides. This is due in part to the lower reflectivity of the nitride air facet. For a device length of 2 mm, the peak to peak separation of the Fabry-Perot fringes is 0.37 nm which is also the experimentally extracted number. From the Fabry-Perot fringes a loss of 20 dB/cm was extracted, which would be large for this nitride waveguide. The reason for this large extracted loss can be the poor facet quality as alluded to earlier.

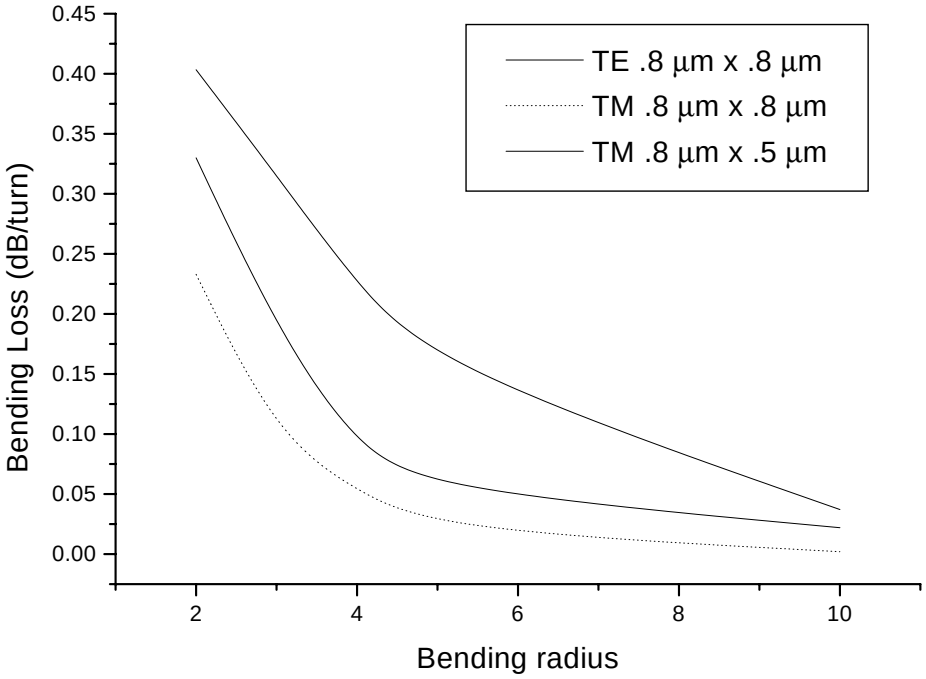

Figure 2-17: Simulated bending losses for a silicon nitride waveguide. The bending losses for >2 μm radius bends are small.

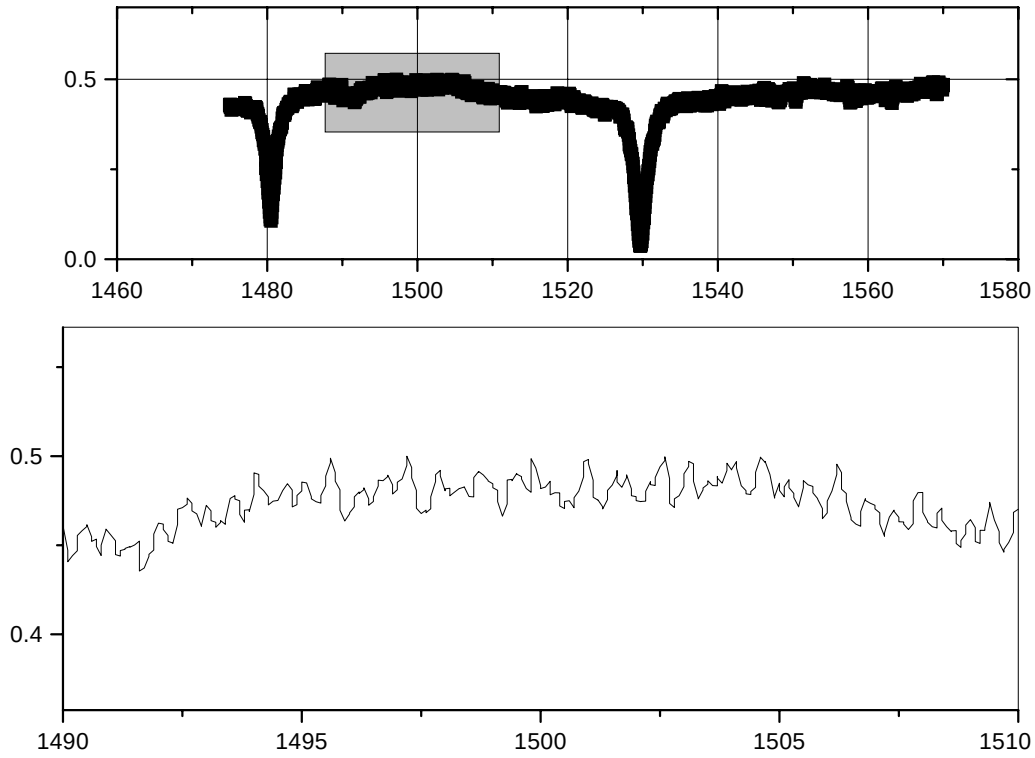

Figure 2-18: Wavelength scan across a 2 mm long nitride waveguide. This scan shows the fine Fabry-Perot resonance peaks separated by approximately 0.45 nm, which corresponds, approximately, to the correct sample length L = 2mm.

2.3.8 SPARROW loss

Paper-clip SPARROW waveguides were fabricated and measured. A loss of 4.5 dB/cm was extracted. This number is close to the theoretical value of 1 dB/cm which was predicted for these waveguides. Most of the non-ideality of the loss can be traced to the thicknesses of the fabricated layers not being correct. In fact process variations of 5-10% were observed. On the other hand, most modern day fabrication facilities have thickness tolerances of about 1-2%, which means that with proper thickness control, these losses will be eliminated.

2.4 Polarization Dependent Loss

2.4.1 PolySi Transmission Loss

When two modes are supported (TE and TM) the TM transmission in the waveguide seems to be much higher. This is borne out both by loss extraction measurements (26 dB/cm for TE only and 20 dB/cm for both TE and TM) and looking at the power transmitted through a waveguide with a polarization analyzer. If TE light is incident on a waveguide with a taper at its incident facet to aid coupling, both TE and TM are measured at the output of the waveguide. However, if TM light is incident on the waveguide only TM is measured at the output of the waveguide.

Although these results seemed surprising at first, it may be easily explained by the fact that the waveguide is asymmetric and the roughness on the side-walls is much larger than on the top and bottom surfaces of the waveguide. I suspect the mixing happens because of the taper, which has rough and narrowing side-walls. This results in a small amount of power coupling from the TE mode into the TM mode and vice versa. Propagating down the waveguide, the TE mode is preferentially attenuated resulting in measurable amounts of TE and TM at the output if the input is TE. If TM is coupled in at the input, the small amount of TE that is generated due to the rough side-walls is attenuated.

Simulation of side-wall roughness BPM mode solving simulation were run to understand why the loss of the TE and TM modes are different. A 0.25 μm high by 0.55 μm waveguide was simulated with lossy side-walls. To make the problem easy the scattering loss was lumped as an imaginary index of -0.005, which corresponds to an α of about 200 cm^{-1}. The thickness of the scattering regions was taken to be 5% of the width on each

side-wall. Running the mode solver in complex mode, the loss of each mode may be computed. A loss of -30 dB/cm was extracted for the TE mode while a loss of -27 dB/cm was extracted for the TM mode. Thus, side-wall roughness explains why there would be polarization dependent loss.

2.5 Dispersion Simulations

Two types of dispersion were studied:

- Group Velocity Dispersion (GVD)
- Modal Dispersion

Group Velocity Dispersion In GVD simulations, a mode simulation of the waveguides is run for each wavelength and a curve of n_{eff} vs. wavelength is obtained. With this information the dispersion curve is easily obtained from equation (2.50). As shown in figure 2-19, dispersion is very small for all three waveguides which were considered: polySi, silicon nitride and SPARROW waveguides, especially if the waveguides are on the order of centimeters long. For a 100GHz bandwidth pulse, the max group delay due to dispersion is less than 100 fs after propagation through a 2 cm long waveguide. Assuming a pulse length on the order of a ps, this group delay is negligible.

Modal Dispersion For modal dispersion simulations, a symmetric waveguide, which would have symmetric TE and TM modes, is perturbed to simulate fabrication error. This perturbation would split the degeneracy of the symmetric modes. By computing the n_{eff} vs. wavelength curves, the modal dispersion, the difference in group velocity of the TE and TM modes can be calculated.

Silicon strip waveguide With a 5% error or 10% maximum fabrication variation, the oxide clad 0.3 μmX 0.3 μm silicon showed a difference in group velocity of 2% (see figure 2-20). Thus, the modal separation after propagation through a 2 cm long sample is on the order of 5ps, which is substantial!

Silicon nitride strip waveguide Even with a 5% error or 10% maximum fabrication variation, the oxide clad 0.8 μmX 0.8 μm silicon nitride showed a difference in group velocity

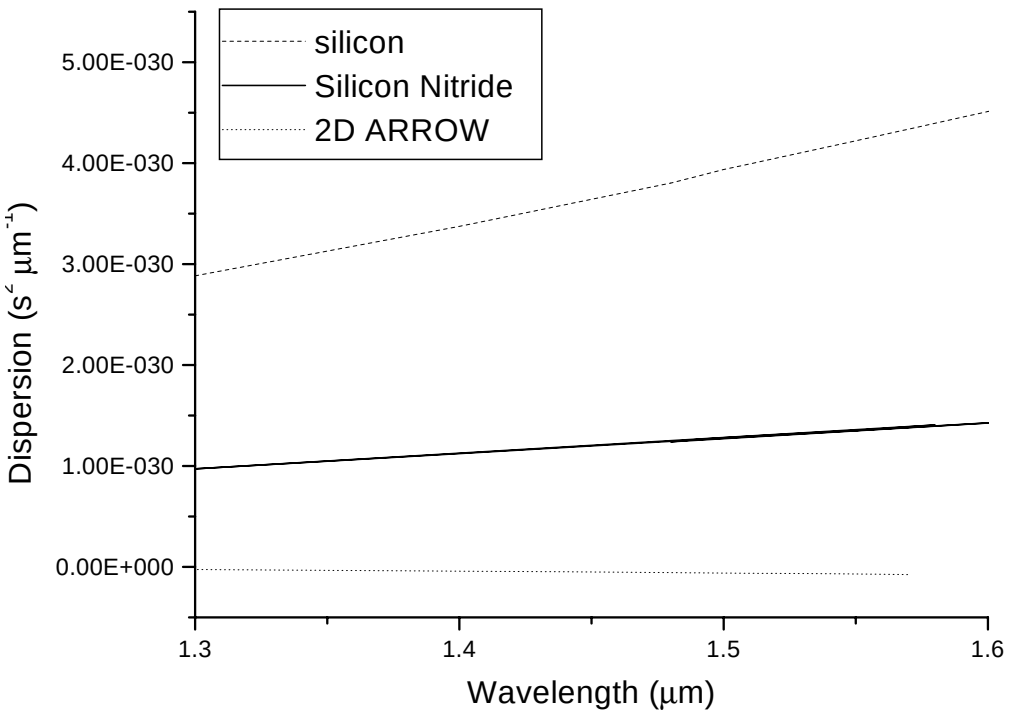

Figure 2-19: Graph of Group Velocity Dispersion of a 2D ARROW, silicon nitride strip and polySi strip waveguides. For a 100GHz bandwidth pulse, the maximum group delay due to dispersion is less than 100 fs after propagation through a 2 cm long waveguide.

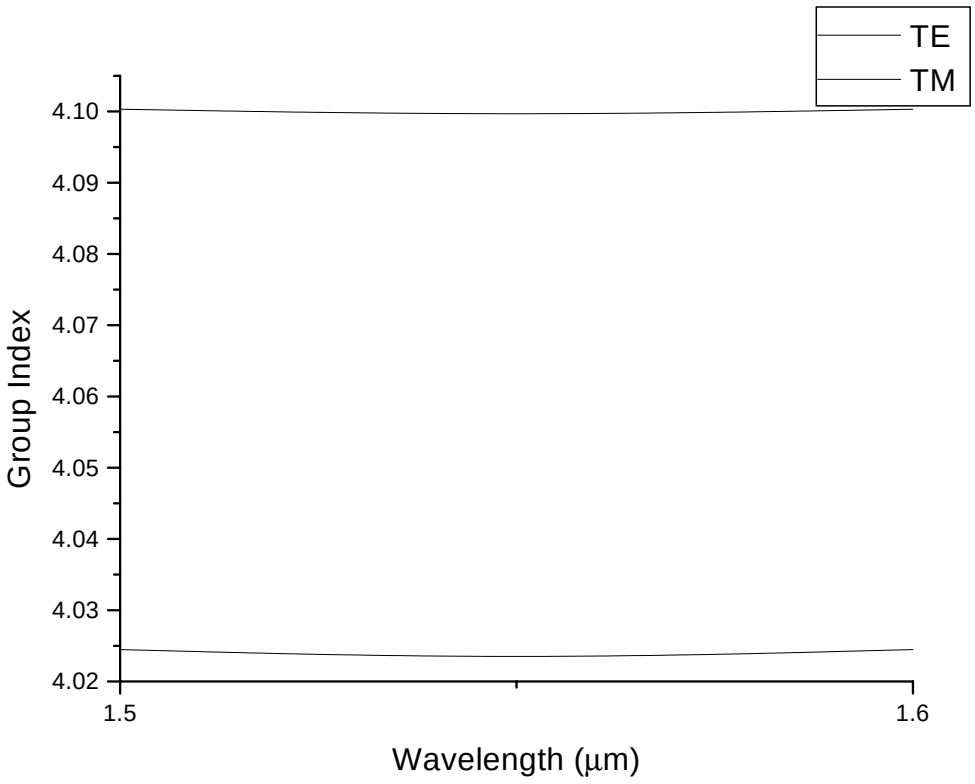

Figure 2-20: Graph of group velocity of TE and TM modes for a 0.3 X 0.27 μm^2 silicon waveguide. A 10% fabrication error in the core size of the waveguide leads to a 2% difference in the group velocity of TE and TM modes, which in turn leads to a 5 ps spread in the pulse after 2 cm of propagation.

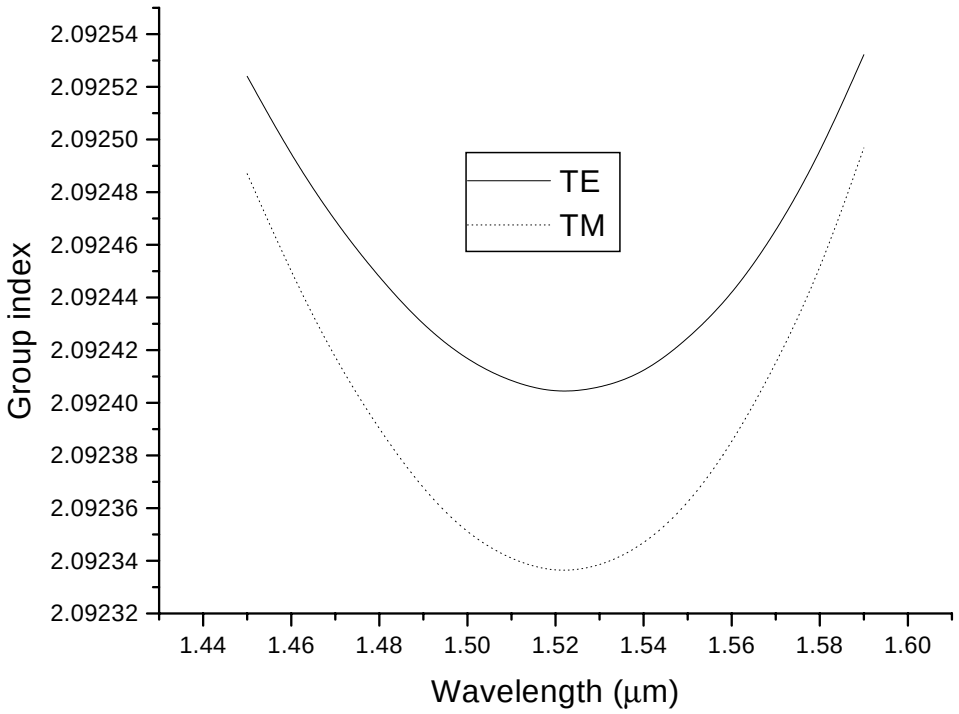

Figure 2-21: Graph of group velocity of TE and TM modes for a 0.8 X 0.72 μm^2 silicon nitride waveguide. A 10% fabrication error in the core size of the waveguide leads to a 0.01% difference in the group velocity of TE and TM modes, which in turn leads to a 10 fs spread in the pulse after 2 cm of propagation.

of 0.01% (see figure 2-21). Thus, the modal separation after propagation through a 2 cm long sample is on the order of 10s of fs which is negligible.

As the index contrast goes up, the modal dispersion problem becomes more severe, since the asymmetry resulting from a fabrication error becomes more severe. One fix for this is to wrap the high index contrast waveguide with a intermediate lower index contrast material. This would alleviate modal dispersion problems arising from fabrication errors.

On the other hand, modal dispersion may be used in sensing applications. This is studied in the next section.

2.6 Integrated optical sensors

Due to the inherent sensitivity of an optical component to its environment, integrated optical sensors provide a platform for accurate and compact sensing. One example which was studied is the chemical sensor.

In a collaboration with SATCON and Boston University, differential TE/TM sensors were studied. A silicon nitride slab waveguide was fabricated at MIT. The thickness of the nitride waveguide was chosen so that a single TE and a single TM mode is supported at $\lambda =$ 633 nm, with the assumption that the incident wave and the waveguide are infinite in extent in the direction orthogonal to the direction of propagation and to the waveguide surfaces. The effective indices of these two modes, n_{TE} and n_{TM} change differently if a material is adsorbed onto the surface. Thus, a phase shift is obtained $\Delta\Phi(t) = \frac{2\pi L}{\lambda}(\Delta n_{TE} - \Delta n_{TM})$. The principle idea is to use a waveguide which is coated with a thin layer of material which has a strong affinity for the substance to be detected. If the material to be detected is present, it will stick to the binding layer of material and the difference in interaction of the evanescent fields of the TE and TM mode can be measured as a difference in phase, by interfering the TE and TM modes together at the output facet. An example of such a layout is shown figure 2-22. Figure 2.6 shows a typical response of of such a chemical sensor.

2.7 Summary

In this chapter, the fundamental building block of microphotonics, the waveguide, was analyzed. High index contrast silicon and silicon nitride waveguides as well as SPARROW

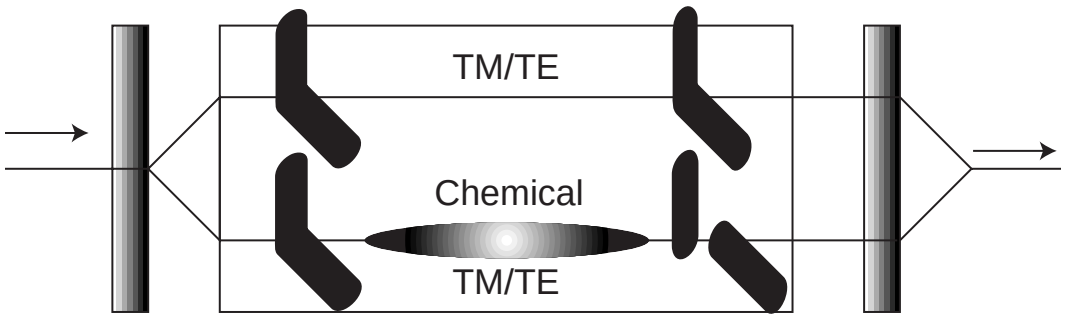

Figure 2-22: Schematic of a differential TE/TM chemical sensor fabricated from a silicon nitride strip waveguide. The top arm will have a different TE/TM phase difference than the bottom arm in the presence of a chemical. This is picked up as a phase shift. The top arm allows for environmental stabilization.

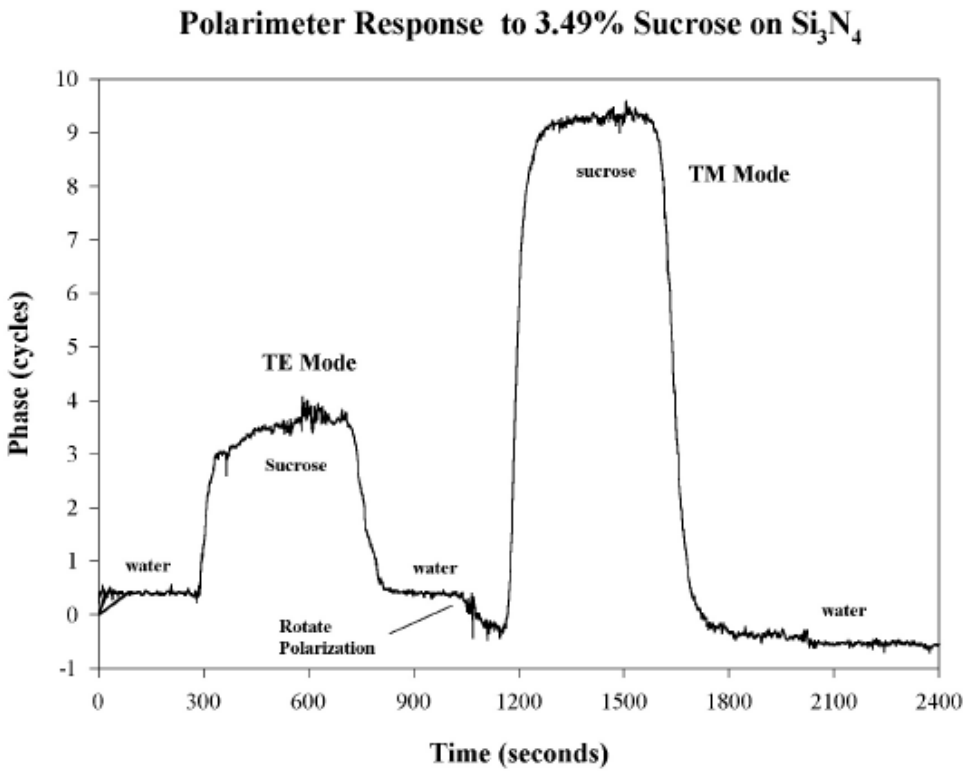

Figure 2-23: Response of a differential TE/TM chemical sensor fabricated at MTL. Using only the TE mode or only the TM mode, the presence of sucrose can be detected. However, when the data are used together, one can make adjustments for temperature drifts. Data courtesy of R. Reider, SATCON. (SatCon Proprietary)

waveguides have been processed with ULSI compatible techniques.

Transmission losses for two types of silicon strip waveguides were measured. The first type of strip waveguide is a strictly single mode waveguide which propagates the TE polarization for which a loss of 26 dB/cm was extracted over a variety of samples. The second is a single mode waveguide which propagates both the TE and TM polarizations for which a loss of 20 dB/cm was extracted.

The losses that are reported here: 26 dB/cm and 14 dB/cm for air clad polySi and single crystal silicon single mode waveguides are the lowest that have ever been measured. [12] This substantial improvement may be attributed to better control of side-wall roughness.

Another important finding is that polarization dispersion and polarization dependent loss is an important factor in high index contrast waveguides. The TM mode of a single mode polySi strip waveguide with a 1:2.5 aspect ratio exhibited, surprisingly, smaller loss than the TE mode. The polarization dependence may be brought about in three ways.

- Design of waveguide. A waveguide may have polarization dependence due to asymmetry in size or in the core or cladding indices.
- Fabrication variation. A well designed waveguide may have polarization dependence due to processing variations in index, size or side-wall roughness.
- Materials Properties. For example stress induced birefringence may cause polarization dependent index of refraction which would interfere with interferometric or resonator devices

Polarization dependent loss may be a good metric for side-wall roughness in optical lithography.

2.7.1 Future work

Further reduction of loss in polySi and silicon on insulator waveguides is possible. In fact, with the recently reported side-wall roughness figure of 1.3 nm from Lincoln Labs [55], Lee, using the analysis developed in [56] has determined it is possible to fabricate single mode Smart Cut (tm) silicon on insulator waveguides with losses of less than 5 dB/cm. The ultimate limitation of single crystal silicon waveguide (with no side-wall roughness) would be the absorption loss, which is much less than 1 dB/cm. As proposed by [42], anisotropic etching of silicon waveguides may provide the best means of achieving this low loss.

For polySi waveguides, the transmission is further limited by the top surface loss, which is determined by the grain boundaries meeting the top surface of the waveguide. The natural corrugation that results from this feature may be the ultimate limiting factor in the loss of the waveguides. Toyoda, has proposed the use of surface smoothing by cluster ion implants. In addition, roughness reduction from 4 nm to less than 1 nm RMS may be possible with CMP.

The challenges facing silicon nitride waveguides are two-fold. The first is the large stress induced birefringence in silicon nitride, which would result in polarization dependence and the second is the difficulty in preparing good facets. Techniques developed for facet preparation of oxide and silicon waveguides, do not work well for facet preparation of silicon nitride waveguides.

Finally, better control and understanding of the polarization dependence of loss is also needed. Again this problem will be alleviated by the improvements in line edge roughness. Nitride waveguides alleviate the loss problem due to its lower index contrast, its amorphous core, which leads to smoother surfaces. In addition it is easily deposited by PECVD which is a low temperature process and does not require annealing. Furthermore, polarization problems related to fabrication error and scattering are reduced.

Chapter 3

Waveguide Bends, Splitters and Switches

In this chapter, three kinds of routing devices which are based on waveguides are studied: bends, splitters and switches.

3.1 Bends

Low loss, small sized bends are important in integrated optics as they allow one to route signals from any point to point. The reason why bent waveguides always radiate power is because there is a phase mismatch between the E-field in the core and the E-field in cladding [57, 58, 59]. When the maximum phase velocity of the evanescent field in the outer cladding is less than the phase velocity of the mode in the core, power is radiated. Since radiation loss occurs from the cladding, the bending losses will be negligible in waveguide systems where the mode is confined to a small region. Thus, bending losses are minimized when the index contrast between the core and the cladding is increased due to the smaller evanescent field in the cladding.

3.1.1 Calculation of loss

Several analytical methods have been proposed and applied to waveguides [57, 58, 59]. However, these methods invariably break down when applied to small radius high index contrast waveguides [42].

Bending losses can be quite accurately calculated by the BPM method by using a conformal mapping technique [10] which transforms the index profile of a curved waveguide with a constant radius of curvature to an index profile of a straight waveguide [42]. The lossy mode of the conformal mapped waveguide can be solved, and the loss can be extracted.

If the bending radius, R, is much larger than the width of the waveguide then the index $n(x, y)$ after conformal mapping approximates to:

$$n(x, y) \rightarrow n(x, y)\left(1 + \frac{\rho}{R}\right) \tag{3.1}$$

This simple transformation, captures the physics of the bending problem. When the waveguide is bent, the index of the outer cladding is increased; see figure 3-1. Thus, light is able to couple into the radiation modes. As the waveguide is bent more, the index slope is larger and more light is able to couple out.

Mode overlap Using the conformal mapping technique, it is possible to calculate numerically a lossy mode for the bent waveguide section. If one then uses the mode overlap method to calculate the transmission from the straight waveguide section to the bending section, the loss that is obtained is several orders of magnitude too high. One reason for this is that the bends are so short (a 2 μm radius 90^o bend in silicon is only 3.5 wavelengths long) that higher order lossy modes may be able to transfer their energy with low loss. As a result of the difficulty in predicting the loss in bends, numerical methods like FDTD and BPM are most suitable for theoretical bending loss analysis.

3.1.2 Experiments

Micron sized single mode bends were studied with SOI, polySi and silicon nitride waveguides. Two different experimental techniques were used to experimentally extract bending losses.

Multiple bend technique In this technique, groups of waveguides with 4 8 and 12 bends respectively were measured. The power transmitted in dB was plotted against the number of bends. The slope of the line of best fit is then the loss in dB/turn.

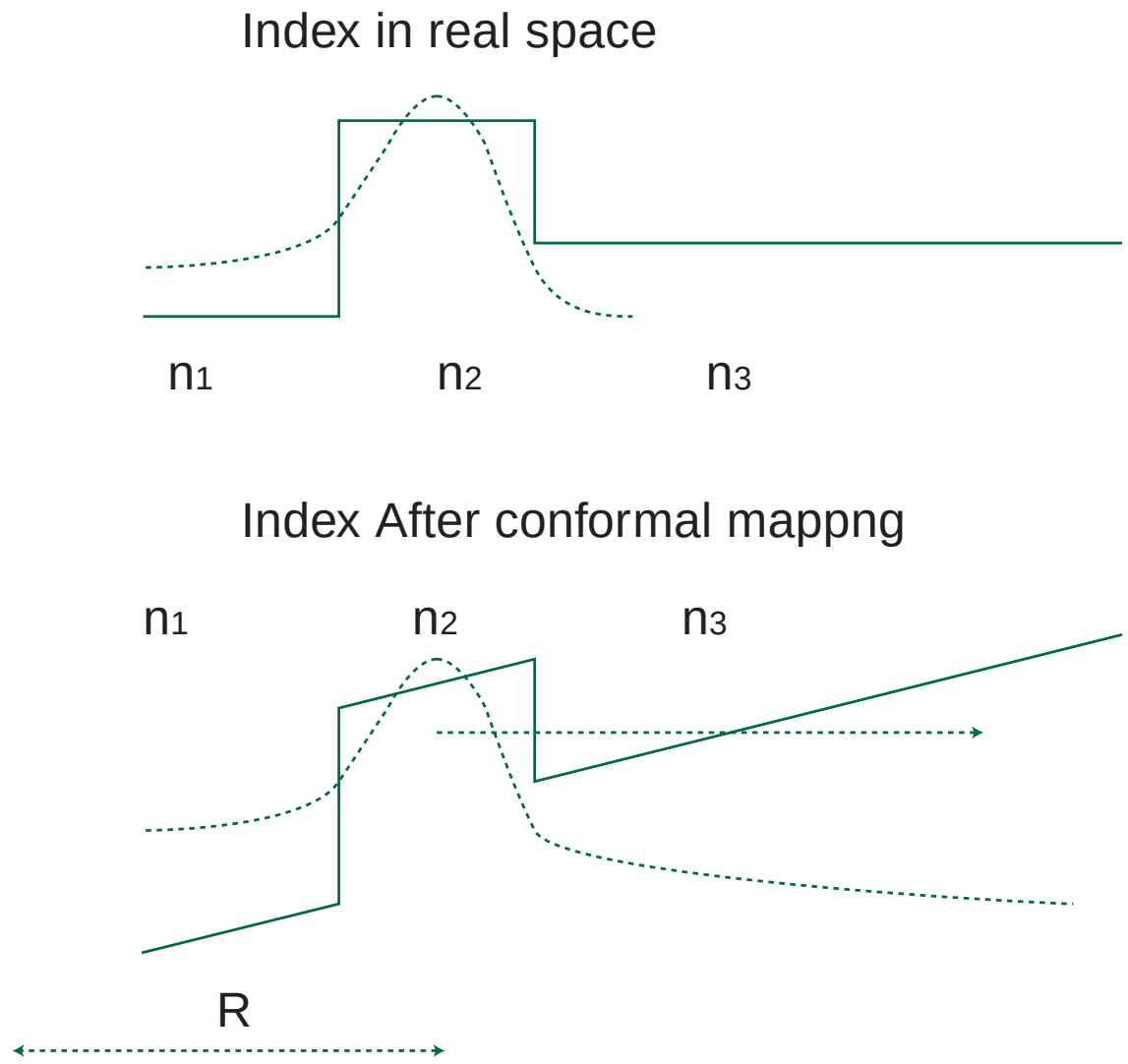

Figure 3-1: Conformal transformation proposed by Heiblum et al [10] for studying bending loss in BPM.

Loss extraction from ring resonator

In a method similar to waveguide transmission loss extraction, the loss per bend can be calculated. From equation (2.54),

$$\alpha = \frac{2\pi n_{\text{eff}}}{\lambda Q_l} \tag{3.2}$$

$$\text{Loss/bend in dB} = \alpha \times .25 \text{ circumference of ring} \tag{3.3}$$

$$\text{Loss/bend in dB} = \frac{4.3\pi^2 n_{\text{eff}} R}{\lambda Q_l} \tag{3.4}$$

We now consider the simulated and experimental bending losses of the traditional round bend for SOI, polySi and silicon nitride waveguides respectively.

3.1.3 SOI Round bends

Intel process The loss of 1 μm, 3 μm and 10 μm bends were experimentally extracted and plotted in figure 3-2. The results show that the loss is higher than predicted by BPM. This is expected since BPM loss neglects any side-wall scattering loss. Nevertheless the loss in dB/turn is small especially for the 3 μm bend for which a loss of 0.15$\pm$0.05 dB/turn was extracted. This small loss is sufficient for routing applications, since a total of ten bends will lead to a loss of 1.5 dB or 30% power loss.

3.1.4 PolySi Round Bends

Intel process The experimentally extracted bending loss for bends of 1, 3, 5 and 25 μm bends are plotted in figure 3-2, These values are much higher than those of the equivalent of SOI material and what was published by Foresi [12]. It is believed that the multi-moded polySi waveguide is the most logical explanation for such a high loss. From figure 2-15, the cross-section of a waveguide fabricated at Intel was taken and the waveguide in that picture was multi-moded. More details of the polarization dependence are presented in the next section.

Lincoln Labs process The bending loss of 1 μm bends was extracted using the multiple bend technique. The value of 0.5 dB/turn is smaller than that obtained in the Intel process. Loss in dB/turn for the 3 and 5 μm rings are 0.012 dB/turn and 0.015 dB/turn respectively. For a 2 μm ring a Q_l of 3000 is extracted which corresponds to a loss of 0.047 dB/turn!

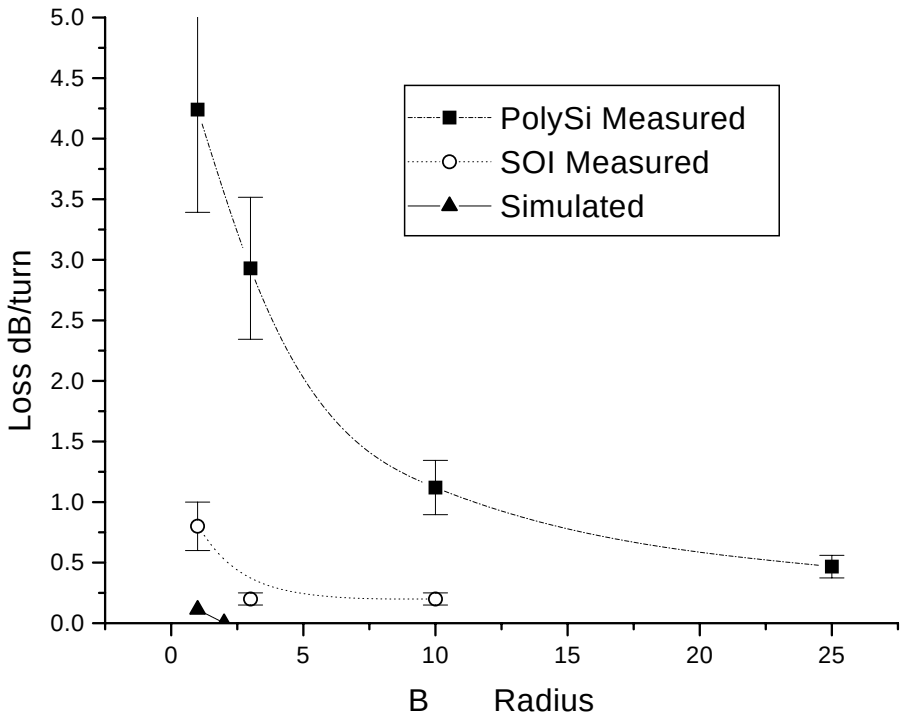

Figure 3-2: Measured and BPM simulated loss for SOI and polySi bends fabricated at Intel Corp. Simulated losses are much less than the SOI measured bending loss because side-wall roughness is neglected in the simulation. PolySi bending losses are much larger than the SOI bending loss because the TM mode in the polySi waveguides dominates the bending loss. The TM mode does not propagate in the SOI waveguides. The radius on the x-axis is the outer radius of the bend.

These loss values are much smaller than that extracted from the direct measurement of the Intel SOI material. These results would be consistent better side-wall roughness control in the Lincoln Labs process as mentioned in section 2.3.5.

3.1.5 Polarization dependent bending loss

As explained in section 2.4, the Intel SOI waveguides guided only one (TE) polarization and the Intel polySi waveguides guided at least two polarizations. The bending losses of the 1 μm radius bends for these materials were 0.8 and 4 dB/turn respectively, a 1:5 ratio. In addition, when a polarizer as a polarization analyzer, the loss of the TE and TM modes around the bends in Intel polySi waveguides was studied. Invariably, the TE mode exhibited much lower loss than TM bends going around bends.

A more careful study revealed that if a polySi waveguide which guided both TE and TM has any bend at all, the TM mode will be strongly suppressed. The amount of TM light coupled out of a waveguide with 4 bends is much smaller than the amount of light coupled out of a straight waveguide. This loss is so large that we can only put an lower bound of 5 dB/bend for the TM mode.

Another very interesting point is that the larger bending loss for TM in the waveguide seems to conflict with the lower transmission loss for TM than for TE. In section 2.4, TM exhibited lower transmission loss than TE. The opposite is true for bending loss. To study why there is such a strong dependence of loss on polarization and to explain the seemingly contradictory dependence of bending loss on polarization, the loss for a 1 μm (outer radius) bend was simulated, with the same parameters used in section 2.4. Without side-wall roughness this dependence of the loss on the polarization cannot be explained. However, with side-wall roughness, the ratio of the bending loss in TE to that of TM was 1:3. Thus, the big difference in loss between the two polarizations may be explained by the difference in the magnitude of interaction of the side-wall roughness with the two modes.

The implications of this dependence of loss on polarization is important since it implies that for high index contrast waveguides at least, the side-wall roughness must be well controlled to minimize potential problems with polarization loss.

3.1.6 Silicon nitride waveguides round bends

The losses of silicon nitride bends were extracted from ring resonance results because the power variation form waveguide to waveguide was too high to yield any meaningful results for the multiple bend measurement technique. However, meaningful loss numbers are easily extracted from ring resonance data.

The losses in dB/turn for the 2, 3 and 4 μm rings are 0.074 dB/turn, 0.035 dB/turn and 0.013 dB/turn respectively for a 0.5 μm x 0.8 μm silicon nitride waveguide. For all intents and purposes, these losses are negligible. The simulated losses for this waveguide are .48 dB/turn, 0.37 dB/turn and 0.39 dB/turn respectively. It is surprising that these losses are so large, given that one expects the simulated losses would be much smaller than the experimentally determined losses. One possible explanation for this anomalously low loss is a higher than expected core index. In the next chapter, the core index is extracted independently as explained in figure 4-11. Using the same core index of 2.4 that was used to fit the data in figure 4-11, the simulated losses would be 0.08 dB/turn, 0.003 dB/turn and 0.0003 dB/turn respectively, which is more consistent with the extracted loss numbers. See figure 4-11.

3.1.7 HTC bends

C. Manolatou et al proposed a two dimensional structure in her paper based on a two-dimensional high transmission cavity (HTC) with a polygonal shape [60]. The cavity structure allowed her to design high transmission low loss cavity bends and splitters, with bandwidths exceeding 100 nm and transmission greater 95%. In this work, a three-dimensional cavity was fabricated based on the 2-D design.

The design of the high transmission cavity (HTC) is a polygon, with one side at 45 degree angle to the incoming and outgoing waveguides, (See figure 3-3). A bend may be made be adding two waveguides. (see figure 3-4). The HTC bend may be understand in two ways. The first is to look at the 45^o facet as a "reflector". As light enters through one waveguide it is "reflected" off the 45^o facet. In addition, the extra material on the inside of the HTC acts to pull the mode away from the outer wall, improving the mode matching of the bending section with respect to the input and output waveguides, which in turn reduces the loss of the bend. The other way to understand the HTC is to analyze it as a low Q

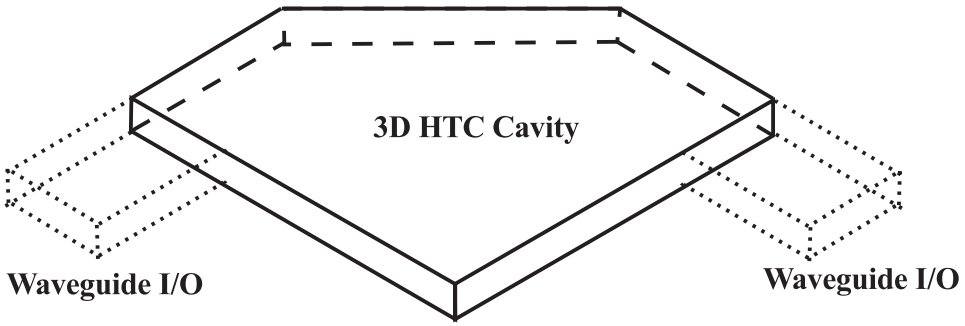

Figure 3-3: Schematic of the HTC.

resonator. The resonator is strongly coupled to the input and output waveguides resulting in its low Q and large transmission bandwidth.

PolySi HTCs

The bending loss of three different sizes of HTC bends (see figure 3-4) fabricated on the same mask as the 1 μm bends fabricated at Lincoln Labs, was extracted using the multiple bend technique. The value of 0.3 dB/turn for the best HTC bend design is smaller than the loss value obtained for the round bend.

Loss in dB/turn was also extracted from the transmission spectra of traveling wave resonators constructed with HTC bends (see figure 3-5). These resonators were proposed by Lee as a method of making traveling wave resonators in silicon on insulator devices using anisotropic etching techniques. This resonator consisted of four HTCs and straight waveguides to form the resonator. The measured Q was 750 and the loss of the HTC was extracted to be 0.2 dB/turn, which is consistent with the number extracted from the multiple bend measurement.

Silicon nitride HTCs

The experiment was repeated for silicon nitride waveguides. The HTC was not expected to work as well for silicon nitride waveguides because the index contrast of these waveguides was smaller. Like all previous silicon nitride multiple bend/paper-clip measurements, attempts to get meaningful loss data from measurements of many waveguides failed. However, loss numbers were obtained from the traveling wave resonators.

From a resonator with 6 μm by 12 μm straight edges a Q_l of 350 was extracted, from which a loss of 0.76 dB/turn was calculated. This loss was surprising since the HTC

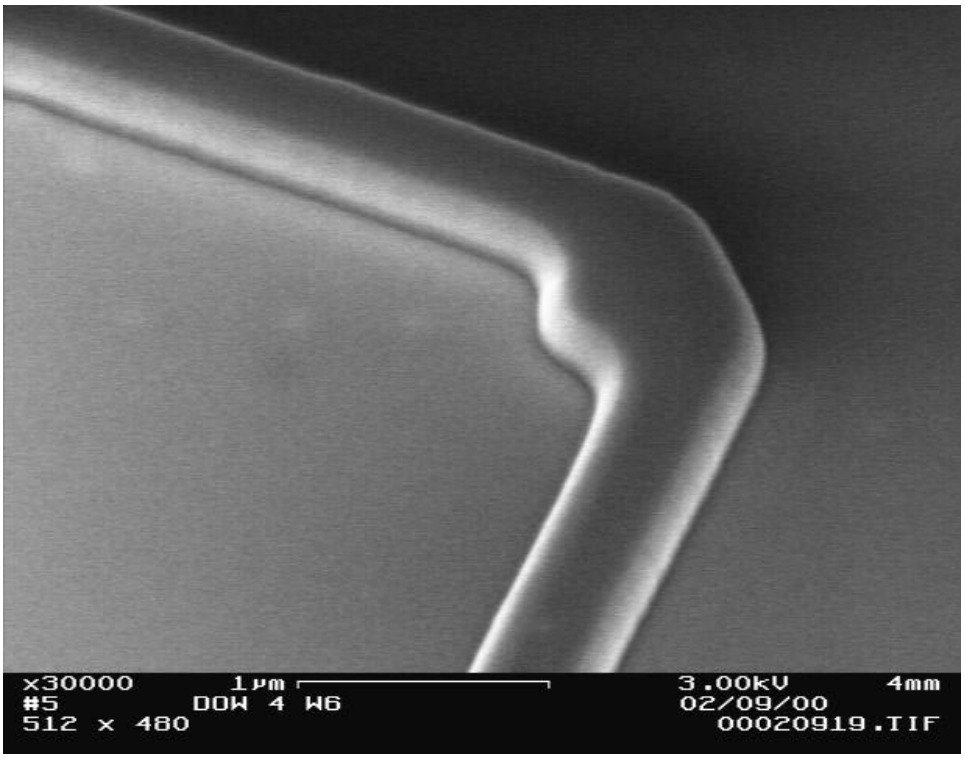

Figure 3-4: SEM of the HTC bend fabricated in polySi. The HTC occupies an area of about 0.5 μm^2 and is the tightest bend ever made for a wavelength of 1.55 μm.

dimensions were not optimized for silicon nitride waveguides. On the other hand, HTC losses are expected to be higher in silicon nitride waveguides because the confinement of the cavity modes improves when the index contrast is higher. Another way of looking at this is, as the index contrast is raised, the reflectivity off the 45^o angle is improved. This improved reflectivity, in turn, reduces the bending loss.

Advantage of HTC over round bends

The advantage of the new HTC design vs. previous designs may be summed up in its small size, low transmission loss. The HTC bends are less than 0.5 μm^2 and have power transmission in excess of 98%. Traditional round bends can be made with very low loss, but to get the same loss the round bend must be bigger. A comparison of HTCs and 1 μm radius round bends is summarized in table 3.1.

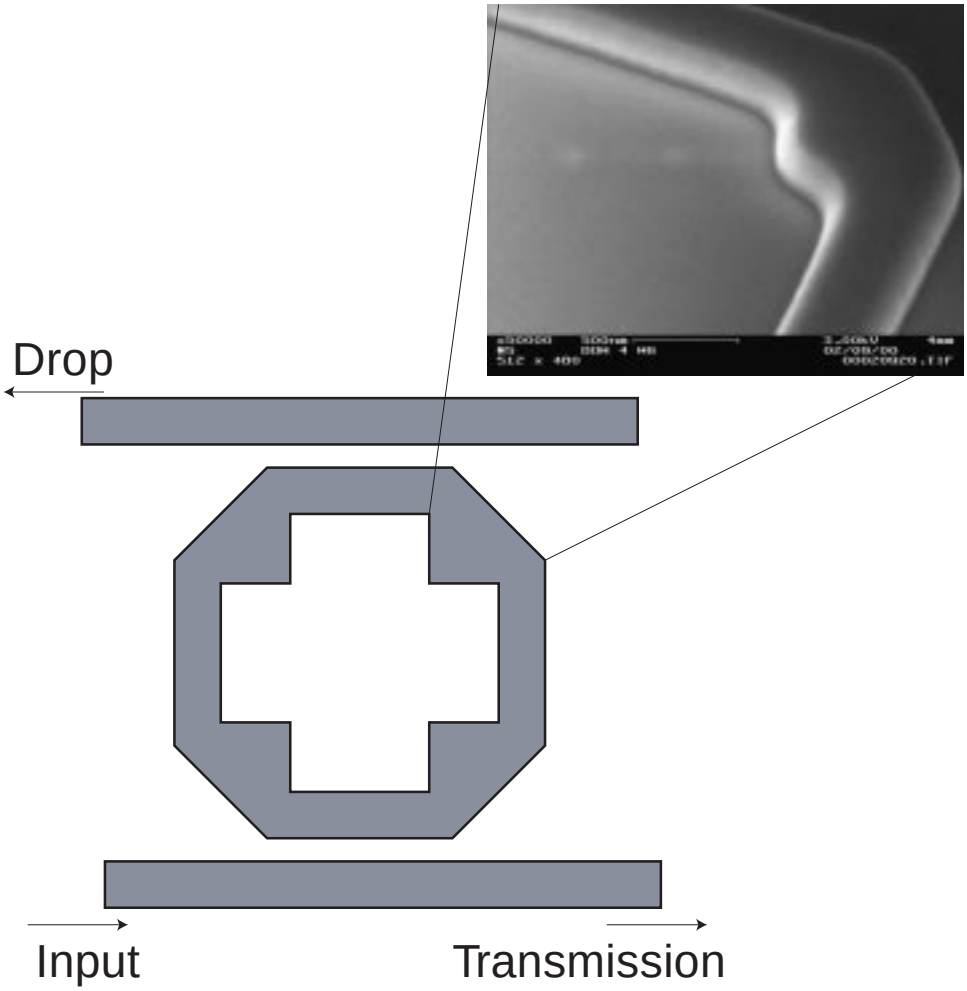

Figure 3-5: Schematic of an HTC resonator. The HTC resonator is a traveling wave resonator using HTC bends, with a loss limited Q of 750. The principle of operation of the HTC resonator is similar to that of a ring, described in chapter 4. The low Q is a result of the higher loss of HTC bends compared to 3 μm radius bends.

Type	Fabrication process	Material	Loss (dB/turn)
R=1 μm Round bends	Intel	SOI	0.8
	Intel	PolySi	4.2
	L. Labs	PolySi	0.5
HTC	L. Labs	PolySi	0.3
R=2 μm Round bends	L. Labs	PolySi	0.012
HTC	L. Labs	Nitride	0.76
R=2 μm Round bends	L. Labs	Nitride	0.074

Table 3.1: Table summarizing bending losses in small HTC and 1 and 2 μm radius round bends. Silicon HTC bends outperform R=1 μm bends. However, larger radii bends R=2 μm for both polySi and silicon nitride are both extremely compact and have negligible loss. Empirically, the HTC is useful for turns with radius on the order of the width of the waveguide.

3.2 Splitters

A substantial amount of work in the literature has focussed on splitters in low index contrast waveguides. High index contrast waveguides enable the design of very small splitters (order of 100s of sq. microns) with low loss. The Y-split [12] method of splitting has been shown in high index contrast waveguides. Here, we focus on schemes to increase the splitting ratio, by using the Y-split method and two other methods which have not been previously shown in high index contrast waveguides.

3.2.1 Y-Splitters

2^o half angle 1x2 and 1x4 Y-splitters were fabricated using polySi using both the Intel and the Lincoln Labs process. The loss per split was calculated as follows:

$$\text{Loss in dB per split} = 10\log\left(\frac{\text{total power in all 4 ports of the 1x4 splitter}}{\text{total power in both ports of the 1x2 splitter}}\right) \qquad (3.5)$$

The loss calculated for Y-splits processed by the Intel process was 3 dB/split. The loss extracted from the Y-splits processed by the Lincoln labs process was 0.15 dB/split, which is significantly smaller than previously measured. This low loss was probably due to the very fine lithography that was possible. Previous attempts at small Y-splits were hampered by a rounded "crotch" of the junction [12]. With the finer lithography, the size of this non-ideality is reduced.

The power uniformity of these devices was good due to the inherent symmetry of the Y-split. The benchmark $\frac{\sigma}{\mu}$ (standard deviation / mean), was 0.5 for the Intel Y-splits and 0.3 for the Lincoln Labs splits.

3.2.2 HTC Splitters

A splitter may be made by joining two HTCs back to back (see figure 3-6) and may be thought of as two coupled resonators. The reason why such HTC splits are important is the geometry of the HTC split device; since this is essentially a 90^o split, the splitting area is small. One of the important functions of a splitter is to route the 2 split signals away from each other. The HTC does this most rapidly since the split waveguides leave the splitting point in opposite directions.

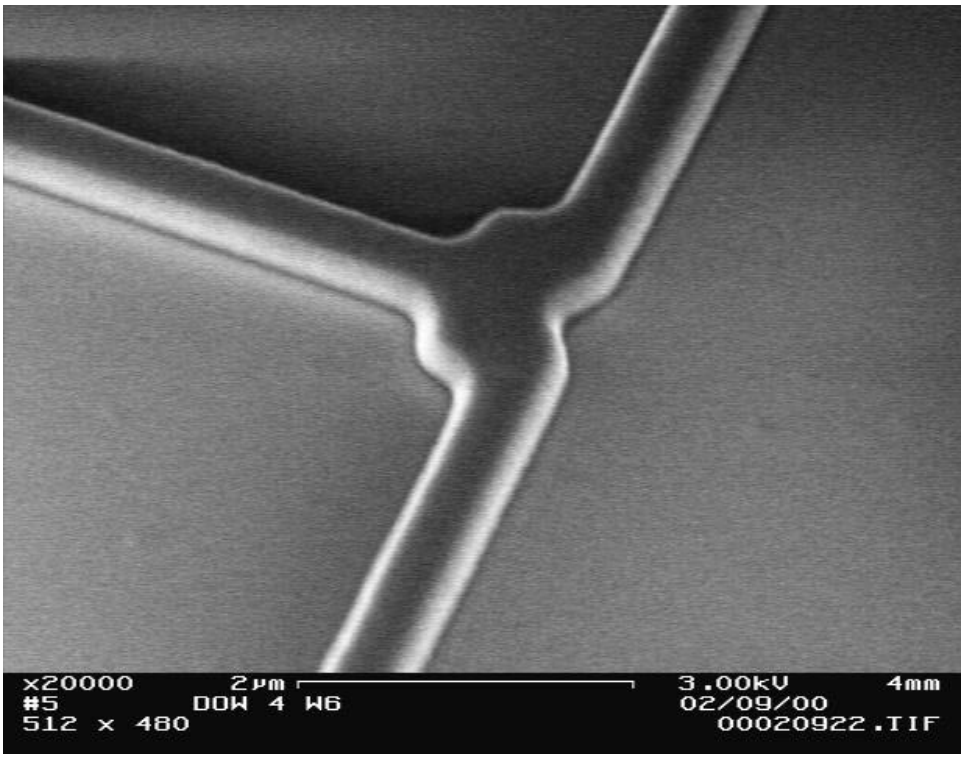

Figure 3-6: SEM of HTC split fabricated in polySi. This is smallest 1x2 split ever made at a wavelength of 1.55 μm. The measured loss was -1.2 dB, but will be improved with an optimized design.

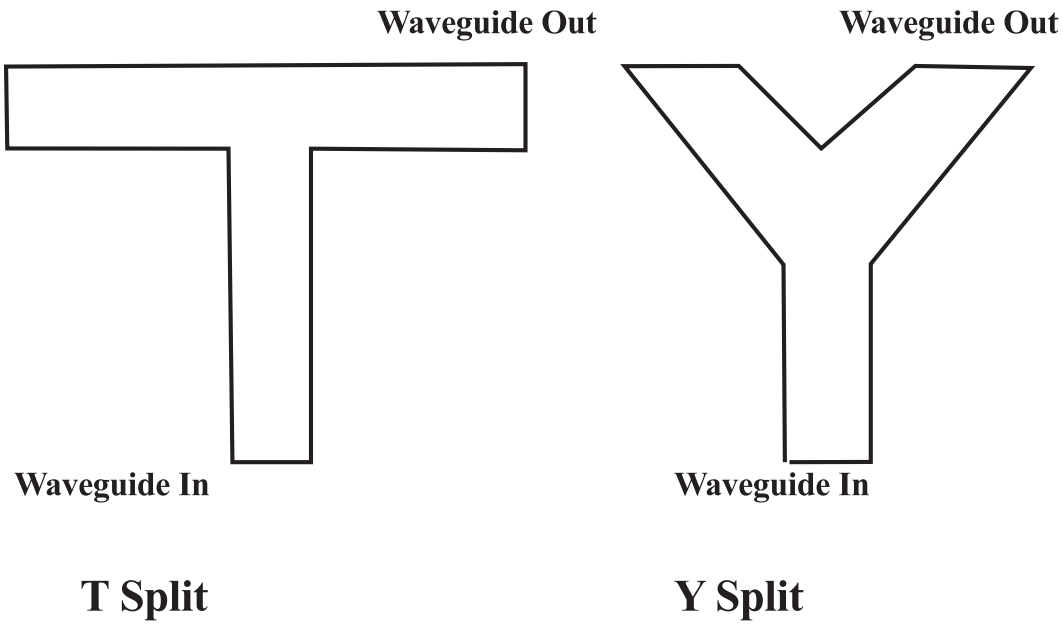

Figure 3-7: T vs. Y-splits. The T-Split device is much more compact than a Y-Split. The Y-split device is designed to have minimal perturbation to the mode. Hence a small split angle leads to very low loss.

PolySi HTCs The transmission loss of the HTC splitter fabricated in polysilicon was approximately -1.2 dB, which is large when compared to the -0.15 dB loss extracted for the Y-split fabricated in the same mask. The high loss is due to the use of a non-optimal design. With an optimal design this loss will be lower. However, note that this power loss is equivalent to the loss reported by Foresi et al [12] where up to 15 degree splits were reported. In terms of size, these HTC splitters are the most efficient ever measured since they occupy a very small area. See figure 3-7. Again the power uniformity of these devices was good due to the inherent symmetry of the device 0. The benchmark $\frac{\sigma}{\mu}$ (standard deviation / mean), was 0.2, which is significantly better than the Y-splits.

The main advantage of a HTC T-split vs. a traditional Y-split is its small size since a Y-split must incorporate a small split angle and larger bends to maintain its low loss nature. On the other hand, in a T-split the waveguides exit opposite to each other, reducing the need for bends. See figure 3-7. The main advantage of a HTC T-split vs a traditional T-split, in which the incoming waveguide terminates abruptly into the output waveguides, is its lower loss (1.2 dB vs. 3dB). Finally the advantage of the HTC T-split vs an MMI (see next section) is its small size and high splitting uniformity. MMIs in general have some, albeit small intrinsic non-uniformities. These results are summarized in table 3.2.

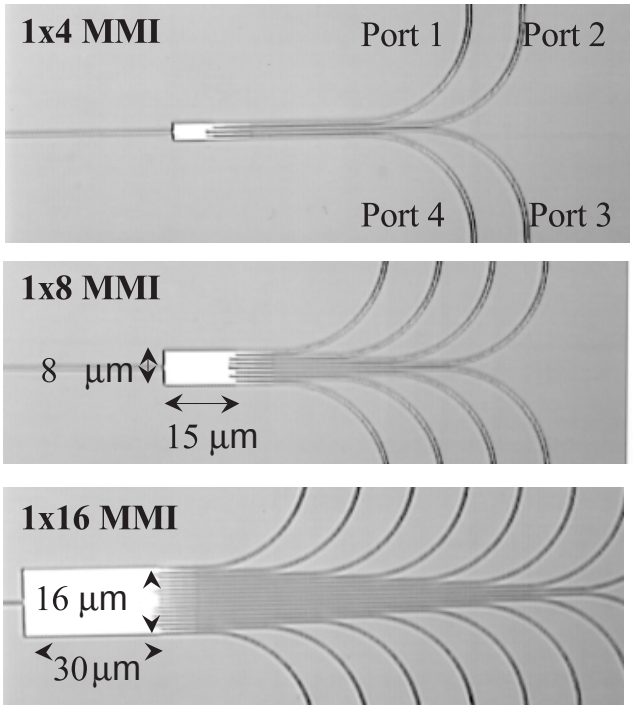

Figure 3-8: Optical micro-graphs of 1x16 MMIs fabricated in silicon. Note the irregularities at the output facet of the MMI boxes. These irregularities are due to the mask design being too fine for the mask fabrication process. As a result of these irregularities, the power in the output waveguides exhibit anomalously large non-uniformities.

3.2.3 Multi-mode interferometers MMIs

Multi-mode interferometers [61, 62, 63, 64, 65, 66] are essentially boxes into which an incoming wave from a single mode waveguide is allowed to diffract. After one or more reflections off the side-walls of the box, the diffracted waves interfere with the reflected waves. This results in interference spots. If output waveguides are placed in regions where the field intensity is high, light may be coupled out of this box into the output waveguides. MMIs allow 1xn splitting in a much more compact space than Y-splitters allow [62]. Multi-mode interferometers may be easily designed by using the beam propagation method. Designs for MMI splitters have been made using 4, 8 and 16 μm wide multi-mode cavities to get 1x4, 1x8 and 1x16 splitting ratios. These are among the smallest splitters that have been fabricated and tested and are more compact than the Y-splitter based systems. See figures 3-9 and 3-10.

These MMIs have been fabricated at Intel Corp.: the losses and splitting efficiency were measured and compared to the more conventional Y-split. Losses in MMIs were computed

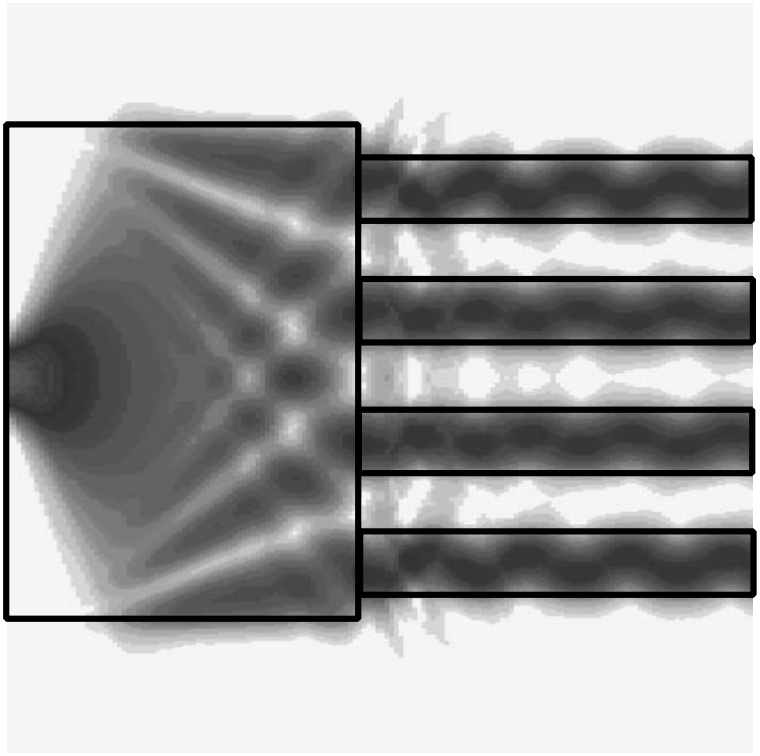

Figure 3-9: Simulation of a 1x4 MMI splitter in silicon. Dimensions are 4 μm x 7.5 μm. Power uniformity $\frac{\sigma}{\mu} < 0.05$

to be 4 dB per box. Thus, for large splitting numbers (1xN), MMIs may be the most efficient method for splitting since loss occurs only at one split.

Unfortunately, the uniformity of the MMIs that were constructed was poor. The benchmark $\frac{\sigma}{\mu}$ (standard deviation / mean), was 0.5. The reason for this however, was the large minimum feature size on the mask. As a result there were gross mask errors on the output side of the MMI box. (See figure 3-8) Further, the power uniformity of these devices is not as good as the Y-splits and the HTC-splits due to the inherent asymmetry of any split ratio greater than 1x2. These results are summarized in table 3.2.

3.3 Modulators and Switches for Silicon waveguides

Integrated optical modulators and switches both aim to achieve large changes in the amplitude of light. The time scales of modulation and switching, however, are different. A switch is required to route signals and its response time is usually on the order of microseconds. Low power dissipation and high efficiency are both necessary for switches. On the

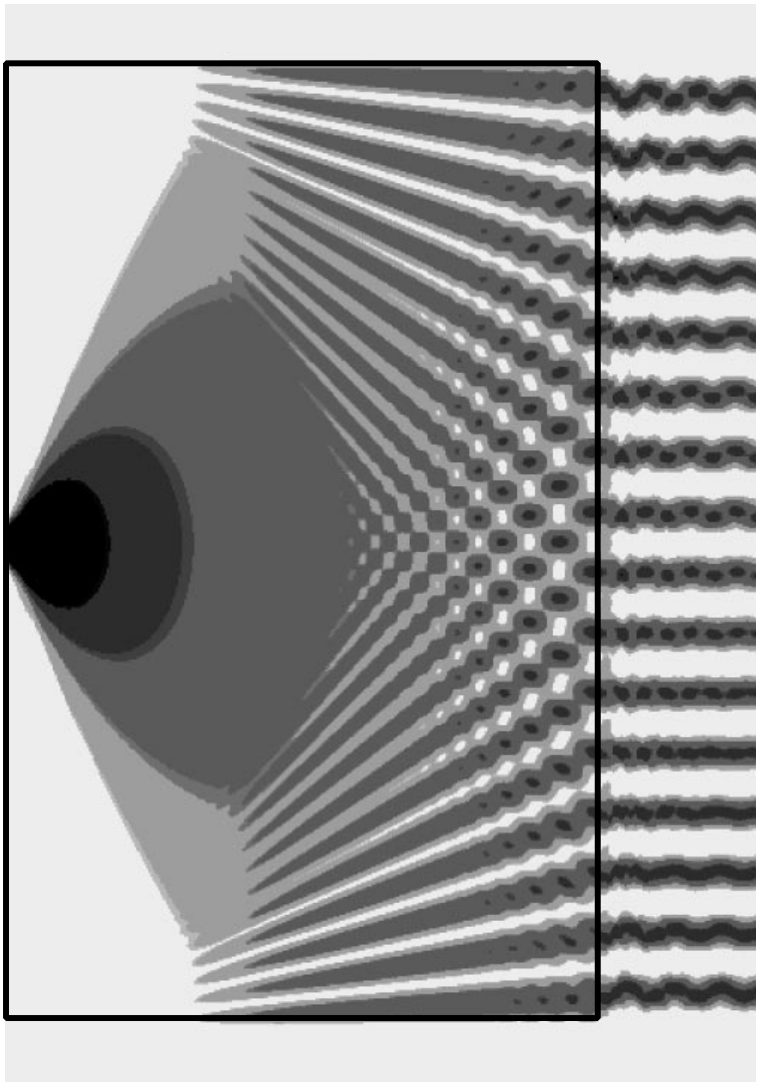

Figure 3-10: Simulation of a 1x16 MMI in silicon. Dimensions are 16 μm x 30 μm. Power uniformity $\frac{\sigma}{\mu} < 0.05$

Split ratio	Split type	Fabricator	Size (μm^2)	Loss (dB)	Uniformity
1x4	Y-split	Intel	480	3	0.5
1x4	Y-split	L Labs	480	0.15	0.3
1x4	HTC	L Labs	<20	1.2	0.2
1x4	MMI	Intel	30	3	0.5
1x16	Y-split	Intel	≈7680	9	0.5
1x16	Y-split	L Labs	≈7680	0.45	0.3
1x16	HTC	L Labs	<320	3.6	0.2
1x16	MMI	Intel	480	3	0.5

Table 3.2: Table showing the tradeoff in loss, size and power splitting uniformity for the three different splitting techniques.

other hand, a modulator encodes data into an optical signal. Since optical data rates are on the order of 1-10 GBit/s, the modulators have to operate at these speeds. In addition, modulation depths of 20 or even 30 dB are frequently required in optical systems. In this thesis, 20 dB modulation depth is taken to be the design requirement.

Physical effects which may be used in external switching and modulation schemes for silicon based optoelectronics are listed below:

- Nonlinear optical effect.

  This is the effect of changing the index of refraction by using an applied electric field.

  Silicon is centro-symmetric so it does not have χ^2 which means one would have to rely on the Kerr effect which is weak. Silicon nitride has a similar problem with weak χ^3. At 0.63 μm (He-Ne line),

$$\kappa_{//} = 6.8 \text{ X } 10^{-18} \text{ cm}^2/\text{V}^{-2}$$
$$\kappa_{\perp} = 2 \text{ X } 10^{-18} \text{ cm}^2/\text{V}^{-2}$$

  These numbers necessitate operation at very high fields, order of tens of kV to get index changes on the order of 0.01.

- Free carrier absorption and refraction [11].

  These processes involve the injection of free carriers in silicon material. The light responds to injected carriers with a phase shift, resulting in a change in the index of refraction depending on the number of carriers present in the material. Thus, by carrier injection and depletion, one can modulate the both phase and amplitude of optical light. The magnitude of the index change and absorption was studied by Soref et al and is shown in figure 3-11 and figure 3-12. Free carrier refraction gives an index change of of about 0.001 to 0.002 with injection levels of 10^{18} cm^{-3}. Above those levels free carrier absorption takes over since the loss mechanism dominates.

  This effect is occurs in silicon and silicon germanium but not in silicon nitride and has been extensively used in the literature in previous demonstrations of optical modulation in silicon. [67, 68, 69, 70, 71, 72].

  Due to absorption at high levels of carrier injection, many electro-refraction modulators require low levels of carrier injection for good modulation depth and low loss.

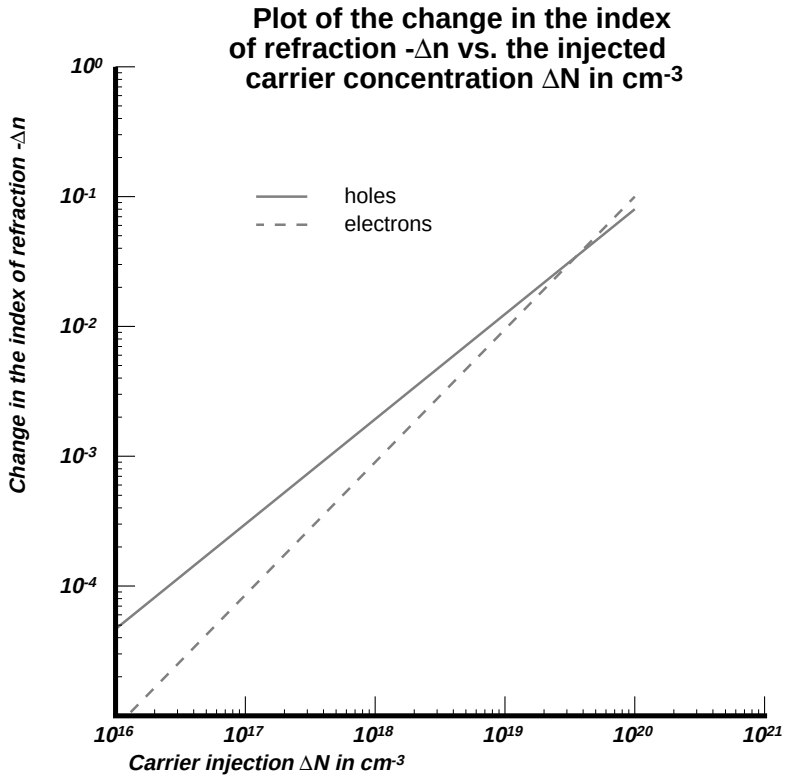

Figure 3-11: Graph of free carrier refraction [11] in silicon.

This effect is useful when waveguide cross-sections are large and when high levels of carrier injection are difficult (e.g. single mode rib waveguides). Modulators based on electro-refraction tend to be long unless resonant cavity structures are used (on the order of mm) because the maximum change in index is $\Delta n \approx 10^{-3}$ for low loss and high modulation depth.

One can also utilize electro-absorption by using high levels of carrier injection (10^{19} cm^{-3}). Thus, modulators with lengths on the order of 100s of microns can be designed to achieve 20 dB modulation depth. This method is useful for small waveguide dimensions (e.g. strip waveguides) where it is possible to inject and remove carriers rapidly.

- Franz Keldysh effect

  In this effect, a large electric field is applied so that there is an effective narrowing in the band gap resulting in a change in absorption. This effect is very weak unless the wavelength to be used is close to the band gap of the material. Furthermore since silicon and silicon germanium are indirect band gap materials, the long tails in

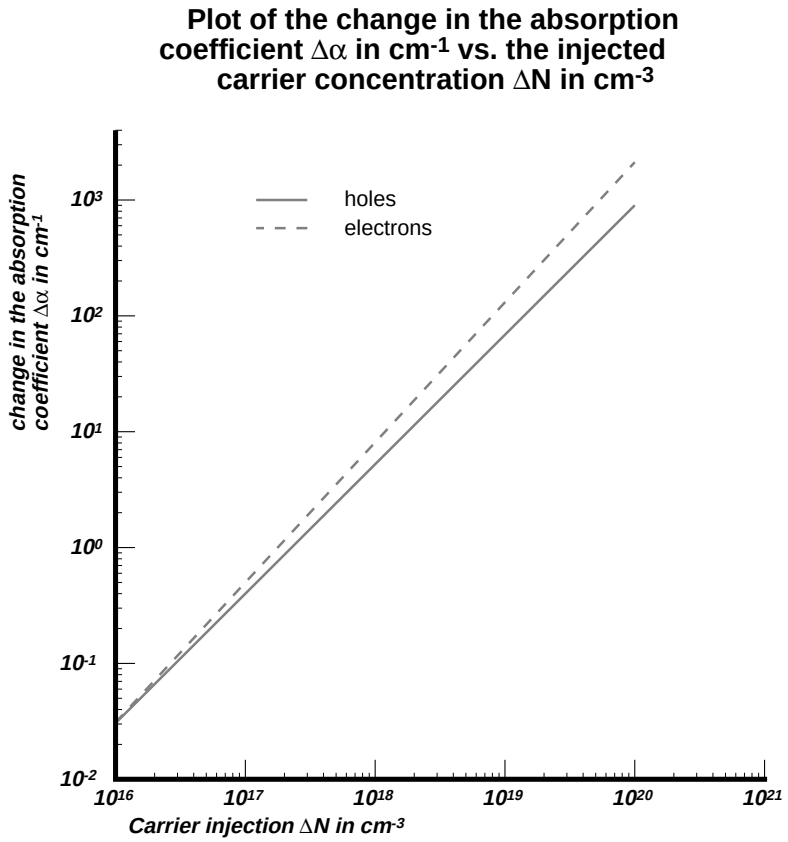

Figure 3-12: Graph of free carrier absorption [11] in silicon.

the absorption spectrum of silicon and silicon germanium would mean that a silicon modulator based on this effect would have poor modulation depth.

- Micro-mechanical modulators

  A micro-mechanical modulator may be made by using a micro-mechanical device coupled to a waveguide device or some material that could change the mode of the waveguide. The idea would be to change the physical structure of the device resulting in a change of the mode of the waveguide and possibly the loss of confinement. An example of such a device can be seen in figure 3-13. The arm is a cantilever beam which can be modulated at high frequency. During the oscillation the arm touches the waveguide and the mode of the waveguide changes. If the arm is made of an absorbing material, the optical mode will decay rapidly in the direction of propagation while the arm is in contact with the waveguide. The main advantage of this device is the absence of any lossy electrical contacts on the waveguide.

- Thermo-optic modulators

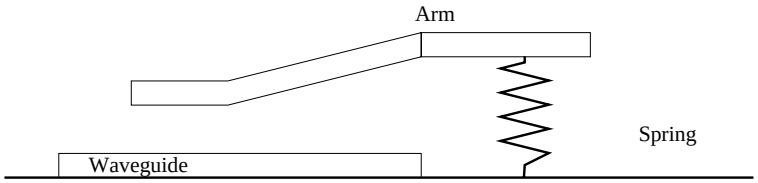

Figure 3-13: Schematic of MEM based modulators in silicon. Diagram shows the unperturbed "on" state. In the off state, the arm contacts the waveguide, resulting in loss.

This involves heating up a waveguide device and changing its core index. This index change can then cause a phase variation which can then be converted to an amplitude by using a resonator or an interferometer. One way of doing this is to use a thermistor which is essentially a heater which uses resistive heating. Thermo-optic tuning for example has been demonstrated for large ring resonators [73]. The problem with this method is that it is slow.

- Electro-optic based modulators

  These modulators are based on the principle of changing the index of the core or cladding by doping or growing a layer of electric-optic material. By applying a field, the index of the core or cladding will change, changing the mode of the device. If designed in a high Q device, small variations of index can result in large modulation effects. One of the pitfalls of this scheme is that it may be difficult to find a electro-optic material that would operate at 1.55 μm.

In this thesis, I have chosen to focus on fully integrated CMOS compatible switches. This precludes the use of more exotic schemes such is hybrid III-V integration on silicon and the use of electro-optic materials such as lithium niobate and electro-optic polymers. As previously mentioned, the most efficient modulators on silicon would be based free carrier refraction and absorption.

Most previous work on modulators in silicon have been based on rib waveguides since they are easier to build and design [42]. The main reason for this is the small difference in the effective index of the core and cladding which means that a small change in the index of the core can result in a large change in the difference in the effective index of the core and cladding. Modulators based on the Mach Zehnder scheme, using a directional coupler [42] as well as electro-absorption [71] have been demonstrated.

One problem with applying the free carrier effect on rib waveguides is that they are

relatively large in size (on the order of several μm in height and width) so diodes of that size have to be built. Thus, switching speeds tend to be slow, on the order of 100 MHz [67, 68, 69, 70, 71, 72, 74, 75].

With single mode strip waveguides, the modulation speed can be much faster and power dissipation smaller. However, their small size leads to other problems. For example, electrical contacting is an issue [42] and will be addressed in the next section.

3.4 Silicon based modulator

On-chip optical modulators enable data to be encoded in a optical carrier by modulating the intensity of light. Fast optical modulation is needed for high speed data communications on a chip. For this application, GHz modulators are needed. On the other hand slow switches are useful for routing applications.

There are two kinds of modulation: direct modulation of the laser source, and external modulation of the laser. It is important to consider external optical modulation since the Si:Er system (see chapter 5) does not lend itself to direct modulation due to its long optical lifetime. Furthermore, if off-chip sources are used, on-chip modulation, will be required to encode data.

As explained before, the fastest method of modulation in silicon is to use free carrier absorption or refraction. The main challenges of the method are contacting the waveguide and achieving the required carrier densities with sufficient speed and with small power dissipation. These issues will be discussed in turn.

3.4.1 Contacting a silicon strip waveguides

In general the most efficient way of injecting carriers into a region with low carrier concentration, is to use a p-i-n diode. This requires the use of metal contacts. The main problem is that the metal contacts on the small strip waveguides interact with the evanescent fields. Thus, if metal contacts are placed near the surface a material, it would absorb the light propagating down the waveguide. An example of a contacting scheme would be to put contacts on the low field intensity region of a waveguide, or to use small tabs on the sides of the waveguides which allow the metal to be placed a distance away from the waveguides.

Contacting multi-moded silicon strip waveguides

For wide (multi-mode) waveguides the optimal design is to put the contacts on the top surfaces waveguide near the side-walls. This allows the formation of a lateral p-n junction across the waveguide or a vertical p-n junction if there is a buried contact.

Mode simulations were run to study how a lossy mode would propagate in a silicon strip waveguide with aluminum (n+ik=1.444-16i) or copper (1-12i) at the edges of the strip waveguide. Several simulations were run for the electro-absorption modulator for silicon waveguides (see section 3.5.2)

Contacting single-moded silicon strip waveguides

BPM was used to study the effect of putting metal on the top surface of the waveguide, the side-wall of the waveguide and on a portion of the top surface of the waveguide.

Mode simulations were run to study how a lossy mode would propagate in a silicon strip waveguide with cross sectional dimensions of 0.2x0.5 μm and with aluminum or copper at the edges of the waveguide.

For narrow (single-mode) waveguides the optimal design is to put metal on the side-wall of the waveguide or at least on the top surface near the side-wall of the waveguide. The α of such side-wall contacts is 640 cm^{-1}, while that of a partially covered top contact is 80 cm^{-1} (40% coverage). A waveguide that is covered completely with copper would exhibit a loss of 440 cm^{-1}. The top cover loss numbers are surprisingly small.

3.4.2 Injecting into silicon strip waveguides

In the previous section, the effect of an absorbing metal contact adjacent to the mode of waveguide is studied. In this section, the amount of injection into a strip waveguide is studied. In order to understand what happens when carriers are injected into a strip waveguide, one must first consider the recombination at the surface and in the bulk.

Surface recombination

Surface recombination can be calculated in terms of the dangling bond density. The Surface Recombination Velocity (SRV), S is defined as:

$$S = N_{db} \cdot \sigma_b \cdot v_{th} \tag{3.6}$$

Surface coating	N_{db} (cm^{-3})	S ($cm\ s^{-1}$)	τ (s)	Flux ($W\ cm^{-2}$ at $\lambda = 810nm$ for 10^{18} cm^{-3} injection)
Bare	10^{14}	10^{5}	10^{-10}	10^{7}
Thermal oxide	10^{11}	10^{2}	10^{-7}	10^{4}
Plasma oxide	10^{12}	10^{3}	10^{-8}	10^{5}

Table 3.3: Minority carrier lifetime in silicon due to surface recombination .

where

$$N_{db} = \text{density of dangling bonds, in} cm^{-2} x \tag{3.7}$$

$$\sigma_b = \text{cross-section} = 10^{-16} cm^2 \tag{3.8}$$

$$v_{th} = \text{carrier velocity} = 10^7 cm/s \tag{3.9}$$

If surface recombination is not limited by diffusion, then the lifetime for recombination on both surfaces of a semiconductor with thickness, t, is

$$\tau = \frac{t}{2S} \tag{3.10}$$

Depending the carrier profile and layer thickness, diffusion may or may not limit the surface recombination rate. If diffusion is too slow, the number of carrier that actually reach the surface is so small that the lifetime in material is equal to the bulk lifetime. Assuming infinite surface recombination, the diffusion lifetime is given by,

$$\tau_{diff} = \frac{\text{Si thickness}^2}{\pi D} \tag{3.11}$$

here D is the carrier diffusion constant, with an assumed a planar profile for 1-D diffusion. With a silicon thickness of 0.2 μm, the diffusion time constant is 10^{-11} seconds. Three silicon surfaces were considered and are listed in table 3.3. From this table, the minority carrier lifetime due to surface recombination completely dominates the diffusion lifetime in single crystal silicon and should be used. Note that the bulk recombination rate in polySi is on the order 10^{-9}s, assuming that the grain boundaries are recombination centers.

Optically injecting carriers

Using the numbers in table 3.3 it is possible to determine the optical flux required to generate the required level of carriers to see electro-optical optical effects. The required incident flux for 10^{18} cm^{-3} carriers is shown in table 3.3. Assuming one electron hole pair per eV of light, the incident laser flux required can be derived as follows. If α_L is the absorption coefficient of the light, the power density absorbed in units of J/cm^{3}s is Iα_L, or Iα_L/q in units of eV/cm^{3}s. Assuming a 1 eV band-gap, the number of carriers generated/unit volume/second is Iα_L/q. Finally, the carrier density can be found by multiplying the generation rate with the recombination time constant. Thus:

$$I = \frac{nq}{\alpha_L \tau} \tag{3.12}$$

The fluxes which are required in table 3.3 are very large. In fact for the case of the bare exposed silicon, the required flux density would melt the silicon!

Electrically injecting carriers

Two injection geometries were studied (see figures 3-14):

- A vertical p-n diode with a depletion width of 0.2 μm
- A horizontal p-n diode with depletion across the width of a multi-moded waveguide which is 4 μm wide

These devices were simulated using Medici using carrier lifetime of 10^{-9} s and the results summarized in figure below.

Horizontal p-n diode The horizontal p-n diode is integrated into a 4 μm waveguide as shown in figure 3-14. The sides of the waveguide are doped heavily with p+ and n+ by implantation. The widths of these heavily doped regions are 0.5 μm and are both covered with metal. This device was simulated with on "on" voltage of 2 V and an off voltage of 1V. This device had a rise time of 1 ns and a fall time of 2 ns, which corresponds to 300 MHz operation. The forward biased current is 12 mA per μm of diode length.

Vertical p-n diode A vertical p-n diode can made using epitaxy to create very sharp doping profiles. A 500A p+ layer is first grown. This is followed by 2000A of undoped

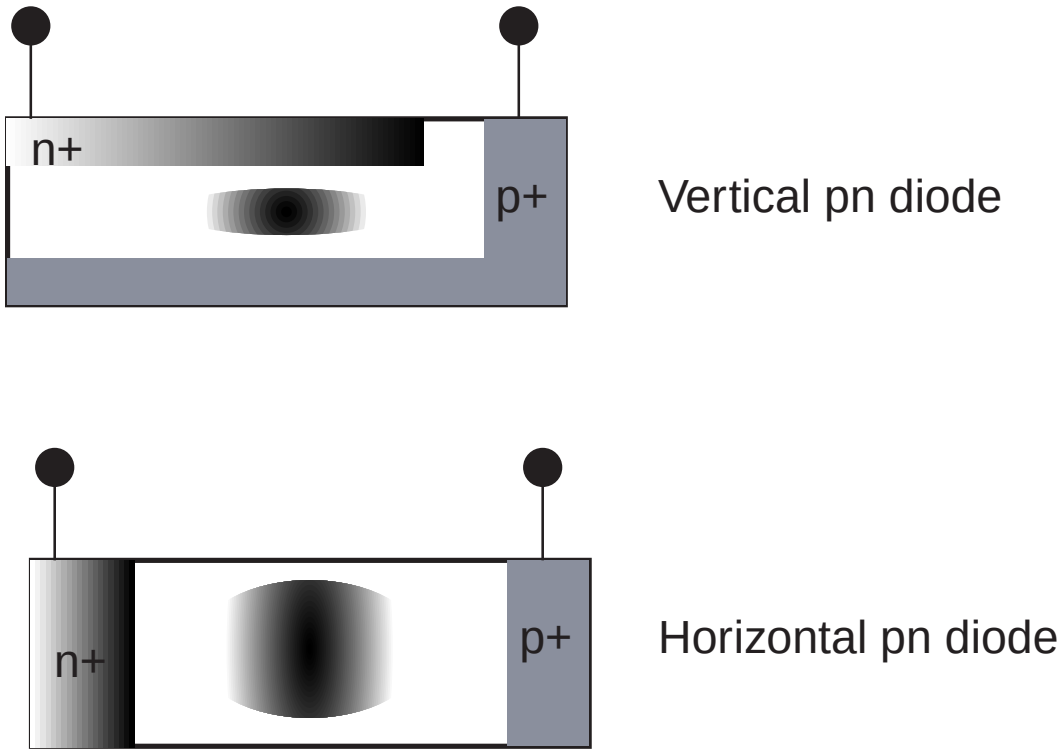

Figure 3-14: Schematic of vertical and horizontal p-n diodes in silicon waveguides.

silicon. Finally this device is capped by 500A n+ layer. This device was simulated with on "on" voltage of 2 V and an off voltage of 1 V. This device had a rise time of 0.18 ns and a fall time of 0.14 ns, which corresponds to 1.5 GHz operation. The forward biased current is 8 mA per μm of diode length.

Series resistance Due to optical absorption, the amount of metal that is used should be minimized. However, due to series resistance, the metal contacts cannot be arbitrarily far away from the p-n diode. These two conflicting requirements need to be optimized. For example in the 30 μm racetracks in the previous sections parts of the depletion region are 6 μm away from the metal contacts.

The series resistance of the vertical p-n diode can be estimated. Assuming a doping concentration of 10^{20} cm^{-3}, the resistivity is 10^{-3} Ω cm. The series resistance of the heavily doped p+ and n+ regions is approximately 100 $\Omega/\mu m$. Thus, a 6 μm long p+ region would have resistance of 600 Ω. The voltage drop for 50 mA of current would be 3 V which implies that the power dissipated due to series resistance would increase the total power dissipation of this device by a factor 2.5 to 600 mW! Similarly the series resistance

of a horizontal p-n diode can be estimated to be 1.5 V, which would increase the power dissipation to 600 mW as well.

The main reason for this large power dissipation is the large recombination rate. On the other hand the large recombination rate also assists in helping the p-n diode turn off by recombining excess carriers.

3.5 Optical Modulation Experiments

This set of experiments involve using optical illumination of carriers into the active region of the device. This enables us to decouple problems with electrical contacting from the fundamental operation of the device.

3.5.1 Optical injection of carriers into straight guides

An experiment like this has already been tried [72], and the authors have been able to show all optical modulation in single crystal silicon. In their paper, they demonstrated transmission of a mode near cutoff and scattering of the light by changing the effective index of silicon so that the mode is cutoff.

In our experiment we hoped to study the effect of high levels optical injection to study the effect of absorption as well as to study the effect of high levels of injection into polySi. One of the difficulties that encountered was the large incident optical power density required. (see table3.3) An SOI waveguide which had been clad by a plasma oxide was illuminated by a 1W 810 nm laser; see figure 3-15. However, due to the fact that the power delivery fiber used with the laser had a mode field diameter of 200 μm, the incident power density was insufficient to create an α which was measurable. On the other hand, a change in the transmission was observed with a time constant of one second. The source of this change is thought to be associated with thermal effects.

3.5.2 Electro-absorption modulator

An electro-absorption modulator may be constructed from a straight waveguide geometry by using carrier injection of about 10^{19} cm^{-3}. Since this corresponds to an alpha of about 200 cm^{-1}, a length of about 0.03 cm (300 μm) will result in absorption factor of about 400 or about 26 dB modulation depth. Note that at these injection levels an index change of

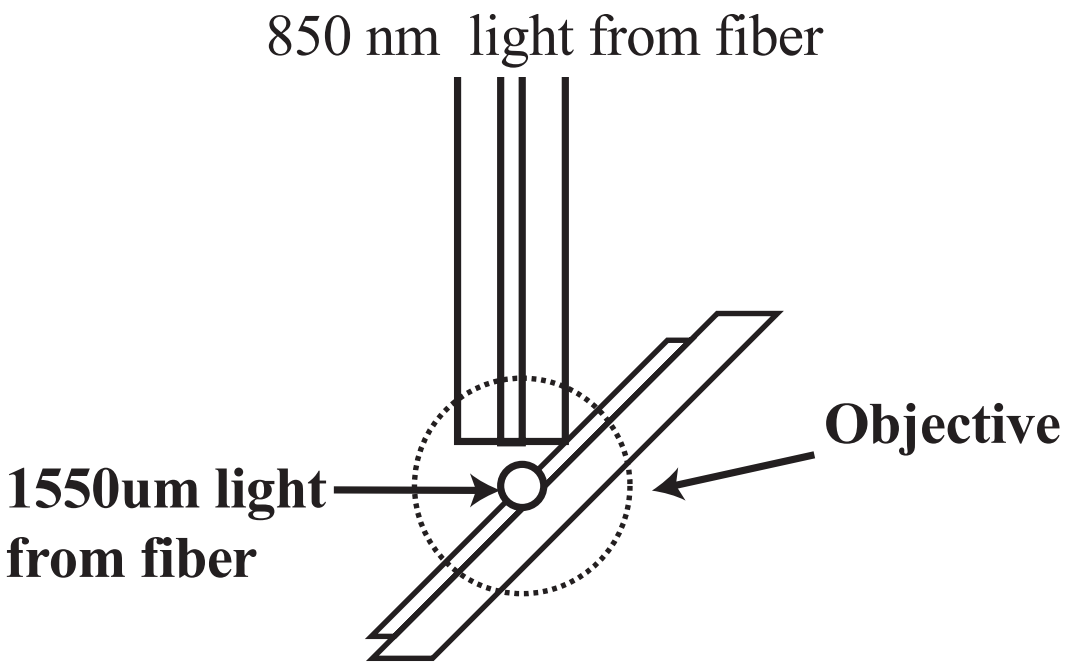

Figure 3-15: Schematic of optical illumination of silicon waveguides.

about 0.01 is observed. If a change in the effective index of the order of 0.01 is assumed the equivalent length of a straight waveguide which would result in a π phase shift is 75 μm.

Two such designs were simulated using BPM and a electronic device simulator, Medici for multi-moded waveguides. In the first waveguide, the metal contacts are placed at the sides of the waveguide (See figure 3-16). However, the insertion loss is 20 dB. An improvement of this design is to use an input waveguide and to put the contacts on tabs which stick out. See figure 3-17. The insertion loss then improves to 5 dB. In both cases the modulation depth is 20 dB (limited by the amount of electrical injection), the device length is 100 μm and the speed is 300 MHz. The reason for the slow speed is the large base width between the p and n regions of the lateral diode. An improvement of this design is to use a vertical injection method shown in figure 3-18. The insertion loss of this device is less than 5 dB and the modulation speed is 2 GHz.

One might want to increase the path length of the straight waveguide by using a micro-cavity with high Q (a ring for example). This would reduce the size of the modulator and hence the power dissipation.

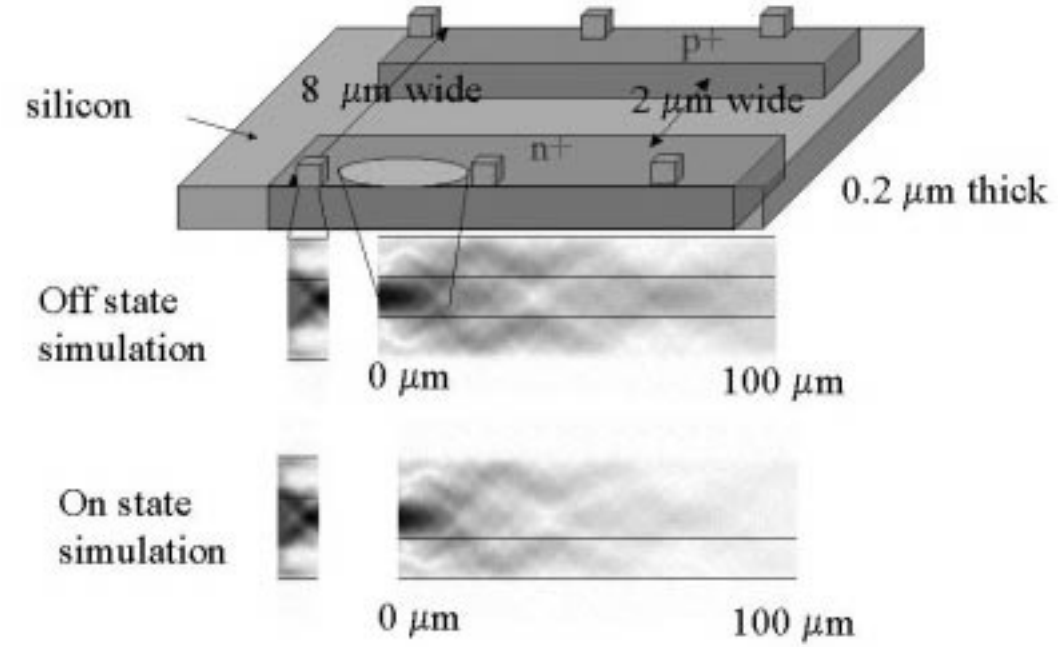

Figure 3-16: Schematic of Electro-absorption modulator. 20 dB modulation is possible, but the insertion loss is 20 dB.

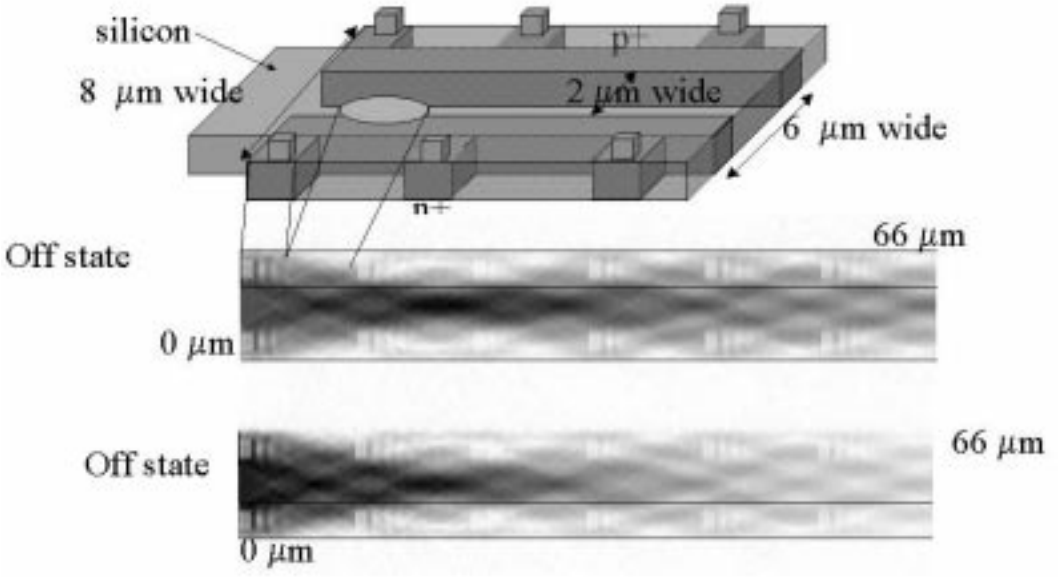

Figure 3-17: Schematic of Electro-absorption modulator with tabs. Using the tabs the insertion loss drops to 5 dB. Repetition rate is 300 MHz.

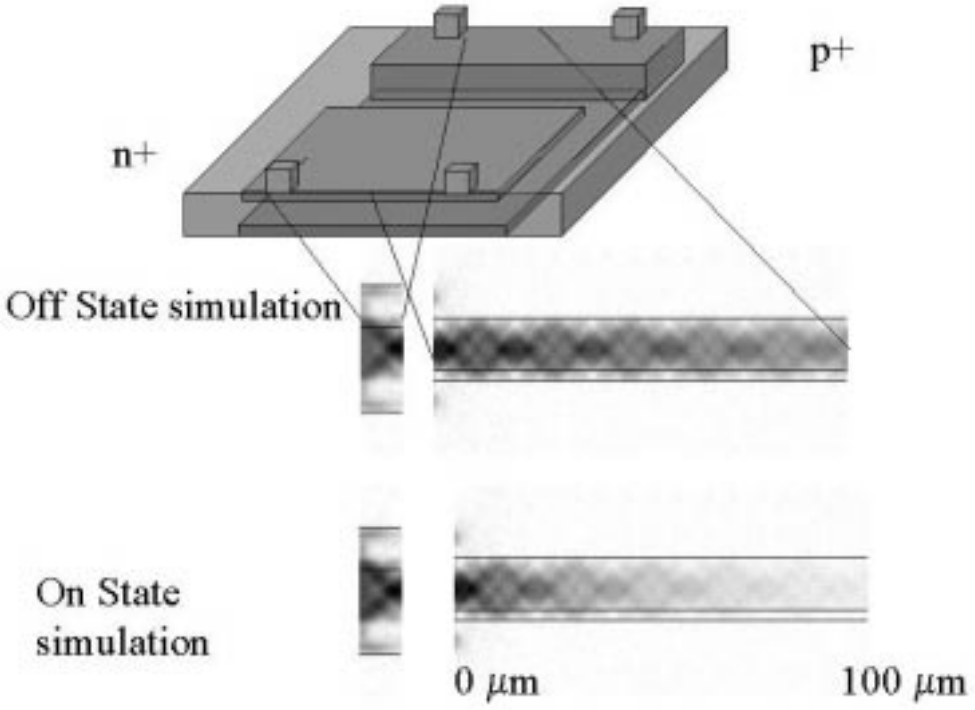

Figure 3-18: Schematic of Electro-absorption modulator using vertical injection. The vertical injection preserves the insertion loss of 5 dB, the modulation depth of 20 dB and improves the repetition rate to 2 GHz

3.6 Summary

3.6.1 Bends

Bending loss has been measured with a great degree of certainty to be less than 0.5 dB/turn for a 1 μm bend. The bending results are summarized in table 3.1 on page 84. Further reduction of bending loss is possible with lower side-wall roughness.

Polarization dependent loss was also observed for bending losses. However, in this case the loss of the TM modes is much higher as would be expected from the geometry of the waveguides. In the future, this bending loss variation on polarization should be carefully analyzed. It is hypothesized that this dependence is due to the polarization dependence of the effect of surface scattering on the modes. The TM polarization is affected more by the sidewall roughness than the TE mode.

3.6.2 Splitters

The splitting results for high index contrast silicon splits are summarized in table 3.2 on page 90. At this juncture there is no clear "best choice" since more work needs to be done to improve the MMIs and HTC splits. The Y-splits on the other hand have been optimized and the performance reported herein is good. The main problem right now is the large power variation in the output arms of the splitters. However, with further optimization, I believe that for small split ratios, HTCs will emerge to be the natural choice, while for enormous split ratios MMIs will be optimal, due to the fact that the loss of the MMI to first order does not grow with split ratio. In addition, the size of both the HTC and MMIs are much smaller than corresponding Y-splitters. It is important to emphasize the fact that the MMI split uniformity and the HTC loss will be improve with better mask design.

3.6.3 Switching and modulation of silicon strip waveguides

The most effective optical modulation method of silicon strip waveguides is the free carrier effect. Unfortunately this requires the placement of contacts very close to the mode which increases optical insertion loss. Furthermore, due to the high injection levels required for absorption, modulators based on free carrier absorption are power hungry. On the other hand, modulators based on free carrier refraction have to be long for large modulation depth. Various schemes for contacting have been studied. The modulators that were fabricated

base on these ideas however, did not work due to processing difficulties.

Several contact-less schemes such as thermo-optic and MEMs based modulator schemes have been proposed. These methods are more suited for slower switching applications. I believe that for high speed optical modulation in silicon to be possible, the use of a more exotic (with respect to the CMOS industry) electro-optic material may be required.

Switches While thermal effects can switch micro-cavity devices, this method is best used for systems with low device densities. As device densities increase, thermal crosstalk increases and may be come unmanageable. Hence better methods of switching need to be found. One idea entails using a MEMs device to induce loss or induce an index change on the ring. Switching action is obtained by placing a material on top of the resonator using a MEMs device. This change of effective index would in turn result in a change in the position of the resonance line. Furthermore if loss can be induced the resonance of the ring will be suppressed completely.

Modulators ULSI compatible GHz modulators while possible, push the envelope of fabrication in silicon. Furthermore, there is no apparent scheme that works faster 5-10GHz. Hence, the next design iteration may require the use of electro-optic materials such as lithium niobate or an EO polymer, which have the advantage of not using electrons and the added advantage of much low power dissipation than p-n junctions.

Sensors The work presented in this chapter on sensors merely scratch the surface of integrated optics based sensors.

Chapter 4

Microresonators

Microresonators are small optical resonators which are several optical wavelengths in size. These resonators can be made very small and with low loss if they are based on high index contrast waveguides. These resonators are important because they may be used as in integrated optics as the basis for more complicated components such as filters.

In this chapter, two kinds of optical traveling resonators were studied: the ring resonator and the microsphere.

4.1 Background

4.1.1 Micro-rings

Micro-cavity ring devices were first proposed by Marticalli in the late 1960s [1]. Micro-cavity resonators have been widely studied in applications for lasers [76, 77] and channel dropping filters [78, 79]. We have previously studied and demonstrated the first 1D photonic band gap (1DPBG) structure that operates at optical wavelengths [80] and micro-ring resonator structures [81] built in silicon on oxide technology (see figure 4-1). Multi-resonator filters [82] based on large, ring resonators [83] and racetrack (see figure 4-4) resonator filters have been demonstrated and reported previously. Circular micro-ring resonators with circumferences on order of tens of micrometers have been demonstrated recently by Foresi [12] and others.

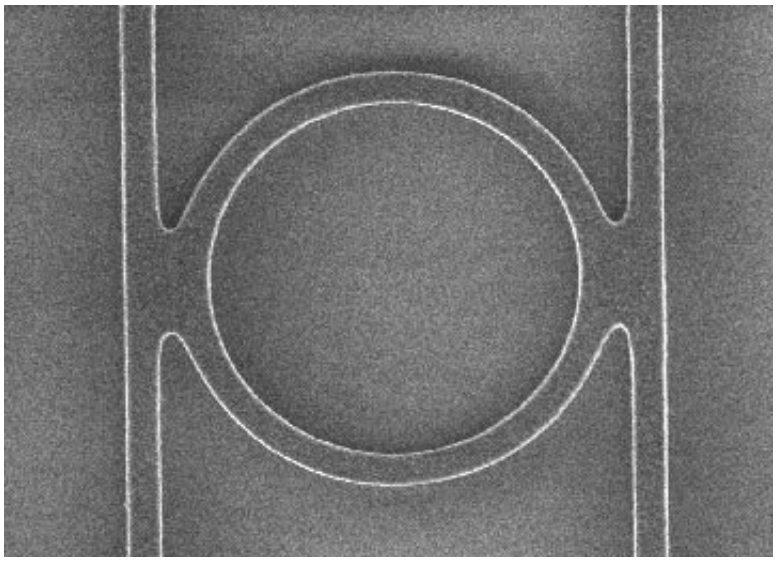

(a) Scanning Electron Micrograph of a micro-ring.

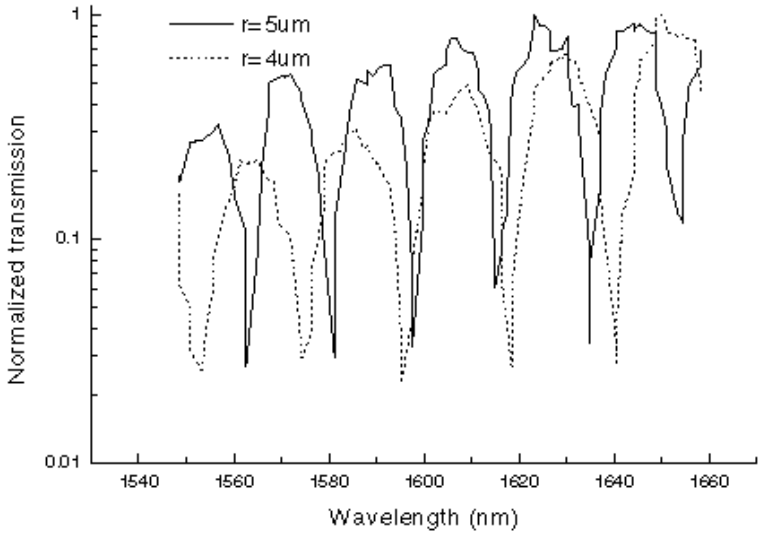

(b) Measured Response of 4 and 5 μm radii rings.

Figure 4-1: One level micro-ring with measured Q of 250 and 25 nm free spectral range[12].

4.1.2 Microspheres

Microspheres are another class micro-cavity resonators. They are essentially spheres of silica made from melting optical fiber. As a result, microspheres have enormous Qs [84, 85]. These spheres have many potential applications; such as extremely narrow filters, sensors and micro-lasers [86].

4.2 Theory

In this section, the theory of coupling of modes, which is used to analyze and to design ring resonators and microsphere resonators, is reviewed. In addition, an explanation of Cavity Quality Q, is reviewed, to provide an intuitive understanding of how this easily extracted parameter is used to analyze the transmission spectra of these resonators.

4.2.1 Coupling of modes

There are two forms of coupling of modes: in space and in time. Both are used in the analysis for rings. In this section, the theory of coupling of modes in time and space as presented by Haus in [3, 87] is summarized.

Coupling of spatial modes This derivation can be found in [3]. As explained in the previous chapter, the solution to Helmholtz equation is a mode $\vec{E}$(x,y) that travels at a propagation constant β. Thus, the amplitude b(z) of the mode for the waveguide propagating in the z direction is

$$\frac{db}{dz} = -j\beta b \tag{4.1}$$

If two waveguides are brought close together their amplitudes will couple. In the limit of very weak coupling, the coupling can be considered to be linear in amplitude. Thus,

$$\frac{db_1}{dz} = -j\beta_1 b_1 + \chi_{12} b_2 \tag{4.2}$$

$$\frac{db_2}{dz} = -j\beta_2 b_2 + \chi_{21} b_1 \tag{4.3}$$

the solution of which can be found in [3]. The essential features of the solution involves a spatially approximately symmetric and an approximately anti-symmetric mode which have propagation constants β_+ and β_- respectively. (see figure 4-2) The propagation constants

are given by:

$$\beta_{\pm} = \frac{\beta_1 + \beta_2}{2} \pm \sqrt{\left(\frac{\beta_1 - \beta_2}{2}\right)^2 - \chi_{12}\chi_{21}} \tag{4.4}$$

For rings, b_1 and b_2 are co-propagating and $\chi_{12}\chi_{21}$ may be reduced to $|\kappa|^2$ due to power conservation arguments. For there to be appreciable coupling $|\beta_1 - \beta_2| \approx |\chi_{12}| \ll |\beta_1|$, which means $\beta_1 \approx \beta_2$

Coupling of resonator modes in time The formulation of coupling of modes in time is the time analog of the formulation of coupling of modes in space. Suppose there are two resonators coupled together with resonance frequencies at ω_1 and ω_2 respectively; then for the case of very small coupling, the coupled mode equations for the amplitudes a(t) of the resonators can be written as a set of perturbed resonators:

$$\frac{da_1}{dt} = -j\omega_1 a_1 + \kappa_{12} a_2 \tag{4.5}$$

$$\frac{da_2}{dt} = -j\omega_2 a_2 + \kappa_{21} a_1 \tag{4.6}$$

The solution of which is analogous to the solution of coupling of modes in space. The essential features of the solution is a splitting of frequencies, with angular frequencies ω_+, ω_- given by

$$\omega_{\pm} = \frac{\omega_1 + \omega_2}{2} \pm \sqrt{\left(\frac{\omega_1 - \omega_2}{2}\right)^2 - \kappa_{12}\kappa_{21}} \tag{4.7}$$

The difference in frequencies is the frequency at which the energy switches back and forth from one resonator to the other. If the coupling is lossless, $\kappa_{12}\kappa_{21} = |\kappa|^2$.

Amplitude of the mode In the previous sections, an implicit understanding of the amplitude, a(t) or b(z) was assumed. —a(t)— can be understood as follows: If a lossless resonator is excited by some means with no external coupling, its amplitude a(t) may be described as

$$\frac{da_+}{dt} = j\omega_o a_+ \tag{4.8}$$

$$\frac{da_-}{dt} = -j\omega_o a_- \tag{4.9}$$

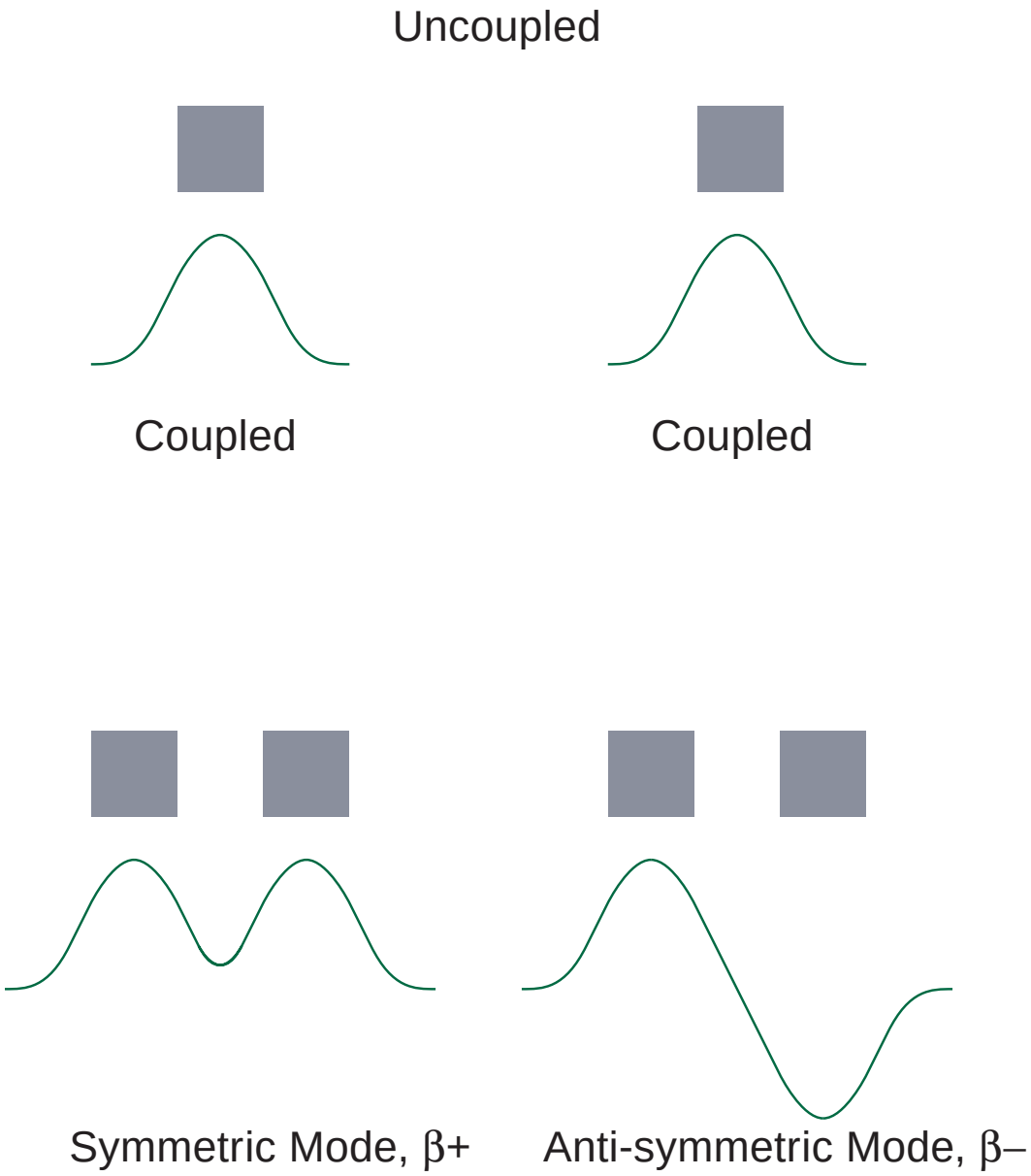

Figure 4-2: Figure showing coupling of modes in space. The symmetric mode has a larger propagation constant (higher effective index) then the anti-symmetric mode.

The solution of which is

$$a_+ = a_{+o}\exp[j\omega_o t] \tag{4.10}$$

$$a_- = a_{-o}\exp[-j\omega_o t] \tag{4.11}$$

That is energy resonates between a pair of out of phase energy forms. These pairs could be inductive and capacitive, kinetic and potential or in this case electric and magnetic. The definition of $a(t) = a_+$ is the positive frequency amplitude of the mode in the resonator. Then $|a(t)|^2$ is total energy in the resonator. Similarly b(z), the amplitude of the mode in the coupling in space formulation is defined as the the positive frequency amplitude of the mode in the waveguide, that is $|b(z)|^2$ is the integrated power of the waveguide mode traveling down the waveguide.

Coupling of a resonator to a waveguide

If there is loss with an amplitude decay time constant from a resonator, τ_l, then a becomes

$$a = a_o\exp[j\omega_o t]\exp\left[\frac{t}{\tau_l}\right] \tag{4.12}$$

and equations (4.8) becomes

$$\frac{da}{dt} = j\omega_o a + \frac{1}{\tau}a \tag{4.13}$$

The decay rate of the energy (or power lost) can be calculated from the amplitude decay given in (4.12) as:

$$|a|^2 = |a_o|^2\exp\left[\frac{-2t}{\tau_l}\right] \tag{4.14}$$

Thus, the power decays with a rate of $\frac{2}{\tau_l}$.

If there is an external waveguide near the resonator energy may be lost with an amplitude decay time constant, τ_e from the resonator to the waveguide in addition to the intrinsic loss, with corresponding time constant τ_l. Further energy may be coupled from the waveguide into the resonator, in much the same way as energy is coupled from resonator to resonator in the coupling of modes in time formulation. If the energy in the waveguide is s_+, then the amount of coupling is treated as a small perturbation and the energy that is coupled may be approximated as linear and written as κs_+. Thus, replacing the factor $\frac{1}{\tau_l}$ in equation

(4.13) with $\left(\frac{1}{\tau_l}+\frac{1}{\tau_e}\right)$ and adding a term κs_+ to describe coupling from an incident wave we may write:

$$\frac{da}{dt} = j\omega_o a + \left(\frac{1}{\tau_l}+\frac{1}{\tau_e}\right) a + \kappa s_+ \tag{4.15}$$

From the principle of time reversal [3] one can prove that κ can be defined as

$$\kappa = \sqrt{\frac{2}{\tau_e}} \exp[j\phi] \tag{4.16}$$

where ϕ is an arbitrary phase. Substituting, into (4.15)

$$\frac{da}{dt} = j\omega_o a + \left(\frac{1}{\tau_l}+\frac{1}{\tau_o}\right) a + \sqrt{\frac{2}{\tau_e}} \exp[j\phi] s_+ \tag{4.17}$$

Equation (4.17) will be used as the basis for the analysis of micro-ring and microsphere resonators.

4.2.2 Cavity Quality, Q

The quality, Q, of a resonator is a measure of how well a resonator retains its energy. Q is defined as the ratio of the stored energy in the resonator to the energy loss from the resonator per unit radian of the cycle of the wave which is stored in the resonator. Using the notation

$$W_s = \text{Energy stored in the resonator} \tag{4.18}$$

$$P_t = \text{Net Energy lost from the resonator per second} \tag{4.19}$$

$$W_t = \text{Net Energy lost from the resonator per radian} \tag{4.20}$$

Thus,

$$Q = \omega \frac{W_s}{P_t} \tag{4.21}$$

or

$$Q = \frac{W_s}{W_t} \tag{4.22}$$

Q, τ and Effective Path Length L_p

Q and L_p is intimately related to the amplitude decay time constant τ described in the previous section. Rewriting (4.18) and (4.19) in terms of a(t):

$$W_s = |a|^2 = |a_o|^2 \exp\left[\frac{-2t}{\tau}\right] \tag{4.23}$$

$$P_t = -\frac{d|a|^2}{dt} = |a_o|^2 \exp\left[\frac{-2t}{\tau}\right] \frac{2t}{\tau} \tag{4.24}$$

$$Q = \omega \frac{W_s}{P_t} = \frac{\omega\tau}{2} \tag{4.25}$$

The effective path length L_p is the average length a photon travels in the cavity:

$$L_p = \beta\tau \tag{4.26}$$

$$L_p = \frac{c}{n_{eff}} \times \frac{2Q}{\omega} = \frac{c}{n_{eff}} \times \frac{2Q}{k_o c} \tag{4.27}$$

$$L_p = \frac{c}{n_{eff}} \times \frac{2Q\lambda}{2\pi c} \tag{4.28}$$

$$L_p = \frac{Q\lambda}{\pi n_{eff}} \tag{4.29}$$

Loss Q

From energy conservation

$$W_t = \sum_i W_i \tag{4.30}$$

where W_i is the energy loss per radian from the resonator due to various sources. Dividing both sides by the stored energy W_s, yields

$$\frac{W_t}{W_s} = \sum_i \frac{W_i}{W_s} \tag{4.31}$$

Defining Q_i, the quality factor of the resonator due to each of the individual sources of loss, ie

$$Q_i = \frac{W_s}{W_i} \tag{4.32}$$

substituting (4.32) and (4.22) into (4.31) yields

$$\frac{1}{Q} = \sum_i \frac{1}{Q_i} \tag{4.33}$$

The two sources of energy lost per radian from the resonator, W_t, that are of interest are

- energy per radian coupled out of the resonator, W_e
- energy per radian lost from the resonator due to radiation, scattering or absorption, W_l

We can then define external Q, Q_e, and loss Q, Q_l as

$$Q_e = \frac{W_s}{W_e} \tag{4.34}$$

$$Q_l = \frac{W_s}{W_l} \tag{4.35}$$

Thus,

$$\frac{1}{Q} = \frac{1}{Q_e} + \frac{1}{Q_l} \tag{4.36}$$

Relation of Q and line-width $\Delta\lambda$

Intuitively Q can be related to the line-width of the resonance. If the Q is very high, this means that the amount of energy lost per wavelength traveled is very small. Thus, light in the resonators stays in the resonator for a many wavelengths and an effective path length $L_p = \frac{Q\lambda}{\pi n_{eff}}$ (see equation (4.29)) may be defined. Over this path length, the light must remain coherent, otherwise the phase cancellation will reduce the amplitude in the resonator. This requirement for coherence puts an upper bound on the line-width $\Delta\lambda$. The phase ϕ can be written as:

$$\phi = \frac{2\pi L_p n_{eff}}{\lambda} \tag{4.37}$$

Differentiating and setting $\Delta\phi \approx \pi$,

$$\Delta\phi = \frac{2\pi L_p n_{eff} \Delta\lambda}{\lambda^2} \tag{4.38}$$

$$\Delta\phi \propto \frac{2\pi Q\lambda\Delta\lambda}{\pi\lambda^2} \tag{4.39}$$

$$Q \propto \frac{\lambda}{\Delta\lambda} \tag{4.40}$$

Another way of deriving the relation, is to realize that the energy loss per radian is proportional to the bandwidth of the light since

$$\Delta E = \Delta(\hbar\omega) = \hbar\Delta\omega \tag{4.41}$$

Then

$$Q = \frac{W_s}{W_t} \tag{4.42}$$

$$Q = \frac{\hbar\omega}{\hbar\Delta\omega} \tag{4.43}$$

$$Q = \frac{\omega}{\Delta\omega} \tag{4.44}$$

$$Q = \frac{\lambda}{\Delta\lambda} \tag{4.45}$$

4.3 Micro-rings and micro-racetracks

A micro-ring involves having an input bus waveguide situated close to a ring that is resonant at wavelengths which match a complete round-trip in the ring. Figure 4-3 shows a schematic of a ring filter.

Power is coupled from the input waveguide into the ring while at the same time power leaks out at the output ports 2 and 3. On resonance, power builds up in the ring until, in equilibrium, the net power coupled from the input waveguide equals that coupled from the ring into the output waveguide 2. Light from the ring couples into waveguide 1-3, but out-of-phase with the input waveguide. This results in destructive interference and no light is transmitted to port 3. If the incoming wavelength is off-resonant, power does not build up in the ring and the light in the waveguide is transmitted via output 3.

The ring on the left is designed for a one level mask with at least 0.25 μm lithography. The ring on the right relies on coupling of light to and from waveguides which are above the ring. This requires a two level mask with 0.5 μm lithography. As with other micro-cavity devices, micro-rings exhibit low modal volumes and high Qs.

An alternate design is the racetrack design in which the ring is replaced with an oval shaped design, with the bus waveguides running parallel to the straight part of the racetracks, as shown in Figure 4-4. The advantage of these racetracks over the more traditional ring design is light in the straight part of the racetrack being exactly phase matched with

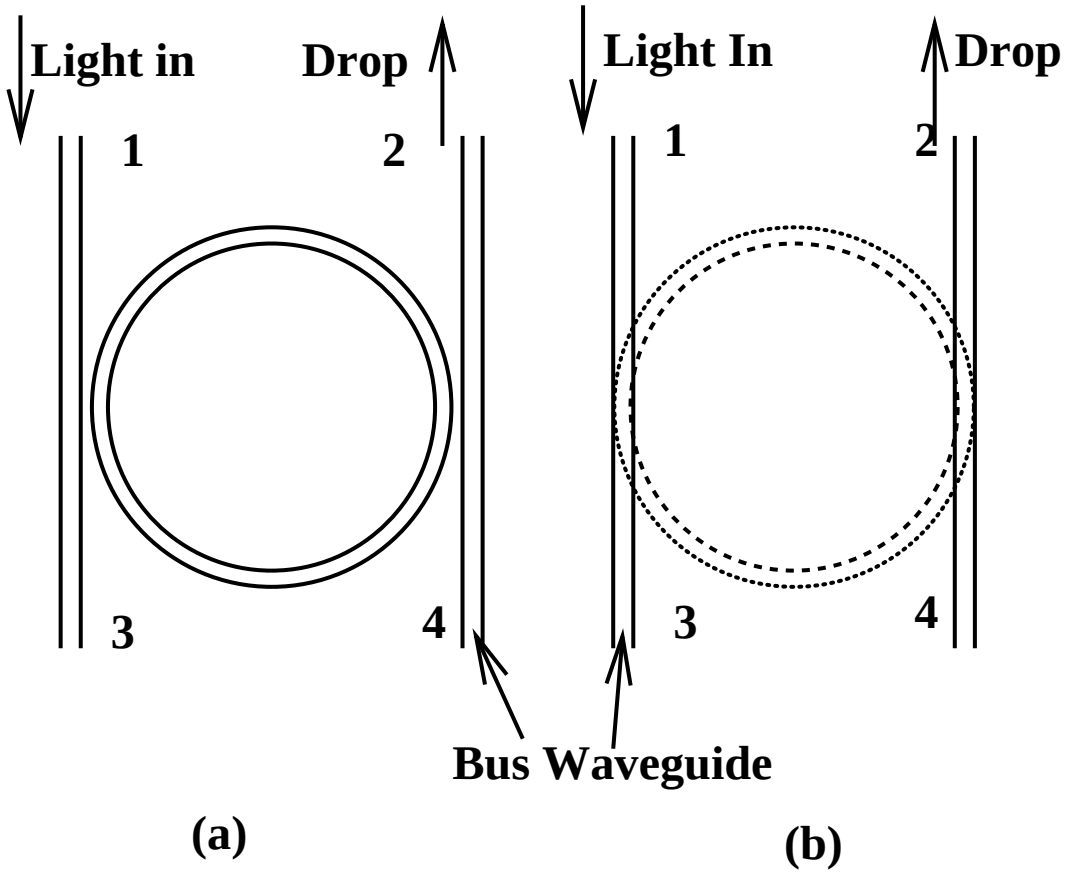

Figure 4-3: (a) Schematic of a one level micro-ring. (b) Schematic of a two level micro-ring resonator. The one level micro-ring uses only one mask but is difficult to fabricate because of the small gap size. The two level micro-ring requires more steps and planarization but the gap size is more easily controlled, since it is determined by film thickness. This results in better control of Q.

that in the bus waveguide resulting in more efficient coupling.

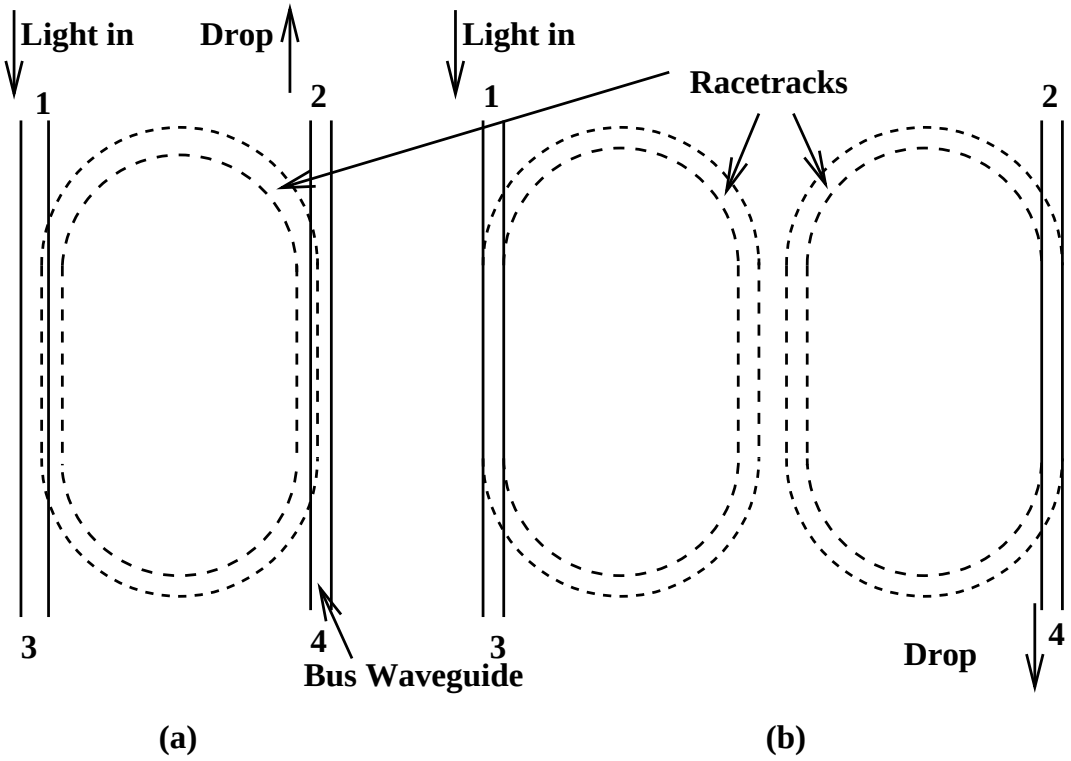

Figure 4-4: (a) Schematic of a racetrack resonator with the bus waveguides offset 0.2 μm from the racetrack (b) Schematic of a double racetrack resonator. The long straight sections of a racetrack resonator enable stronger coupling between the bus and the resonator. This enables the gap between the bus and the resonator to be bigger, resulting in less stringent fabrication tolerances.

4.3.1 Design of ring filters using coupled mode theory

In this section, a summary of the design of rings using coupled mode theory is presented. This analysis is a composite of the analysis derived by Little et al [88] and Manolatou et al [89]. The general formulation for the ring resonator works also for the racetrack resonator with a few corrections. These will be discussed explicitly at the end of this section.

We define a, s_i, s_d, s_t as the ring input, drop and transmitted amplitudes (see figure 4-5). Power drops into the fourth port only if there is roughness in the ring that can set up a counter propagating wave in the ring [90]. In most of the rings that were fabricated, the amount of power in this fourth port is small, so we neglect its presence.

From coupling of modes in time, (4.17), we generate the following coupled mode equa-

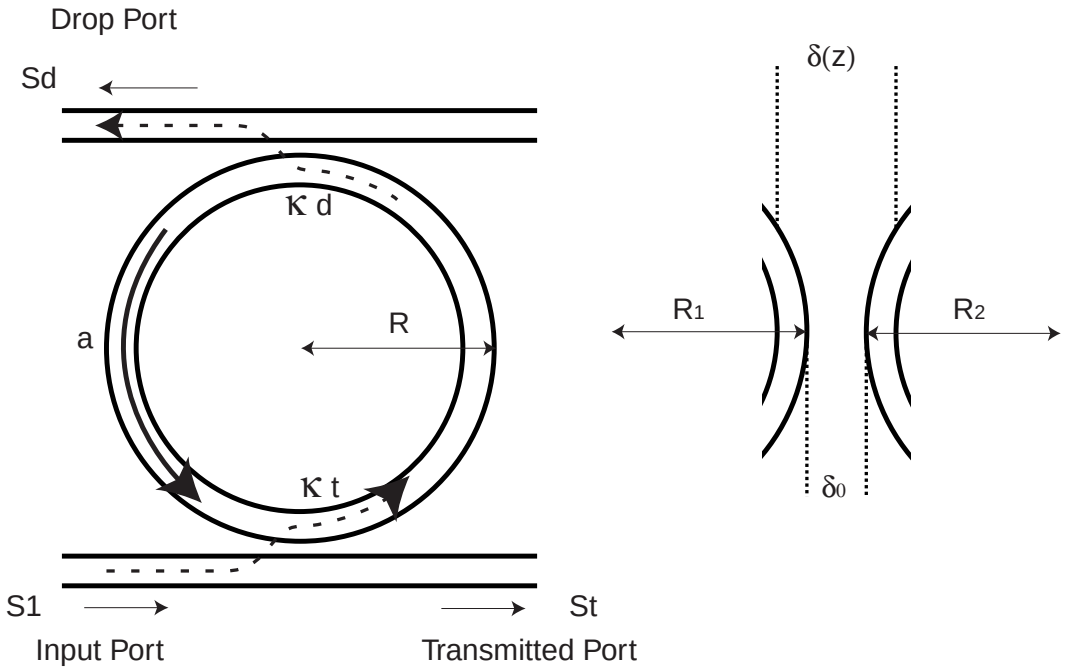

Figure 4-5: Schematic of a micro-ring filter.

tions:

$$\frac{da}{dt} = \left(j\omega_o - \frac{1}{\tau_l} - \frac{1}{\tau_d} - \frac{1}{\tau_t}\right) a + \kappa_t s_i \tag{4.46}$$

$$s_t = \exp[-j\beta d](s_i - \kappa_t^* a) \tag{4.47}$$

$$s_d = \exp[-j\beta d](-\kappa_d^* a) \tag{4.48}$$

where κ_d and κ_t are the coupling constants from the resonator to the drop and transmission waveguides respectively. κ_d and κ_t are related to the time constants τ_d and τ_t by (4.16).

Assuming the input s_i has an $\exp[-j\omega t]$ dependence, the steady state response of the amplitude of the mode in the ring, a, is

$$a = \frac{\sqrt{2}\tau_t \exp[j\phi_i s_i]}{j(\omega - \omega_o) + \frac{1}{\tau_l} + \frac{1}{\tau_t} + \frac{1}{\tau_d}} \tag{4.49}$$

and the drop and transmitted amplitudes of the modes are

$$\frac{s_t}{s_i} = \exp[-j\beta d]\left(1 - \frac{\frac{1}{\tau_t}}{j(\omega - \omega_o) + \frac{1}{\tau_l} + \frac{1}{\tau_t} + \frac{1}{\tau_d}}\right) \tag{4.50}$$

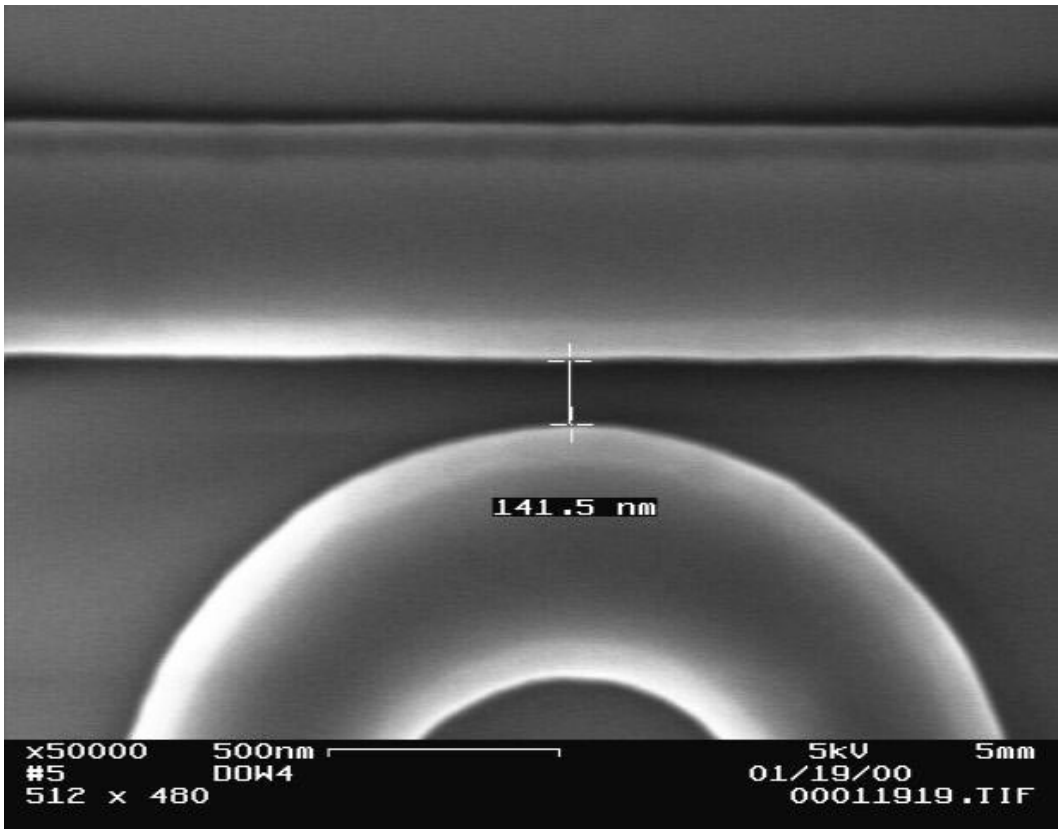

Figure 4-6: Close-up of coupling region fabricated by optical lithography. The small gap size and the exponential dependence of Q on gap size puts severe constraints on the lithography.

$$\frac{s_d}{s_i} = -\exp[-j\beta d]\frac{\sqrt{\frac{4}{\tau_d\tau_t}}\exp[j(\phi_i-\phi_d)]}{j(\omega-\omega_o)+\frac{1}{\tau_l}+\frac{1}{\tau_t}+\frac{1}{\tau_d}} \tag{4.51}$$

Determining the coupling coefficient κ

The value for κ for a real 3-D ring resonator is not easy to obtain analytically. However, it is possible to use a 3-D beam propagation method or a combination of a mode solver and analytical methods to extract an approximate κ. See figure 4-6. The general idea of this method is outlined in [88, 89]. The coupling coefficient, χ for the coupling of modes in space formulation of two adjacent waveguides is first determined as a function of waveguide separation by BPM. A correction is made in the case of the ring since the waveguides are not parallel. The net fraction of power transferred over the entire coupling length from the bus to the waveguide is then found by integrating over the coupling distance. This is κ. Each of these steps is described in detail. The values of κ for the case of a 0.5 μm wide by 0.2 μm high silicon on oxide waveguide and a 0.5 μm wide by 0.8 μm high silicon nitride

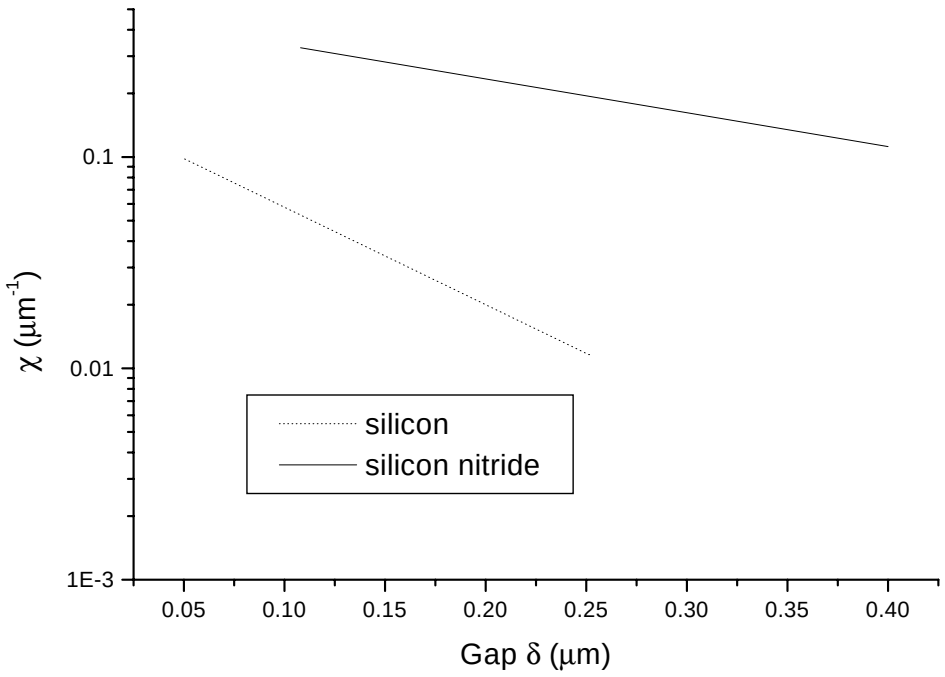

Figure 4-7: Graph of χ as a function of gap distance δ for silicon and for silicon nitride. Note the exponential dependence of χ on the gap size. This is expected since the coupling between the two waveguides is evanescent. From this line plot, α and $\chi[\delta_o]$ in equation (4.52) can be extracted.

waveguide are shown at the end of this section.

χ as a function of gap δ From equation (4.4), it can be seen that with the coupled and uncoupled propagation constants $\beta_{\pm}$ and $\beta_{1,2}$, χ is easily determined. With a BPM mode solver, all four propagation constants can be easily found, and κ can be found as a function of gap distance. Since the coupling strength is a function of the mode overlap and these waveguides are evanescently coupled, in the limit of weak coupling, this function of κ with gap distance δ is a decaying exponential (see figure 4-7) i.e.

$$\chi[\delta] = \chi[\delta_o] \exp[-\alpha\delta] \tag{4.52}$$

Gap δ as a function of z In the case of a ring, the gap can be shown with simple trigonometry to be

$$\delta[z] = \delta_o + R_1 - \sqrt{1 - \frac{z}{R_1}^2} + R_2 - \sqrt{1 - \frac{z}{R_2}^2} \approx \delta_o + \frac{z^2}{2}\left(\frac{1}{R_1} + \frac{1}{R_2}\right) \tag{4.53}$$

The exponential fit is a result of the coupling being evanescent. The evanescent tails are exponential and the coupling coefficient is a function of the amplitude of the evanescent tail. Thus, the coupling coefficient χ is an exponentially decaying function. Since coupling is decaying exponential as a function of gap size, the Taylor series expansion is a good approximation. In addition, there is there is a phase variation $\exp[-j\Delta\beta z]$ between the two waveguides, if the waveguides have propagation constants which differ by $\Delta\beta$. Thus, the total fraction of power coupling from the bus waveguide to the ring waveguide is given by

$$\Xi = \int_z \chi[z] \exp[-j\Delta\beta z] dz \tag{4.54}$$

Coupling coefficient κ Now the spatial coupling coefficient χ between the bus and ring waveguide has to be related to the temporal coupling coefficient κ_t for the resonator and the bus waveguide. To understand their relation we cast the drop power (4.47) as:

$$|s_d|^2 = |\kappa_d|^2 |a|^2 \tag{4.55}$$

which can be understood as the power transmitted in the bus having to be equal to the power coupled to the drop bus from the ring. Thus, the fraction of power transferred from the ring to the drop bus can be written as

$$|\Xi|^2 |A|^2 = |\kappa_d|^2 |a|^2 \tag{4.56}$$

where A(t) is the amplitude of the wave in the ring. The total power stored in the ring as a function of A(t) is

$$|a|^2 = |A|^2 \frac{2\pi R}{v_g} \tag{4.57}$$

Hence, κ_d can be written as a function of Ξ

$$|\kappa_d|^2 = |\Xi|^2 \frac{v_g}{2\pi R} \tag{4.58}$$

The factor $\sqrt{\frac{v_g}{2\pi R}}$ converts the amplitude b(z) of the mode in the bus waveguide to the amplitude a(t) of the mode in the resonator. Thus, $|\kappa|$ may be computed from the integral

$$|\kappa| = \int_z \chi[z] \exp[-j\Delta\beta z] dz \sqrt{\frac{v_g}{2\pi R}} \tag{4.59}$$

After algebra (4.59)is

$$|\kappa| = \chi[\delta_o] \exp\left[-\frac{(\Delta\beta)^2}{4\alpha\gamma}\right] \sqrt{\frac{\pi}{\alpha\gamma}} \sqrt{\frac{v_g}{2\pi R}} \tag{4.60}$$

where

$$\gamma = \frac{1}{2}\left(\frac{1}{R_1} + \frac{1}{R_2}\right) \tag{4.61}$$

Using the above method to calculate κ and Q a plot of Q vs. coupling gap may be constructed for both silicon and silicon nitride rings and racetracks. See figures 4-8 and 4-9 respectively. Assuming that $\Delta\beta$ in equation (4.60) is small, then for a ring $|\kappa|$ becomes

$$|\kappa| = \chi[\delta_o] \sqrt{\frac{v_g}{\alpha}} \tag{4.62}$$

which is independent of radius! On the other hand, if $\Delta\beta$ is non-zero, then $|\kappa|$ decreases as R decreases because $\Delta\beta$, the phase mismatch between the bus and the ring waveguide, increases as the radius increases. This is because the tighter the radius of curvature, the larger the difference in effective index between a straight and a bent waveguide.

For a racetrack, $\Delta\beta$ is zero and equation (4.59) reduces to

$$|\kappa| = \int_z \chi dz \sqrt{\frac{v_g}{L}} \tag{4.63}$$

$$|\kappa| = \chi \sqrt{v_g L} \tag{4.64}$$

where L is the circumference of the racetrack.

Free spectral range of the resonators

The free spectral range is the distance between adjacent resonances. Assuming the dependence of effective index on wavelength can be linearized and the fact that

$$m\lambda = L n_{eff,\lambda} \tag{4.65}$$

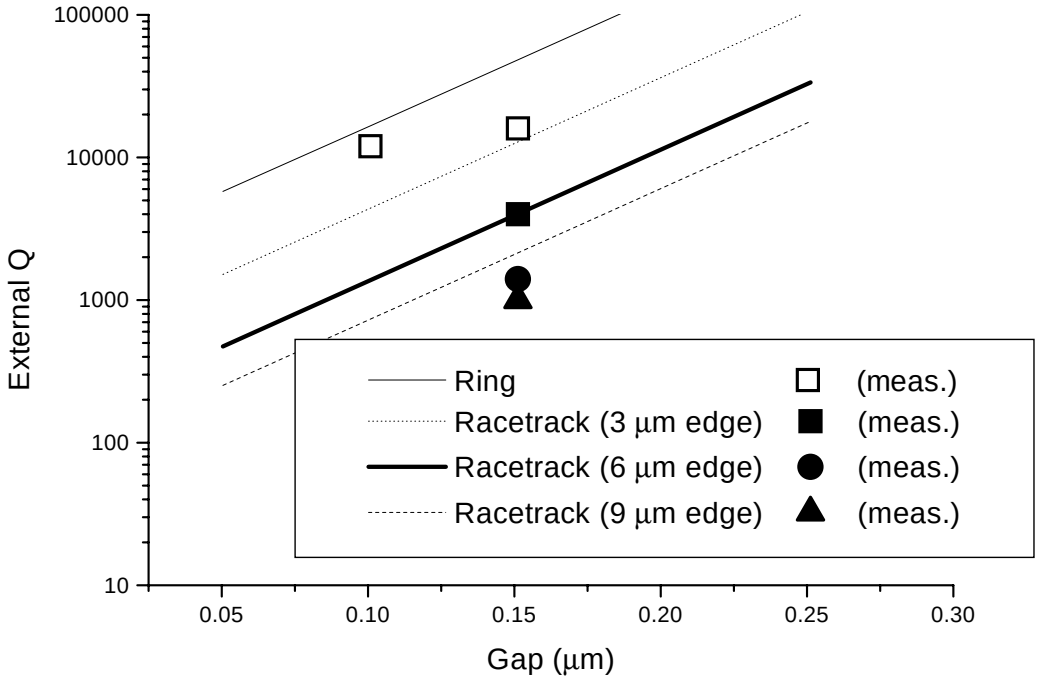

Figure 4-8: Graph of predicted loaded Q for a lossless silicon ring and extracted loaded Qs of fabricated silicon rings. Note that the Q is to first order independent of the ring radius and strongly dependent on the racetrack coupling distance. See equations (4.62) and (4.64). There is a systematic underestimation of the Q of the waveguides which could be due to a small error in the fabrication of the waveguide cross-section.

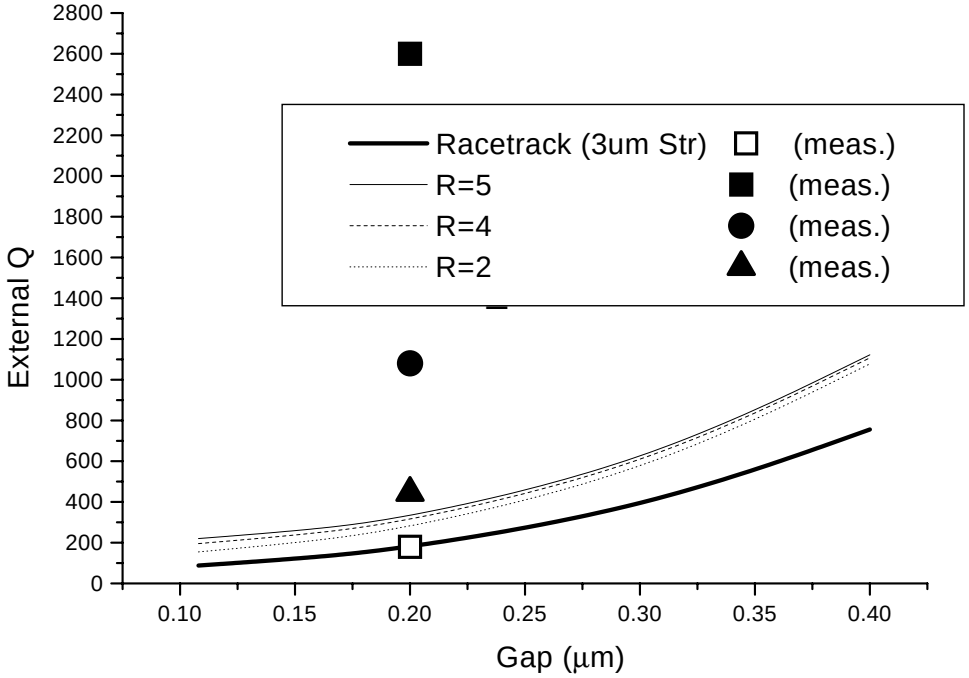

Figure 4-9: Graph of predicted loaded Q for a lossless silicon nitride ring and extracted loaded Qs of fabricated silicon nitride rings. Unlike the predictions for silicon, the predictions for silicon nitride always systematically exceed the measured Q.

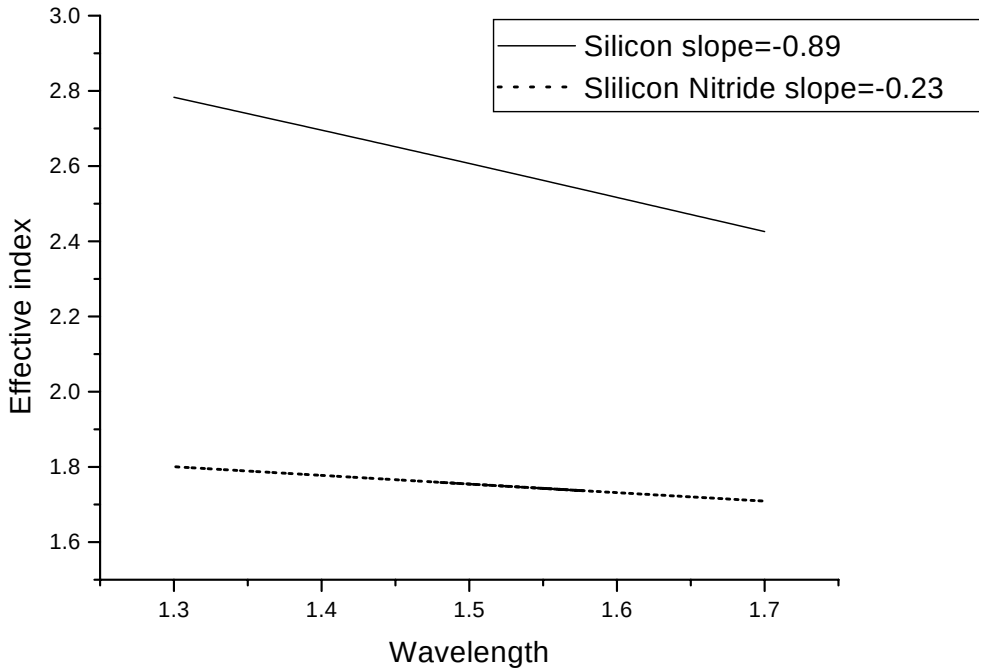

Figure 4-10: Graph of effective index as a function of wavelength for silicon and silicon nitride oxide clad strip waveguides. Note the linear fit over the wavelength of interest.

L=circumference, the theoretical FSR can be derived,

$$FSR \approx \frac{\lambda^2}{Ln_{eff}}(\frac{1}{m} + 1 - \frac{\lambda}{n_{eff}}\frac{dn_{eff}}{d\lambda})^{-1} \tag{4.66}$$

where $m = \frac{Ln_{eff}}{\lambda}$ is the number of wavelengths that fit in the ring. The approximation that the effective index can be linearized as a function of wavelength is good. See figure 4-10. Neglecting this λ dependence for silicon nitride and silicon waveguides leads to errors of 20% and 40% respectively. The gradient $\frac{dn_{eff}}{d\lambda}$ is -0.87 for silicon strip waveguides, -0.22 for silica clad 0.8 μm by 0. 8 μm nitride waveguides and -0.34 for air clad 0.5 μm by 0.8 μm nitride waveguides

A fit of the theoretical and experimental FSR vs. ring or racetrack circumference is plotted in figure 4-11. The extracted FSR of silicon rings is well predicted by equation (4.66). However, the FSR extracted from silicon nitride rings is substantially different from that predicted by equation (4.66) if an index of 2 is used. The data is well fit by a core

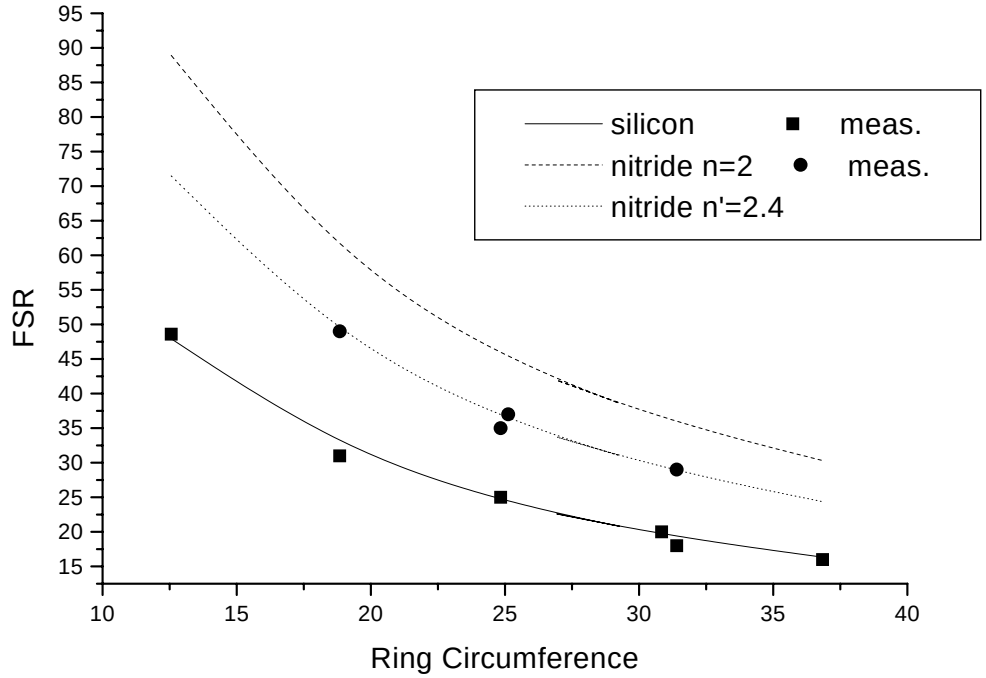

Figure 4-11: Graph of theoretical (equation (4.66)) and experimental FSR for silicon and nitride waveguides. The more accurate fit for silicon is probably due to the fact that the silicon nitride index used is inaccurate. An index of 2.4 is a much better fit to the silicon nitride data, which is consistent with Si rich nitride.

index of 2.4. This observation is consistent with the use of silicon rich silicon nitride which is expected to have a higher index of refraction.

A plot of the dependence of FSR on the index contrast is shown in figure 4-12. There is a trade-off in the dependence of FSR with the index contrast due to the loss limited minimum ring radius and the dependence of FSR with the core index. The higher the core index the smaller the minimum radius and the higher the free spectral range according to equation (4.66). On the other hand, the larger the index of refraction the smaller the FSR according to (4.66). Figure 4-12 shows the the smaller minimum radius dominates over the increases index of refraction. This explains the interest in high index contrast rings. Note that the analysis used to derive the curve in figure 4-12 assumes $Q_l = 1000$ and assumes that there is no loss due to scattering. As will be explored over the next few sections, the largest FSR measured were for the silicon nitride waveguides. This is probably a result of the lower scattering loss in the nitride waveguide than for silicon waveguides of the same

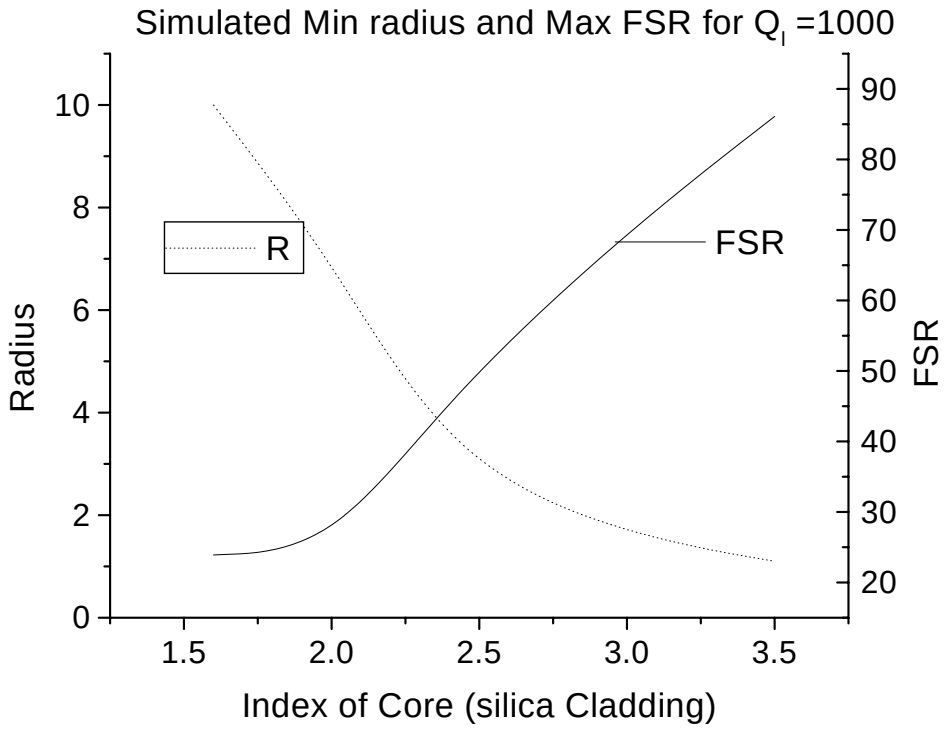

Figure 4-12: Graph of Theoretical FSR vs index contrast. There is a tradeoff between the dependence of FSR on index contrast and the bending loss dependence on index contrast. The increased in FSR with respect to core index neglects the increased scattering loss for higher index contrast waveguides with the same surface roughness

radius.

4.3.2 First order filters

Extraction of data from through and drop responses

When measuring the ring response, the transmission power $\left|\frac{s_t}{s_i}\right|^2$ and the drop power $\left|\frac{s_d}{s_i}\right|^2$ is measured as a function of frequency. If the device is symmetric, then at resonance, $\tau_d = \tau_t$ At resonance, $\omega = \omega_o$ the power responses can derived from equations (4.51) and (4.50)

$$D = \left|\frac{s_t}{s_i}\right|^2 \left(\frac{1}{1+2\frac{\tau_l}{\tau_d}}\right)^2 \tag{4.67}$$

$$T = \left|\frac{s_d}{s_i}\right|^2 = \left(\frac{2\frac{\tau_l}{\tau_d}}{1+2\frac{\tau_l}{\tau_d}}\right) \tag{4.68}$$

$$\sqrt{\frac{D}{T}} = \frac{2\tau_l}{\tau_d} \tag{4.69}$$

Since $Q = \frac{\omega\tau}{2}$ (see (4.25)), one may derive the loss Quality factor, Q_l and the net external Quality factor, $Q_e = Q_d/2$, from the following system of simultaneous equations:

$$\sqrt{\frac{D}{T}} = \frac{2\tau_l}{\tau_d} = \frac{Q_l}{Q_e} \tag{4.70}$$

$$\frac{1}{Q_{measured}} = \frac{\lambda}{\Delta\lambda} = \frac{1}{Q_l} + \frac{1}{Q_e} \tag{4.71}$$

The loss Q was used to determine the loss of bends and straight waveguide sections in the previous chapter.

The Loss Quality factor

The loss quality factor Q_l for a ring can be analyzed from its definition as in equation (4.35).

$$W_s = \frac{1}{2}\int_V \epsilon \cdot E^2 dV \tag{4.72}$$

where V is the volume of the ring. The energy dissipated in time δt

$$W_l = \int_V \frac{1}{2}\epsilon \cdot E^2 - \frac{1}{2}\epsilon \cdot E^2 \exp[-\alpha v_g \delta t] dV \tag{4.73}$$

$$W_l \approx \int_V \frac{1}{2}\epsilon \cdot E^2 dV (1 - \exp[-\alpha v_g \delta t]) \tag{4.74}$$

$$W_l \approx \int_V \frac{1}{2}\epsilon \cdot E^2 dV (\alpha v_g \delta t) \tag{4.75}$$

Thus,

$$Q = \frac{\omega \frac{1}{2}\int_V \epsilon \cdot E^2 dV}{\int_V \frac{1}{2}\epsilon \cdot E^2 dV (\alpha v_g \delta t)} \tag{4.76}$$

$$Q = \frac{\omega}{\alpha v_g} \approx \frac{\beta}{\alpha} \tag{4.77}$$

4.3.3 Higher order filters

Higher order filters can be made be coupling two or more resonators together. From coupling of modes in time, (4.17), the following coupled mode equations are generated for N rings that are in series:

$$s_d = (-\kappa_d^* a_N) \tag{4.78}$$

Number of rings	$\|\kappa\|^2$ for Maximally flat filter
2	$\|\kappa_1\|^2 = 0.250\ \|\kappa\|^4$
3	$\|\kappa_1\|^2 = \|\kappa_2\|^2 = 0.125\ \|\kappa\|^4$
4	$\|\kappa_1\|^2 = \|\kappa_3\|^2 = 0.100\ \|\kappa\|^4$ $\|\kappa_2\|^2 = 0.040\ \|\kappa\|^4$

Table 4.1: Values of coupling coefficient to ensure flat responses

$$\frac{da_N}{dt} = \left(j\omega_N - \frac{1}{\tau_d} - \frac{1}{\tau_l}\right) a_N + \kappa_{N-1} a_{N-1} \tag{4.79}$$

$$\frac{da_i}{dt} = \left(j\omega_i - \frac{1}{\tau_l}\right) a_i + \kappa_i a_{i+1} + \kappa_{i-1} a_{i-1} \tag{4.80}$$

$$\frac{da_1}{dt} = \left(j\omega_1 - \frac{1}{\tau_t} - \frac{1}{\tau_l}\right) a_1 + \kappa_1 a_2 + \kappa_t s_i \tag{4.81}$$

where $i = 2..(N-1)$,

$$|\kappa_i|^2 = |\Xi|^2 \frac{v_{g,i} v_{g,i+1}}{(2\pi R_i)(2\pi R_{i+1})} \tag{4.82}$$

the solution of which is a continued fraction. This solution can be recast as an analog to an LC circuit and knowledge of electrical filter design can be applied. Given a certain ring dimension, the design to generate maximally flat responses or other responses will result in the selection of $|\kappa_i|^2$, which is dependent on the coupling strength $|\kappa_d|^2$ and $|\kappa_t|^2$ between the rings and the drop waveguides. The result for a symmetric structure i.e. $|\kappa_d|^2 = |\kappa_t|^2$ was published in a paper by Little and are reproduced here for completeness. If the values of the coupling coefficients in table 4.1 are chosen and if the rings are all ideal with resonances at ω_o, the responses of symmetric higher order filters are all of the form:

$$\frac{1}{1 + k(N) \cdot \left(\frac{\omega - \omega_o}{2\omega_o}\right)^{2N}} \tag{4.83}$$

where k(N) is a constant.

PolySi rings

Rings 1 to 5 μm radius polySi rings have been fabricated. None of the 1 μm rings had ring responses. However, ring responses were extracted from 2 to 5 μm radius rings. Results for the 5 μm radius ring in figure 4-13 are shown in figures 4-14 and 4-15. The Q of the 5μm ring is between 7000 and 10000 and the FSR is 21 nm. A comparison between the ring resonances with three different radii are shown in figure 4-18.

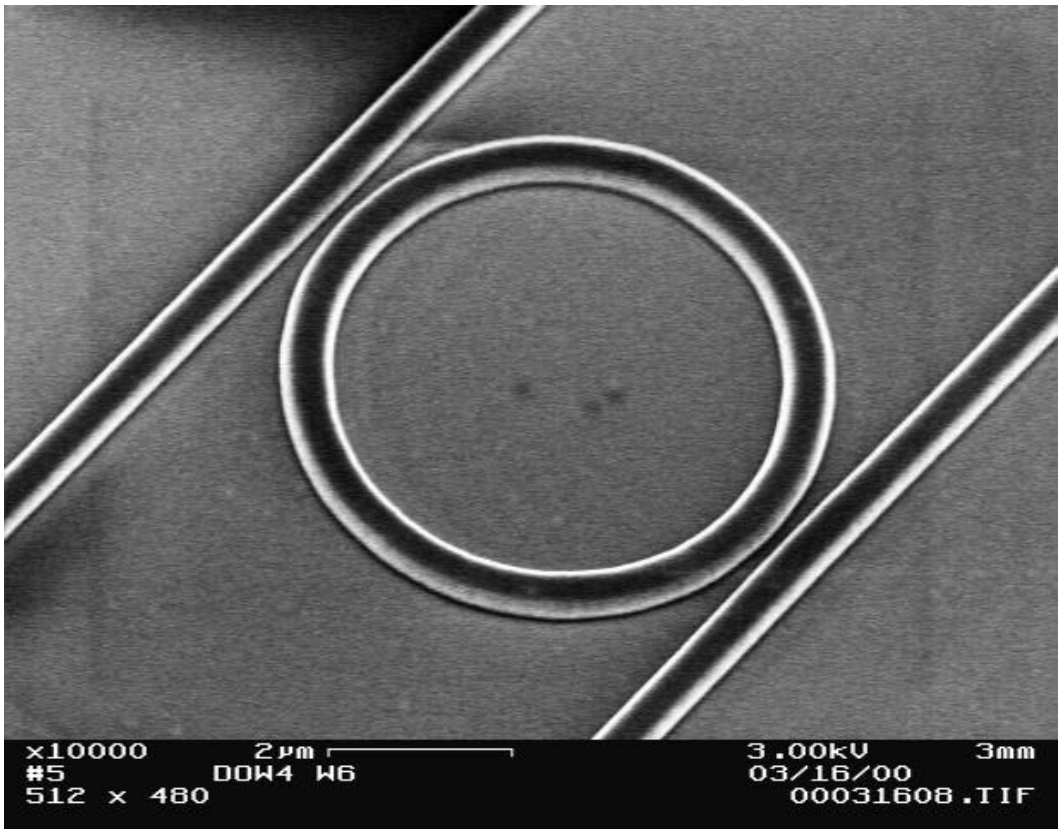

Figure 4-13: SEM of a 5 μm radius polySi ring resonator. This is the first ring resonator fabricated by optical lithography with a cleared gap.

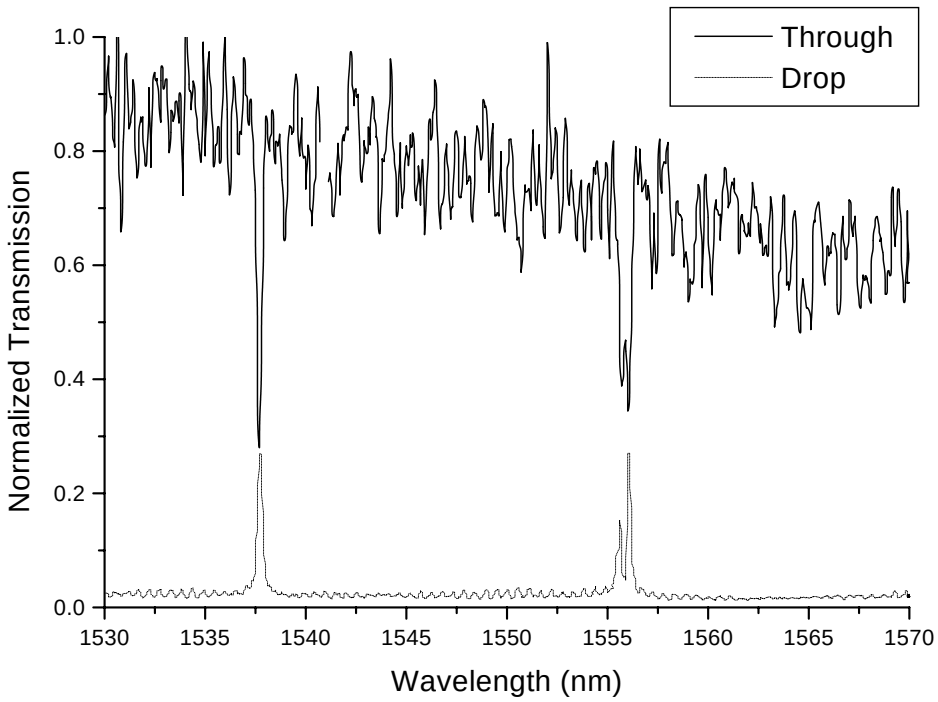

Figure 4-14: Transmission and drop port scan of a 5 μm radius polySi ring with gap size of 0.2 μm. The wavelength scan through the transmission port is noisy because of Fabry-Perot resonances. Q is between 7000 and 10000 and the FSR is 21 nm.

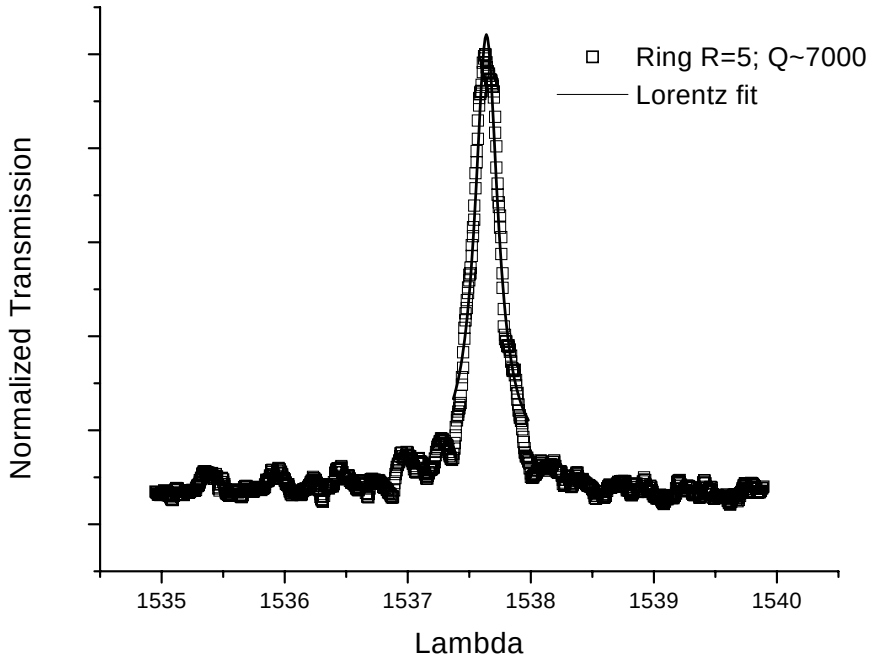

Figure 4-15: High resolution drop port scan of a 5 μm radius silicon ring with gap size of 0.2 μm. The extracted Q of 7000 is a convolution of of Fabry-Perot and the Lorentzian response of the ring. The symmetry of the response and the lack of Fabry-Perot structure on the peak indicates that the null of the Fabry-Perot coincides with the peak of the response. Thus the peak is "broadened" and the Q so extracted is an underestimate.

Racetracks The circumferences of the racetracks that were fabricated range from 24 to 36 μm. A SEM of a typical 30 μm circumference racetrack is shown in figure 4-16, while the response of the racetrack is shown in figure 4-17. The efficiency of this racetrack is

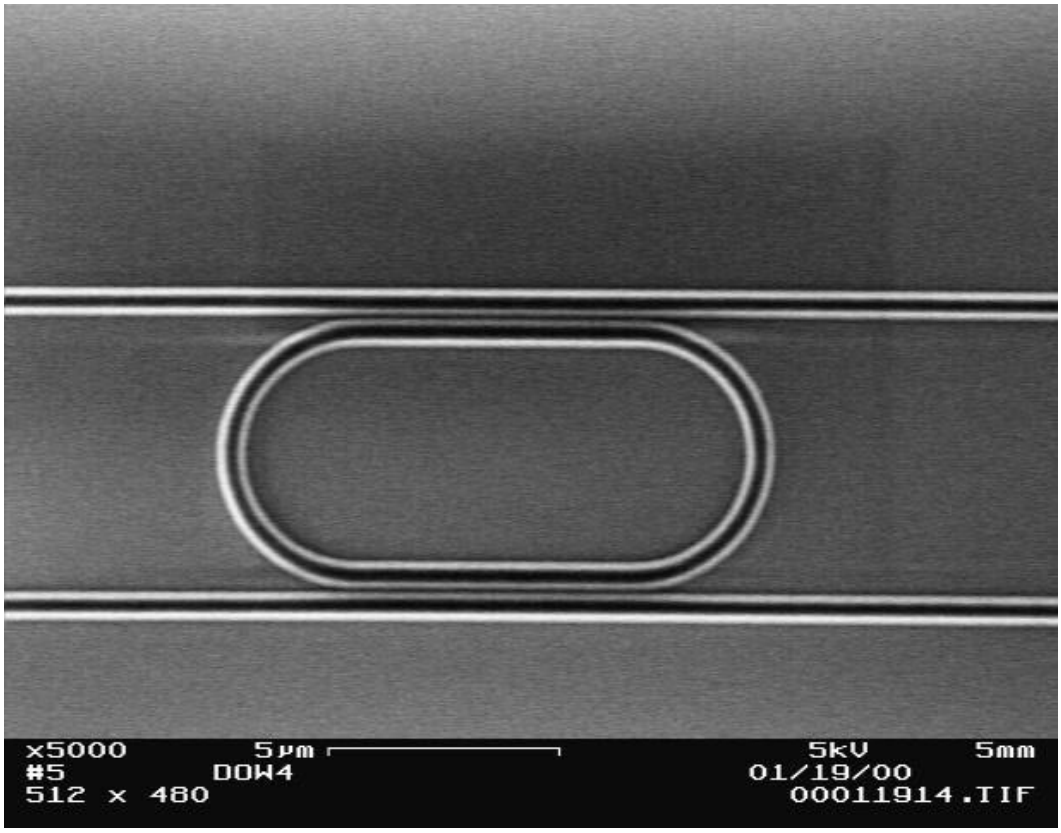

Figure 4-16: SEM of 30 μm circumference polySi racetrack. This is the first racetrack resonator fabricated by optical lithography with a cleared gap.

very high. In fact for the case of the 30 and 36 μm circumference racetrack (with Q=1400 and 850 respectively), the efficiency is close to 100% (see figure 4-17)! The main reason for this is that the large straight sections result in a long overlap region between the bus waveguide and the ring. Thus, in turn results in large coupling and small external Q. Since the external Q dominates the loss Q, the drop efficiency is high. (See equation (4.70)).

Multi-level vs. single-level In order to control the Q of these racetracks with greater accuracy, the bus waveguides are placed at two different positions with respect to the ring or racetrack. The first configuration involved running the bus waveguide right over the ring or racetrack while in the second configuration the bus waveguides are offset by 0.2 μm from the center of the ring waveguides as shown in Figure 4-4.

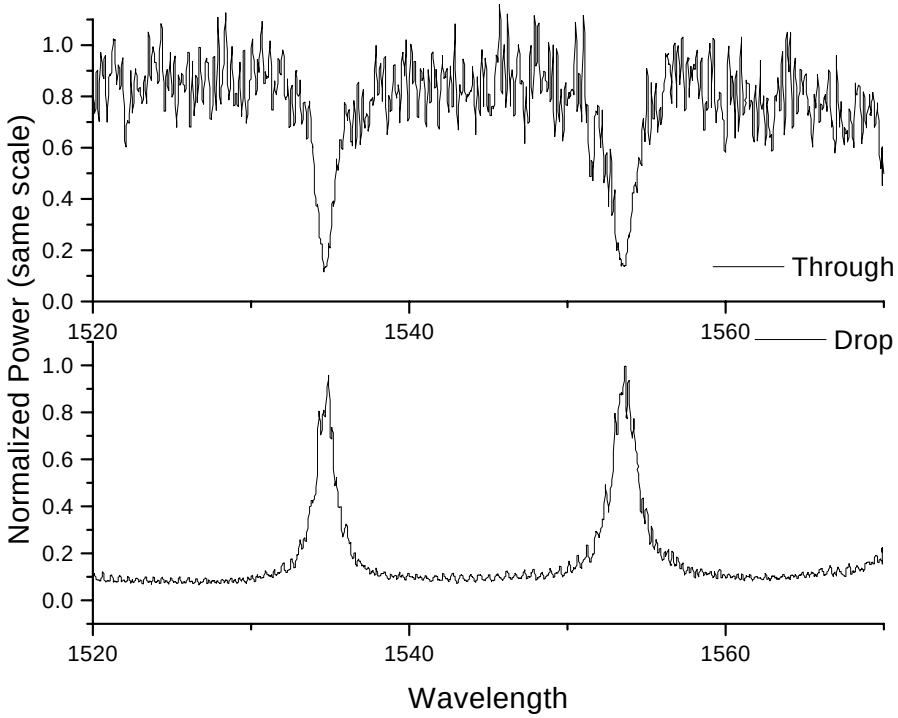

Figure 4-17: 30 μm circumference polySi racetrack resonance. The resonances are much broader than in figure 4-15 because of the stronger coupling for the racetrack resonator. However, the efficiencies are much better, because the device is now external Q limited.

Q vs. Circumference The drop responses of 3 different radii ring resonators are shown in figure 4-18. As expected the FSR range increases with decreasing with radius of curvature, implying that the Qs of the small radius rings are somewhat loss limited or at least have loss Qs which are small enough to affect external Q (section 4.3.1). In addition, three racetrack resonator shapes were made. A 3 μm radius of curvature was used with 3, 6 and 9 μm straight sections. The responses are plotted in figure 4-19. As expected the Qs decreased with the longer straight sections, from 2700 to 1400 to 850. The Qs are approximately inversely proportional to the the length of the straight sections which would be the case if the loss Q is small compared to the external Q. Thus, the ring Qs appear to be loss limited while the racetrack Qs appear to be external Q limited.

Q vs. Gap Figure 4-20 shows the change in the response of the rings with different gap sizes. The large change in the Q is a result of the large change in external Q due to the exponential dependence of coupling coefficient on the gap size. The fact that the Q does change implies that the external Q is on the same order of magnitude as the loss Q.

Higher ordered filters Higher order rings and racetrack resonators were also fabricated using multiple rings and racetracks between each pair of bus waveguides. A distance of 0.5 μm separates these rings and racetracks from one another. A top-view SEM picture of 2 coupled racetracks are shown in figure 4-21 and a top-view SEM picture of 3 coupled 5 μm radius rings are shown in figure 4-22. There were two distinct types or responses that were observed; the type of response which these rigs exhibited correlated with the choice of fabrication location used.

Lincoln Labs process The responses of the higher order ring responses for rings fabricated at Lincoln Labs are shown in figure 4-23. As expected, the 2nd order ring response is much narrower than the single ring response. However, the top of the response does not exhibit the characteristic flat-top response of a second order Butterworth filter.

Intel process Figure 4-24 shows the spectral response of first, second and third order racetracks fabricated at Intel. The spectra of the second and third order filters are interesting because the spurious features due to the higher order TM mode which can be seen in the first order filter are significantly reduced in the higher order spectra. The TM mode

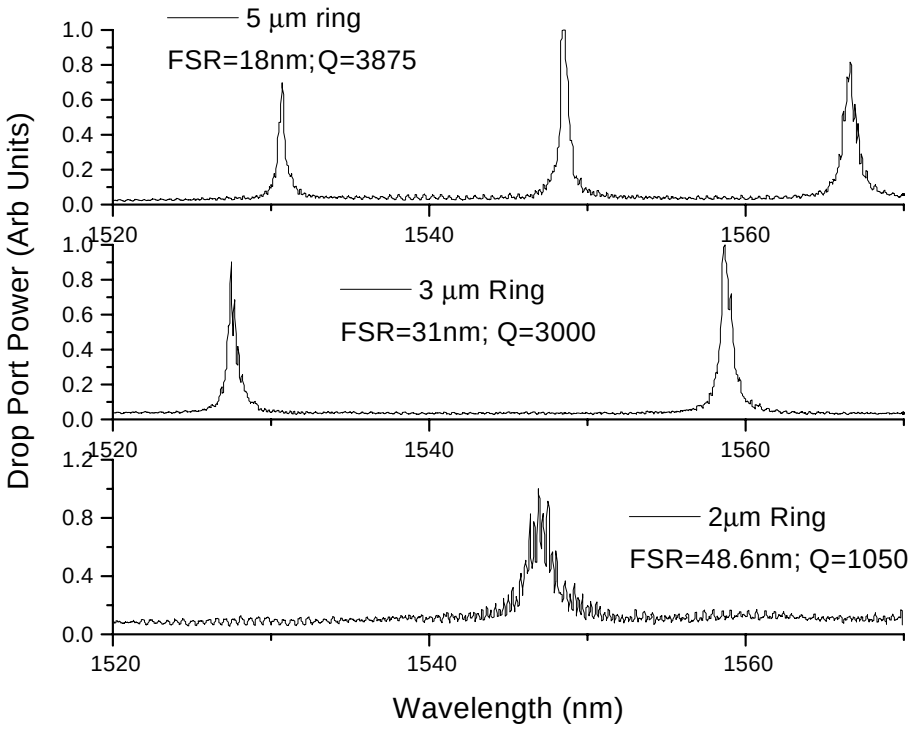

Figure 4-18: Drop port responses of 3 polySi ring resonators. The responses reflect the correct increase in FSR with decreasing radius. In addition, the Q decreases with decreasing radius contrary to equation (4.62). The reason for this is radiation and scattering losses increase as the bending radius decreases and the resonance response becomes increasingly loss limited.

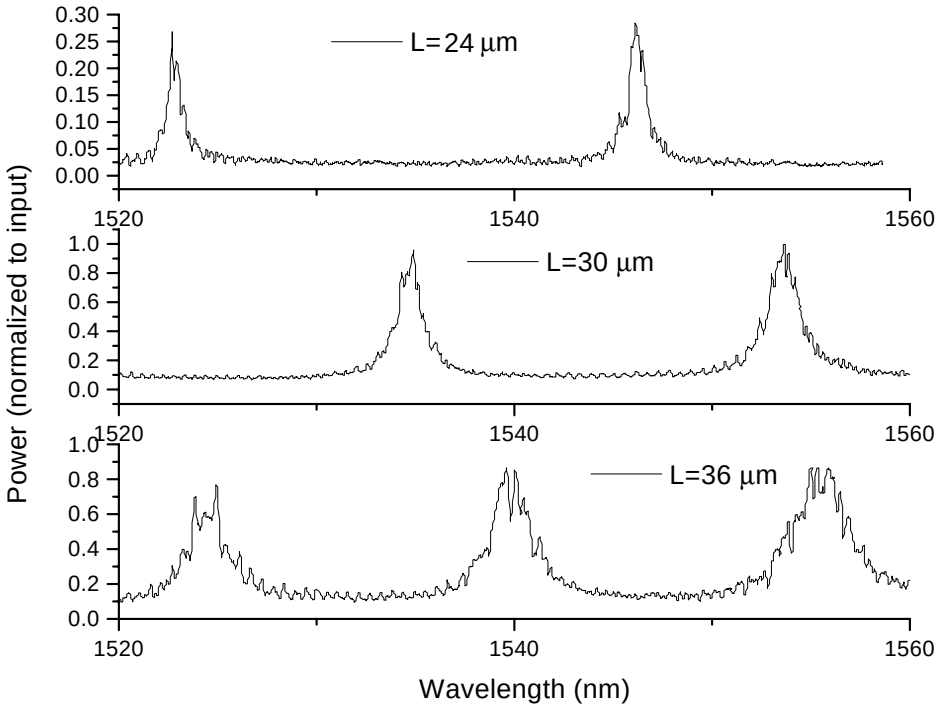

Figure 4-19: Drop port responses of 3 polySi racetrack resonators. The straight sections are varied to change the Q and FSR while the radius of curvature stays the same. The FSR and the Q increase with decreasing circumference L as expected. The Q increases because the coupling distance becomes shorter with decreasing L.

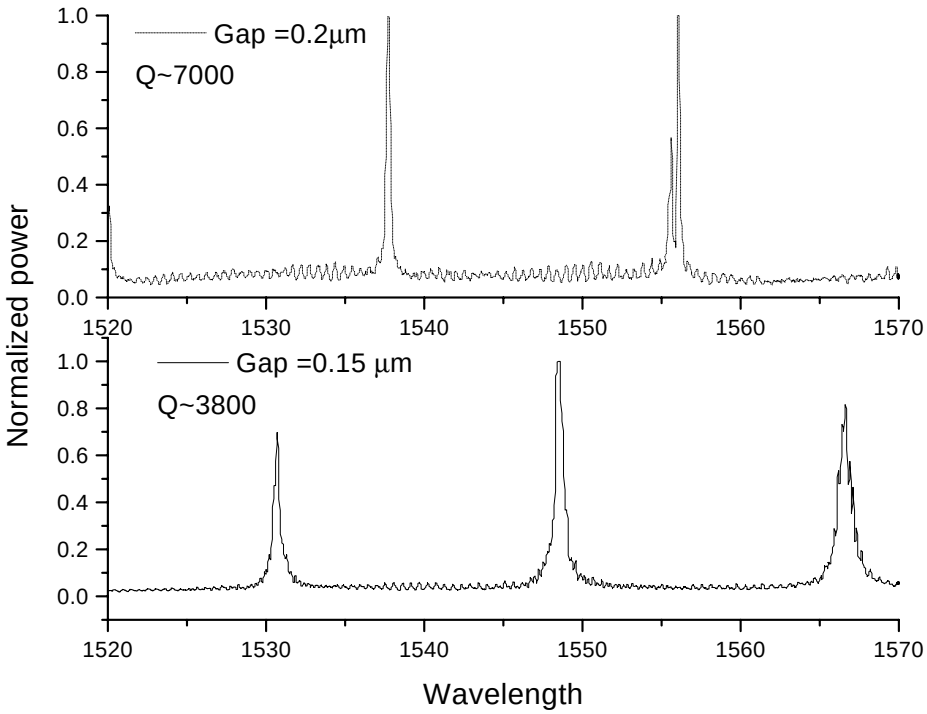

Figure 4-20: Graph showing the change in response between two polySi rings of similar circumference but different gap. As expected, as the gap size increases, the Q increases due to reduced power coupling efficiency from the ring to the bus.

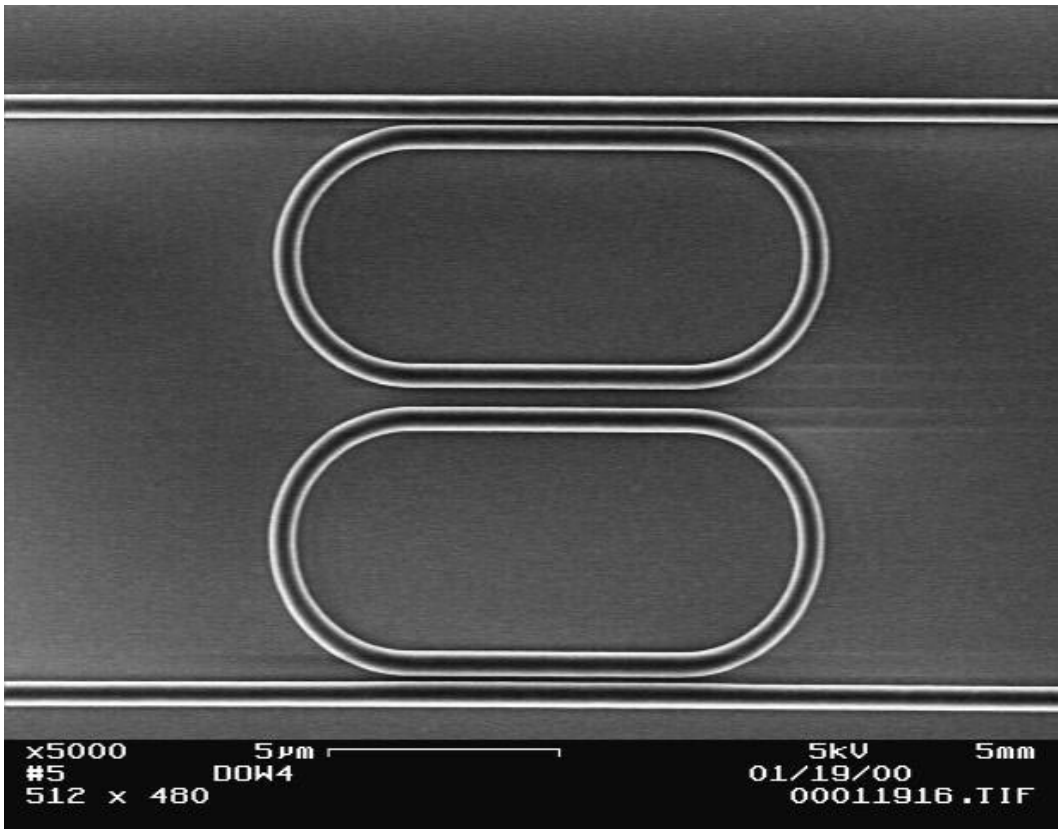

Figure 4-21: SEM of 2 coupled 30 μm circumference polySi racetrack resonators. The racetrack resonators have mirror and rotational symmetry, so they should be identical.

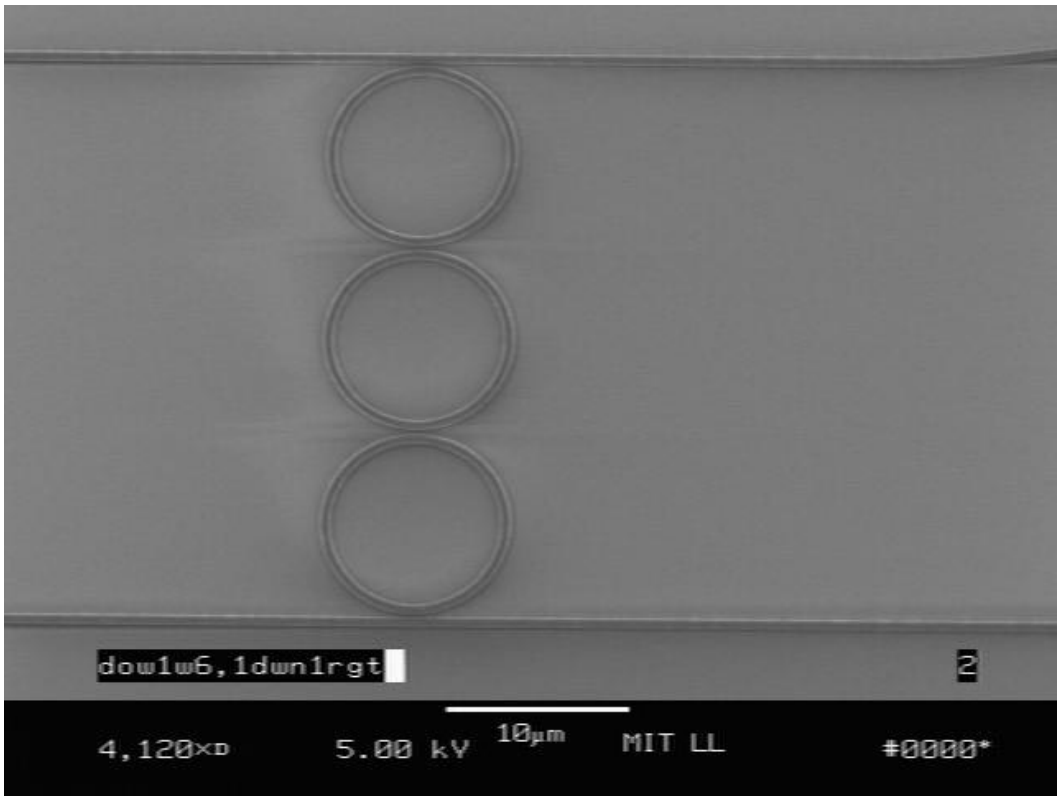

Figure 4-22: SEM of 3 coupled 5 μm radius polySi ring resonators. The middle ring does not have the same symmetry so the resonance frequency of the middle ring may be slightly different from the other two rings.

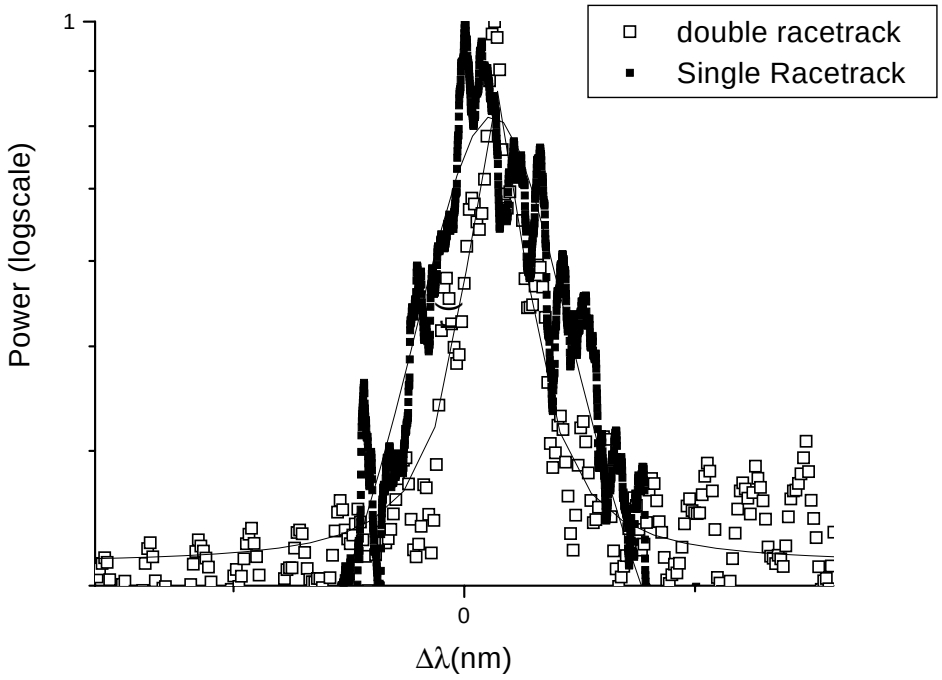

Figure 4-23: High resolution drop port scan of single and double 5 μm radii polySi rings with gap size of 0.2 μm. A narrowing of the resonance line and faster roll-off is observed. However, no flat top resonance is seen.

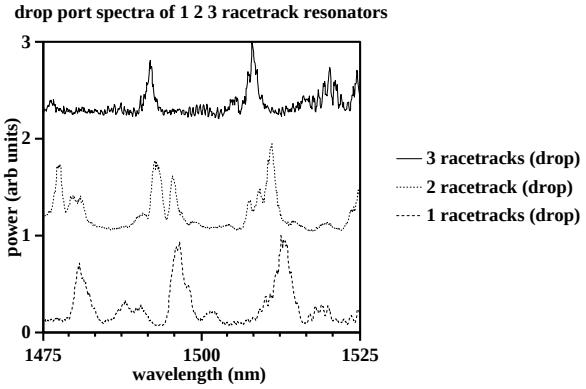

Figure 4-24: Drop port response of multi-ordered micro-racetrack filters using 36 μm circumference polySi racetracks with offset waveguides (see Figure 4-4). The bottom spectrum is from a filter with a single racetrack resonator (peak positions of 1481 nm, 1497 nm and 1513 nm) , the middle spectrum is from a filter with double racetrack resonators (peak positions of 1477, 1493 and 1511 nm), while the top spectrum is from a filter with triple racetrack resonators (peak positions of 1492 nm and 1508 nm). Q = 1000 and FSR = 16 nm.

has higher bending loss than the TE mode so the Q of the TM mode is much smaller than the Q of the TE ring mode. Further, the effective indices of the TE and TM modes are different, so the resonance peak positions are different.

The efficiency of the second order resonator is about 6% while that of the third order ring is 0.3%. The Qs are approximately 1000. The first order racetrack filter is singly peaked and the second order racetrack filter is doubly peaked which suggests that the rings are either very strongly coupled to each other or that the rings are slightly off resonance from each other. The low efficiencies imply that off-resonance is the more likely cause. These rings were fabricated side by side, meaning that they are virtually identical. Thus, for these higher order rings to work well, a tuning mechanism might be necessary.

Higher order ring responses with fabrication error In order to understand the higher order ring responses, 2nd order ring responses were analyzed theoretically to determine the effect of fabrication error on the response of the ring. Figure 4-25 shows the effect of not having the exactly identical ring resonance positions in a multi-ring filter. Here we see that the doubly peaked resonances observed in the Intel fabrication process (figure 4-24) are well predicted. An estimate can be made of the difference in the resonance frequencies of the two rings since it is just the difference in the peak positions of the doubly peaked responses. From figure 4-24 the difference in the resonance peak positions is 4 nm which corresponds to a difference in circumference of 0.25%.

It is however, more difficult to explain the sharper response of the ring resonances shown in figure 4-23. If the 2 ring system is not symmetric, the coupling and hence the Q of one ring will be different from the other. This scenario is calculated in figure 4.3.3. Thus, the resonance of a 2 ringed system will look sharp and narrow if the gaps of the rings are not symmetric.

SOI Ring

The largest Qs were measured on SOI rings. In fact, a Q of 14000 was measured, with a FWHM of 0.1 nm. There is some difficulty interpreting these high Q result since the line-width of the resonance is masked somewhat by the 0.2 nm Fabry-Perot resonances, especially in the case of SOI material. Due to the low loss nature of the SOI waveguide, the Fabry-Perot resonances are extremely strong. Fabry-Perot resonances can be shown

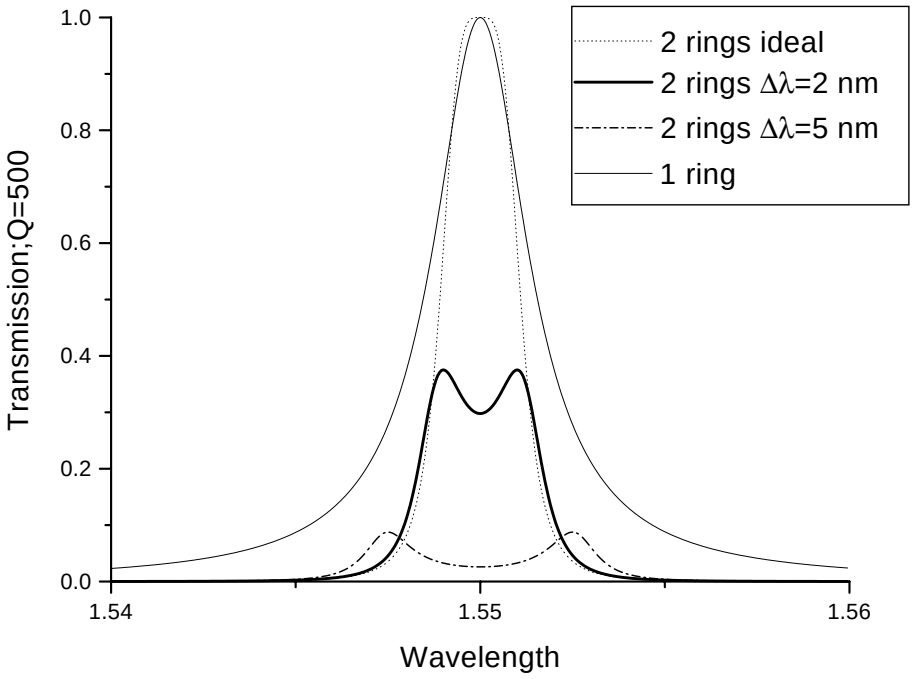

Figure 4-25: Ideal ring resonances with Q=1000 for 2 rings showing the effect of offset resonances. In this figure, the ring Qs are identical and their coupling efficiencies are the same. With offset resonances, the response of a double ring becomes a doubly peaked response which explains the observation in figure 4-24.

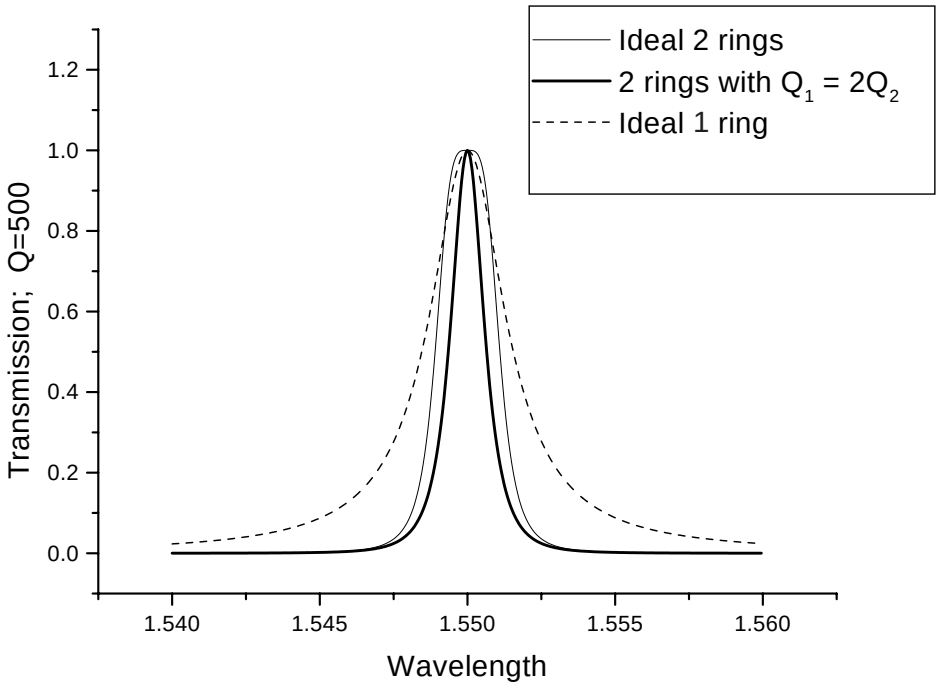

Figure 4-26: Ideal ring resonances for 2 rings with differing Qs or coupling strengths. In the calculation, one ring was assumed to have a Q of 1000 while the second had a Q of 2000. The resulting response is not a flat top resonance but is instead a sharply peaked response which is narrower than the Q=1000 response

analytically to affect the measured external Q. A 0.1 nm FWHM Lorentzian response was overlapped on top of a 0.2 nm Fabry-Perot noise. Depending on the position of the peak with respect to the Fabry-Perot response, the measured line-width changed from 0.08 nm to 0.26 nm. On the other hand, it is believed that the 14000 number is close to the true external Q of the ring. Using Q of 14000, a loss of 14 dB/cm was extracted and is consistent with the loss of 10 dB/cm which was extracted from the Fabry-Perot resonances.

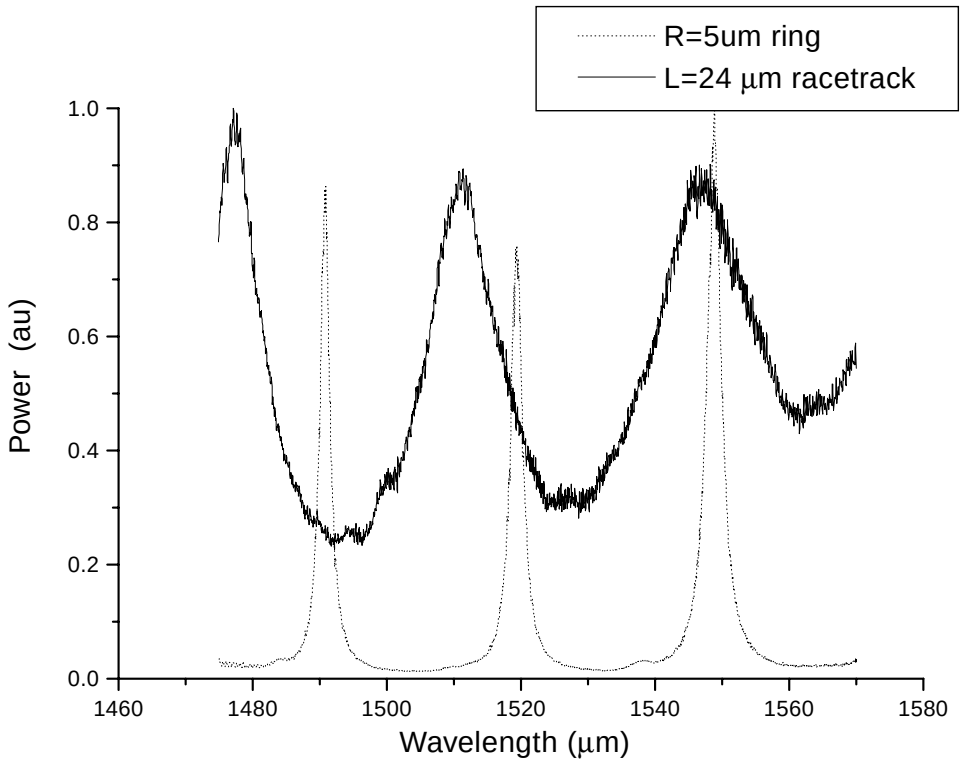

Figure 4-27: Ring vs. racetrack drop port response for silicon nitride. Due to the very strong coupling between the nitride waveguides, the Q of the racetrack is much smaller than the Q for the ring

Silicon Nitride rings

Silicon nitride rings were fabricated from the same 0.5 μm wide by 0.8 μm high PECVD waveguides studied in the previous chapter.

Ring vs. racetracks A comparison between the ring and racetrack resonances with the same gap size and approximately the same path length is shown in figure 4-27. Due to the much larger coupling region for the racetrack, the Qs for the racetrack are much lower than the Qs for the ring.

Q vs. Radius The ring responses as a function of radius are shown in figure 4-28. The Qs decreased as a function of decreasing radius of curvature, indicating that loss is the limiting factor of Q. If loss were not limiting, Q should increase with decreasing radius of curvature since the coupling becomes weaker as radius decreases, due to the increase in $\Delta\beta$ as the radius decreases.

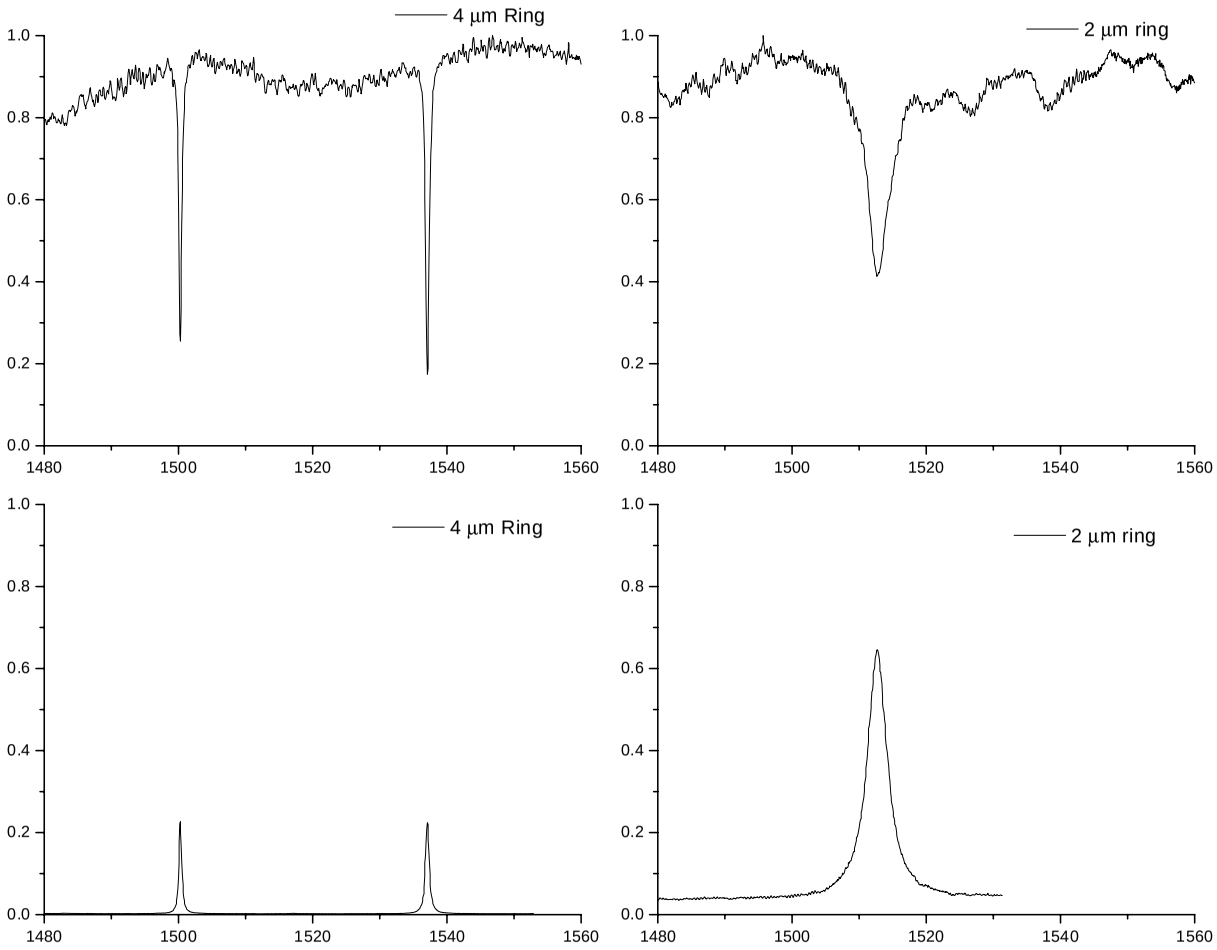

Figure 4-28: Nitride ring response as a function of radius. Similar to what was observed in polySi rings, the FSR increases and the Q decreases with decreasing radius, indicating that the rings are in the loss limited regime.

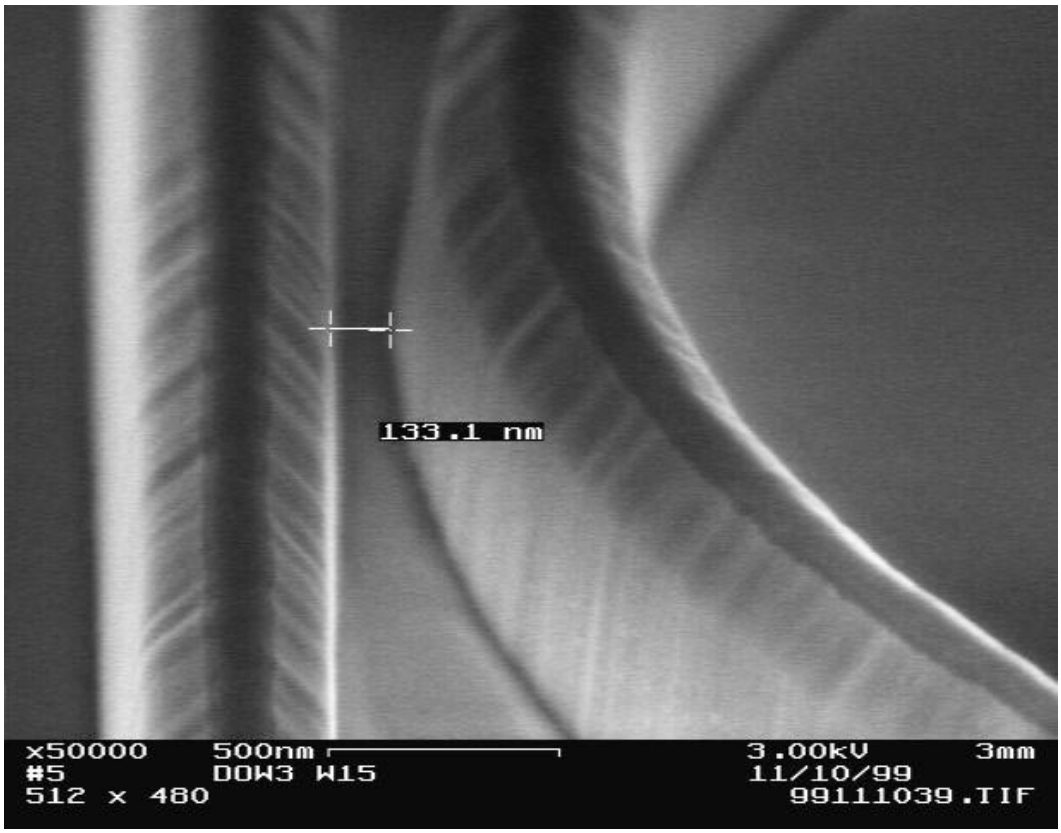

Figure 4-29: SEM of a lithographically defined nitride gap. As a result of mask erosion, the side-walls are not vertical. To get the correct predicted Q, it is necessary to use the correct cross-section of the waveguide. This excess etching may explain why the calculations consistently underestimated the silicon nitride external Qs. (See figure 4-9)

Q vs. Gap From the theory section earlier in this chapter, the Q of the ring is a strong function of gap size, if the coupling Q is much less than the loss Q. The latter regime of operation is important if the efficiency of the ring is to be high. In the case of the silicon nitride system, the effect of gap on Q is shown in figure 4-30. Note that the lithographically defined gap (figure 4-29) is different from the designed gap. The Q of a silicon nitride ring response is a much weaker function of gap than expected which is probably an indication of the fact that the Qs are loss limited.

Higher ordered filters The best higher order, especially third and fourth order ring filters that have been reported have been in silicon nitride rings. Figure 4-31 shows the second third and fourth order filters with the signature of more rapid roll off. The second and fourth order ring filters showed a narrowing of the filter characteristic and a flat top passband.while the third order ring filter showed spectral broadening with three distinct

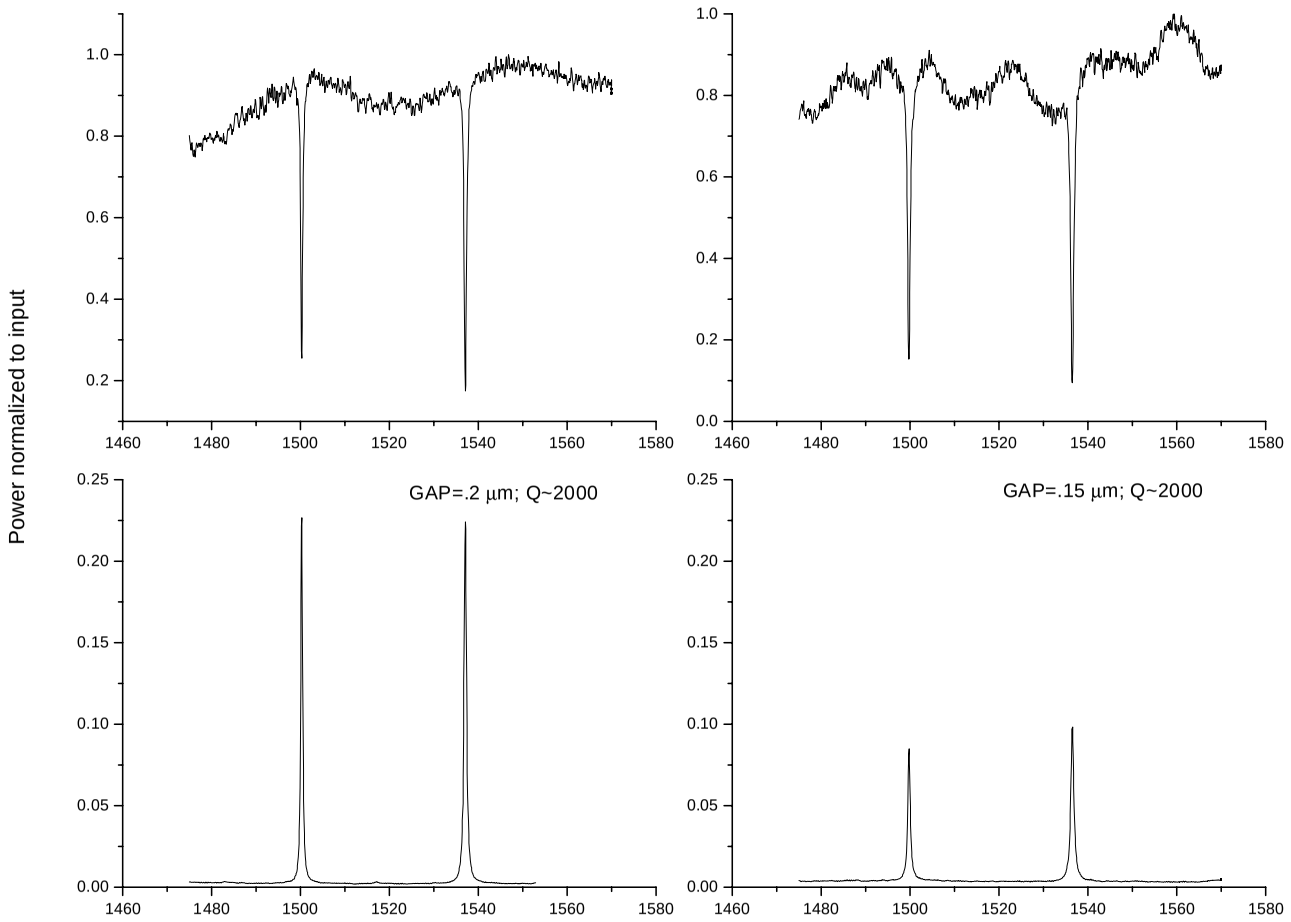

Figure 4-30: Nitride ring response as a function of designed gap distance. Since the ring sizes are the same, the FSRs are approximately the same: 35 nm. Unlike the polySi rings, the Q is independent of the gap size, meaning the rings are loss limited.

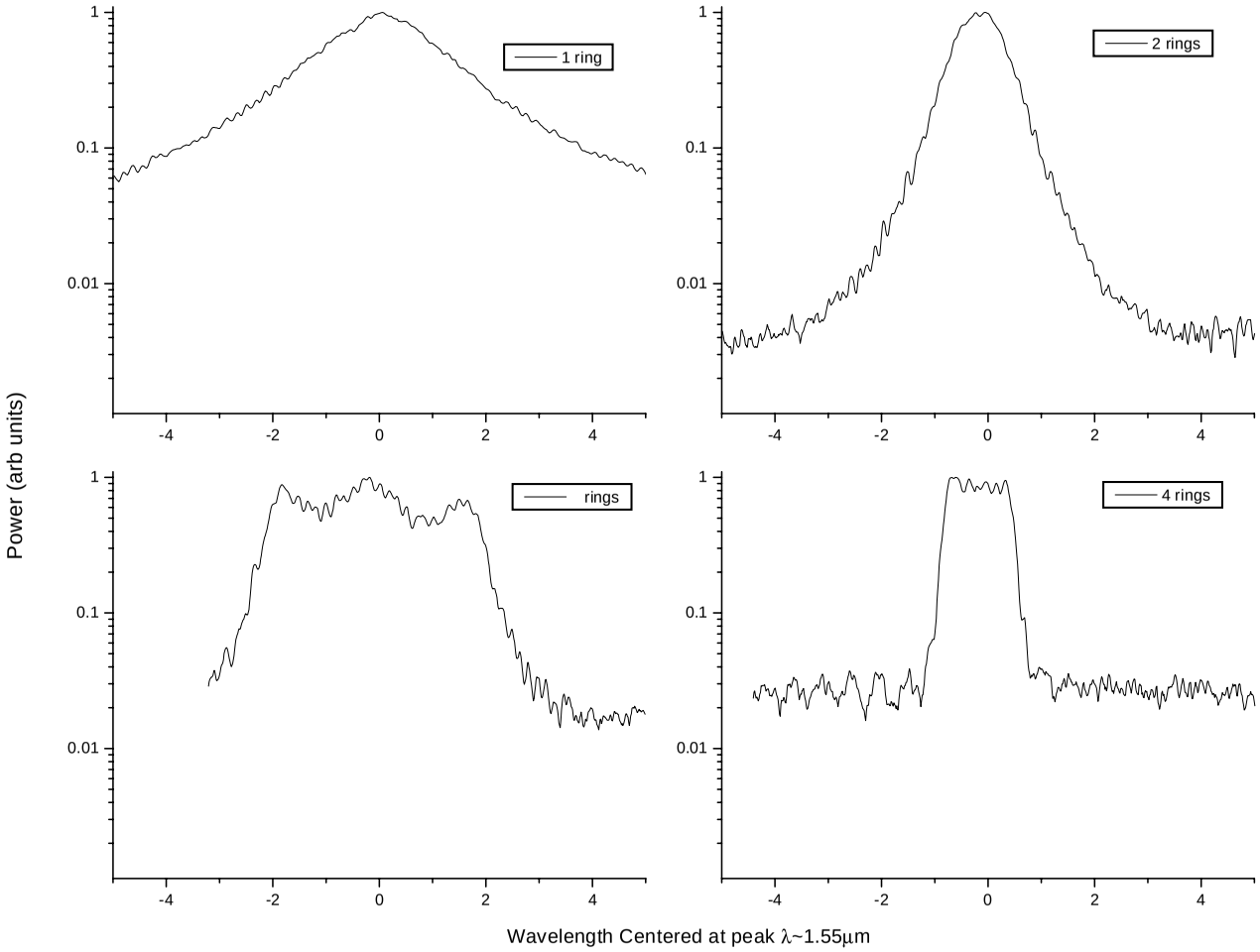

Figure 4-31: Higher order silicon nitride ring filter responses. The second and fourth order filter response is much narrower than the first order response. The third order filter has three distinct peaks possibly due to having three rings of different resonance positions as a result of the inherent asymmetry of this device. The roll-offs of the first, second, third and fourth order responses were close to their respective theoretical 6, 12, 18 and 24 dB/octave roll-off.

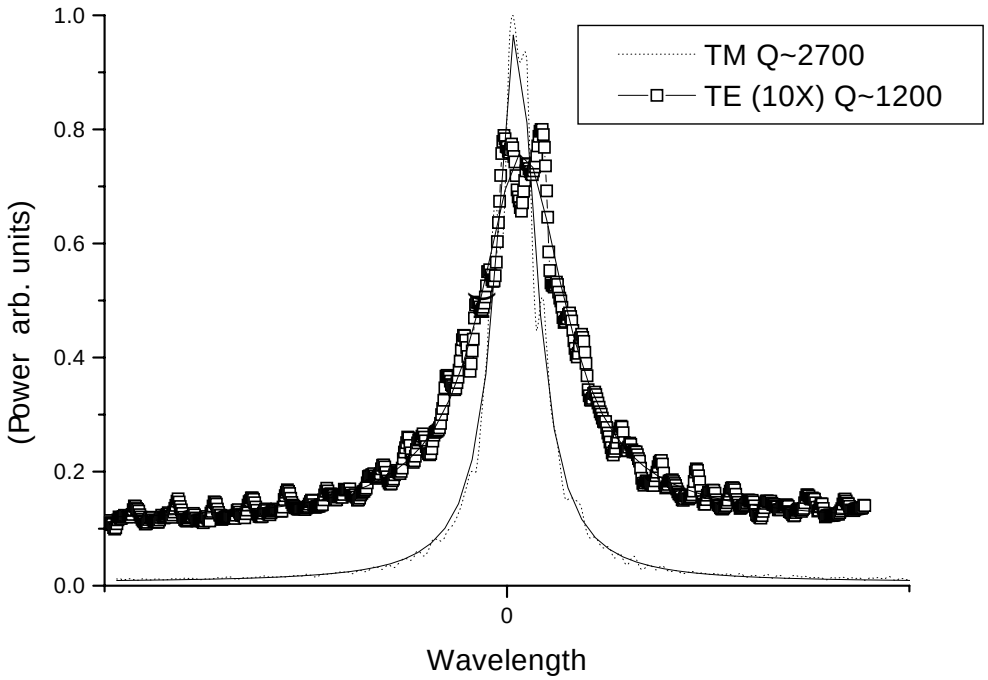

Figure 4-32: Nitride ring response as a function of polarization. The TE mode had a higher loss than the TM mode, so the Q, as expected, is lower.

peaks. The roll-offs of the first, second, third and fourth order responses were close to their respective theoretical 6, 12, 18 and 24 dB/octave roll-off.

The efficiency of power transfer to the drop port resonances of these rings are, however, on the order of 10%. This is a combination of the intrinsic loss of the fabricated 5 μm radius ring and a slight variation of the ring resonance with wavelength.

Polarization dependence Figure 4-32 shows the nitride ring response as a function of polarization. The waveguides that were fabricated had both TE and TM modes. Due to the asymmetry of the waveguide, the TM mode is less lossy and this is reflected in there being a higher Q for the TM mode. If we can fabricate to 1% tolerance we can bring the TE and TM to within 0.1 by increasing the width of the nitride waveguide.

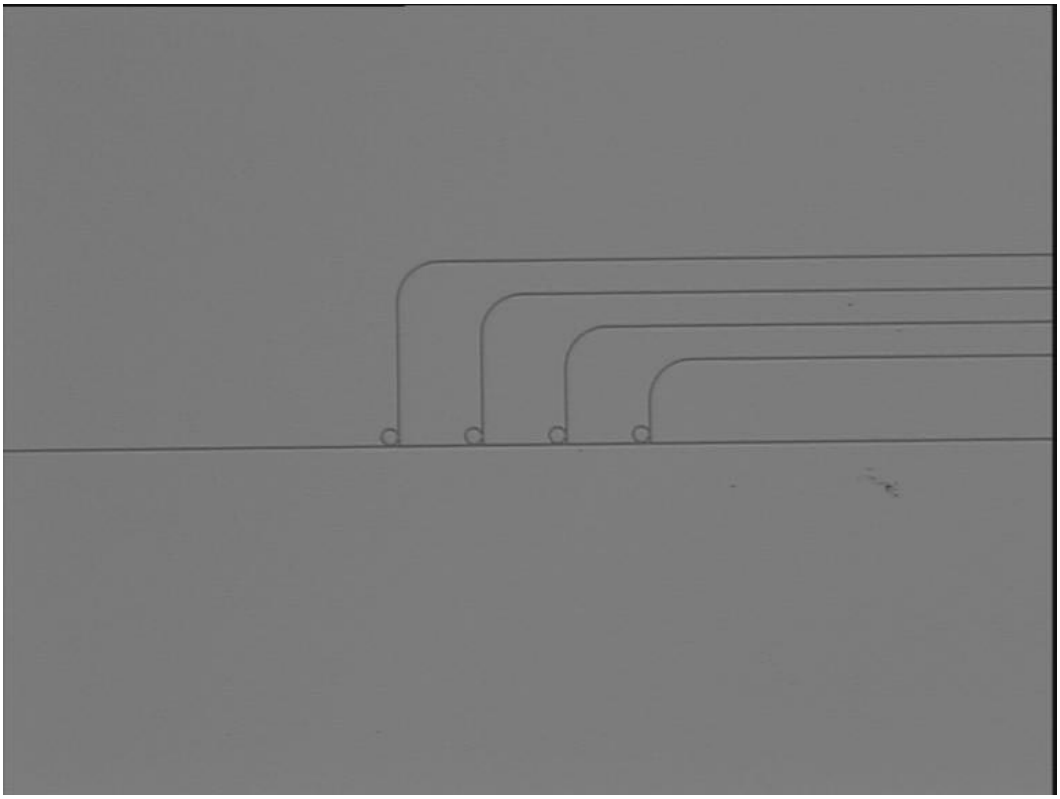

Figure 4-33: Micro-graph of 1x4 WDM. Light enters from the left and on ring resonance drops into one of the four drop waveguides through the ring

4.4 WDM demultiplexers

Wavelength Division Multiplexing is a recent trend in fiber optic communications. It involves multiple colors of light to encode signals, each color being a separate channel. This enables the upgrade of embedded fiber systems to much higher bit rates than they were initially designed for. WDM demultiplexers are one component of WDM schemes. These devices take an incoming stream of light with several channels and split them into their component channels. An example of a WDM layout based on rings is shown in figure 4-33. This is a device with four 5 μm radius rings each differing in size by 0.4% in radius. This represents a channel separation of approximately 4 nm which in turn puts a limit on the free spectral range (it has to be greater than (4-1)x4 = 12 nm) and the Q, to ensure that the channel separation is several times the width of the line. Using similar analysis as in

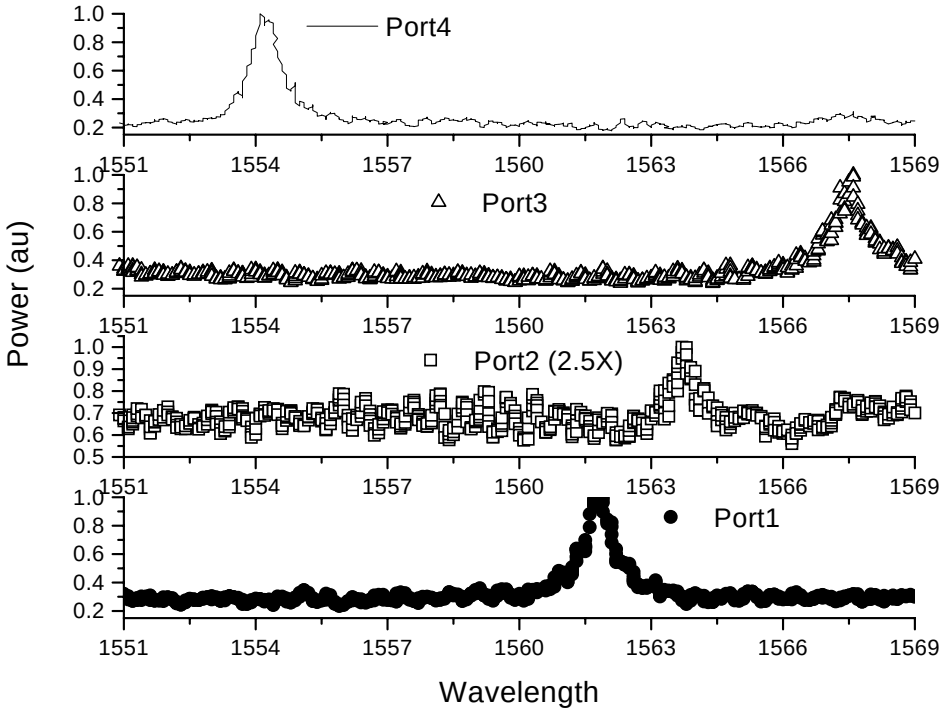

Figure 4-34: Output spectra of a 1x4 WDM based on rings implemented on silicon. Channel spacing= 4 nm. FWHM $\approx$ 0.8 nm

(4.66), the channel spacing may be found:

$$\frac{\Delta\lambda}{\lambda} = \frac{\frac{\Delta R}{R}}{1 - \frac{\lambda}{n_{eff}}\frac{dn_{eff}}{d\lambda}} \tag{4.84}$$

These WDM demultiplexers were fabricated both in silicon and silicon nitride strip waveguides. A Q value of 1850 was extracted for fabricated polySi rings with a channel separation of 4 nm. A Q value of 850 was extracted for fabricated silicon nitride rings with a channel separation of 4 nm. There is a tradeoff between having a small Q for fabrication tolerance so that the desired channel is dropped and a large Q for minimum WDM filter channel cross-talk. An analysis will be presented in the next chapter.

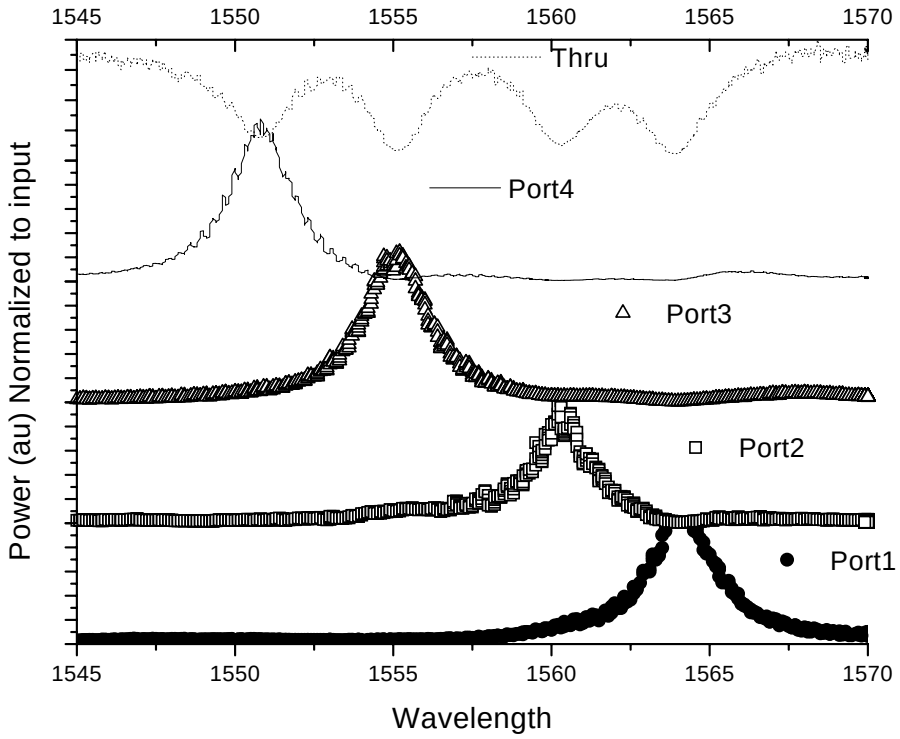

Figure 4-35: Output spectra of a 1x4 WDM based on rings implemented on silicon nitride. Channel spacing= 4 nm. FWHM $\approx$ 1.8 nm

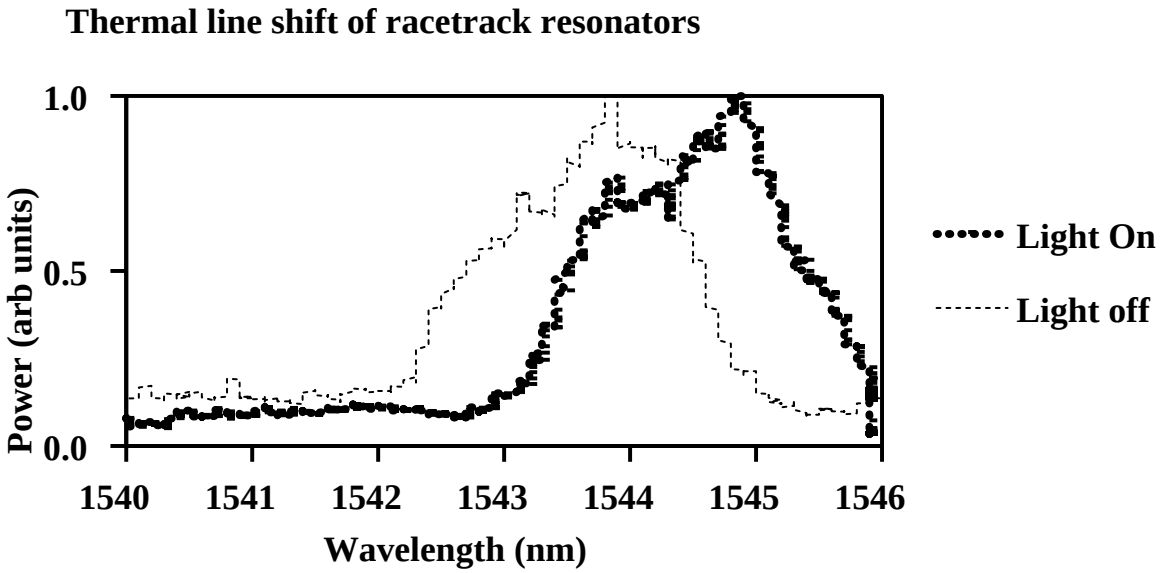

Figure 4-36: Thermo-optic modulation of a single silicon racetrack filter using an 810 nm light source to heat the substrate. A 1 nm shift was observed.

4.5 Ring based switches

4.5.1 Thermal switches

In chapter 3, it was shown that heating can change the resonance position of a ring. Heating the micro-ring, has been reported previously [91, 92, 73]. Here we study the time response of thermal effects.

To study the effect of thermal tuning on these polySi rings, an 810 nm laser light source was focussed on the rings. This irradiation resulted in heating of the substrate and the effect of the heating is shown in Figure 4-36, with the line red shifting by 1 nm. Heating can change the index of refraction of the silicon by $4\text{x}10^{-6}\text{K}^{-1}$. Thermal expansion of the ring is also possible and the coefficient of thermal expansion of silicon is $3\text{x}10^{-6}\text{K}^{-1}$. The combination of both effects would correspond to a temperature rise of 45K. An alternative explanation of change of index by electron-hole injection, would require an injection level of 10^{18} cm^{-3}. When silver paste was used to thermally ground the device, this modulation disappeared, confirming that it is thermo-optic in its mechanism.

Frequency response of optically activated thermal switch Using the set up in figure 3-15, a ring was illuminated by a 1W 810 nm laser. This laser was modulated at speeds from 1 to 100 kHz. 1550 nm light was coupled into the ring and a wavelength scan

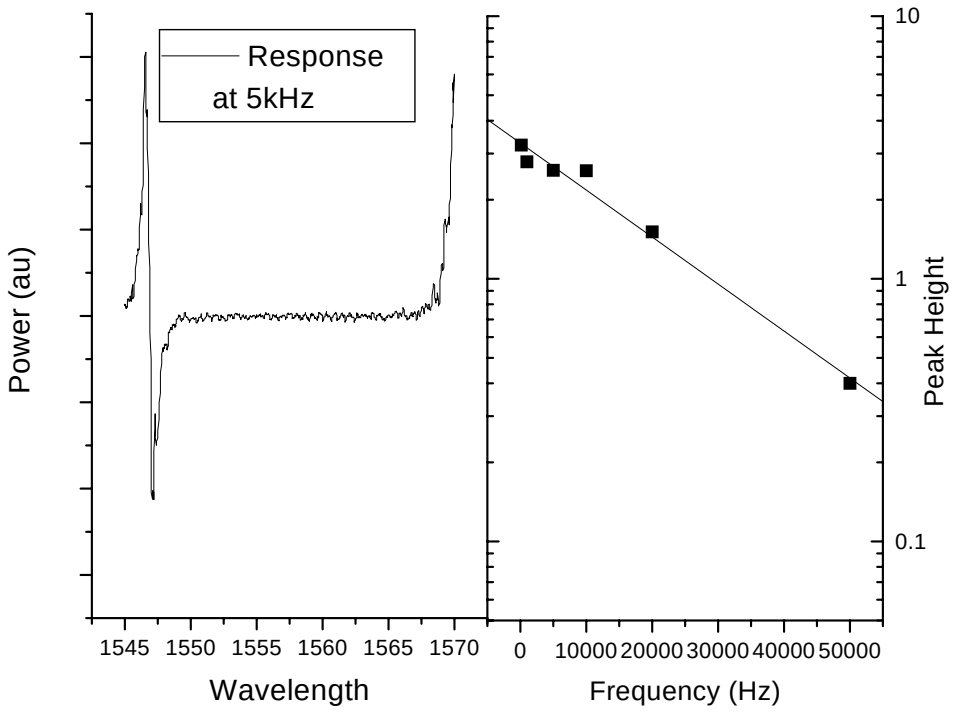

Figure 4-37: Plot of frequency response of thermal modulation.

was taken at the drop port of the ring. The drop port signal was locked in the modulation of the 810 nm light and a scan was taken. The response is plotted in figure 4-37 and shows a thermally activated change in line position that has response out to 50kHz.

4.5.2 Micro-mechanical switch

A micro-mechanical switch may be used to tune and detune a ring resonance. An experiment was run to study how this might work. The drop spectrum of a silicon 30 μm circumference racetrack was analyzed. The drop spectra was taken before, during and after a fiber was lowered into contact with the surface of the racetrack. The graph in figure 4-38 shows the ring resonance line red shifts when the fiber was lowered and then restored after the fiber had been raised. There was hysteresis and broadening of Q due to loss (probably due to dirt on the fiber). The theoretical line-shift can be found by estimating the effective indices of a silicon racetrack with and without a top silica cladding. These indices were found to give an effective index change of 0.8%, which corresponds to a line shift of 12 nm. The fact the line-shift was much smaller than that indicates that the fiber was not in intimate

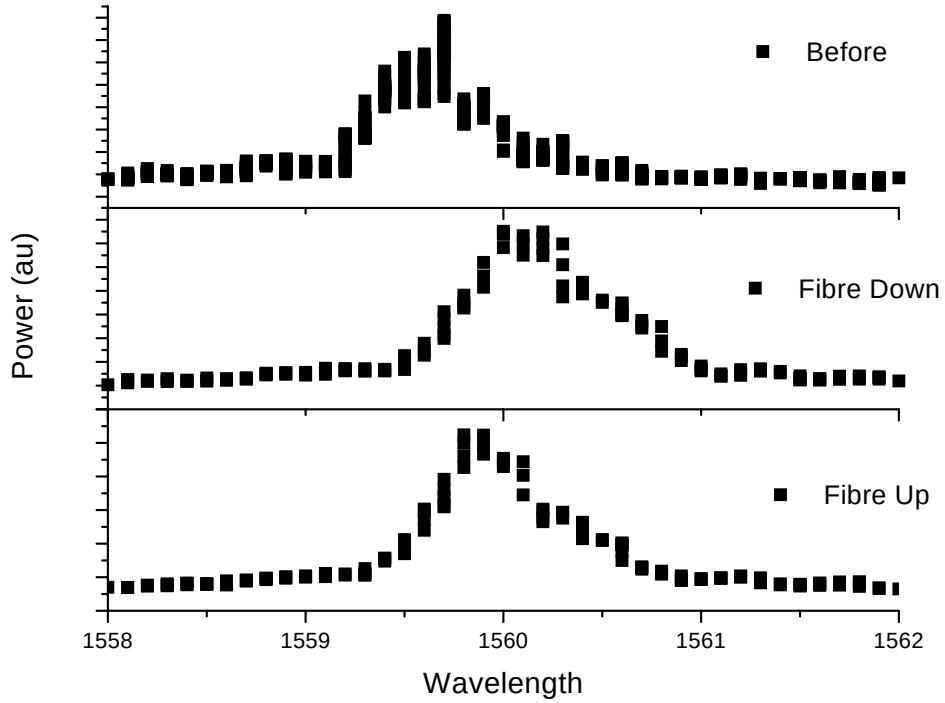

Figure 4-38: Before, during and after lowering the fiber onto a silicon ring. When the fiber is down the effective index increases and the resonance position red shifts by 0.5 nm. When the fiber is raised the line relaxes towards its initial position. The hysteresis is probably due to dirt.

contact with the ring. However, this experiment shows that, it is possible to shift the line of the ring without destroying the ring. This in fact may be another method of tuning the rings.

4.5.3 Ring based modulator

A ring, coupled to input and output waveguides, acts as a micro-cavity. One could therefore envision a modulator in which free carriers are injected into the ring to change the effective index of the ring either by changing the real part of the index or the imaginary part i.e. absorption. In the first effect where the real part of the index is changed, one would expect that the resonance line would shift; the second effect of changing the absorption, would result in the quenching of the power transfer to the ring. [42]

An estimate can be made as to the index change required to result in a sufficient shift in the line to result in modulation: it has to be on the order of $\frac{n_{eff}}{Q}$. Thus, for cavity with Q of 1000 in silicon, the index change has to be about 0.01, which corresponds to about 10^{19} cm^{-3} injection. A higher Q of 10000 will result in a smaller index change requirement of 0.001 resulting in an injection requirement of say 10^{18} cm^{-3}. Note that at carrier injection levels of 10^{19} cm^{-3} absorption effects might dominate and power transfer to the ring may be limited.

From the previous chapter, power dissipation of a horizontal p-n diode integrated into a 1 μm radius, 30 μm circumference racetrack would be 360 mW; the power dissipation of a vertical p-n diode integrated into a 1 μm radius, 30 μm circumference racetrack would be 240 mW!

Contacting rings on the side-wall

Intuitively, the best place to contact a ring is on the outer side-wall, that is the side-wall, with the smaller bending radius. See figure 4-39. With an outer radius of 1.25 μm and a copper thickness of 0.1 μm on the inner radius, a Q_l of 1000 is possible. If the copper thickness is 0.2 μm a Q_l of 380 is possible. Note that while the Q_ls are somewhat respectable, this is not yet a practical device since two metal contacts are needed to allow current to flow through the ring and any metal on any of the other surfaces would quench the Q_l. There are two geometries of contacting a ring/racetrack resonator which would be practical and would increase the Q_l. The first is to take a ring with larger radius and place 0.5 μm long

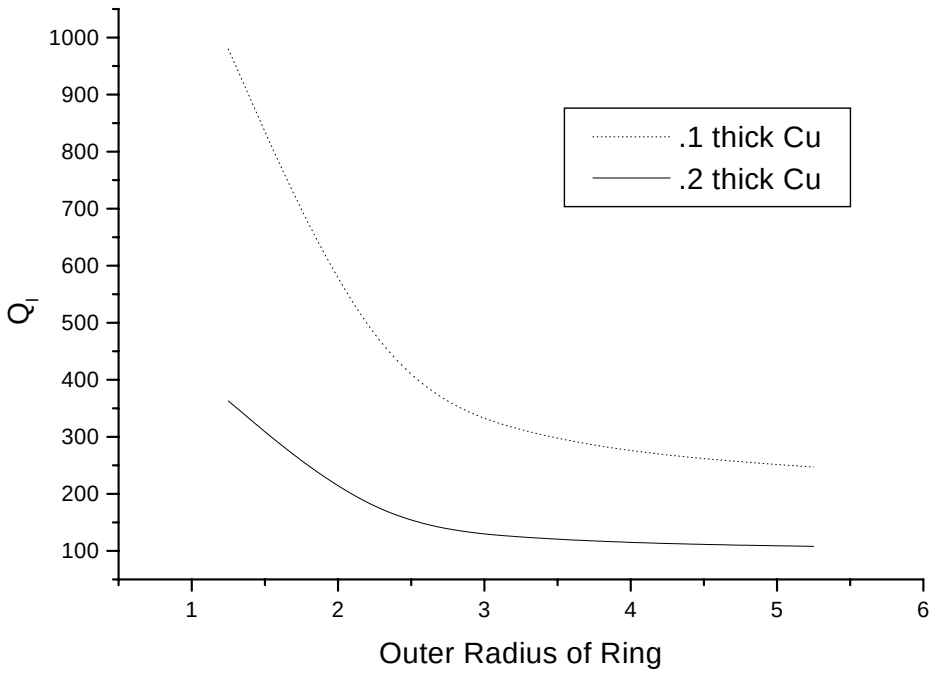

Figure 4-39: Plot of Q_l vs ring radius contacted on the inner radius of a ring. Even with metal on the sidewall, Q_l of 1000 is possible. See figure 4-40 for a field profile. As the radius decreases, the field sticks less to the outer wall and starts interacting with the metal on the inner wall. Hence, the loss increases.

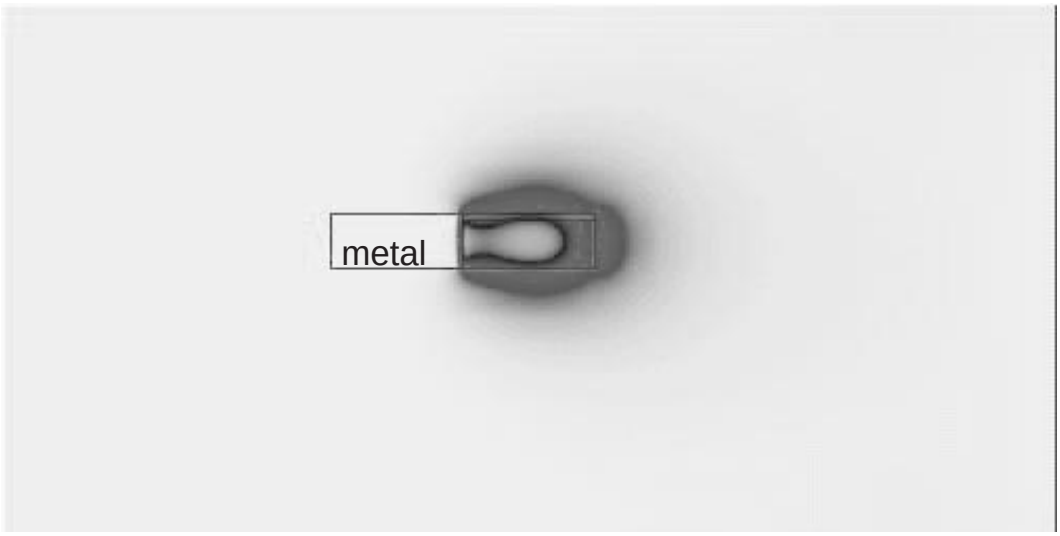

Figure 4-40: Field profile side-wall contacted silicon waveguide. Q_l of a ring so constructed would be 1000. Note the large perturbation of the field.

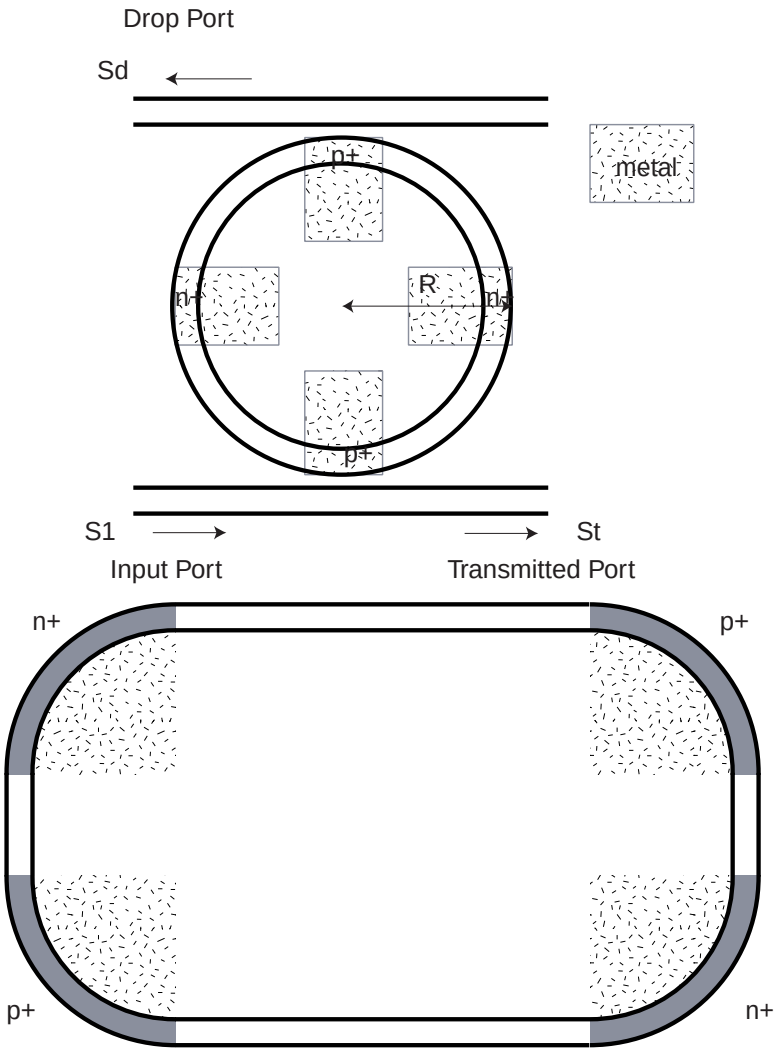

Figure 4-41: Schematic of a ring and racetrack contacting schemes

contacts on the inside wall of the ring. One of the problems with this method is that light may be coupled into the backward propagating wave. A second method would be to use a racetrack with small sharp bends at the corners. See figure 4-41 and 4-42. This would allow the use of low loss bends. Unfortunately fabrication of these side-wall contacted waveguides are difficult and would require CMP. The field profile of a side-wall contacted waveguide is shown in figure 4-42.

Contacting the top surface

When the top surface of a ring is contacted, an optimization can be made. The first is to realize that the top surface is much larger than the side-wall, and in fact the entire top

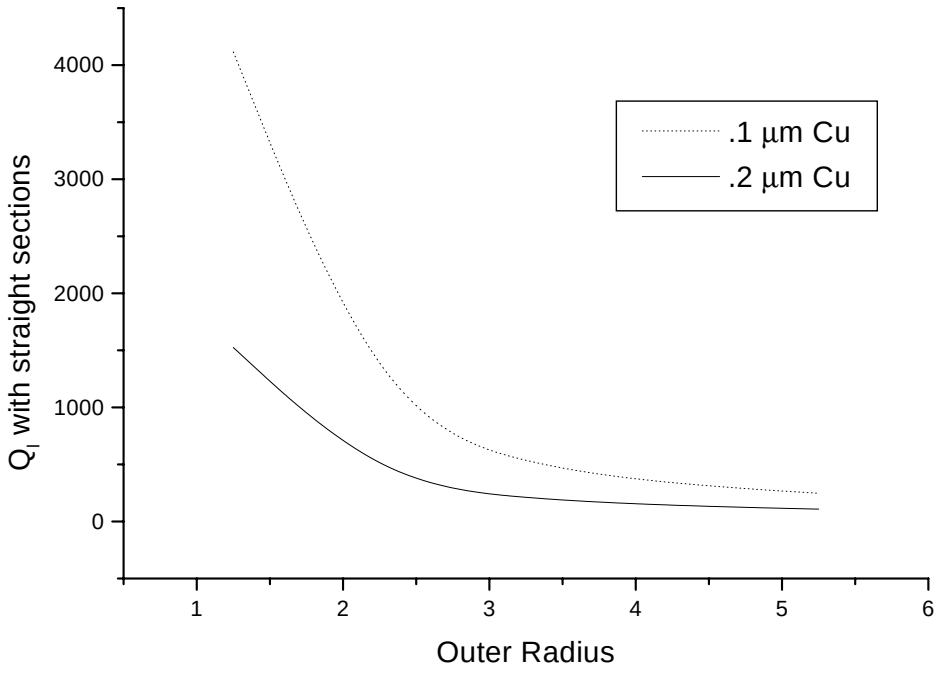

Figure 4-42: Plot of Q_l vs ring contacted on the inner radius of a racetrack. The circumference of the racetrack is chosen to give the same FSR as a 5 μm radius ring. The longer resonator cavity increases the Q_l since the loss per round trip is conserved but the path length per round trip is increased.

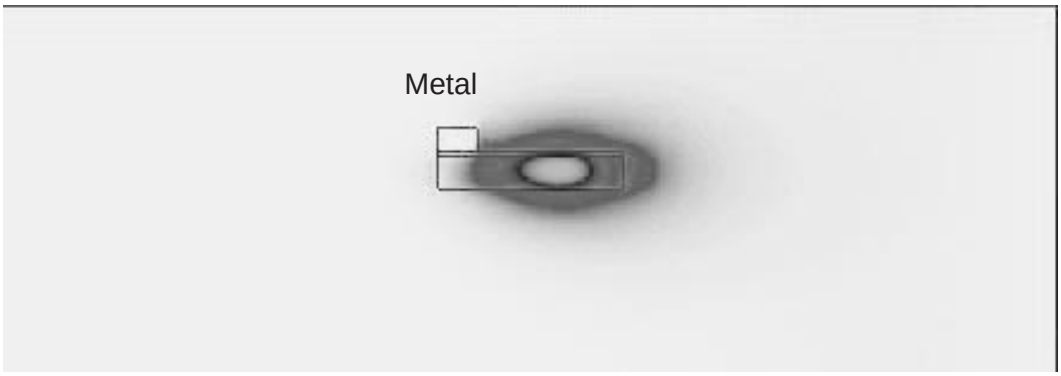

Figure 4-43: Field profile top contacted silicon waveguide with width of 0.7 μm. The wider width means the waveguide is multi-moded. However, the presence of the metal attenuates all but the fundamental mode rapidly. The Q_l of TE_0 mode is 10000. The Q_l of all the other modes are less than 100.

surface need not be contacted. The inner portion of the top surface can be contacted and since the field in the ring tends to squeeze into the outer wall, the losses of such a waveguide would be minimal. In fact, with proper design a loss Q, Q_l of 10000 can be obtained with a 1 μm radius ring. This ring would have a width of 0.7 μm and a metal width of 0.2 μm on the top of the inner radius of the waveguide. The reason why a larger width can be used is the presence of the metal which increases the loss of all the higher order modes which would otherwise have propagated in a metal-less waveguide. The loss Qs of the higher order modes are less than 100. If the racetrack idea is used to lengthen the round trip circumference, loss Qs of 40000 can be generated! These results are summarized in figure 4-43.

4.5.4 Optical injection of carriers into rings

In this experiment an above band-gap laser was used to illuminate a silicon ring generating electron hole pairs. The change of the position of the resonances of the rings was measured as a function of frequency of modulation. Unfortunately the effects which were seen were largely thermal, again due to the fact that the critical power density for observable electro-refraction was not reached. All the effects which were seen were thermal, the results of which were summarized in chapter 3.

4.6 Microspheres

Microspheres are 3-dimensional analogs to 2-dimensional micro-disks and micro-rings. Whispering gallery modes in the microsphere give the microsphere high quality factors. In fact, Q values of 10^{10} for silica microspheres have been measured [84, 85] in vacuum. In air, Q values of 10^8 have been measured. Silica microspheres have particularly high Qs because they can be fabricated with few surface imperfections and low absorption losses. Applications of microspheres include micro-laser [86], narrow band filters and sensors.

The main problem with silica microspheres is that it is very difficult to couple light into and out of the sphere, due to the high Q and the low effective index of the mode. Successful coupling into and out of microspheres has been demonstrated using tapered optical fiber and fiber prism coupling [93, 94]. These methods are, however, not robust, and for practical deployment of microspheres, integration with planar waveguide technology would be best.

In this section, work on coupling microspheres to ULSI compatible silica ARROW waveguides is reviewed. This work was a collaboration with J.P. Laine and B.E. Little in Professor H.A. Haus' group [7, 8, 9].

4.6.1 Coupling to a microsphere [7]

The problem of coupling to a microsphere is similar to the problem of coupling to a micro-ring. Looking at the analysis to derive κ for a micro-ring, one can determine the optimal conditions to get good and efficient coupling into a microsphere. Recall equation (4.59)

$$|\kappa| = \int_z \chi[z] \exp[-j\Delta\beta z] dz \sqrt{\frac{v_g}{2\pi R}} \tag{4.85}$$

for the coupling coefficient for a ring. The main factors which contribute to the strength of coupling are the size of the spatial coupling coefficient $\chi[z]$ and the size of the phase mismatch between the mode of the bus waveguide and the mode in the microsphere $\Delta\beta$. Thus, for maximum coupling efficiency $\chi[z]$ must be large which means the overlap integral for the mode of the microsphere and the mode of the input bus most be large. More importantly, the phase mismatch $\exp[-j\Delta\beta z]$ must be minimized. The phase velocity of a silica microsphere is close to the phase velocity of silica fiber and silica waveguides.

Silica waveguides which are used in silicon optical bench technology would be optimal if they could be used to couple light into a microsphere. However, the requirement for a thick

cladding on the bottom of the waveguide to optically isolate the waveguide from the high index contrast substrate and the resulting requirement of a thick top cladding to ensure the propagation of a mode, implies that this waveguide would have a mode which is "insulated" from an impinging microsphere.

The approach developed in the collaboration was to use a SPARROW waveguide which was described in the previous chapter. Such a waveguide has a anti-reflective alternating high and low index contrast quarter wavelength reflecting stack that would allow for a low loss air clad silicon oxide waveguide. This arrangement would enable the close proximity of a mode of the SPARROW to a mode of the microsphere with the added advantage that the modes would have very close effective indices. Note that the effective index of the lowest order mode of a SPARROW waveguide is smaller than effective index of the fundamental mode of the sphere. Hence the SPARROW waveguides will tend to excite higher order modes of the sphere [8].

4.6.2 Fabrication

The fabrication of SPARROWs was described in Chapter 2. Microspheres are fabricated by iteratively arc-melting cleaved or etch tapered fiber tips. The surface tension of the molten silica pulls the silica into a sphere. The diameters of the spheres were approximately 400 μm, with effective index of the fundamental mode of about 1.43. These spheres were coupled to the SPARROWs guides with widths of 4, 6, 8 and 10 μm, with effective indices on the order of 1.38 to 1.39.

4.6.3 Experimental set-up

The experimental set-up used a laser diode with a piezo-controlled Bragg grating to dither the wavelength over a range of 0.24 nm with a resolution of approximately 0.002 pm. A Fabry Perot etalon was used to stabilize the measurement system and to calibrate the resonance line-widths. The SPARROW waveguides and microspheres were mounted on high resolution stages to allow for fine adjustments. Finally a fiber lens was used to couple light into the waveguide while an objective was used to collect the output light.

4.6.4 Q and efficiency measurements [8]

A power extraction efficiency, defined as the ratio power of the depth of the resonance to the transmitted power, of 95% was extracted with a Q of approximately 0.5x10^8. See figure 4-44. A lower Q sphere exhibited an even more impressive power extraction coupling efficiency of 98.4%.

Note that the power coupled in this way is lost. An estimate of the loss Q can be found from equation (4.50). Since there is no drop port the term $\frac{1}{\tau_d} = 0$. Then the ratio of the power transmitted to the power incident at resonance ($\omega = \omega_o$) is given by

$$\left|\frac{s_t}{s_i}\right|^2 = \left(\frac{\frac{1}{\tau_l}}{\frac{1}{\tau_l} + \frac{1}{\tau_t}}\right)^2 \tag{4.86}$$

Using the relations (4.36) and (4.25)

$$Q_l = \frac{Q_m}{\sqrt{\left|\frac{s_t}{s_i}\right|^2}} \tag{4.87}$$

Thus, the sphere with 95% extraction efficiency and with a Q_e of approximately 0.5x10^8 has a Q_l of 2x10^8, while the sphere with 98.4% extraction efficiency and with a Q_e of approximately 1x10^6 has a Q_l of 8x10^6. Note that in the absence of loss, or at least in the case of the loss Q being much bigger than the external Q, the power transmitted is 100%. These deep resonances imply that the external Q must approach the loss Q of the sphere. It is important to realize that in the microsphere coupling measurements, the power extraction efficiency is an important number to consider. The reason for this is that it is very difficult to get light coupled into the sphere. Most coupling techniques that can excite the microsphere mode, exhibit coupling efficiencies which are on the order of a percent to tens of percent. In the case of lower power extraction efficiencies, the power could be coupling in and out of the microsphere with low loss due to the external Q being much smaller than the loss Q, or it could be that the coupling between the sphere and the waveguide/fiber is so weak that light is just not extracted efficiently. If, however, by changing the coupling parameters a large amount of light is extracted from the waveguide at resonance, then this result is indicative of very efficient coupling. The lack of such an operating point on the other hand is indicative of external Q being so large that it is always completely dominated

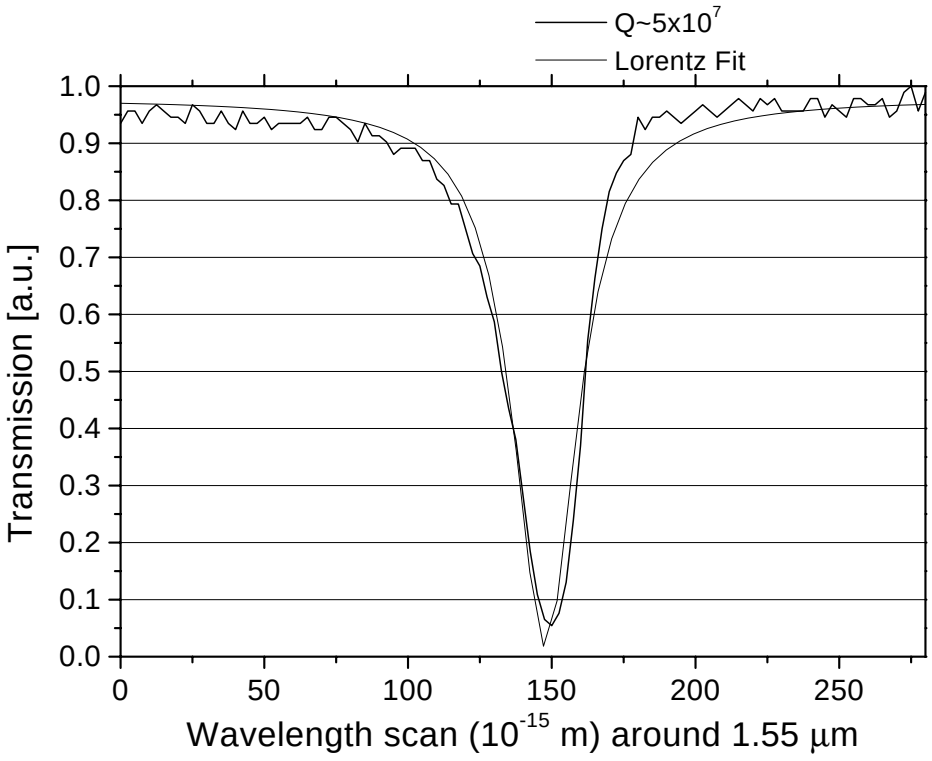

Figure 4-44: High Q microsphere resonance with >90% coupling efficiency measured by a SPARROW waveguide.

by the loss Q. Finally, in filter or sensor applications, the presence of such a deep resonance is useful since it is easily detected with high signal to noise ratio.

Mounting One of the main advantages of the SPARROW method is the possibility of mounting the sphere to the waveguide chip to create a practical device. The main problem so far is that electrostatic forces and van der Waal's forces attract the sphere to the SPARROW waveguide. Thus, this puts a lower bound on the standoff distance between the sphere and the SPARROW waveguide, which in turn limits the dynamic range of this device.

4.6.5 Microsphere response as a function of position

The microsphere was translated both vertically with respect to the SPARROW waveguide and horizontally across the waveguide. Each of these translations are now considered in turn.

Q vs. gap distance [8]

The plot of the microsphere resonance line-width as a function of vertical distance is shown in figure 4-45. There is an exponential decay in the line-width with increasing vertical displacement from the SPARROW waveguide. This displacement is measured from a piezo-controlled micro-positioning system with feedback, which has an approximately 10 nm accuracy. The exponential fit is expected since the coupling is evanescent. Since the evanescent tails are exponential and the coupling coefficient is a function of the amplitude of the evanescent tail, the coupling coefficient κ is an exponentially decaying function. Thus, from (4.16), $\tau_e = \tau_d = \frac{2}{\kappa^2}$ and $Q = \frac{\omega\tau}{2}$, both τ and Q are exponentially increasing functions of gap distance. The line-width $\Delta\lambda$ is given $Q = \frac{\lambda}{\Delta\lambda}$, which leads to the conclusion that line-width should indeed by an exponentially decaying function of gap.

Mapping of modes [8]

The plot of the line-width as a function of lateral displacement across the width of the waveguide is shown in figure 4-46. The figure shows a periodic undulation of line-width with respect to waveguide position. These undulations in the line-width in fact are a mapping of a polar-mode field profile [95]. At this juncture is is important to recall that the effective index of th SPARROW mode is lower than the sphere fundamental mode, so

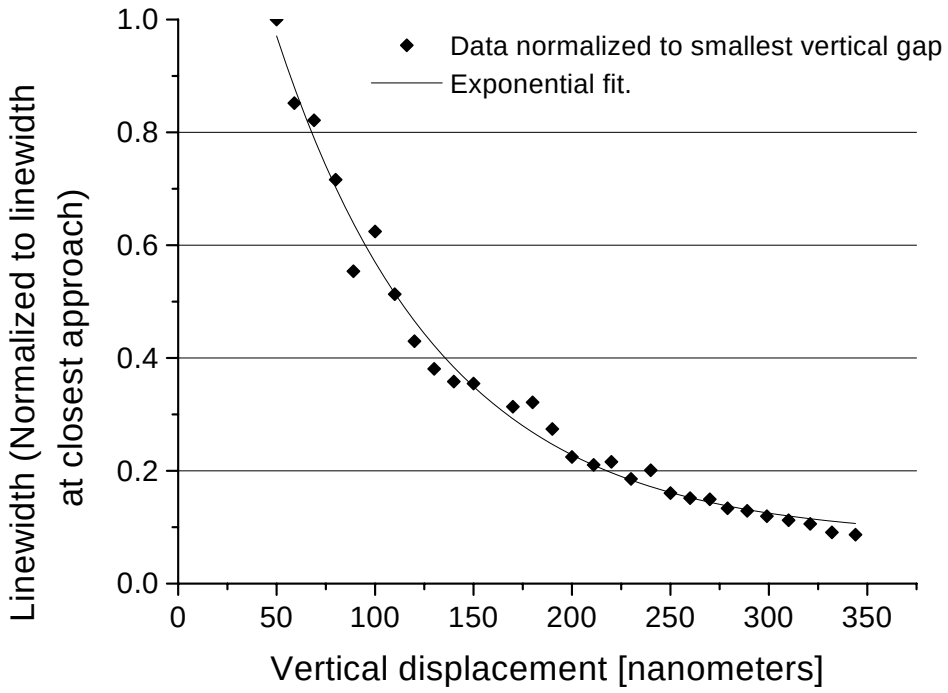

Figure 4-45: Microsphere resonance vs. gap. As expected, the line-width, which is inversely proportional to Q, is a decaying exponential as displacement increases.

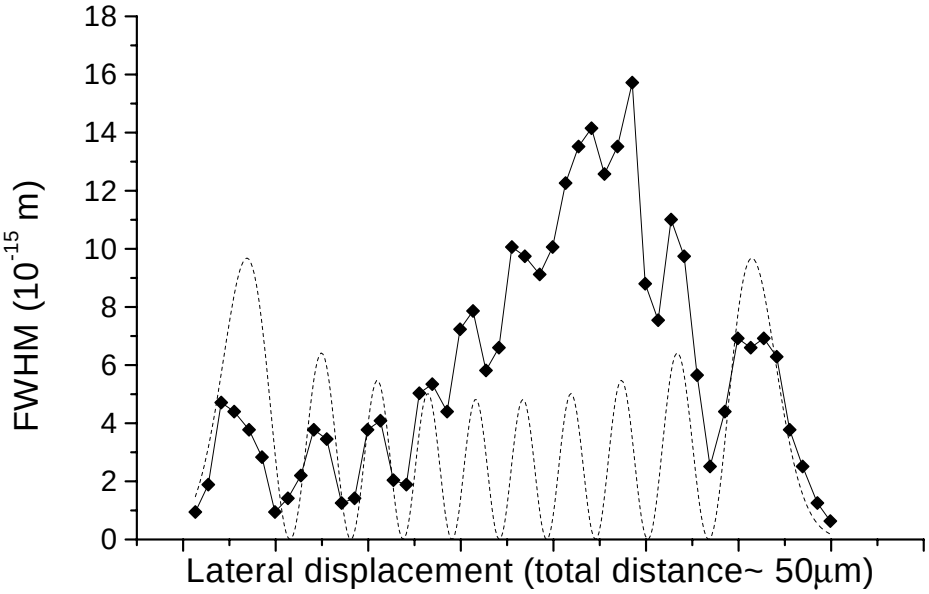

Figure 4-46: Line-width vs. lateral position of sphere across the waveguide. The dotted line is a fit of an ideal high order polar mode.

the SPARROW excites higher order modes. If the sphere and the SPARROW were perfect, all the sphere radial modes that can be excited would be degenerate and the line-width the periodic undulation behavior shown in figure 4-46 would not be exhibited. The lifting of the degeneracy due to imperfections allow such a mode to be mapped by near field microscopy [95]. Moving the sphere across the waveguide effectively changes coupling constant since the overlap integral between the split sphere modes would be maximal at the maxima of the radial mode of the sphere which would in turn correspond to the region of largest line-width.

4.6.6 Channel dropping characteristics [9]

A microsphere was coupled to two almost parallel SPARROWs, as schematically illustrated in figure 4-47. The drop and transmission spectra of a microsphere are shown in figure 4-48. Light was coupled from a fiber lens into the first waveguide which shall be termed the transmission bus and light was detected at the end of both outputs. On microsphere

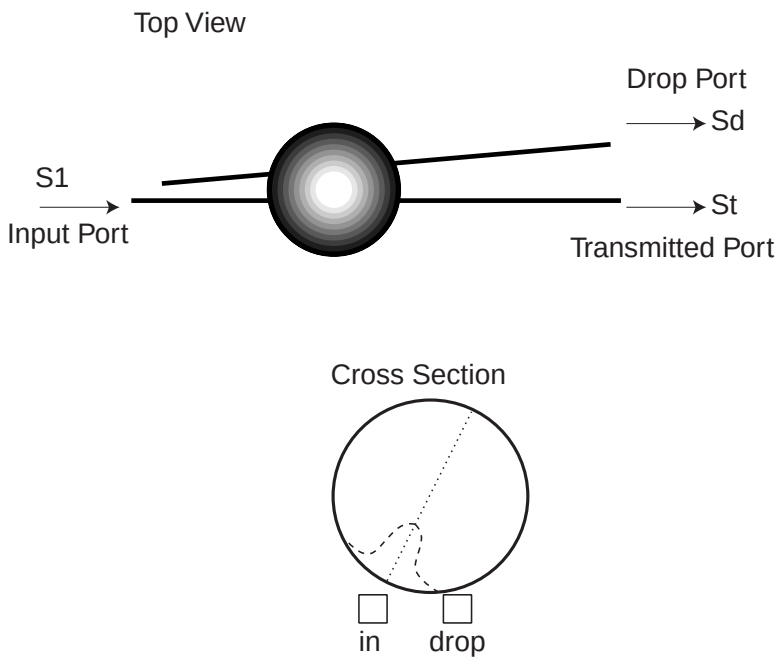

Figure 4-47: Microsphere channel dropping filter schematic. Power enters through the input port. On microsphere resonance, a polar mode is excited and the field evanescently couples into the drop port. Otherwise, the power leaves via the transmitted port.

resonance, the light is coupled from the bus waveguide into the sphere and excites a whisper gallery mode which goes around the great circle of the sphere [96]. Most of the power would go into the mode which has approximately the same direction as the transmitted wave, to preserve the phase matching condition. Since this is a high order polar mode, the extent of its field is large and it can couple into an adjacent waveguide. Thus, the system is very similar to the case of a ring resonator with following exceptions. The first is that the "dropped" light on resonance is propagating in the same direction as the light in the transmission waveguide. The reason this is that the adjacent drop waveguide is on the same "side" of the sphere, with respect to the mode, as the transmission waveguide. The second difference between the sphere and the micro-rings and micro-racetracks described previously, is that the assumption that the system is symmetric is almost certainly not true. This difference in coupling coefficients between the sphere and the two waveguides results in the transmission Q being different from the drop Q. See equations (4.51) and (4.50). Using these equations it is possible to extract τ_l, $Q\tau_d$, τ_t or equivalently Q_l, Q_d, Q_t. (4.51) and (4.50) give two equations based on the power at resonance. An additional equation can be generated by substituting $(\omega - \omega_o) = \frac{\omega}{Q}$ into (4.51). The Q values extracted are:

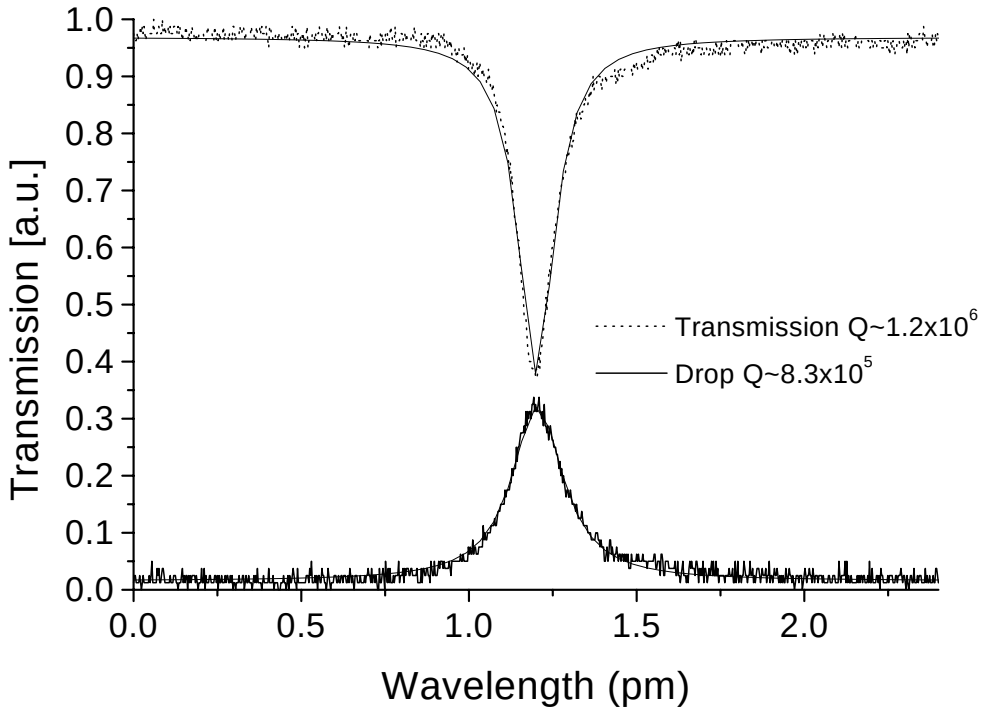

Figure 4-48: Microsphere channel dropping filter response. The Q of the drop port is smaller than the transmitted port due to the asymmetric coupling configuration.

$Q_l = 4.3 \times 10^6$, $Q_d = 4.5 \times 10^6$ and $Q_t = 8.3 \times 10^6$. The loss and loaded Qs are consistent with values extracted previously for the single ring case.

4.6.7 Micro-cavity Sensors

An example of a micro-cavity sensor is the microsphere coupled to an ARROW waveguide, which may act as an accelerometer; see figure 4-49. Suspending a microsphere above the ARROW waveguide by fixing its stem to the chip. The microsphere can now act as an accelerometer. If force is imparted on this chip, the sphere will move towards or away from the waveguide due to inertia. This small movement can be picked up a change in line-width as shown in figure 4-45.

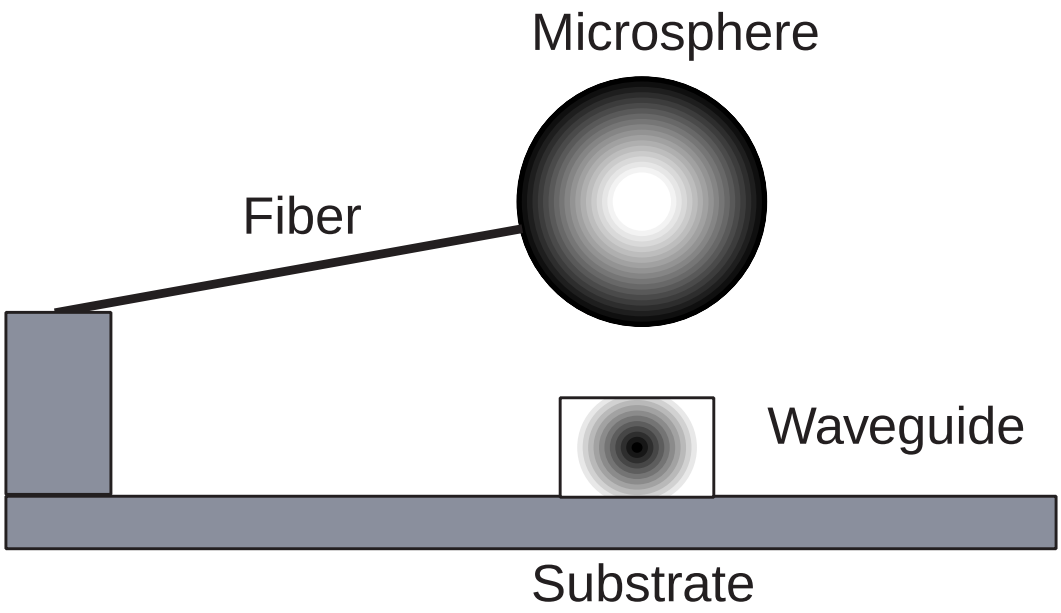

Figure 4-49: Schematic of microsphere accelerometer. When the system is accelerated, the fiber deflects due to inertia and the microsphere either moves towards or away from the waveguide, resulting in a change in microsphere resonance line-width.

4.7 Summary

In this chapter, ULSI compatible waveguide structures integrated with micro-resonators have been studied. Qs of 10^4 and efficiencies close to 100% were achieved in high index contrast ring resonators and Qs of 10^8 were achieved in microsphere resonators. Higher order ring resonances exhibit flat top responses and the expected higher roll-off in resonance. More importantly, a thermal tuning mechanism for micro-rings was demonstrated. In addition, 95% coupling efficiency between a SPARROW waveguide and a microsphere was achieved.

Several integrated silicon micro-photonic devices were reviewed. Integrated optical switches that operate at several kHz can be made out of thermally activated micro-ring resonators. ULSI compatible high speed GHz modulators have been designed but are difficult to fabricate. 1x4 wavelength division multiplexing devices have been for the first time demonstrated in high index contrast silicon and silicon nitride strip waveguide systems. Finally, the high sensitivity of optical components to their surroundings and to small length changes were used to build highly accurate and sensitive force sensors.

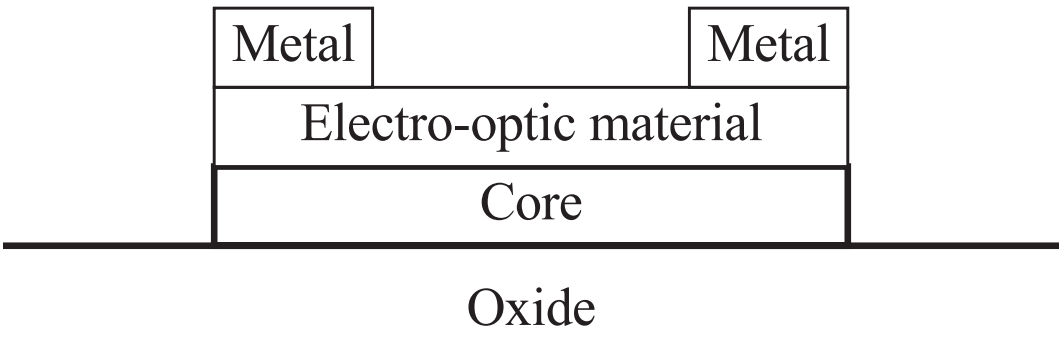

Figure 4-50: Schematic for electro-optic effect in rings

4.7.1 Future work

Rings Although effective ring action has been demonstrated, the efficiency of the rings is still not very high. 100% efficiency has been measured for silicon racetracks but the efficiencies of silicon and silicon nitride rings are only between 10% and 25%. This shows that the loss Qs are on the same order as the external Q of these devices. On the other hand, if the designs are such that the external Q of these devices are less than the loss Qs, much higher efficiencies can be obtained. Finally fabrication errors are still too large to make the rings without tuning. This problem should be tackled both from the fabrication standpoint and the tuning standpoint. With this problem solved, multi-ringed responses should be much better.

One scheme to modulate the rings, proposed with Professor Kimerling, would involve depositing an electro-optic material as the cladding material of resonators in high index contrast waveguide system; see figure 4-50. An example of such a system would be a silicon waveguide with a LiNbO3 cladding. Switching action is obtained by applying a modest voltage across a short distance near the resonator. This would change the index of the cladding and hence the effective index of the mode in the resonator. This change of effective index would in turn result in a change in the position of the resonance line. Since an electro-optic effect is used, this device would be very fast.

Microspheres Although mounting of a microsphere on a chip with ARROW waveguides has been demonstrated, there have been some difficulties with mounting the sphere a small distance form the waveguide. Van Der Waal's and electrostatic forces attract the sphere to the waveguide. Hence this problem needs to be addressed for SPARROW integrated

microspheres to become useful.

Another interesting experiment would be to make the ARROW out of silicon oxynitride (n_{eff} $\approx$1.5), which would enable coupling to sphere modes of only the highest effective index (lowest order modes).

Filters The designs of the current 1x4 WDM demultiplexers in silicon and silicon nitride were not optimized. Attempts should be made to fabricate working devices that meet a channel spacing design and a cross talk specification. Further, it is important to integrate some tuning mechanism for the rings since the wavelength of resonance of the rings and hence the drop wavelengths are all currently fabricated open loop. As mentioned earlier, small errors in fabrication can move the line positions by several nm. Some analysis should be made to determine if multi-rings are necessary to minimize channel spacing and cross talk.

Chapter 5

Conclusion

In this thesis, a study of a spectrum of technologies required for integration of devices in silicon microphotonics is presented. For silicon microphotonics to materialize, discrete components such as waveguides and filters need to be integrated with more complex devices such as switches and modulators to form complete systems.

5.1 Systems design & integration

In this section, some of the applications of ULSI compatible integrated optics are studied from a high level. Issues with respect to integrating the various components into these applications are discussed. The four systems applications which will be reviewed are:

1. Optical clock distribution
2. Optical input and output for chip to chip communication
3. On chip optical communication
4. Integrated optics applications for fiber optic networks

Each of these systems applications will be discussed in turn.

5.1.1 Optical clock distribution

The idea of optical clock distribution is based on the fact that as chips sizes get larger and clock speeds get faster, clock skew requirements becomes so stringent that electronic clock distribution at speeds above several GHz become difficult. This problem is compounded

by the fact that it is difficult to predict the load on the clock circuit. This difference in the loading as well as the propagation delay down the clock interconnect results in clock skew problems. Significant clock-speed improvements in future ULSI technology can be hampered in the future by skew and power requirements.

In optical clock distribution, a rapidly modulated signal is launched down an input waveguide. The signal is then split and detected at the end points corresponding to local electronic clock distribution cells. The number of the clock distribution end points will depend on the size of the local optical to electronic clock signal circuitry as well as the optical clock generation system.

Optical clock distribution schemes which have been proposed include

- hybrid schemes detection schemes
- free space
- illumination from back using sub-band-gap light
- holographic imaging

One possible system is a series of single mode, silicon nitride waveguides integrated into small mode matched silicon or polySi detectors. This system would have the advantage of using silicon detectors because above band-gap light can be used. Since this wavelength could affect any underlying electronic circuitry by photo-generation, the light should be waveguided, ruling out the free space illumination methods. A further advantage of waveguiding is that the field intensities are high so the detectors can be extremely small and fast. The requirements for the integrated optical clock distribution system proposed above are:

- good waveguide system
- high efficiency detectors
- low power, high gain, low noise amplifier circuits to amplify detector photo-current. In addition, it is helpful to have an
- on-chip light source and high speed modulator, although the requirements may be satisfied with
- off-chip source, nitride waveguides and silicon detectors at 632 or 860 nm.

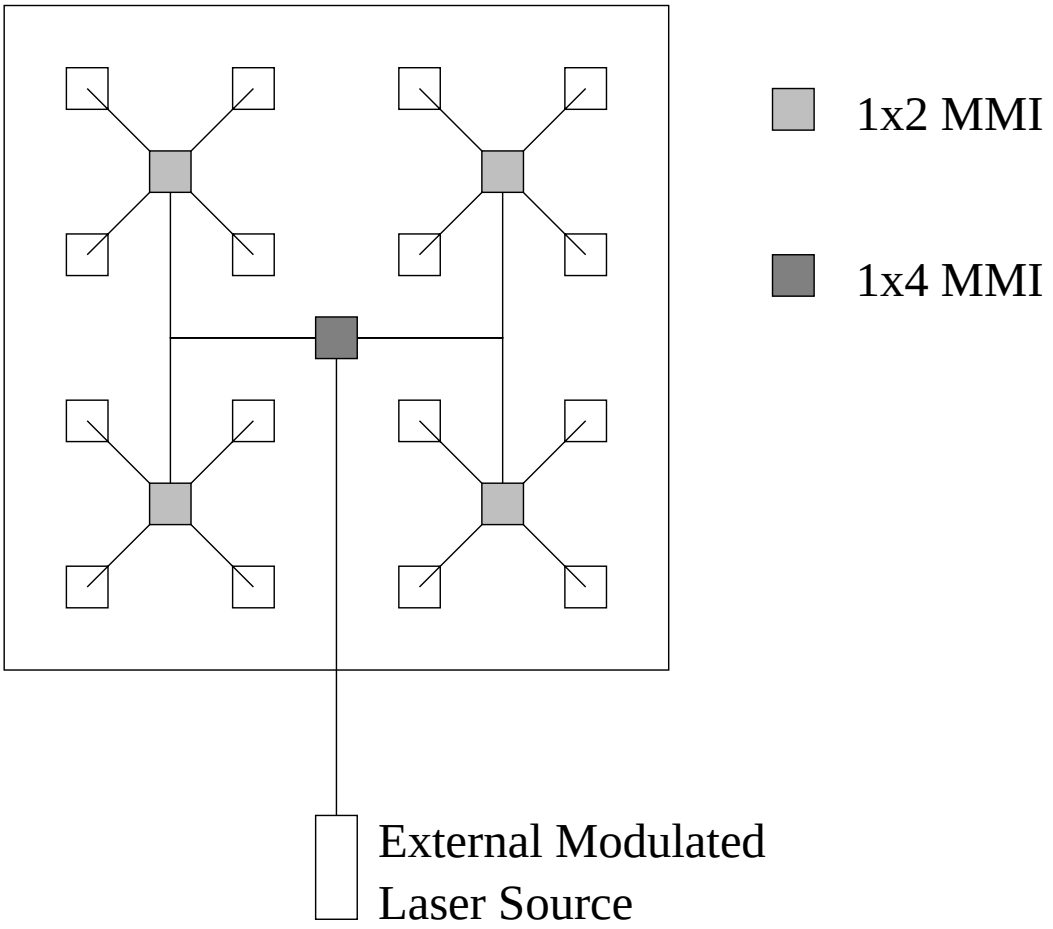

Figure 5-1: Schematic of optical clock distribution.

The main advantage of such a scheme is that the clock can be run as fast as the detector circuitry can be run. Long electrical lines can be eliminated, reducing digital noise and cross talk due to field and power coupling that would have otherwise occurred in these lines. The optical portion of the clock is essentially load-less, so the clock generation circuit can be decoupled from the load [97, 13, 98].

Experiments In a collaboration with S. L. Sam and Professor Chandrakasan, a chip with an optical detector integrated into a receiver circuit was fabricated using a 0.35 μm process in MOSIS. S. L. Sam, designed and simulated a circuit that could trans-amplify 10 μA current to 1V voltage at speed of 1GHz. To design a detector in MOSIS, a lateral p-n junction was made, with a base width of 0.35 μm. In order to ensure that the detector could operate at 1 GHz, the entire detector and receiver circuitry was protected by a 1 μm layer metal with a 0.35 μm opening. Unfortunately this slit also causes diffraction of

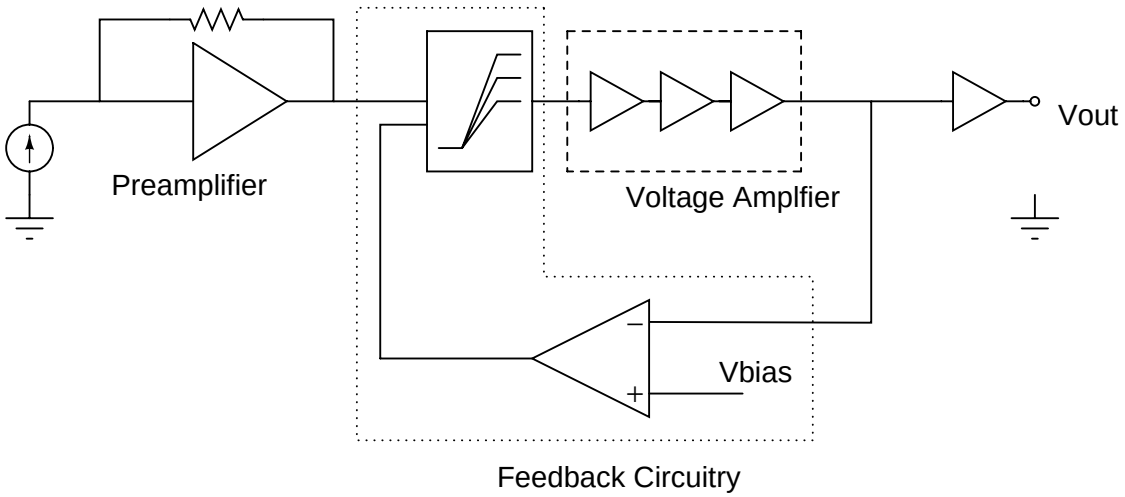

Figure 5-2: Schematic of the receiver circuit designed by Sam [99] and fabricated at MOSIS

the incoming optical signal, and attenuates the amount of power that actually reaches the detector. When tested with a 0.5 W laser, with a spot size of 200 μm X 200 μm, the output current was about 0.05 mA, which means that the detector responsivity was 0.1 mA/W. See figure 5-1.

Optically clocked latches Another idea that would be a quantum leap has been proposed in discussions with Professor Chandrakasan, was the idea of an optically triggered latch (see figure 5-3); an optical detector which is embedded in a latch can be used as on optical trigger to the latch. The advantage of this scheme is that it removes the need for an amplifier and is potentially very fast. The difficulty of this scheme is that there are about one million latches in a CPU. Each detector requires 50 μA to switch which implies that the total optical power required would be 50 W! One way around this would be to use a small duty cycle laser, like a short pulsed high repetition rate mode locked laser diode (MLLD). With a duty cycle of 1% the time averaged optical power that is required is reduced to 0.5W. At 10GHz, a 1% duty cycle pulse corresponds to a repetition rate of 100 ps and a pulse width of 1 ps.

5.1.2 Optical I/O for ICs

Optical data communications is a general class of systems in which data is brought on and off-chip via optical means. In figure 5-4, a WDM optical data communication system is shown.

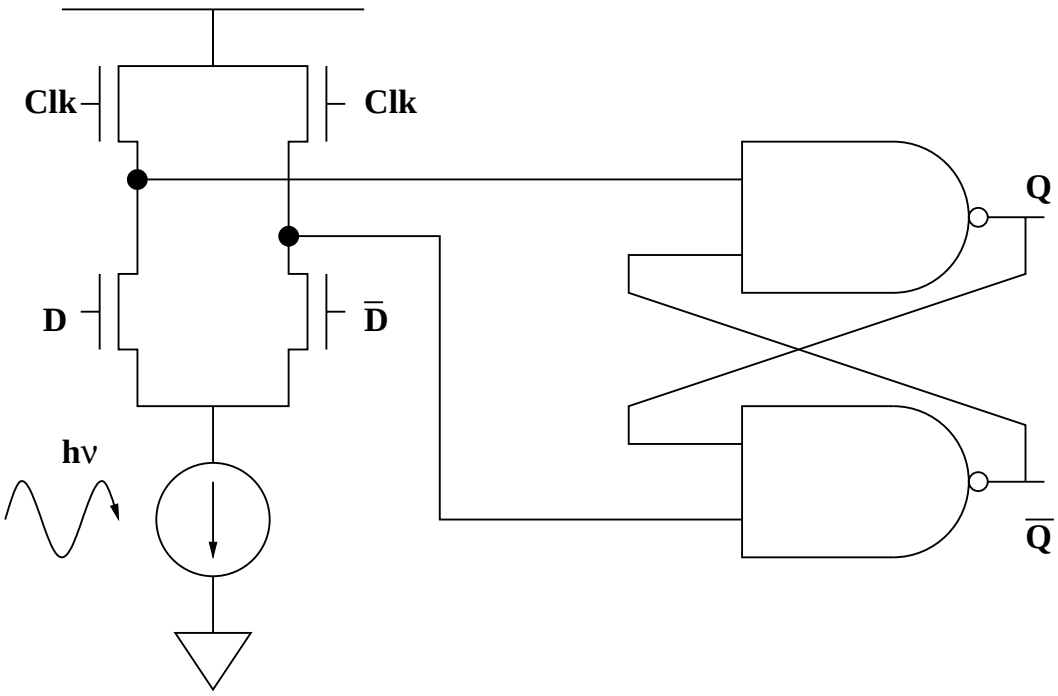

Figure 5-3: Million points of light. Schematic of on optically triggered latch [99]. The current needed to switch the latch is estimated to be 50 μA. Assuming 1 W/A sensitivity, the required incident optical power is 50 μW.

On-chip data communication requires the same components as the optical clock system mentioned before. In addition, this system requires the presence of an electro-optical modulator that can operate at the designed clock speed of the chip. This means that sub-band-gap light has to be used since it is difficult to design a modulator that can run at such high speeds with silicon nitride.

Current work has concentrated on a wavelength of 1.54-1.55 μm to take advantage of the Si:Er emission line. For an optical interconnect system, a monolithic light source would be useful but not necessary. Even monolithic light sources would require a modulator, so the major difference between the hybrid scheme and the monolithic scheme is cost. More work needs to be done on the annealing condition of Er in polySi. In addition, Er should be implanted in SOI rings since the implant and annealing conditions of SOI are better understood.

Analysis of optical vs. electrical interconnects The plot of the time delay of optical interconnect vs. electrical interconnects was derived by Zhang et al [99]. This is plotted in figure 5-5. The optical interconnect scheme used numbers derived by Sam et al (see previous

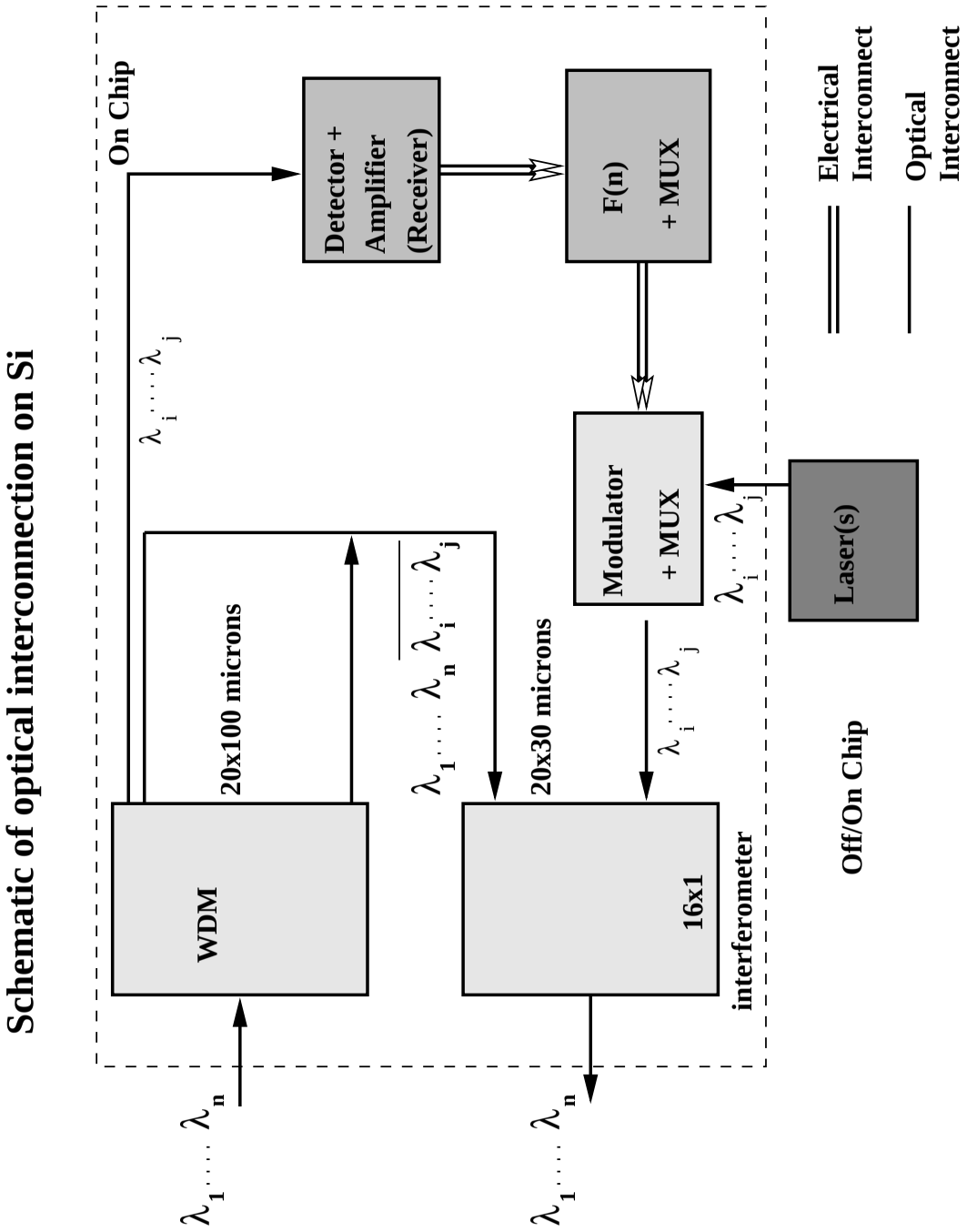

Figure 5-4: Schematic of optical data communication.

section) for the detector and an equal delay for the modulator. This data therefore, has the implicit assumption that the amplifier circuitry is made with a 0.35 μm process. With CMOS scaling, the amplifier speeds will increase, pushing the line for the optical interconnection down further. For interconnect lines of over 2 cm (e.g. chip to chip interconnects), there are definitely advantages to using optical lines.

5.2 Optical system on chip for Fiber Optic systems

The scheme for optical data communications also applies to integration with optical fiber systems. The key challenge would be to find a suitable fiber waveguide coupling scheme. Optical fiber systems require either electrical multiplexing schemes or all optical ones. At the end point, the optical signal must be converted to an electronic one meaning that some form of integrated optoelectronics is also important. Monolithic integration of optics with electronics is thus useful for both end point as well as multiplexing in the electrical domain. In addition, high density optical interconnection enables the fabrication of optical systems on a chip, which allows high functionality without cost.

5.3 On chip optical data communication

Full scale optical interconnection, in which different sections of a chip communicate via optical interconnects, requires, in addition to all the optical and electro-optical elements mentioned previously, many small narrow band lasers or a few high powered broad band lasers coupled with good WDM scheme. An on-chip optical switch is also required. A schematic for optical interconnects is shown in Figure 5-6.

Multi-Chip Modules The above schemes may be easily extended to multi-chip modules, allowing high speed integration of chips in a module. In a multi-chip module, a several chips are integrated into a single package. There is usually a high speed interconnection between the chips within the package and much slower interconnection to and from the package. If the chips are integrated using a piece of silicon wafer, one could envision very high speed optical interconnection between these chips, using the waveguiding techniques which have been studied in this thesis.

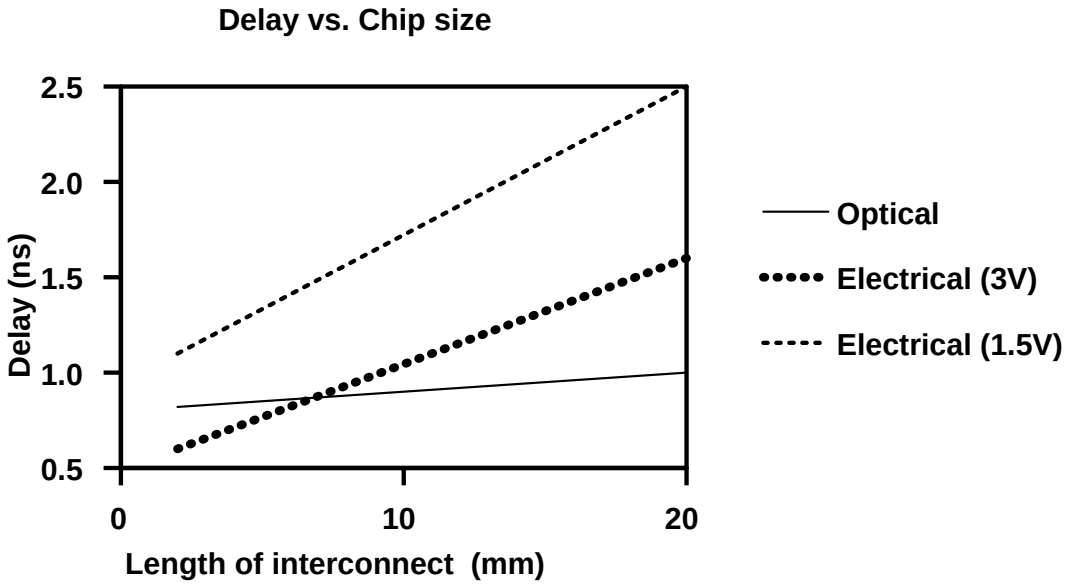

Figure 5-5: Figure showing the trade-off between electrical and optical interconnection schemes.

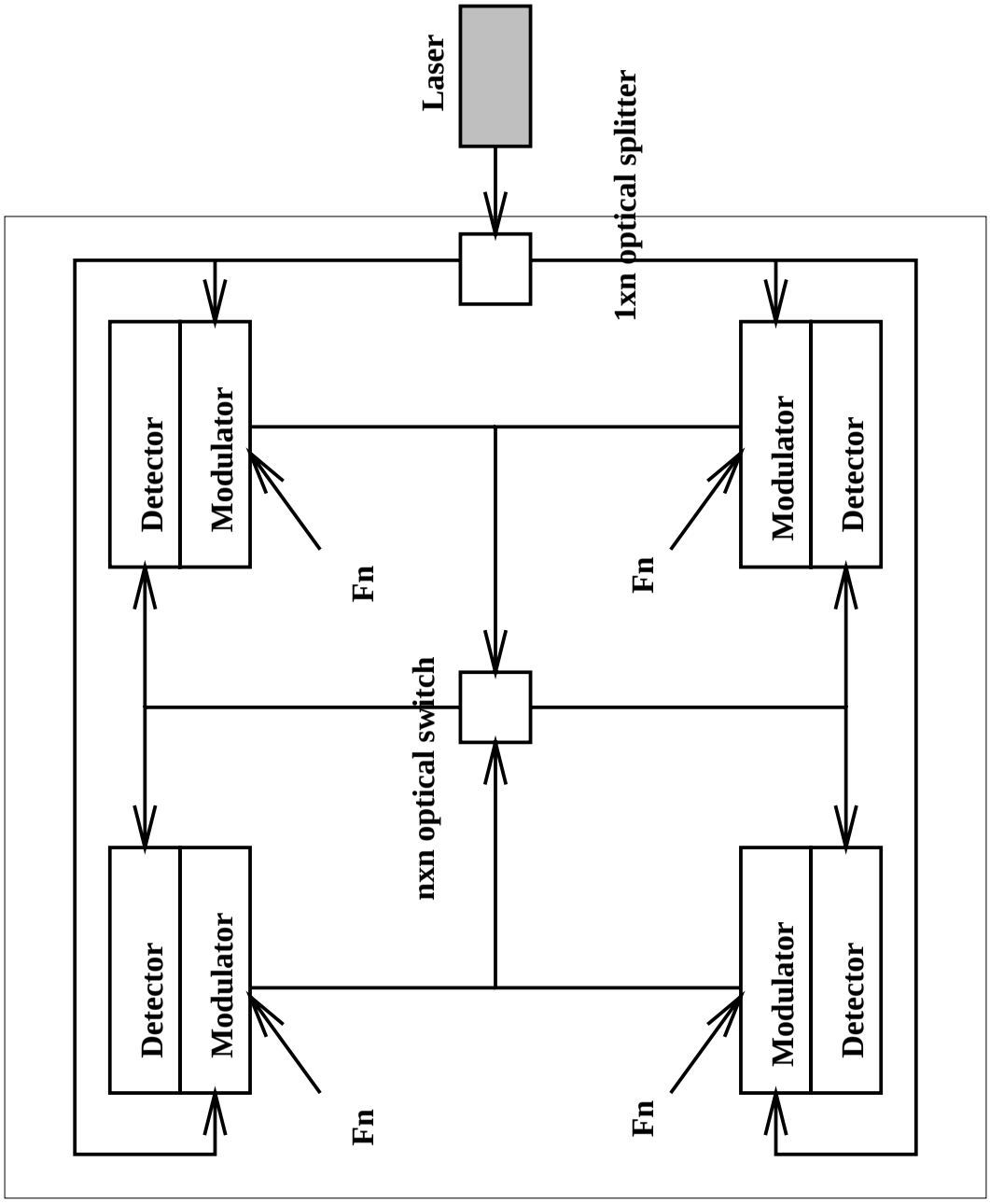

Figure 5-6: Schematic of Optical Interconnects.

5.4 Polarization Control

One of the major challenges raised in chapter 2, is the fact that the polarization dependence of the waveguides needs to be controlled. The main problems with polarization dependence are:

- polarization dependent loss, where the loss of one mode is much greater than the other, which leads to noise if the input polarization is a randomly changing. This is brought about by asymmetry in core/cladding interface roughness and size due to design or fabrication error.

- polarization mode dispersion, where the two modes have different group velocities, resulting in pulse broadening. This may brought about due to variations in size, which may be due to design or fabrication error.

- noise in filters because the filters may have different responses for each polarization. Small amounts of polarization dependent loss and polarization mode dispersion can change the response of narrow filters. This effect is arguably the more critical than the first two.

There are several ways to deal with polarization in waveguides. The first is to make the waveguide anti-symmetric, so that only one of the polarizations survives. This is the idea behind the 0.2 μm X 0.5 μm silicon waveguide, in which only the TE mode may propagate. In systems such as on chip optical clock distribution, the incoming polarization is controlled and this may be a viable option. However, if the incoming polarization changes randomly, then this method is akin to infinite polarization dependent loss and this may not be the best solution. The problem of randomly incident polarization is critical in integrated optics applications for fiber optic networks, since it is difficult to predict the polarization of light coming out of a long distance optical fiber. On the other hand, Professor Ippen, has proposed the use of two sets of chips, one with a set of waveguides that handles only TE and the other that handles only TM. In this way, the polarization dependence is dependent only on the accuracy of the filters on the chips.

Another way to deal with polarization is to reduce the index contrast of the waveguide, which immediately alleviates the polarization dependent loss and the polarization mode

dispersion of the waveguides. Again, the polarization dependence of the filter responses may not be completely addressed.

A third and most direct way to deal with polarization is simply to design waveguides with polarization tolerance (symmetric waveguides), to improve core/cladding interface roughness and to improve fabrication tolerance control.

5.5 Integration Issues

In this section, integration of various components like detectors and modulators with waveguides is studied. If the modes of each of the components are very different the coupling efficiencies from one component to the next will be low.

5.5.1 Coupling

Different components can have different modal shapes. For example an input fiber can have a mode size of 5-10 μm vs. 0.2 μm X 0.5 μm for a strip waveguide. The small mode overlap implies that if a cleaved fiber is butt coupled to a silicon strip waveguide the efficiency will be smaller than 1%, which is poor.

Fiber to waveguide coupling

Fiber to waveguide coupling is the most critical coupling problem [12] for high index contrast waveguides, because the mode sizes of fibers and the high index contrast waveguides are so different.

Reflection off the polished facet in end-fire coupling is also a problem, (see equation (2.56)), especially with silicon waveguides.

Fiber lensed coupling A lensed tipped fiber, is a fiber which is terminated by conical end. This enables the mode of the fiber to be focussed to a spot which is about 2 in diameter. Although this spot size is a much bigger than high index contrast silicon waveguides, the size of the mode is much smaller than that of the fiber itself. The coupling efficiency of fiber lensed coupling is between 12-15 dB. While this is a substantial improvement over butt coupling methods, a significant amount of power is still lost on coupling.

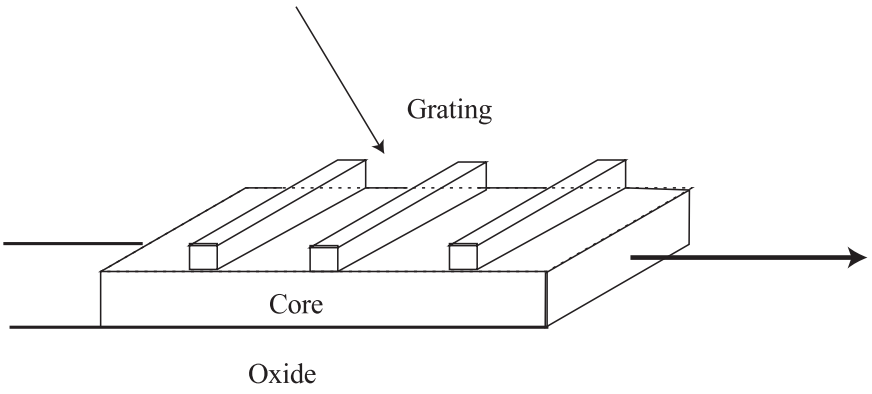

Figure 5-7: Schematic of grating coupling.

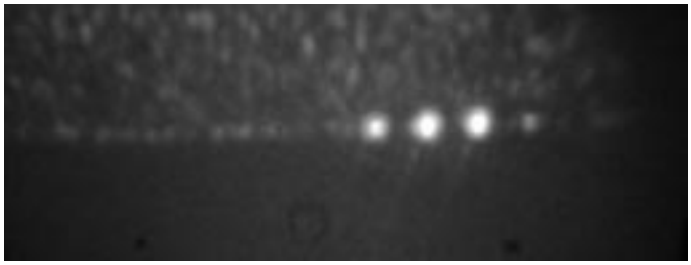

Figure 5-8: Picture showing the output of 3 grating coupled waveguides.

Grating coupling The principle of grating coupling is to use a grating to deflect the light into the waveguide. If the Bragg angle of the dominant scattered mode is equal to the angle of the mode in the waveguide, efficient coupling is possible [100]. Grating coupling is most efficient when the incident wave is a plane wave and is commonly to couple plane waves into slab waveguide systems. Grating coupling was attempted on silicon nitride and silicon waveguides. In order to minimize the number of masks, the grating strength used was 100%. The period of the grating Λ was chosen so that with an incident angle at normal incidence, the angle of the first order mode is at the critical angle, ϕ. Then, the Bragg condition reduces to

$$\Lambda \sin\phi = m\frac{\lambda}{n_{eff}} \tag{5.1}$$

The period of the grating is thus approximately 1 μm. Unfortunately the coupling efficiency is poor because the size of the grating is limited by the width of the taper that was used. Furthermore, the strength of the grating was not optimized. Finally, the grating period assumed an incident plane wave. Obviously this is not true since the grating size is so small. In fact the incident light is a Gaussian. Future designs would take this into account

to optimize the coupling efficiency [101].

The main advantage of grating coupling is that it enables vertical integration of fibers onto the chip. This would in turn increase the number of fibers which can be integrated on a chip. If the width of a single mode fiber (including cladding) is 0.5 mm, then one can fit at most 80 fibers around the perimeter of a 1 cm by 1 cm chip, but one can fit 400 fibers vertically into a 1 cm by 1 cm chip.

5.5.2 Waveguide to detector coupling

In general, the waveguiding material (whether it is silicon or silicon nitride) has to have wider band-gap than the detector material. This would enable the waveguide material to be transparent and the detector material to be absorptive. On the other hand, a wider band-gap material, also has a smaller index. This means that there is an index mismatch between the waveguide and the detector. The size of the single mode strip waveguides are so small that it is easier to make detectors which are bigger than the waveguides. This, however, leads to a modal mismatch problem. In this section, we consider two cases to study efficient coupling.

High index contrast between detector and waveguide

This would be the case for a Ge detector with a silicon waveguide [38]. In this case, due to the smaller index mismatch, coupling efficiencies approaching 100% are easily achievable by terminating the waveguide into a detector of the same cross-sectional area.

Low index contrast between detector and waveguide

This would be the case for a silicon nitride waveguide with a germanium or silicon detector. The easiest structure to fabricate would be a low index waveguide directly over the high index detector. However, the amount light absorption that occurs is minimal especially if the detector waveguide coupling length is small. Over a distance of 10 μm less than 10% of the light couples into the detector. For higher efficiency the nitride waveguide should terminate into the Ge detector. A one-time reflection occurs resulting in 10% of the light being lost but 95% of the remaining light can be captured by the Ge detector.

There are, however, fabrication difficulties with terminating a waveguide onto a detector this way. The easiest way might be to use Chemo-Mechanical Polishing (CMP) Another

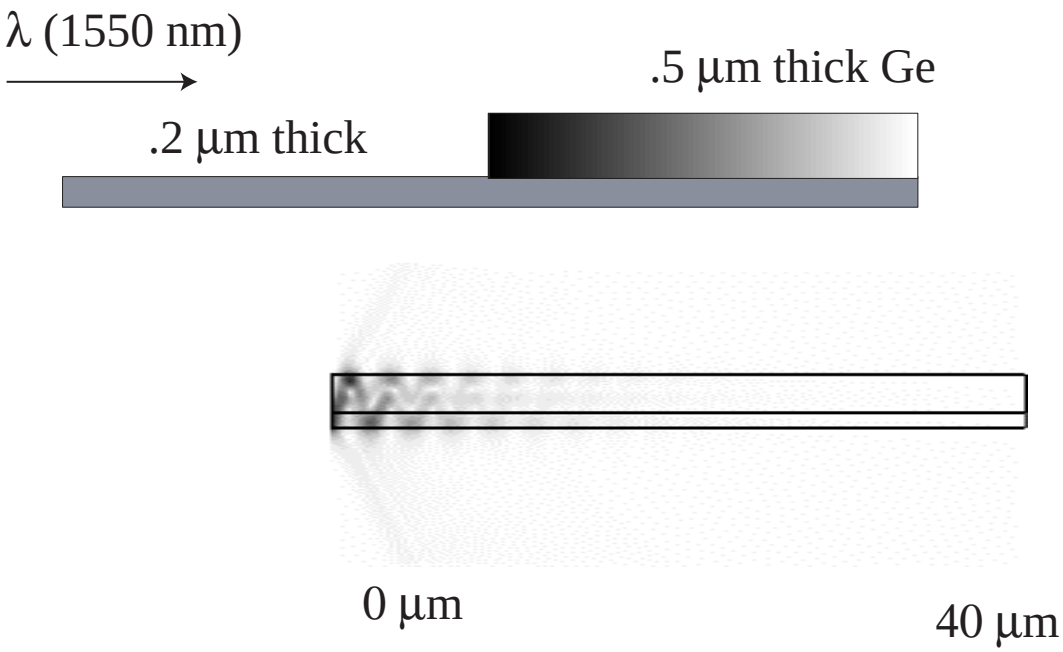

Figure 5-9: Schematic of high Δn waveguide - detector integration. Due to good index matching, it is not difficult to integrate a detector to a high index waveguide. In this figure ,a detector is grown on top of a single crystalline silicon waveguide.

idea would be to use a grating, which would be able to diffract the light into the detector. Another complication arises in the case of Ge grown by selective epitaxy because of the sloped mesa walls. These mesa walls act as very good reflectors if a low index waveguide is run over the side-wall. As a result most of the power in the low index waveguide will be reflected straight up and away from the detector material. No satisfactory solution has been found to this problem, other than an additional mesa etch to remove this sloping side-wall.

5.5.3 Emitters

As has been previously mentioned, due to the indirect band-gap nature of silicon, light emission in silicon is difficult. The following three schemes have been proposed as means of integrating light emitters on silicon.

Hybrid schemes

Hybrid schemes to integrate light emitters on silicon has seen the most research activity work, in part because this scheme can be readily implemented in a laboratory. Examples of hybrid schemes include, integration of GaAs and other III-V based lasers and LEDS as

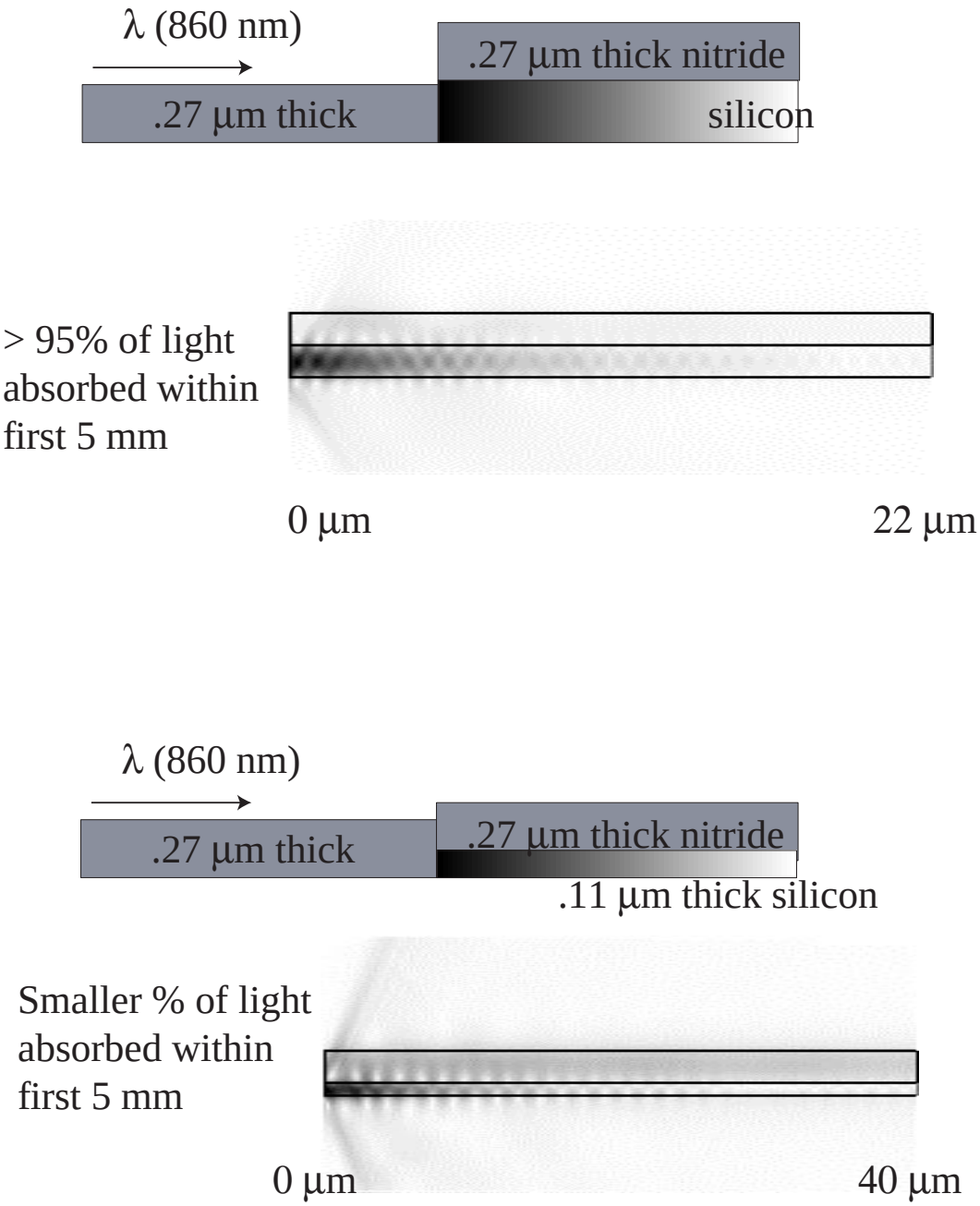

Figure 5-10: Schematic of low Δ n waveguide-detector integration. This is difficult because the power has a tendency to reflect off the detector waveguide interface. Thus butt coupling is most efficient.

well as detectors on a silicon substrate. This hybridization has been achieved by (in order of decreasing integration):

- epitaxy of GaAs on silicon and SiGe substrates, which would provide seamless opto-electronic integration to silicon. However, the processing involved is difficult.
- bonding GaAs sources and detectors to the substrate. Although this is a straight forward concept, there exist alignment issues with respect to electronic contacts and more importantly to optical waveguides.
- off-chip inter-connection of III-V and other sources. Alignment here is reduced to the external fiber to waveguide coupling. However, most of the advantages of integration, such as low cost production is lost in this scheme.

Silicon optical bench technology has also been widely used [102, 103]. In this case on-chip Er doped silica amplifiers may be envisioned but these have to optically pumped.

Polymer based emitters have also been proposed. These are interesting since they are reasonably cheap to make, and have been proven to give reasonable intensity. In addition, there is a lot of active research in electro-optic polymers and polymer waveguides in general [104, 104]. They do suffer from relatively short lifetimes (measured in the tens of thousands of hours).

Silicon based emitters

Er implanted in silicon has been extensively studied as it has a sharp luminescence at a wavelength of 1550 nm. [34, 35]. One of the problems with erbium in silicon is that its non-optical de-excitation mechanism at room temperature is much faster than its optical de-excitation mechanism. This means that most of the time of the excited Er de-excites non-optically and the total amount of Er which does end up emitting light is very small. Thus efficiencies of room temperature devices are low. Micro-cavity devices [105, 106, 107, 108] have been shown to enhance the spontaneous emission of light emitting diodes [109, 110, 111]. An obvious extension to this work is to implant Er into high Q silicon rings.

Experiment Porous silicon and Erbium doped silicon [34] have been proposed as means of having light emission from silicon. To study this technology, $10^{16} cm^{-2}$ Er and O were co-implanted into polySi rings fabricated at Lincoln Labs. To ensure that the Er is uniformly

distributed multiple implants were used. After implants the rings were annealed at 600^{o}C for 16 hours and at 800^{o}C for 30 minutes [112]. However, after the implant the polySi waveguides exhibited higher loss and it was difficult to get any transmission through the waveguides. This problem needs to be investigated further.

5.5.4 Detectors

The type of detector used depends on the wavelength chosen. For wavelengths of light above 1 μm, Ge, SiGe detectors have to be used.

Below 1 μm however, silicon detectors can be used with great efficacy. Numerous papers have been published about using silicon detectors in integrated optics [27].

Single crystalline detectors

Single crystalline SiGe and silicon detectors have high quantum and collection efficiency which is useful when the material has an absorption coefficient on the order of a 100 cm^{-1}.

However, they tend either to be large or exhibit poor modal confinement because they cannot be grown on top of on amorphous oxide layer. As a result, coupling of energy from a small, well confined waveguide to a large, weakly confined detector, is extremely inefficient due to modal mismatch between the detector and the waveguide [37]. Thus a significant quantity of the light may be radiated and lost especially if the absorption coefficient of the material is not large.

Polycrystalline detectors

Conversely polySi detectors can be grown on oxide so the optical mode of the detector can be matched to that of the detector. However, these detectors may face problems with dark current, quantum efficiency, collection efficiency and carrier sweep out time.

The principle behind using polycrystalline detectors with waveguides is that if they can be made small enough the collection efficiency and carrier sweep out times problems may be minimized, resulting in small low capacitance devices. The dark current can be made small if high resistivity polySi is used.

By monolithically integrating a polySi detector with silicon nitride waveguides or a polycrystalline germanium detector, one might be able to get essentially a 100% coupling efficiency which is much better than the coupling efficiencies of the large single crystalline

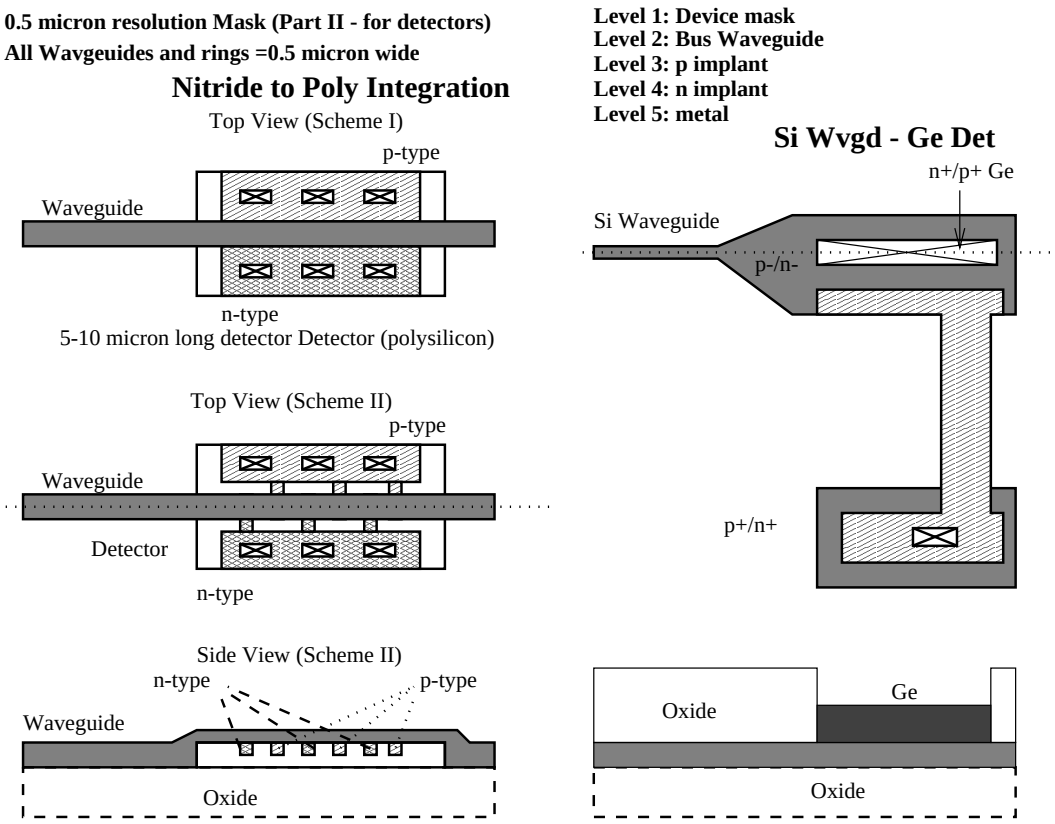

Figure 5-11: Schematic of and fabrication of a polySi detector.

detectors. The only drawback of such a scheme would be grain boundary induced recombination which would kill quantum efficiency. One possible design would be to flare the waveguide from 0.5 μm wide to about 1 to 2 μm wide to increase the space with which one might be able to put contacts on the detector.

5.6 Loss budget

One of the most important issues in optical interconnection is loss. Reduction of loss reduces the power requirement on the emitters, reduces the need for amplifiers and improves the signal to noise ratio. For example, in the case of the optical clock distribution circuit shown in figure 5-1, an optical power of 10 μA is required at the detector. Taking figure 5-1 as a baseline, the total insertion loss of using single mode 0.5 μm X 0.2 μm SOI waveguides can be calculated using the data found in this thesis. If one assumes total wavelength of 1 cm,

10 bends, 4 Y-splits to achieve 1x16 splitting ratio, then from chapters 2, 3 and 5

$$\begin{aligned}
\text{Transmission Loss} &= 14\text{dB/cm} \\
\text{Splitting loss} &= 0.15\text{dB/split} \\
\text{Bending loss (R} = 2\ \mu\text{m)} &= 0.02\text{dB/bend} \\
\text{Coupling Loss: Fiber to Waveguide} &= 12\text{dB} \\
\text{Coupling Loss: Waveguide to Detector} &= 1\text{dB} \\
\text{Total insertion Loss} &= 28\text{dB}
\end{aligned}$$

This loss is substantial. For silicon nitride waveguide, the losses will be substantially lower. From power transmission experiments, the transmission and fiber to waveguide coupling loss is improved by at least 10 dB. Thus the total insertion loss for a nitride waveguide system is 20 dB, the extra 2 dB being a correction for poorer power coupling from the waveguide to the detector. The required optical power for an optical clocking system based on silicon nitride is 16 mW, which is certainly a power level which is achievable from off the shelf VCSEL components. The analysis above uses values obtained from what has already been achieved in this thesis.

We predict an improvement in the transmission loss to 5 dB/cm using the improved surface roughness loss that has already been demonstrated by Lincoln Labs. Correspondingly an improvement to 5 dB has been predicted for fiber to waveguide coupling. Hence it is possible that the total insertion loss may reach 12 dB for the baseline SOI system and under 10 dB for the baseline nitride system in the near future.

Loss is more critical in the "Million Points of Light" system, since the sum of required peak optical power at the detectors is approximately 50 W. Further, a traditional split may not be efficient at such high split ratios. In fact, the most efficient way of routing such a signal would be to split the signal into 100 equal parts (using an MMI) and then utilizing a low efficiency detector to waveguide coupling method to switch the individual latches. However, at such high powers, non-linear effects will dominate the loss! Thus an optical amplifier would be useful in such a system so that the input power need not be too high and the signal can be regeneratively amplified as it propagates around the chip.

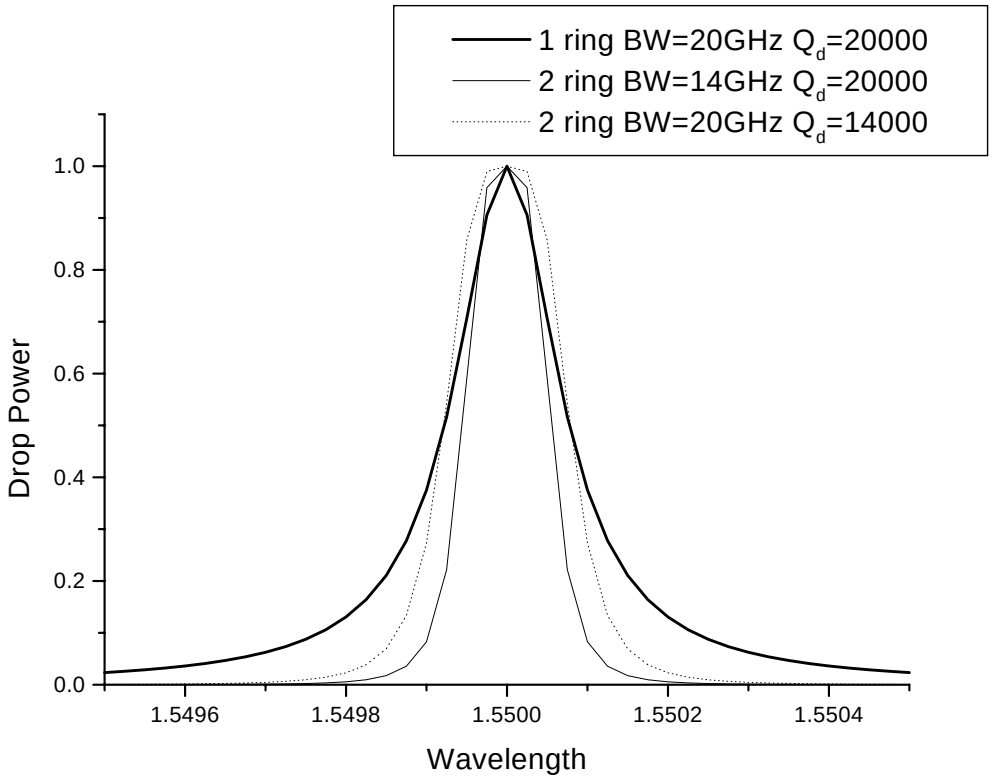

Figure 5-12: Figure showing the ring response as a function of Q_d, which is dependent on gap size. A higher order ring will have a response with smaller bandwidth than the response of a single ring of the same gap size.

5.7 WDM in rings: Q and bandwidth

In chapter 4, a 1X4 WDM De-multiplexor was demonstrated using a device with 4 rings of slight different size. In WDM, the shape of the filter should be as close to a top hat function as possible, since this would allow the maximum bandwidth to pass and 0 cross talk to occur.

Single ring and the associated multi-ring filters can be explained in terms of electrical filter design. The responses of a single and double rings with Q_d=2000 are plotted in figure 5-12. Q_d = 2*Q is the Quality factor due to the coupling of the ring to the drop waveguide and is strictly determined by the size of the gap between the drop and the ring waveguide. The half power bandwidth of a single ring is $\Delta\omega = \frac{\omega}{Q} = \frac{2\omega}{Q_d}$. However, the half power bandwidth of a double ring is different, due to the fact that there is mutual coupling between the rings. Thus to achieve the same half power band-with $Q_d = 14000$. Hence, the gap size must be decreased to preserve the half power bandwidth.

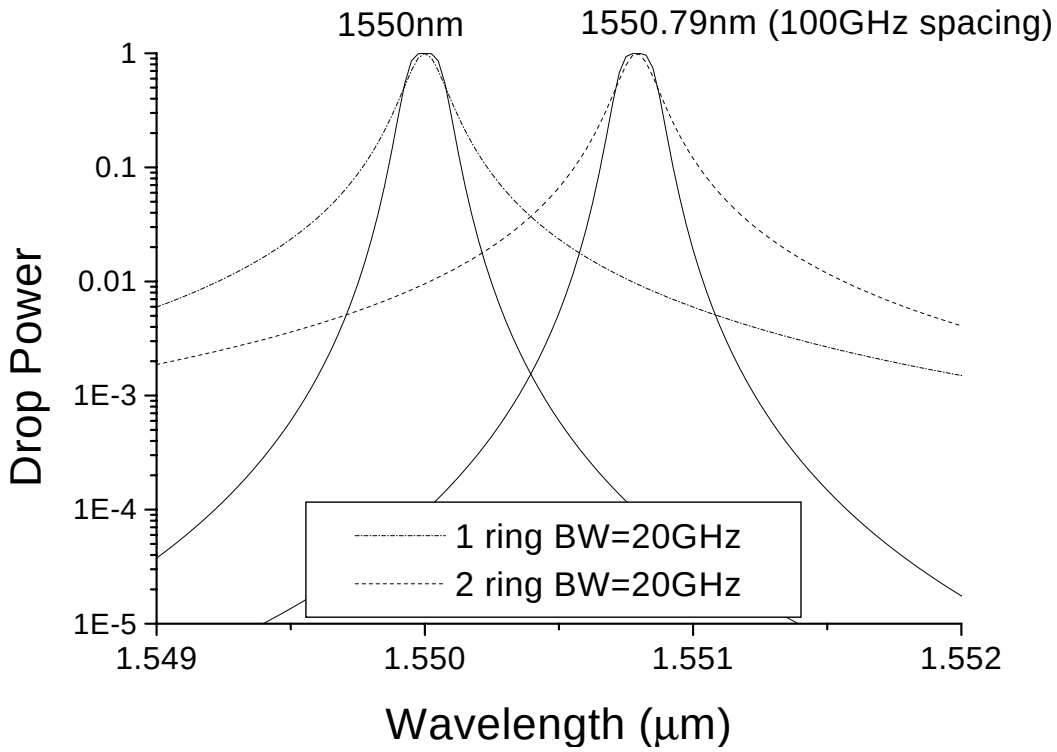

Figure 5-13: Response of single and double rings with 20 GHz bandwidth resonances separated by 100 GHz. The cross-talk for the single ring case is -20 dB. The cross talk for the double ring case is -40 dB.

A single ring resonator has a Lorentzian response. Thus, two very closely spaced single ring resonances will have significant crosstalk. Using the same 20 GHz half power bandwidth shown in figure 5-12, and using a 100 GHz channel spacing one of the ITU standards), we observe significant channel cross talk of about -20 dB (see figure 5-13. This performance is poor; even though the effective channel bandwidth is less than one fifth of the channel spacing, the cross talk is high. Using a 2 rings with the same half power bandwidth, the cross talk is reduced to -40 dB.

5.8 Silicon Microphotonics: The challenge

Silicon microphotonics and integrated optics in general are at exciting crossroads. With the ability to integrate optics onto small silicon chips, one can reduce the size of an optical switching network node from the size of a building to the size of a small box. In the same way, an equivalent of ENIAC, the world's first electronic computer, can now fit in an

area not much bigger than a dime and can run several orders of magnitude faster than its predecessor.

Of course, life would not be exciting without challenges and challenges abound for silicon microphotonics. Some of these are listed here:

- polarization control
- waveguide sidewall roughness especially in high index contrast waveguides
- ring resonator tuning and fabrication inaccuracy
- high speed modulation
- coupling from component to component (especially fiber to waveguide coupling)

If these difficulties are overcome, microphotonics may one day be as common place as microelectronics.

Bibliography

[1] E.A.J. Marcatili. Dielectric rectangular waveguide and directional coupler for integrated optic. *Bell Syst. Tech J.*, page 2071, 1969.

[2] J. A. Kong. *Electromagnetic Wave Theory.* Wiley Interscience, 1990.

[3] H. A. Haus. *Waves and fields in Optioelectronics.* Prentice Hall, 1984.

[4] *Apollo photonics: TFDS manual.*

[5] W. Huang, C. Xu, S. T. Chu, and S. K. Chaudhuri. The finite-difference vector beam propagation method: analysis and assessment. *J. Light. Tech.*, 10(3):295, 1992.

[6] Jay N. Damask. *Integrated-Optic Grating-Based Filters For Optical Communication System.* PhD thesis, MIT, 1996.

[7] B.E. Little, J. P. Laine, D. R. Lim, H. A. Haus, L. C. Kimerling, and S. T. Chu. Pedastal antiresonant reflecting waveguides for robust coupling to microsphere resonators and for microphotonics circuits. *Optics Letters*, 1, 2000.

[8] J. P. Laine, B. E. Little, D. R. Lim, H. C. Tapalian, L. C. Kimerling, and H. A. Haus. Characterization of microsphere whispering-gallery-mode excitation by pedeastal antiresonant reflective waveguide coupler. To be published.

[9] J. P. Laine, D. R. Lim, B. E. Little, H. C. Tapalian, L. C. Kimerling, and H. A. Haus. Planar integrated wavelength-dropping device based on pedastal anti-resonant reflecting waveguides and high-q silica microspheres. To be published.

[10] M. Heiblum and J Harris. Analysis of curved optical waveguides by conformal transformation. *IEEE J. of Quantum Electronics*, QE-11:75, 1975.

[11] R. A. Soref and J. P. Lorenzo. All-silicon active and passive guided-wave components for lambda =1.3and 1.6 mu m. *IEEE J. of Quant. Electron*, QE-22:873, 1986.

[12] James S. Foresi. *Optical Confinement and Light Guiding in High Dielectric COntarst Materials Systems.* PhD thesis, MIT, 1997.

[13] D. Miller and H. Ozaktas. Limit to the bit-rate capacity of electrical interconnects frm the asepect ratio of the system architecture. *Journal of Parallel and Distributed Computing*, October 1996. Special Issue on Parallel Computing with Optical Inteconnects.

[14] Debra Koker. Optimization of infrared optical properties of polysilicon for integrated optics. PhD Thesis Proposal.

[15] Institution of Electrical Engineers. *Properties of Silicon.* 1988.

[16] Sze SM. *Physics of Semiconductor Device.* Wiley Interscience, 1981.

[17] Siddiqi SA and Nazar F M. *Materials chemistry and physics*, 2:157–160, 1994.

[18] B. Saleh and M. Teich. *Fundamentals of photonics.* Wiley-Interscience, 1991.

[19] H. Kogelnik. *Guided-Wave Optoelectronics.* Springer Verlag, 1988.

[20] *Apollo photonics: OWMS manual.*

[21] M A Duguay, Y. Kokubun, and T L Koch. Antiresonant refelcting optical waveguides in sio2-si multilayer structures. *Applied Physics Letters*, 49(1):13, 1986.

[22] Y. Kokubun, T. Baba, and T. Sakaki. *Electron. Lett.*, 22:892, 1996.

[23] Freye R, Th. Delonge, and H. Fouckhardt. Two-dimensional arrows. *Journal of Optical Communications*, 16:42–47, 1993.

[24] T. Baba, Y. Kokubun, and H. Wanatanabe. Monolithic integration of an arrow-type demultiplexer and photodetector in the shorter wavelength region. *Journal of Lightwave technology*, 8:99, 1990.

[25] J. M. Kubica. A rigorous design method for antiresonant reflecting optical waveguides. *IEEE Photonics Technology Letters*, 6:1460, 1994.

[26] V.G. Pan'kin and V. V. Shashkin. Electrooptic effect in silicon nitride. *Sov. Tech. Phys. Lett.*, 4(4):420, 1996.

[27] U. Hilleringmann and K. Goser. Optoelectronic system integration on silicon: Waveguides, photodetectors, and vlsi cmos circuits on one chip. *Applied Physics Letters*, 68:170, 1996.

[28] P. May, S. Basu, G.L.T. Chu, and G. Arjavalingam. Model dispersion and attenuation measurements of silicon nitride and silicon oxynitride waveguides using a streak camera. *Journal of Lightwave Technology*, 8(2):235, 1996.

[29] H. J. Lee, C. H. Henry, K. J. Orlowsky, R. F. Kazarinov, and T. Y. Kometani. Refractive-index despersion of phosphosilicate glass, thermal oxide, and silicon nitride films on silicon. *Applied Optics*, 27:4104, 1988.

[30] M. Hanabusa and Y. Fukuda. Single-step fabrication of ridge-type glass optical waveguides by laser chemical vapor deposition. *Applied Optics*, 28:11, 1989.

[31] M. Ohtani and M. Hanabusa. Silicon nitride ridge-type optical waveguides fabricated on oxidized silicon by laser direct writing. *Applied Optics*, 31:5830, 1992.

[32] S. Sriram, W. D. Paltrow, and C. S. Liu. Low-loss optical waveguides using plasma-deposited silicon nitride. *Applied Optics*, 22:3664, 1983.

[33] J. Aarnio and P. Heimla. Birefringence control and dispersion charactersitics of silicon oxy nitride optical waveguides. *Ekectronics Letters*, 27:2317, 1991.

[34] B. Zheng, J. Michel, F. Ren, L Kimerling, D. Jacobson, and J Poate. Room termpartaure sharp line electroluminsescence at λ=1.54μm from an er doped silicon light emitting diode. *Applied Physics Letters*, 1994.

[35] Y. G. F. Ren, J. Michel, Q. Sun-Paduano, B. Zheng, H. Kitagawa, D. C. Jacobson, J. M. Poate, and L. C. Kimerling. Rare earth doped semiconductors. In G. S. Pemrenke, P. B. Klein, and D. W. Langer, editors, *MRS Proc.*, volume 31, Pittsburgh, PA, 1993.

[36] L. Giovane, L. Liao, D Lim, and A. Argawal et. al. $Si_{0.5}ge_{0.5}$ relaxed buffer photodetectors and low-loss polycrystalline silicon waveguides for integrated optical interconnects at $\lambda = 1.3\mu$m. In *Proceedings for SPIE Photonics West Wan Jose 1997*, 1997.

[37] L. Giovane, D Lim, L Kimerling, and E Fitzgerald. Strong absorption gesi on si materials for 1.3 μm photodetection. In *EMC*, 1997.

[38] Hsin-Chiao Luan, D.R. Lim, K.K. Lee, K.M. Chen, J.G. Sandland, K. Wada, and L.C. Kimerling. High-quality ge epilayers on si with low threading-dislocation densities. *Applied Physics Letters*, 75:2909, 1999.

[39] R. A. Soref and B. R. Bennett. Electro-optical effects in silicon. *IEEE J. of Quant. Electron*, QE-23:123, 1987.

[40] R. A. Soref, J. Schmidtchen, and K. Petermann. Large single-mode rib waveguides in gesi-si and si-on-sio2. *IEEE JQE*, 27(8):1971, 1991.

[41] B. L. Weiss, G. T. Reed, S. K. Toh, R. A. Soref, and F. Namavar. Optical waveguides in simox structures. *IEEE Phot. Technol. Lett.*, 3(19), 1991.

[42] Desmond Lim. Simulation of single mode si waveguides and electro-optic coupling modulators. S.B. Thesis.

[43] U. Fischer, T. Zinke, J. R. Kropp, F. Arndt, and K. Petermann. 0.1 db/cm waveguide losses in single-mode soi rib waveguides. *IEEE Phot. Tech. Lett.*, 8(5):647, 1996.

[44] U. Fischer, T. Zinke, B. Schuppert, and K. Petermann. Single-mode optical switches based on soi waveguides with large cross-section. *Electron. Lett.*, 30(5):406, 1994.

[45] Marcie Black. Loss in polysilicon waveguides. Master's thesis, MIT, 1995.

[46] J. S. Foresi, M. R. Black, A. M. Agarwal, and L. C. Kimerling. Losses in polycrystalline silicon waveguides. *Appl. Phys. Lett.*, 68:2052, 1996.

[47] A. M. Agarwal, L. Liao, J. S. Foresi, M. R. Black, X. Duan, and L. C. Kimerling. Low-loss polycrystalline silicon waveguides for silicon photonics. *J. Appl. Phys.*, 80(11), 1996.

[48] W. B. Jackson, N. M. Johnson, and D. K. Biegelsen. Density of gap states of silicon grain boundaries determined by optical absorption. *Appl. Phys. Lett.*, 43(2):195, 1983.

[49] S. P. Wesolowski R. E. Jones, Jr. Electrical, thermoelectric, and optical properties of strongly degenerate polycrystalline silicon films. *J. Appl. Phys*, 56:1701, 1984.

[50] Ling Liao. Low loss polysilicon waveguides for silicon photonics. Master's thesis, MIT, 1997.

[51] L. Liao, D. Lim, J. Foresi, and X. Duan et. al. Effect of grains and grain boundaries in polycrystalline silicon waveguides. In *EMC*, 1997.

[52] P.K. Tien. Light waves in thin films and integrated optics. *Aplied Optics*, 10(11):2395, 1971.

[53] B. E. Little. A variational coupled-mode theory including radiation loss for grating-assisted couplers. *J. of Lightwave Tech.*, 14(2):188, 1996.

[54] G. Tittelbach, B. Rchter, and W. Karthe. Comparison of three transmission methods for integrated optical waveguide prpagation loss measurements. *Pure Appl. Optics*, 2, 1993.

[55] S.C. Palmateer C. Nelson. Critical dimension control for .13 μm lithography phase iv final report. Technical report, Sematech, 1999.

[56] K. K. Lee, D. R. Lim, H-C Luan, A. Agarwal, J. S. Foresi, and L. C. Kimerling. The effect of size and roughness on light transmision in a si/sio$_2$ waveguide: Experiments and model. Submitted to App. Phys. Lett., 2000.

[57] J. Foresi, D. Lim, A. Agarwal, and L. Kimerling. Small radius bends and large angle splitters in soi waveguides. In *Optoelectronics '97 Sysmposium Silicon-based Monolithic and Hybrid Optoelectronics Devices*, 1997.

[58] D. Marcuse. Bending losses of the asymmetric slab waveguide. *Bell Syst. Tech. J.*, 50(8):2551, 1971.

[59] E.A.J. Marcatili. Bends in optical dielectric guides. *Bell Syst. Tech J.*, page 2103, 1969.

[60] C. Manolatou, S.G. Johnson, S. Fan, P.R. Villeneuve, H.A. Haus, and J.D. Joannopoulos. High-density integrated optics. *Journal of Lightwave Technology*, 17(9), 1999.

[61] R. Ulrich and G. Ankele. Self-imaging in homogeneous planar optical waveguides. *Applied Physics Letters*, 27(6):337, September 1975.

[62] T. Rasmussen, J. Rasmussen, and J. Povlsen. Design and performance evaluation of 1-by-64 multimode interference power splitter for optical communications. *Journal of light wave technology*, 13(10):2069, October 1995.

[63] D.S. Levy, R. Scarmozzino, Y. M. Li, and T. M. Osgood. A new design for ultracompact multimode interference-based 2x2 couplers. *IEEE Photonics Technology Letters*, 10:96, 1998.

[64] D.S. Levy, R. Scarmozzino, and T. M. Osgood. Length reduction of tapered nxn mmmi devices. *IEEE Photonics Technology Letters*, 10:830, 1998.

[65] L. B. Soldano and E. C. M. Pennings. Optical multi-mode interference devices based on self-imaging: Principles and applications. *Journal of Lightwave Technology*, 13:615, 1997.

[66] S. Kareenahalli, M. Dagenais, D. Stone, and T. J. Tayag. Experimental confirmation of phase relationships of multimode interference splitters using a shearing-type near-field sagnac interferometer. *IEEE Photonics Technology Letters*, 9:937, 1997.

[67] C.C. Wang, M. Currie, S. Alexandrou, and T. Y. Hsiang. Ultrafast all-silicon light modulator. *Optics Letters*, page 1453, 1994.

[68] M. Liu and S. Chou. High modulation depth and short-cavity-length silicon fabry-perot modulator with two bragg reflectors. *Applied Physics Letters*, page 170, 1996.

[69] G. Cocorullo, M. Iodice, and I. Rendina. All-silicon fabry-perot modulator based on the thermo-optic effect. *Optics Letters*, (6):420, 1996.

[70] W. Wiszniewski, R. Collins, and B. Pailthorpe. Mechanical light modulator fabircated on a silicon chip using simox technology. *Sensors and Actuators A*, 43:170–174, 1994.

[71] G. Treyz, P May, and J. Halbout. Silicon optical modulators at 1.3 microns based on free carrier absorption. *IEEE Electron Device Letters*, 12(6), June 1991.

[72] R. Normandin, D. Houghton, and M. Simard-Normandin. All-optical, silicon based, fiber optic modulator using a near cutoff region. *Can. J. Phys.*, 67:412, 1989.

[73] P. Heimala, P. Katila, and J. Aarnio. Integrated optical ring resonator on silicon with thermal tuning and in situ temperature measurement. *SPIE*, 2695:71, 1996.

[74] H. Chao and G. Neudeck. Fabry-perot optical intensity modulator using merged epitaxial lateral overgrowth silicon films. *SPIE*, 1779:164, 1992.

[75] A. Cutolo, M. Iodice, P. Spirito, and L. Zeni. Silicon electro-optic modulator based on a three terminal device integrated in a low-loss single-mode soi waveguide. *Journal of Lightwave Technology*, 15:505, 1997.

[76] A. F. Levi, R. E. Slusher, S L. McCall, J. L. Glass a nd S. J. Pearton, and R. A. Logan. Directional light coupling from microdisk lasers. *Applied Physics Letters*, 62:561–563, 1993.

[77] J. P. Zhang, D. Y. Chu, S. L. Wu, S. T. Ho, W. G. Bi, C. W. Yu, and R. C. Tiberio. Photonics wire laser. *Phys. Rev. Lett.*, 75:2678–2681, 1995.

[78] B. E. Little, S. T. Chu, H. A. Haus, J. S. Foresi, and J. P. Laine. Microring resonator channel dropping filter. *Journal of Lightwave Technology*, 15:998–1005, 1997.

[79] D. Rafidazeh, J. P. Zhang, S. C. Hagness, A. Taflove, K. A. Stair, S. T. Ho, and R.C. Tiberio. Waveguide-coupled algaas/gaas microcavity ring and disk resona tors with high finesse and 21.8 nm free spectral range. *Optics Letters*, 22:1244–1246, 1997.

[80] J. S. Foresi, P. R. Villeneuve, J. Ferrera, E. R. Th oen, G. Steinmeyer, S. Fan, J. D. Joannopoulos, L. C. Kimerling, Henry I. Smith, and E. P. Ippen. Photonic-bandgap microcavities in optical waveguides. *Nature*, 390:143–145, 1997.

[81] B. E. Little, J. S. Foresi, G. Steinmeyer, E. R. Thoen, S. T. Chu, H. A. Haus, E. P. Ippen, L. C. Kimerling, and W. Greene. Ultra-compact si-sio$_2$ microring resonator optical channel dropping filters. *IEE Photonics Technology Letters*, 10:549–551, 1998.

[82] C. K. Madsen and J. Zhao. Postfabrication optimization of an autoregressive planar waveg uide lattice filter. *Applied Optics*, 36:642–647, 1997.

[83] S. Suzuki, K. Shuto, and Y. Hibino. Integrated-optic ring resonators with two stacked layers of si lica waveguide on si. *IEEE Photonics Technology Letters*, 4:1256–1258, 1992.

[84] L. Collot, V. Lefevre-Seguin, M. Brune, J.M. Raimond, and S. Haroche. Very high-q whispering gallery mode resonances observed on fused silica microspheres. *Europhys. Lett.*, 23:327, 1993.

[85] M. L. Gorodetsky, A. A. Savchenkov, and V.S. Ilchenko. Ultimate q of optical microsphere resonators. *Optics Letters*, 21:453, 1996.

[86] F. Treussart, N. Dubreuil, J. Knight, V. Sandoghdar, j. Hare, V. Lefervre-Seguin, J. M. Raimond, and S. Harche. Microlasers based on silica microspheres. *Ann. Telecommun.*, 52:557, 1997.

[87] H. A. Haus and W. Huang. Coupled mode theory. *Proceedings of the IEEE*, 79:1505, 1991.

[88] B.E. Little, S.T. Chu, H.A. Haus, J.Foresi, and J.P. Laine. Microring resonator channel dropping filters. *Journal of Lightwave Technology*, 15:998, 1997.

[89] C. Manolatou, M.J. Khan, P.R. Villeneuve S. Fan, Haus HA, and Joannopoulos JD. Coupling of modes analysis of resonant channel add-drop filters. *IEEE Journal of Quantum Electronics*, 35:1322, 1999.

[90] B. E. Little, J.-P. Laine, and S. T. Chu. Surface-roughness-induced contradirectional coupling in ring a nd disk resonators. *Optics Letters*, 22:4–6, 1997.

[91] P. Heimala, P. Katila, K. Aarnio, and A. Heinåmåk i. Thermally tunable integrated optical ring resonator with poly- si thermistor. *Journal of Lightwave Technology*, 14:2260–2267, 1996.

[92] D. Rafizadeh, J. P. Zhang, S. C. Hagness, A. Taflove, K. A. Stair, and S. T. Ho. Temperature tuning of microcavity ring and disk resonators at 1.5μm. In *IEEE LEOS 10th Annual Meeting*, volume WT2, pages 162–163, 1997.

[93] L Maleki V. S. Ilchenko, X. S. Yao. Pigtailing the high-q microsphere cavity: a simple fiber coupler for optical whispering-gallery modes. *Optics Letters*, 24:723, 1999.

[94] J. C. Knight, G. Cheung, F. Jacques, and T. A. Birks. Phase-matched excitation of whispering-gallery-mode resonances by a fiber taper. *Optics Letters*, 22:1129, 1997.

[95] S Schiller and R Byer. High-resolution spectroscopy of whispering gallery modes in large dielectric spheres. *Optics Letters*, 16:1138, 1991.

[96] C. Ming, G. Hunziker, and K. Vahala. Fiber-optic add-drop device based on a silica microsphere whispering gallery mode system. *photonics Technology Letters*, 11:686, 1999.

[97] A. V. Krishnamoorthy. Firehouse architectures for free-space optically-interconnected vlsi circuits. *Journal of Parallel and Distributed Computing*, November 1996. Special Issue on Parallel Computing with Optical Inteconnects.

[98] A. Krishnamoorthy. Scaling optoelectronic-vlsi circuits into the 21st century: A technology road. *IEEE Journal of Selected Topics in Quantum Electronics*, 2(1):55, April 1996.

[99] Interconnect focus center annual review.

[100] G. W. Taylor and C. Kwan. Diffraction into a corrugated waveguide from normally incident radiation. *Journal of Lightwave Technology*, 16:2393, 1998.

[101] T. Liao, S. Sheard, M. Li, J. Zhu, and P. Prewett. High effciency focusing wavguide grating coupler with parallelogramic groove profiling. *Journal Of Lightwave Technolog*, 15:1142, 1997.

[102] Y. Shani, C. Henry, R. Kistler, R. Kazarinov, and K. Orlowsky. Integrated optic adiabatic devices on silicon. *IEEE Journal of Quantum Electronics*, 27(3), March 1991.

[103] R. Adar, Y. Shani, C.H. Henry, R. C. Kistler, G. E. Bonder, and N. A. Olsson. Measurement of very low-loss silica on silicon waveguides with a ring resonator. *Appl. Phys. Lett.*, 58:444, 1991.

[104] S. J. Bai, R. J. Spry, M. D. Alexander Jr., and J. R. Barkley. Optical attenuation in planar waveguides of unidirectionally oriented copolyester film. *J. Appl. Phys.*, 79(12):9326, 1996.

[105] M. Unlu and S. Strite. Resonant cavity enhanced photonics devices. *J. Appl. Phys.*, 78(2):607, July 1995.

[106] S. Haroche and J. M. Raimond. Cavity quantum electrodynamics. *Sci. Amer.*, page 54, April 1993.

[107] H. Yokoyama. Physics and device applications of optical microcavities. *Science*, 256:66, 1992.

[108] Y. Yamamoto, S. Machida, and G. Bjork. Micro-cavity semiconductor lasers with controlled spontaneous emission. *Opt. Quant. Elec.*, 24:S215, 1992.

[109] D. Kleppner. Turning off the vacuum. *Phys. Rev. Lett*, 47(4):233, 1981.

[110] E. Yablonovitch. Inhibited spontaneous emission in solid-state physics and electronics. *Phys. Rev. Lett.*, 58(20):2059, 1987.

[111] A. M. Vredenberg, N. E. J. Hunt, E. F. Schubert, D. C. Jacobson, J. M. Poate, and G. J. Zydzik. Erbium implantation in optical microcavities for controlled spontaneous emission. *Phys. Rev. Lett.*, 71(4):517, 1993.

[112] Thomas D Chen. *Energy Transfer and Luminescence Enhancement in Er-doped Silicon.* PhD thesis, MIT, 1999.

[113] M. Bruel. Application of hydrogen ion beams to silicon on insulator material technology. *Nucl. Inst. Meth. Phys. Res. B*, 108:313, 1996.

[114] A. Himeno, K. Kato, and T. Miya. Silica-based planar lightwave circuits. *IEEE Journal of selected topics in Quantum Elctronics*, 4:913, 1998.

[115] J. J. G. Allen, S. P. Shipley, and N. Nourshargh. Silica-based integrated optic components. *Optical Engineering*, 32:1011, 1993.

[116] B. E. Little, S. T. Chu, W. Pan, D. Ripin, T. Kane ko, and E. Ippen. Vertically coupled glass microring resonator channel dropping filters. *IEEE Photonics Technology Letters*, 11:215–7, 1999.

[117] M. J. Khan, C. Manolatou, S. Fan, P.R. Villeneuve, Haus HA, and Joannopoulos JD. Mode-coupling analysis of multipole symmetric resonant add/drop filters. *IEEE Journal of Quantum Electronics*, 35:1451, 1999.

[118] C. Dragone, C. A. Edwards, and R. C. Kistler. Integrated optics n x n multiplexer on silicon. *IEEE Photonics Technology Letters*, 3:896, 1991.

[119] C. Dragone. Efficicent nxn star couplers using fourier optics. *Journal of Lightwave Technology*, 7:479, 1989.

[120] C. Dragone, C. H. Henry, I. P. Kaminow, and R. C. Kistler. Efficeint multichannel integrated optics star coupler on silicon. *IEE Photonics Technology Letters*, 1:241, 1989.

[121] R. Adar, C. H. Henry, C. Dragone, R.C. Kistler, and M. A. Milbrodt. Broad-band array multiplexers made with silica waveguides on silicon. *Journal of Lightwave Technology*, 11:212, 1993.

[122] H. Takahashi, S. Suzuki, K. Kato, and I. Nishi. Arrawyed-waveguide grating for wavelength division multi/demultiplexer with nanometre resolution. *Electronics Letters*, 26:87, 1990.

[123] M. Zirngibl, C. H. Joyner, L. W. Stulz, T. Gaiffe, and C. Dragone. Polarisation independent 8x8 waveguide grating multiplexer on inp. *Electronics Letters*, 29:201, 1993.

[124] H. Bissessur, F. Gaborit, B. Martin, P. Pagnod-Rossiaux, J.-L. Peyre, and M. Renaud. 16 channel phased array wavelength demultiplexer on inp with low polarisation sensitivty. *Electronics Letters*, 30:337, 1994.

[125] Polymeric arrayed-waveguide grating multiplexer operating around 1.3 micron. Y. hida and y. inoue and s. imamura. *Electronics Letters*, 30:959, 1994.

[126] N. F. Hartman, J. Cobb, and J. G. Edwards. Optical system-on-achip for chemical and biochemical sensing: the platform. *SPIE Vol. 3537*, page 302, 1998.

[127] W. Lukosz, C. Stamm, H. R. Moser, R. Rryf, and J. Dubendorfer. Difference interferometer with new phase-measurement method as integrated-optical refractometer, humdity sensor biosensor. *Sensors and Actuators B*, 38-39:316, 1997.

[128] C. Stamm and W. Lukosz. Integarted optical difference interferometer as immunosensor. *Sensors and Actuators B*, 31:1996, 1996.

[129] P. Ayras, D. F. Geraghty, S. Honkanen, K. M. Grace, B Swanson, K. Shroul, X. Yang, P. Katila, M. Leppihalme, A. Tervonen, and N. Peyghambarian. Thin film waveguide sensors for chemical detection. *SPIE vol. 3537*, page 310, 1998.

[130] R. Blum, M. Sprave, Jurgen Sablotny, and Manfred Eich. High-electric-field poling of nonlinear optical polymers. *Journal of the Optical society of America B*, 15:318, 1998.

[131] Y. Murakami and M. Ikeda. Single-mode optical y-branching circuit using deposited silica guides. *Electron. Lett.*, 17(12):411, 1981.

[132] J. E. Goell. A circular-harmonic computer analysis of rectangular dielectric waveguides. *Bell Syst. Tech. J.*, page 2133, 1969.

[133] D. Zurhelle, O.Blume, S. Popp, and J. Muller. Highely efficient waveguide-detector coupling structures for integrated opto-electronical circuits on silicon. *Journal of Lightwave Technology*, 14(3):410, March 1996.

[134] Y. Shani, C. Henry, R. Kistler, R. Kazarinov, and K. Orlowsky. Integrated optic adiabatic devices on silicon. *IEEE Journal of Quantum Electronics*, 27(3):556, March 1991.

[135] H. Ennen, G. Pomrenke, A. Axmann, K. Eisele, and J. Schneider W. Haydl. 1.54-mu m luminescence of erbium-implanted iii-v semiconductors and silicon. *Appl. Phys. Lett.*, 43:301, 1983.

[136] Y. Yamamoto, S. Machida, Y. Horikoshi, K. Igeta, and G. Bjork. Enhanced and inhibited spontaneous emission of free excitons in gaas quantum wells in a microcavity. *Opt. Comm*, 80(5,6):337, 1991.

[137] E. Yablonovitch, T. J. Gmitter, R. D. Meade, A. M. Rappe, K. D. Brommer, and J. D. Joannopoulos. 3-dimensional photonic band structure. *Phys. Rev. Lett.*, 67(24):3380, 1991.

[138] J. Humlicek. *Properties of strained and relaxed silicon and germanium*, chapter 4.6 Optical Spectroscopy of SiGe, page 116. INSPEC, 1995.

[139] C.C. Wang, S. Alexandrou, D. Jacobs-Perkins, and T. Hsiang. Comparison of the picosecond characteristics of silicon and silicon on sapphire metal-semiconductor metal photodiodes. *Appl. Phys. Lett*, 64(26):3578, June 1994.